

Imperial College London
Department of Electrical and Electronic Engineering

Polymer-Based 3-D Printing of G-Band Metal-Pipe Rectangular Waveguide Components

Roshan Suresh Payapulli

March 2023

Submitted in part fulfilment of the requirements for
the degree of Doctor of Philosophy (PhD) in
Electrical and Electronic Engineering of Imperial College London and
the Diploma of Imperial College London

Declaration of Originality

I herewith certify that to the best of my knowledge; the content of this dissertation is my own work. All the material which is not my own work has been properly acknowledged. The research presented in this dissertation was conducted by me under the supervision of Prof. Stepan Lucyszyn.

Copyright Declaration

The copyright of this thesis rests with the author. Unless otherwise indicated, its contents are licensed under a Creative Commons Attribution-Non Commercial 4.0 International Licence (CC BY-NC).

Under this licence, you may copy and redistribute the material in any medium or format. You may also create and distribute modified versions of the work. This is on the condition that: you credit the author and do not use it, or any derivative works, for a commercial purpose.

When reusing or sharing this work, ensure you make the licence terms clear to others by naming the licence and linking to the licence text. Where a work has been adapted, you should indicate that the work has been changed and describe those changes.

Please seek permission from the copyright holder for uses of this work that are not included in this licence or permitted under UK Copyright Law.

Table of Contents

Declaration of Originality	2
Copyright Declaration	3
Table of Contents	4
Acknowledgements.....	8
Abstract.....	9
List of Figures	12
List of Tables.....	19
List of Symbols.....	20
List of Abbreviations.....	24
List of Frequency Bands and Waveguide Designations.....	27
1. Overview of Polymer-Based 3-D Printing for Millimeter-Wave MPRWGs	28
1.1. Introduction	28
1.2. Typical Polymer-Based 3-D Printing Techniques.....	30
1.2.1 Fused deposition modeling (FDM)	31
1.2.2 Selective Laser Sintering (SLS)	32
1.2.3 Vat Photopolymerization (VP).....	33
1.2.4 Material Jetting (MJ)	34
1.3. Comparison of Vat Photopolymerization Techniques.....	35
1.3.1 Stereolithographic Apparatus (SLA).....	35
1.3.2 Digital Light Processing (DLP).....	35
1.3.3 Masked Stereolithographic Apparatus (MSLA).....	36
1.4. 3-D Printing Procedure	37
1.4.1 Printer and Resin Choice	37
1.4.2 Post-Processing	38
1.5. Timeline of Component Generations	38
1.6. Health and Safety Considerations.....	39
1.7. Conclusion	41
1.8. References	42

2. Overview of Rectangular Waveguide and Network Theory	46
2.1. Introduction	46
2.2. Rectangular Waveguide Theory	47
2.3. Fundamentals of Microwave and Millimeter-Wave Network Analysis..	51
2.4. Measurements	53
2.4.1 Insertion Loss	53
2.4.2 Return Loss	54
2.4.3 Mismatch Loss Attenuation.....	55
2.4.4 Dissipative Attenuation	55
2.4.5 Time Domain Reflectometry (TDR)	56
2.5. Conclusion	58
2.6. References	59
3. Trends on Polymer-Based 3-D Printing for Millimeter-wave MPRWGs	60
3.1. Thru Lines.....	60
3.2. 90° Twists	64
3.3. Bandpass Filters.....	68
3.4. Conclusion	71
3.5. References	73
4. G-Band Polymer-Based 3-D Printed MPRWG Standard Designs and Thru Lines.....	79
4.1 Introduction	79
4.2 1 st Generation.....	79
4.2.1 Design.....	79
4.2.2 Measurements.....	82
4.3 2 nd Generation.....	82
4.3.1 Design.....	82
4.3.2 Fabrication.....	83
4.3.3 Measurements.....	85
4.4 3 rd Generation	90
4.4.1 Design.....	90
4.4.2 Fabrication.....	92
4.4.3 Measurements.....	94
4.5 4 th Generation	98
4.5.1 Design.....	98

4.5.2	Fabrication.....	98
4.5.3	Measurements.....	101
4.6	Conclusion	110
4.7	References	112
5.	G-band Polymer-Based 3-D Printed MPRWG 90° Twists	116
5.1	Introduction	116
5.2	1 st Generation.....	116
5.2.1	Design.....	116
5.2.2	Fabrication.....	118
5.2.3	Measurements.....	119
5.3	4 th Generation	122
5.3.1	Design.....	122
5.3.2	Fabrication.....	123
5.3.3	Measurements.....	126
5.4	Conclusion	133
5.5	References	135
6.	Design, Optimization, and Fabrication of MSLA-Printed G-band MPRWG BPFs.....	136
6.1	Introduction	136
6.2	Standard BPF Design Procedure	137
6.3	1 st Generation.....	142
6.3.1	Design.....	142
6.3.2	Fabrication.....	144
6.3.3	Measurements.....	145
6.4	4 th Generation TOII-coupled BPFs.....	148
6.4.1	Design.....	148
6.4.2	Fabrication.....	150
6.4.3	Measurements.....	152
6.5	4 th Generation SDII-coupled BPFs	155
6.5.1	Design.....	155
6.5.2	Fabrication.....	162
6.5.3	Measurements.....	163
6.6	Conclusion	170
6.7	References	171

7. Additional Attenuation due to Conductor Surface Roughness in MPRWGs	172
7.1 Introduction	172
7.2 Surface Roughness of 3-D Printed Components	173
7.3 Surface Roughness of Commercial Waveguides.....	178
7.4 Conclusion	180
7.5 References	181
8. Applications of MPRWGs in Millimeter-Wave Radiometer Front-End Subsystems	183
8.1 Introduction	183
8.2 Radiometer Design	184
8.3 Current Implementations	185
8.3.1 ‘Submillimeter-wave Radiometer (SMR)’ on ‘Odin’	186
8.4 3-D Printed Millimeter-Wave Subsystem	188
8.4.1 HITRAN on the Web simulations	188
8.4.2 Subsystem Design	189
8.5 Conclusions	192
8.6 References	193
9. Discussion and Conclusions	195
Publications.....	199
Published and Peer-Reviewed Journal Articles.....	199
Appendix	200
Silver Electroless Plating Procedure	200
Equipment.....	200
Personal Protective Equipment	201

Acknowledgements

I would firstly like to extend my utmost gratitude to my supervisor, Prof. Stepan Lucyszyn, for his guidance and support throughout my PhD, providing essential insight and feedback on the direction and presentation of the work. Thank you to the Engineering and Physical Sciences Research Council (EPSRC) and Airbus for providing funding for this PhD, and to the U.K. Space Agency’s Centre for Earth Observation Instrumentation (CEOI) for providing funding for most of the research undertaken here.

Many thanks to my colleagues and collaborators at Imperial College London, without whom this work would not have been possible; in particular to Dr. Sang-Hee Shin and Liyan Zhu, and also to Dr. Attique Dawood, Ian Rossuck, and Saleh Komies.

I would like to extend my gratitude to Dr. Steven Wright, Dr. Munir Ahmad, Dr. Christos Papavassiliou, Prof. Andrew Holmes, and Dr. Zahid Durrani for their invaluable discussions and advice. Many thanks to our administrators, Susan Brace, Lina Brazinskaite, and Vanessa Rodriguez-Gonzalez, for promptly completing necessary purchase orders and important paperwork. I would also like to extend one final “Qiyu” to my GBs in the Optical and Semiconductor Devices research group.

A massive thank you to Prof. Nick Ridler, Dr. Manoj Stanley, and Dr. Xiaobang Shang, our collaborators at the U.K.’s National Physical Laboratory (NPL), for their help and guidance when undertaking the measurements presented in this thesis.

I would like to thank my entire family, especially my parents, Suresh James Payapulli and Minu Maria Koshy, and my grandmother, Mrs. Claramma John, for their continual prayers, love, and support.

Finally, I would like to add a dedication to the memory of my grandfather, Mr. George Koshy Polachirakel.

Abstract

The objective of this thesis is to investigate the use of low-cost polymer-based 3-D printing for G-band (140 to 220 GHz) metal-pipe rectangular waveguide (MPRWG) components. First, various preliminary designs are investigated. Then, a successful ‘trough-and-lid’ assembly is demonstrated, which mitigates against the main design challenges for split-block waveguide construction at upper-millimeter-wave frequencies (*ca.* 100 GHz to 300 GHz), and can be realized using low-cost 3-D printing and conventional metal plating techniques. With this assembly, inexpensive masked stereolithographic apparatus (MSLA) 3-D printers and a standard commercial copper electroplating service are used. The trough-and-lid assembly is expected to provide a standard solution for the low-cost and low loss realization of most MPRWG implementations above 100 GHz; previously, this was infeasible without the use of high-cost, state-of-the-art 3-D printing and/or custom-developed metal plating techniques. Three different component types are successfully demonstrated: (i) straight thru lines; (ii) 90° twists; and (iii) bandpass filters (BPFs). Along with frequency-domain S-parameter measurements, a detailed time-domain reflectometry analysis is also included. For the more accurate characterization of these components, the additional insertion loss due to conductor surface roughness is investigated. Finally, the integration of an MPRWG component into a millimeter-wave subsystem, which is based on the design of a radiometer front-end, is presented.

Chapter 1 provides an overview of current trends in 3-D printing for microwave and millimeter-wave waveguides. A detailed and exhaustive (at the time of writing) literature review for MPRWG thru lines, 90° twists and BPFs is given. This provides valuable insight into the design challenges that account for the dearth in low-cost and low loss 3-D printed MPRWG implementations above *ca.* 100 GHz.

Chapter 2 provides an overview of polymer-based 3-D printing techniques, with a focus on the vat polymerization technologies that are typically employed in the production of millimeter -wave MPRWGs. A comparison with other polymer-based

3-D printing technologies is included, with an explanation for the choice of masked stereolithographic apparatus (MSLA) technology. Furthermore, details on the fabrication procedure are given, in addition to a discussion on the creation of a safe lab environment. Finally, a short summary of the four Generations of G-band MPRWG design is given, which shall be referred to throughout the thesis.

Chapter 3 presents the basics of waveguide theory, which is essential for understanding the basics of their electromagnetic operation, and microwave and millimeter-wave network theory, to understand the measurements that are necessary for their characterization.

Chapter 4 investigates the design, fabrication, and measurement of MPRWG thru lines. First, preliminary generations of MPRWG are presented, with a discussion on potential improvements for subsequent generations. Then, the ‘trough-and-lid’ assembly is introduced and investigated, which is used to produce 3rd and 4th Gen. 3-D printed thru lines. These serve as a proof-of-concept for this design solution. Frequency- and time-domain analysis is included in their characterization.

Chapter 5 follows up on Chapter 4 by investigating the design, fabrication, and measurement of MPRWG 90° twists. Again, preliminary generations of MPRWG are presented, with a discussion on potential improvements for subsequent generations. Then, the ‘trough-and-lid’ assembly is employed to produce 4th generation twists, which demonstrates that more complex internal geometries are possible. Frequency- and time-domain analysis is included in their characterization. These are the first examples of 3-D printed twists operating above 110 GHz.

Chapter 6 investigates the design, fabrication, and measurement of MPRWG bandpass filters (BPFs). Three different designs per Generation are chosen, with lower-, mid-, and upper-band center frequencies. The 1st Generation is presented, with a discussion on potential improvements. Then, the ‘trough-and-lid’ assembly is employed to produce 4th Generation G-band BPFs, using transverse offset inductive irises (TOIIs) and symmetrical diaphragm inductive irises (SDIIs). Furthermore, the passband frequency-shifting effects of iris corner rounding are

investigated, with a unique systematic compensation technique developed and applied to all SDII-coupled BPFs. The TOII-coupled BPFs are the first examples of polymer-based 3-D printed BPFs operating above 110 GHz.

Chapter 7 investigates the contribution of conductor surface roughness to additional insertion loss in waveguides. Two modifications of the Hemispherical physical surface roughness model are provided, which were applied to frequency-domain dissipative attenuation and time-domain reflectometry measurements in Chapters 4 and 5.

Chapter 8 introduces a potential application of these MPRWGs: integration within millimeter-wave radiometer front-end subsystems. An overview of radiometer design is given, with a description of an existing satellite-based radiometer system. Finally, a polymer-based 3-D printed subsystem is presented, which was based on the previously introduced example. The 183.3 GHz TOII-coupled BPF is integrated into this subsystem, and the measured results are presented.

List of Figures

FIGURE 1.1: Classification of 3-D printing technologies according to the employed material [14].....	30
FIGURE 1.2: Schematic of the FDM printing process.....	31
FIGURE 1.3: Schematic of SLS 3-D printing	33
FIGURE 1.4: Schematic of the VP printing process.	33
FIGURE 1.5: Schematic of the MJ printing process.	34
FIGURE 1.6: Schematic of the three main VP technologies: (a) SLA; (b) DLP; and (c) MSLA printing [24].....	37
FIGURE 1.7: Photograph of 3-D printing and post-processing lab set-up.....	40
FIGURE 2.1: Geometry of an air-filled rectangular waveguide.	47
FIGURE 2.2: Representation of a two-port network: (a) definition of incident and reflected waves, and power delivered to each part of the network, with power quantities for Port 1 being driven; and (b) signal flow graph.	52
FIGURE 3.1: Internal geometry of a 90° twist: (a) stepped transition, designed by Al-Tarifi and Filipovic [19]; and (b) smooth transition, as used in this thesis.	65
FIGURE 4.1: Schematic of the RF choke design from Lewis et al. [5].	81
FIGURE 4.2: Close-up of the 1st Gen. MPRWG BPF aperture, showing RF choke and a deviating symmetrical E-plane split.....	81
FIGURE 4.3: Flange view of the print orientation in Chitubox, showing support structures.....	83
FIGURE 4.4: Flange view images of the single-block 10.4 mm MPRWG thru line:	

(a) full component; and (b) close-up of channel.....	84
FIGURE 4.5: Two-port waveguide measurement setup, with VNA screen displaying the frequency-domain response (top panel) and time-domain response (bottom panel). The DUT here is a 3-D printed 90° twist connected to a COTS 90° twist.....	85
FIGURE 4.6: Reflection measurements for the 3-D printed 10.4 mm thru lines..	87
FIGURE 4.7: Transmission results for the 3-D printed 7.4 mm and 10.4 mm thru lines (close-up of ideal calculated and EM simulated responses in the inset).....	88
FIGURE 4.8: Dissipative attenuation for the 3-D printed 7.4 mm and 10.4 mm thru lines: (a) per meter; and (b) per guided wavelength.	89
FIGURE 4.9: Flange view illustration of the trough-and-lid assembly, showing lips in contact with the flat top part.....	91
FIGURE 4.10: Flange view of print orientations in Chitubox, showing support structures.....	92
FIGURE 4.11: Fully assembled 3rd Gen. WR-5 MPRWG thru lines after copper plating.	93
FIGURE 4.12: Reflection measurements for the 3-D printed 7.4 mm and 10.4 mm thru lines.	95
FIGURE 4.13: Transmission results for the 3-D printed 7.4 mm and 10.4 mm thru lines.....	96
FIGURE 4.14: Dissipative attenuation for the 3-D printed 7.4 mm and 10.4 mm thru lines: (a) per meter; and (b) per guided wavelength.....	97
FIGURE 4.15: Comparison between 3rd and 4th Gen. 3-D printed MPRWG thru lines: (a) 3rd Gen. 3-D printed 10.4 mm thru line, bottom part, before plating; (b) 4th Gen. 3-D printed 10.4 mm thru line, bottom part, before plating; (c) 3rd Gen., after plating; and (d) 4th Gen., after plating.	98

FIGURE 4.16: 4th Gen. WR-5 MPRWG thru lines: (a) disassembled 3-D printed 10.4 mm thru line, before plating; (b) disassembled, after plating, showing stainless steel dowel pins; (c) fully assembled 3-D printed 10.4 mm thru line, after plating; and (d) 25.4 mm COTS counterpart from VDI [29].....	100
FIGURE 4.17: Flange view microphotograph of the trough-and-lid assembly for a thru line, showing lips in contact with the flat top part.	101
FIGURE 4.18: Reflection measurements of the 3-D printed and COTS thru lines.	102
FIGURE 4.19: Transmission results for the 3-D printed and COTS thru lines... 104	
FIGURE 4.20: Dissipative attenuation for the 3-D printed 7.4 mm and 10.4 mm thru lines: (a) per meter; and (b) per guided wavelength.....	105
FIGURE 4.21: Emulated TDR re-simulations and measurements for the 3-D printed thru lines: (a) MWO re-simulated setup for the reduced width 7.4 mm thru line; (b) 7.4 mm thru line traces; and (c) 10.4 mm thru line traces.	108
FIGURE 5.1: HFSS simulation results for the WR-5 thru and 90° twist (insets show internal CAD layouts of the components) having length $L = 31.75$ mm.....	117
FIGURE 5.2: Flange view of the Chitubox print orientation for the 1 st Gen. twist, showing support structures: (a) port aligned with broad wall perpendicular to the build plate; and (b) other port aligned with broad wall parallel to the build plate.	118
FIGURE 5.3: 1st Gen. WR-5 MPRWG 31.75 mm 90° twists: (a) disassembled 3-D printed and copper electroplated split-block parts; and (b) two fully assembled 90° twists in cascade.....	119
FIGURE 5.4: Reflection measurements for a cascade connection of two 1st Gen. 3-D printed 90° twists.	120
FIGURE 5.5: Transmission measurements for a cascade connection of two 1st Gen.	

3-D printed 90° twists.....	121
FIGURE 5.6: Close-up of the 1st Gen. 90° twist channel, showing edge rounding.	122
FIGURE 5.7: Flange views of print orientations in Chitubox for the 4 th Gen. twist, showing support structures.	124
FIGURE 5.8: 4th Gen. WR-5 MPRWG 31.75 mm 90° twists: (a) disassembled 3- D printed and copper electroplated bottom part (twisting trough); (b) disassembled top part (twisting lid); (c) fully assembled; and (d) COTS counterpart from Pasternack [2].	125
FIGURE 5.9: One-port reflection measurements for the 3-D printed and COTS #1 twists (terminated with a wave impedance matched load).	127
FIGURE 5.10: Two-port EM simulations and measurements for Cascades #1 and #2: (a) reflection; and (b) transmission.....	129
FIGURE 5.11: TDR measurements and EM re-simulations: (a) one-port for the 3- D printed and COTS #1 twists terminated with a VDI matched load; and (b) two- port for Cascade #1.....	132
FIGURE 6.1: Plan view illustration of a symmetrical 5 th order waveguide BPF, showing ideal rectangular geometries: (a) SDII-coupled; (b) TOII-coupled.	138
FIGURE 6.2: EM simulations for obtaining input/output resonator and iris dimensions: (a) plan view of simulated structure; and (b) transmission results, showing center frequency and 3-dB bandwidth.	140
FIGURE 6.3: EM simulations for obtaining internal resonator and iris dimensions: (a) plan view of simulated structure; and (b) transmission results, showing two resonance frequencies.	141
FIGURE 6.4: 3-D printed and copper electroplated 5 th order Chebyshev SDII- coupled BPFs: (a) full component; and (b) microphotograph of the internal structure	

for one split-block part of the 183.3 GHz exemplar, with key linear BPF dimensions labelled and feed lengths omitted; red rectangles highlight the peripheries of the cavities.	145
FIGURE 6.5: EM simulated and measured two-port S-parameter G-band responses for the 1 st Gen. SDII-coupled 150 GHz BPF.	146
FIGURE 6.6: EM simulated and measured two-port S-parameter G-band responses for the 1 st Gen. SDII-coupled 183.3 GHz BPF.	147
FIGURE 6.7: EM simulated and measured two-port S-parameter G-band responses for the 1 st Gen. SDII-coupled 204.5 GHz BPF.	148
FIGURE 6.8: Comparison between different Generations of 3-D printed transverse offset inductive iris-coupled (TOII) BPFs (before plating, bottom parts only): (a) 3 rd Gen., using the Elegoo Mars; and (b) 4 th Gen., using the Elegoo Mars 2 Pro.	150
FIGURE 6.9: Plan view microphotograph of the internal structure for a 3-D printed and copper electroplated 5 th order Butterworth 183.3 GHz TOII-coupled BPF, with cavity resonators labelled and feed lengths omitted. Red rectangles highlight the peripheries of the cavities.	151
FIGURE 6.10: EM simulated and measured two-port S-parameter G-band response for the 7.4 mm long TOII-coupled 150 GHz BPF.	152
FIGURE 6.11: EM simulated and measured two-port S-parameter G-band response for the 7.4 mm long TOII-coupled 183.3 GHz BPF.	153
FIGURE 6.12: EM simulated and measured two-port S-parameter G-band response for the 7.1 mm long TOII-coupled 204.5 GHz BPF.	154
FIGURE 6.13: All types of rounding occurring on an SDII: (a) CAD isometric representation; and (b) 3-D printed and copper electroplated, plan view microphotograph.	157

FIGURE 6.14: Plan view illustration of a single cavity resonator, having two inductive irises: (a) non-rounded; and (b) rounded.158

FIGURE 6.15: ICR compensation simulations applied to the 155 GHz SDII-coupled BPF, with yellow and blue arrows indicating frequency shifting due to detuning and compensation, respectively: (a) Cavity #3 only; and (b) complete BPF.161

FIGURE 6.16: Plan view microphotographs of the internal structure for 3-D printed and copper electroplated 5th order Butterworth 175 GHz SDII-coupled BPFs, with ICR compensation. Cavity resonators are labelled, and feed lengths are omitted. Red rectangles highlight the peripheries of the cavities.162

FIGURE 6.17: EM simulated, measured and EM re-simulated two-port S-parameter responses for the 10.4 mm long SDII-coupled 155 GHz BPF, with ICR compensation applied: (a) full G-band responses; and (b) close-up passband transmission responses, with the 10.4 mm reference thru line included.164

FIGURE 6.18: EM simulated, measured and EM re-simulated two-port S-parameter responses for the 7.4 mm long SDII-coupled 175 GHz BPF, with ICR compensation applied: (a) full G-band responses; and (b) close-up passband transmission responses, with the 7.4 mm reference thru line included.....166

FIGURE 6.19: EM simulated, measured and EM re-simulated two-port S-parameter responses for the 7.1 mm long SDII -coupled 200 GHz BPF, with ICR compensation applied: (a) full G-band responses; and (b) close-up passband transmission responses, with the 7.4 mm reference thru line included.168

FIGURE 7.1: SEM images for the 155 GHz BPF: (a) iris sidewalls; and (b) plan view of the bottom of the MPRWG trough and one iris aperture.....174

FIGURE 7.2: The Hemispherical surface roughness model, represented by a single hemispherical protrusion positioned on a flat plane, with incident plane wave propagating parallel to the flat surface: (a) plan view; and (b) side view [9].....175

FIGURE 7.3: Flann submillimeter seamless waveguides: (a) total attenuation

measurements, with ideal calculated values and COTS thru line measurements; and (b) effective roughness coefficient $K_{eff}(fL)$	179
FIGURE 8.1: A Dicke radiometer block diagram.....	184
FIGURE 8.2: Block diagram of the SMR on the Odin satellite, adapted from Frisk et al. [14]. Red boxes indicate passive components that can currently be realized using 3-D printing, dashed red boxes indicate more demanding higher frequency candidates, and dotted red boxes represent advanced hybrid active/passive solutions.....	186
FIGURE 8.3: HotW simulations showing specific attenuation for five different sea-level atmospheric models; the absorption lines for N ₂ O and ClO are shown in the inset.....	189
FIGURE 8.4: 3-D printed sub-THz subsystem: (a) block diagram overview of design; and (b) plan view photograph, with the 183.3 GHz BPF integrated.....	191
FIGURE 8.5: Assembled subsystem measurement integrated with the 3-D printed and copper electroplated 183.3 GHz TOII-coupled BPF, introduced in Chapter 6.3.1.....	192

List of Tables

TABLE 3.1: Millimeter-wave 3-D printed and COTS thru lines.	63
TABLE 3.2: Microwave and mm-wave 3-D printed 90° twists operating above 8 GHz. (*measured step length/ λ_{gL} and †COTS components that I measured),	67
TABLE 3.3: Millimeter-wave 3-D printed MPRWG BPFs.	71
TABLE 4.1: Comparative costs (at the time of writing) for G-band thru lines with COTS components and their 3-D printed counterparts (*costs available online).	94
TABLE 5.1: Comparative costs (at the time of writing) for G-band 90° twists with COTS components and their 3-D printed counterparts (*costs available online).	126
TABLE 6.1: Allocated frequency bands of scientific interest for satellite passive remote sensing within G-band (140 to 220 GHz) [3].	143
TABLE 6.2: Ideal designed linear BPF dimensions for the SDII-coupled 150 GHz, 183.3 GHz, and 204.5 GHz BPFs, with bandwidths of 2.5 GHz, 17 GHz, and 9 GHz, respectively.....	144
TABLE 6.3: Ideal designed linear BPF dimensions for the TOII-coupled 150 GHz, 183.3 GHz, and 204.5 GHz BPFs, with bandwidths of 6 GHz, 17 GHz, and 9 GHz, respectively.	150
TABLE 6.4: Non-rounded and compensated linear BPF dimensions for the SDII-coupled 155 GHz, 175 GHz, and 200 GHz BPFs, with bandwidths of 15.5 GHz, 17.5 GHz, and 20 GHz, respectively.	161

List of Symbols

Symbol	Description	Unit
\mathcal{A}	Absorptance	
α'_D	Input dissipative attenuation per unit length	dB/m
a	Waveguide internal cross-sectional width	mm
a_1	Voltage wave incident on Port 1	V
a_2	Voltage wave incident on Port 2	V
A_{base}	Area of the hemisphere base	m^2
A_{tile}	Area of the flat tile on which the hemisphere is positioned	m^2
b	Waveguide internal cross-sectional height	mm
b_1	Voltage wave transmitted/reflected from Port 1	V
b_2	Voltage wave transmitted/reflected from Port 2	V
BW	Bandwidth	Hz
c_0	Speed of light in a vacuum	ms^{-2}
d_{peaks}	Separation distance between adjacent hemispherical protrusions	m
E_x	Electric field strength, x -component	$V \cdot m^{-1}$
E_y	Electric field strength, y -component	$V \cdot m^{-1}$
E_z	Electric field strength, z -component	$V \cdot m^{-1}$
f	Frequency	GHz
f_0	Center frequency	GHz
FBW	Fractional bandwidth	%
$f_{c,10}$	TE ₁₀ mode cut-off frequency	GHz

f_L	Lower band-edge frequency	Hz
H_x	Magnetic field strength, x -component	A·m ⁻¹
H_y	Magnetic field strength, y -component	A·m ⁻¹
H_z	Magnetic field strength, z -component	A·m ⁻¹
IL	Insertion loss	dB
k	Angular wavenumber	rad·m ⁻¹
K	Surface roughness coefficient	
k_0	Angular wavenumber in free space	rad·m ⁻¹
k_c	Cut-off angular wavenumber	rad·m ⁻¹
L	Physical waveguide length	m
P_A	Power absorbed/dissipated by a network	W
P_I	Incident power	W
P_L	Transmitted power	W
P_R	Reflected power	W
P_T	True power delivered to a network	W
Q_L	Loaded Q-factor	
\mathcal{R}	Reflectance	
R_a	Mean profile surface roughness	mm
r_{base}	Average hemispherical radius	m
RL	Return loss	dB
R_q	RMS profile surface roughness	mm
R_s	Classical conductor surface resistance	Ω
S_{11}	Forward reflection coefficient	

S_{12}	Reverse transmission coefficient	
S_{21}	Forward transmission coefficient	
S_{22}	Reverse reflection coefficient	
t	Time	s
T_A	Antenna temperature	K
T_B	Brightness temperature	K
T_R	Reference temperature	K
v_g	Group velocity	$\text{m}\cdot\text{s}^{-1}$
v_p	Phase velocity	$\text{m}\cdot\text{s}^{-1}$
Z	Impedance	Ω
Z_0	Characteristic impedance	Ω
Z_s	Classical conductor surface impedance	Ω
α	Attenuation constant	
α_C	Attenuation constant due to conductor losses, TE ₁₀ mode	
α_M	Input mismatch loss attenuation	dB
α_T	Total attenuation	dB
β	Propagation constant	
δ	Skin depth	μm
ε_r	Effective relative permittivity	
η_0	Free space impedance	Ω
λ	Wavelength	mm
λ_0	Wavelength in free space	mm
λ_g	Guided wavelength in waveguide, TE ₁₀ mode	mm

μ_0	Free space permeability	N·A ⁻²
ρ_0	Bulk resistivity	Ω·m
σ_0	Bulk conductivity	S/m
σ_t	Total cross-section (Hemispherical model)	m ²
Φ	Phase angle	°
ω	Angular frequency	rad·s ⁻¹
\mathcal{T}	Transmittance	

List of Abbreviations

Abbreviation	Description
ABS	Acrylonitrile butadiene styrene
BPF	Band-pass filter
CAD	Computer-aided design
CNC	Computer numerical control
COSHH	Control of Substances Hazardous to Health
COTS	Commercial-off-the-shelf
DC	Direct current
DLP	Digital light processing
DUT	Device under test
DUT	Device-under-test
EDM	Electronic discharge machining
EM	Electromagnetic
FDM	Fused deposition modelling
FFF	Fused filament fabrication
FSS	Frequency selective surface
HEPA	High-efficiency particulate absorbing
HFSS	High-Frequency Structure Simulator
ICL	Imperial College London
ICR	Iris corner rounding
IEEE	Institute of Electrical and Electronics Engineers
IPA	Isopropanol

IR	Infrared
ITU	International Telecommunications Union
LCD	Liquid crystal display
MJ	Material jetting
MLS	Micro laser sintering
MPRWG	Metal-pipe rectangular waveguide
MSLA	Masked stereolithographic apparatus
MWO	Microwave Office
NPL	National Physical Laboratory
OMT	Orthogonal mode transducer
PEC	Perfect electrical conductor
PLA	Polylactic acid
RF	Radio frequency
RMS	Root-mean-square
SDII	Symmetrical diaphragm inductive iris
SLA	Stereolithographic apparatus
SLM	Selective laser melting
SLS	Selective laser sintering
SMR	Submillimeterwave Radiometer
SSC	Swedish Space Corporation
TDR	Time-domain reflectometry
TE	Transverse electric
TEM	Transverse electromagnetic
TM	Transverse magnetic
TOII	Transverse offset inductive iris

TRL	Thru-Reflect-Line
UV	Ultraviolet
VDI	Virginia Diodes Inc.
VNA	Vector network analyzer
VOC	Volatile organic compound
VP	Vat photopolymerization
WMO	World Meteorological Organization

List of Frequency Bands and Waveguide Designations

X-band	WR-90	-	8 to 12 GHz
Ku-band	WR-62	-	12 to 18 GHz
Ka-band	WR-28	-	26.5 to 40 GHz
Q-band	WR-22	-	33 to 50 GHz
V-band	WR-15	-	50 to 75 GHz
E-band	WR-12	-	60 to 90 GHz
W-band	WR-10	WM-2540	75 to 110 GHz
D-band	WR-6	WM-1651	110 to 170 GHz
G-band	WR-5	WM-1295	140 to 220 GHz
-	WR-3.4	WM-864	220 to 330 GHz
-	WR-2.2	WM-570	325 to 500 GHz
-	WR-1.5	WM-380	500 to 750 GHz
-	-	WM-250	750 GHz to 1.1 THz

1. Overview of Polymer-Based 3-D Printing for Millimeter-Wave MPRWGs

1.1. Introduction

This chapter gives an overview of the different polymer-based 3-D printing technologies, their suitability for upper-mm-wave MPRWGs, and the production process employed to manufacture the components presented throughout this thesis.

Manufacturing technologies are typically categorized in one of three groups: (i) formative; (ii) subtractive, and (iii) additive manufacturing [1]. Conventionally, MPRWGs are produced using either formative or subtractive manufacturing technologies (collectively referred to here as machining technologies).

Formative manufacturing involves the controlled plastic deformation of the initial material until the desired shape is obtained, which is typically realized through the application of heat and/or pressure. For the production of MPRWGs, drawing through a rectangular die is the most commonly used example of a formative manufacturing technique. This is usually employed at microwave (3 GHz to 30 GHz) and lower-millimeter-wave (30 GHz to *ca.* 100 GHz) frequencies. Several drawing iterations may be needed to achieve a rectangular cross-section [2]. Initial equipment costs for formative manufacturing technologies are very high, due to the requirement for custom-made machine tools (e.g., molds, dies, and equipment used to manipulate the initial material). However, once operational, standardized components can be manufactured at a high volume and high speed, thereby reducing the cost per part due to economies of scale.

Subtractive manufacturing involves cutting away from a solid block of initial material (known as a ‘blank’) to produce the desired part [3]. Generally, machine operations involve a combination of cutting, milling, drilling, and turning. Final fabricated parts exhibit an extremely high dimensional accuracy and excellent surface finish. Examples of subtractive manufacturing technologies employed for MPRWGs include computerized numerically controlled (CNC) milling and electronic discharge machining (EDM) with spark erosion. Initial equipment costs are lower in comparison to formative manufacturing (though still relatively high). Once operational, parts are manufactured at

a comparatively lower speed and higher cost, requiring the work of skilled machinists. This makes subtractive manufacturing suitable for high-end applications, with low to moderate volumes and simple geometries. As a result, waveguide components operating at upper-millimeter-wave (*ca.* 100 GHz to 300 GHz) and terahertz (THz) frequencies (300 GHz to 3 THz) typically employ this technique.

In contrast, additive manufacturing (more commonly known as 3-D printing) involves adding material layer-by-layer until the desired part is obtained. This is quickly gaining popularity for rapid prototyping and small-batch manufacturing of bespoke passive microwave, millimeter-wave (30 GHz to 300 GHz), and THz components. When compared with here as machining technologies, in general, it offers the potential for weight reduction, minimal waste, the ability to manufacture more geometrically complex structures, fast turnaround and significant cost savings. 3-D printing has previously been limited to prototyping, but there is now considerable potential in manufacturing operational components at low volumes, especially where geometrical complexity is also necessary. However, the main limitations thus far have been poorer dimensional accuracy and surface quality when compared to subtractive manufacturing. With the cost and manufacturing accuracy of commercially available 3-D printers rapidly improving, and as research in this field advances, the performance gap with subtractive manufacturing is expected to become narrower.

To this end, this thesis demonstrates polymer-based 3-D printed G-band (140 to 220 GHz) metal-pipe rectangular waveguides (MPRWGs), which were reported in a research article that was recently published in *IEEE Access* [4]. This follows on from previous work on a fully polymer-based 3-D printed integrated front-end subsystem [5], based on the design of a passive microwave radiometer, which combines quasi-optical [6] and MPRWG components [7].

The operating principle of an MPRWG is simple: electromagnetic (EM) energy launches into the input port and propagates by reflecting off the sidewalls, confining energy to within the structure and thus eliminating the spreading losses associated with free-space spherical wave transmission [8]. When compared to transmission lines (e.g., microstrip or coplanar waveguide), MPRWGs exhibit much lower dissipative attenuation due to ohmic losses, having infinite isolation and a much higher power handling capacity,

making them essential for applications that require high sensitivity (e.g., radiometry, communications, and radar) or high output power (e.g., communications and radar). Further discussion on this will be given in Chapter 8. Commercially machined MPRWGs are typically slow and expensive to fabricate, and are significantly heavier than transmission lines. Manufacturing costs are significantly exacerbated at upper-millimeter-wave frequencies, as smaller apertures and internal features require greater mechanical accuracy.

Polymer-based 3-D printing currently represents a promising alternative to subtractive manufacturing and metal-based 3-D printing for MPRWGs operating up to upper-millimetre-wave frequencies. For example, ICL have previously reported a number of MPRWG components operating up to 1.1 THz [9]-[13]. In general, above D-band (110 to 170 GHz), high-cost printing has been required due to its high resolution, often in conjunction with custom-developed metal plating techniques, which substantially reduces cost savings. Furthermore, little has been reported on polymer-based 3-D printing of MPRWG components with added functionality (e.g., twisting or filtering) above W-band (75 to 110 GHz).

1.2. Typical Polymer-Based 3-D Printing Techniques

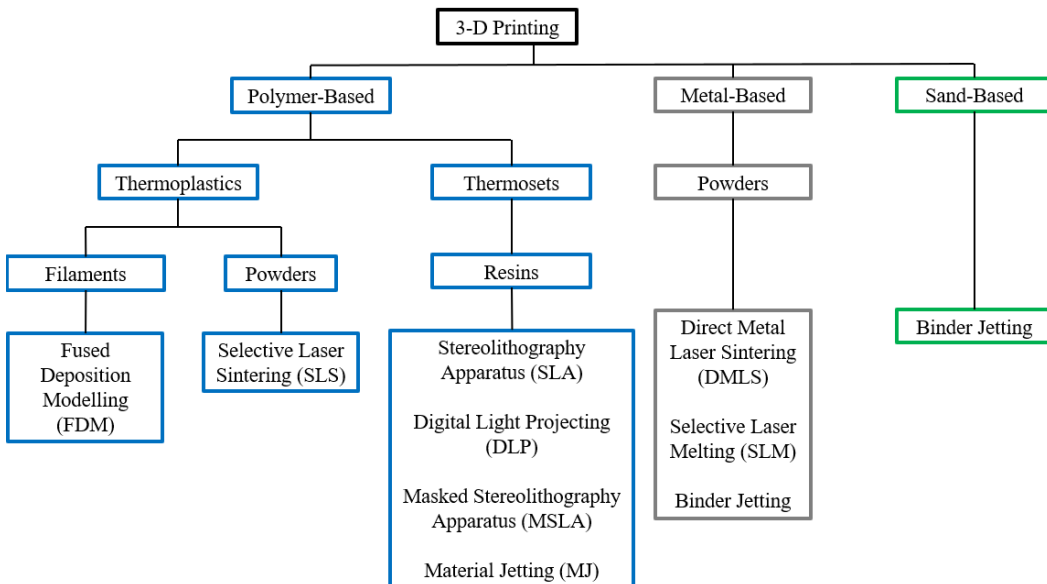


FIGURE 1.1: Classification of 3-D printing technologies according to the employed material [14].

Figure 2.1 gives an overview of the main 3-D printing technologies that are currently in use, which are arranged by their employed materials. For polymer-based 3-D printing, either thermoplastics or thermoset plastics are used. The former are solid at room temperature; the material is heated to above its glass transition temperature to allow mechanical manipulation. The latter are liquid resins at room temperature; ultraviolet (UV) light is used to selectively cure the resin into a solid material.

1.2.1 Fused deposition modeling (FDM)

Also known as fused filament fabrication (FFF), FDM is the most widely used 3-D printing technology, due to its low cost (typically ~\$200 to ~\$1000 for desktop models), wide range of available materials, ease of setup and use, and large build volume [15]. It is an example of a ‘Material Extrusion’ printing process. A simplified diagram that explains the printing procedure is shown in Fig. 2.2. Here, a thermoplastic polymer filament, most commonly polylactic acid (PLA) or acrylonitrile butadiene styrene (ABS), is pushed through a heated nozzle and deposited in a precise path. This process is repeated layer-by-layer, until the desired part is obtained. Dimensional accuracy is typically ~0.1 mm, which is further degraded due to warping and shrinkage [14]. Since the deposited filament exhibits a circular/elliptical cross-section, layer-lines are visible in every printed part.

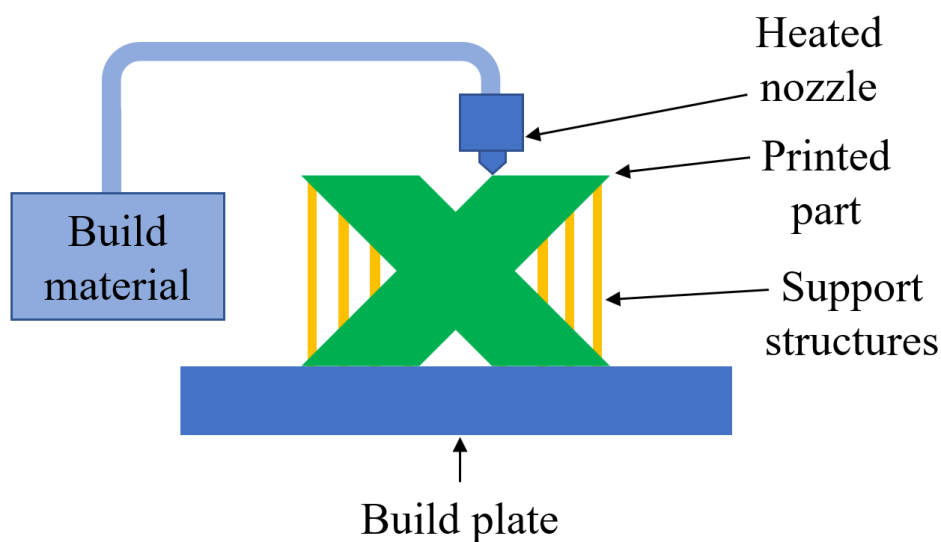


FIGURE 1.2: Schematic of the FDM printing process.

This technology has been successfully employed in MPRWGs at microwave and lower-millimetre frequencies, up to Ka-band (26.5 to 40 GHz) [15]. However, due to its relatively low dimensional accuracy and visible layer-lines, it is unsuitable for millimetre-wave applications.

1.2.2 Selective Laser Sintering (SLS)

SLS is a type of powder bed fusion printing technology, which is analogous to direct metal laser sintering (DMLS) for metal-based 3-D printing. A simplified diagram that explains the printing procedure is shown in Fig. 2.3. Here, a thermoplastic powder is deposited in a thin layer onto a build plate, and a laser source selectively heats the powder such that the exposed areas are fused together (i.e., sintered). This process is repeated until the desired part is obtained. The part is suspended in the un-sintered powder, avoiding the need for support structures, which typically degrade surface quality in FDM, vat photopolymerization (VP), and material jetting (MJ) printing. Furthermore, fabricated parts exhibit a relatively high tensile strength and high accuracy (though less accurate in comparison to VP and MJ, and warping and shrinkage may occur), with a fast fabrication time and a large build volume. However, due to the requirement for a well-ventilated, temperature-controlled chamber and a specialized post-processing procedure, SLS printers are large and expensive, with even low-end printers typically costing over \$10,000 [16]. Therefore, SLS is typically employed to manufacture functional parts that may be subject to mechanical stress (e.g., joint replacements) at a relatively higher production volume than FDM, VP, or MJ. MPRWGs have been demonstrated using SLS in BPFs operating with a center frequency of 91.25 GHz [17].

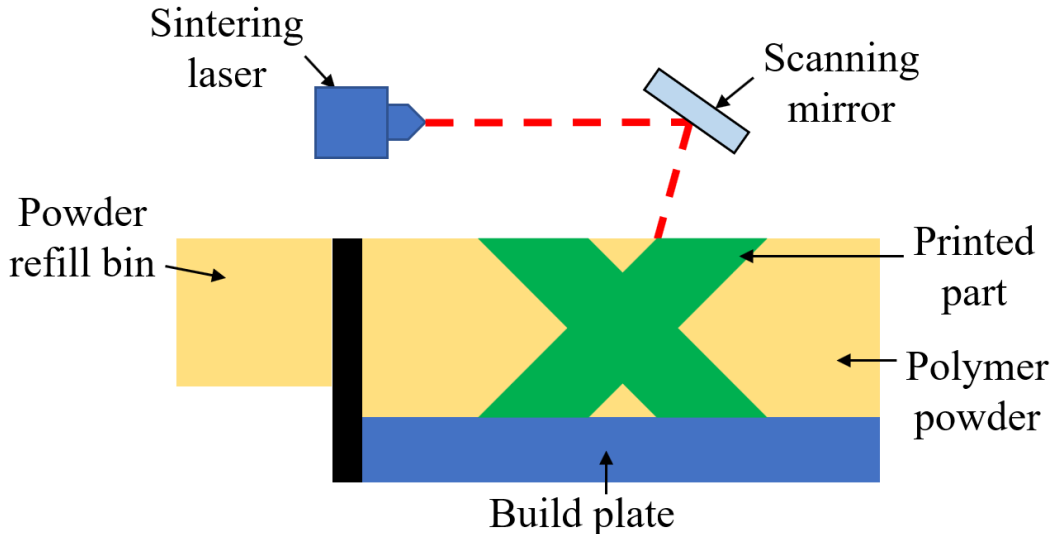


FIGURE 1.3: Schematic of SLS 3-D printing.

1.2.3 Vat Photopolymerization (VP)

Vat photopolymerization is a category of 3-D printing that employs a thermoset UV curable photopolymer resin, contained within a vat or tank with a transparent bottom, with each layer constructed by selectively exposing the bottom of the vat to a UV light source (typically a laser, lamp, or projector). A simplified diagram that explains the printing procedure is shown in Fig. 2.4. There are three main examples of this technology, which are explained in Chapter 2.3.

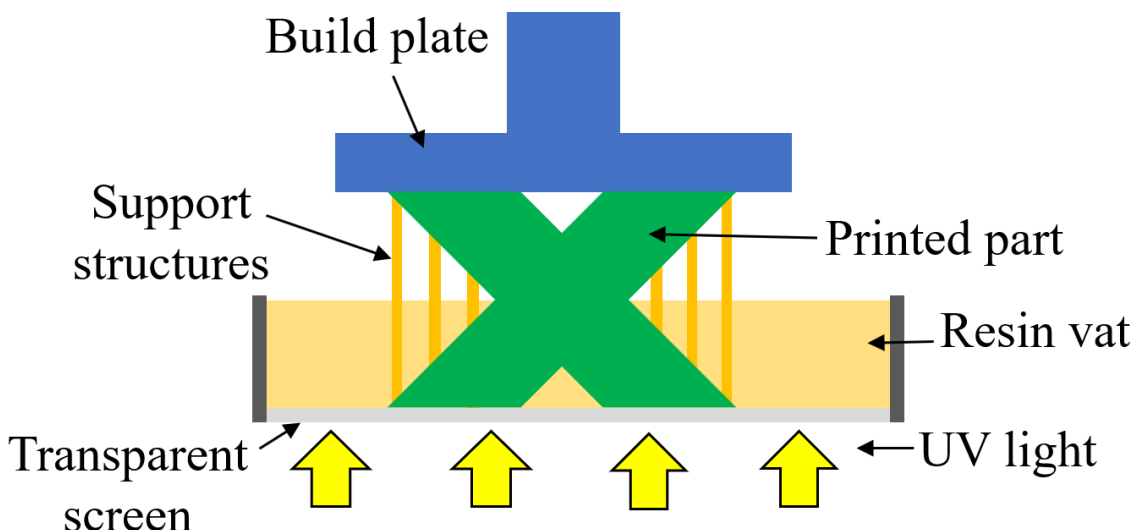


FIGURE 1.4: Schematic of the VP printing process.

These have gained popularity in the last decade due to their low cost (typically ~\$200 to ~\$1000 for desktop models, and this is still rapidly reducing), high accuracy, high precision, and smooth surface finish. As a result, they have been successfully utilized in 3-D printed MPRWGs up to J-band (220 to 325 GHz) by von Bieren et al. [18] using a high-cost, ultra-high-resolution 3-D printer.

1.2.4 Material Jetting (MJ)

For MJ, droplets of thermoset UV-curable photopolymer are precisely deposited and immediately cured, using inkjet heads with in-built UV lamps [19]. A dissolvable support material is simultaneously deposited, which is removed during post-processing. A simplified diagram that explains the printing procedure is shown in Fig. 2.5. As MJ printers deposit material is a line-by-line process for each layer, the total printing time is significantly reduced. Furthermore, MJ is typically considered to be the most dimensionally accurate form of 3-D printing, as photopolymer droplets are precisely deposited, and the warping that is associated with thermoplastic materials does not occur (though shrinkage may occur for relatively large parts). Surface quality is comparable to injection molded parts.

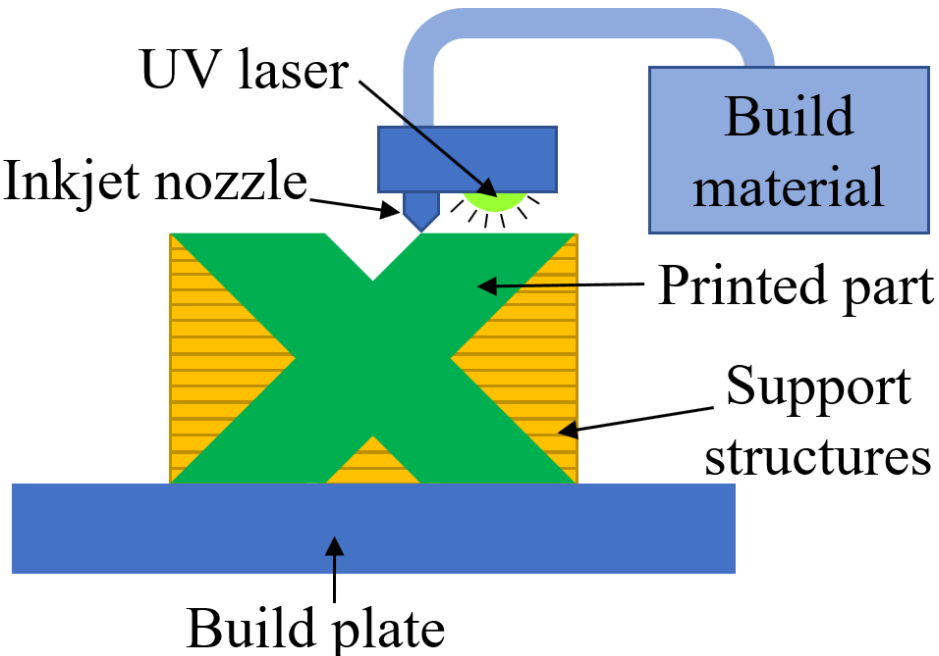


FIGURE 1.5: Schematic of the MJ printing process.

1.3. Comparison of Vat Photopolymerization Techniques

Due to the high resolution and low cost of their associated 3-D printers, VP is the most suitable candidate for manufacturing low-cost and low loss MPRWGs. This Section covers the different implementations of VP technology, with a comparison of advantages and disadvantages.

1.3.1 Stereolithographic Apparatus (SLA)

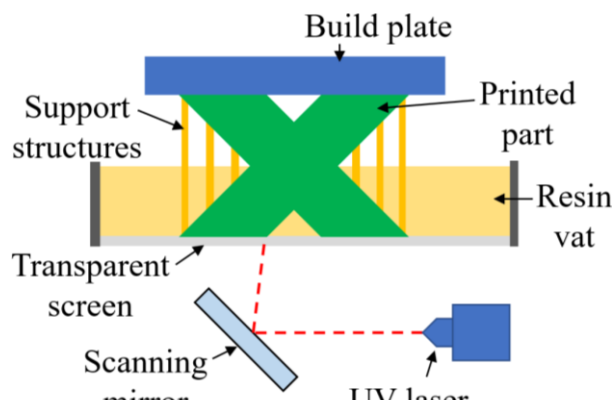
SLA is currently the most commonly used VP technology [14]. A UV laser is used as the light source, which scans across the bottom of the resin vat using scanning mirrors, as shown in Fig. 2.6(a). Dimensional tolerances depend primarily on the laser spot size, which is 85 μm for the Formlabs Form 3 printer (considered the state-of-the-art in desktop SLA equipment) [21]. As the laser spot typically has a circular cross-section, a smooth surface quality is produced (comparable to that of injection molded plastic parts). However, for this reason, SLA is not ideal for producing sharp corner and edge features, with sub-mm rounding radii. Desktop printers typically cost around \$2,000 to \$5,000.

1.3.2 Digital Light Processing (DLP)

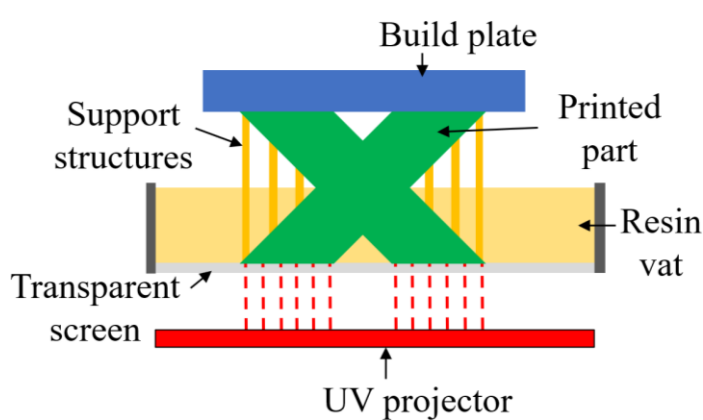
In contrast to SLA printing, DLP employs a digital light projector to illuminate an image of the entire layer onto the bottom of the resin vat, as shown in Fig. 2.6(b). Standard DLP projectors use square pixels, producing a layer of voxels (i.e., volume pixels) for each illumination. Since entire layers are printed simultaneously, DLP can achieve significantly faster print times in comparison to SLA. Dimensional tolerance is determined by pixel height and width, which is 90 $\mu\text{m} \times 64 \mu\text{m}$ for a standard commercial DLP printer [22]. Significant cost reduction is achieved when compared to SLA printers, typically around \$600 to \$2,000 for desktop models, due to the avoidance of scanning mirrors and other optical components. Sharper features can be printed, though surface quality is not as smooth as SLA printing.

1.3.3 Masked Stereolithographic Apparatus (MSLA)

MSLA printing operates similarly to DLP printing, with entire layers being printed simultaneously. However, in contrast to using a projector, a liquid crystal display (LCD) screen is used to selectively block light from (i.e., mask) a UV lamp, as shown in Fig. 2.6(c). If all pixels are turned off, the UV lamp completely illuminates the bottom of the tank; with all pixels turned on, the LCD screen completely blocks all UV light. Resolution is determined by the pixel height and width, which is 22 μm for the most recent commercially available printer [23]. Lower costs can be achieved when compared to DLP printers, typically around \$100 to \$500 for desktop models, due to the replacement of the high-resolution projector with the cheaper LCD masking screen and UV lamp. As a result, MSLA printing is rapidly gaining popularity, improving in resolution, and reducing in cost. Similarly to DLP, sharp features can be achieved on fabricated parts, though surface quality is not as smooth as SLA.



(a)



(b)

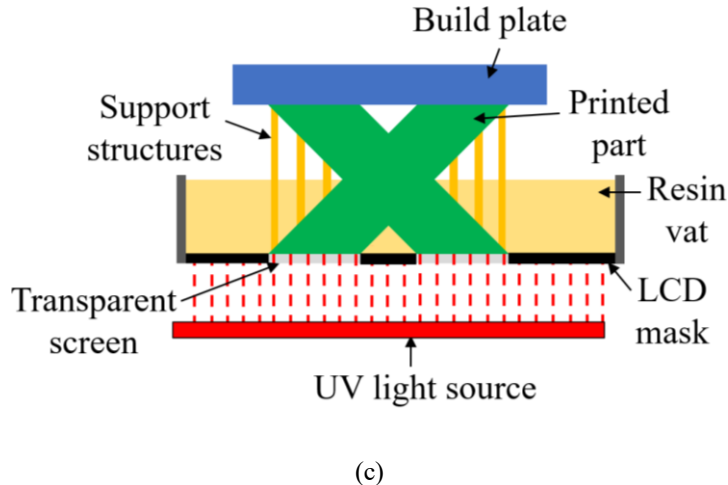


FIGURE 1.6: Schematic of the three main VP technologies: (a) SLA; (b) DLP; and (c) MSLA printing [24].

1.4. 3-D Printing Procedure

1.4.1 Printer and Resin Choice

MSLA printers, being the least expensive high-resolution VP technology on the market, were used to undertake all 3-D printing of MPRWGs in this thesis. Two different printers were employed:

1. The \$135 Elegoo Mars, having a maximum print volume of $120 \text{ mm} \times 68 \text{ mm} \times 155 \text{ mm}$ [25]. This model has a 2K monochrome LCD mask, with a $46.9 \mu\text{m} \times 47.2 \mu\text{m}$ pixel size.
2. The \$230 Elegoo Mars 2 Pro, having a maximum print volume of $129 \text{ mm} \times 80 \text{ mm} \times 160 \text{ mm}$ [26]. This model also has a 2K monochrome LCD mask, with a $49.4 \mu\text{m} \times 50.4 \mu\text{m}$ pixel size. Despite the larger pixel size, it offers a higher dimensional accuracy and sharper features than the Elegoo Mars due to hardware updates.

In both cases, the Elegoo Water Washable Rapid Resin (Ceramic Grey) was used, which provides high accuracy, low shrinkage, and can be cleaned with water (i.e., without organic solvents).

The orientation of each part on the printer’s build plate is set using the Chitubox Basic slicer software [27]. The employed metalization processes are discussed along with the introduction of each respective component.

1.4.2 Post-Processing

A standard room temperature post-processing procedure was employed for all printed parts, to remove all mechanical support structures and uncured resin residue. This is undertaken using the following steps: (i) remove parts from the build plate; (ii) mechanically remove all support structures; (iii) pre-rinse in water; (iv) place in an ultrasonic water bath for 2 minutes; (v) water-jet clean and soft brush trough corners and grooves, to remove uncured resin residue; (vi) dry with compressed air; and (vii) post-UV cure in natural light for at least 4 hours. Note that using a UV lamp for faster post-curing was avoided, since this can result in warping, shrinkage, and layer delamination.

1.5. Timeline of Component Generations

The components introduced here were manufactured from March 2020 to September 2021, with four major design iteration phases using different printing and metalization processes. Each of these are referred to here as a ‘Generation’ (Gen.). The following is a list of these Generations, which are referred to throughout this document. I undertook all 3-D printing and some of the plating, with all measurements being performed at NPL.

1st Generation: printed using an Elegoo Mars and metalized using a commercial copper electroplating service. A split-block waveguide design was used.

Fabricated: February 2020. Measured: March 2020.

2nd Generation: printed using an Elegoo Mars and metalized using in-house silver electroless plating. A single-block waveguide design was introduced.

Fabricated: April 2021. Measured: May 2021.

3rd Generation: printed using an Elegoo Mars and metalized using a commercial copper electroplating service. The ‘trough-and-lid’ assembly approach was introduced.

Fabricated: May 2021. Measured: June 2021.

4th Generation: printed using an Elegoo Mars 2 Pro and metalized using a commercial copper electroplating service. The ‘trough-and-lid’ assembly approach was continued.

Fabricated: June to August 2021. Measured: July to September 2021.

1.6. Health and Safety Considerations

At various instances during the production process, several hours of 3-D printing and post-processing were required per day, with our research group employing multiple 3-D printers that would often run in parallel. To mitigate exposure to volatile organic compounds (VOCs), airborne particulates, and any other workplace hazards associated with 3-D printing [28]-[29], stringent health and safety considerations were required. The lab in which the printing was conducted had not been previously utilized for this application; therefore, a bespoke set-up for safe 3-D printing was required. All the necessary approvals were obtained (e.g., COSHH forms for organic solvents and Local Exhaust Ventilation certification for recirculating fume cabinets).

A commercial recirculating fume cabinet [30] was used to provide fume extraction for the MSLA printers, with pre-, HEPA, and active carbon filters used to remove particulates and primary VOCs that are released by the photocurable resin before, during, and after printing [31]. Post-processing with organic solvents was also conducted within this cabinet.

Moreover, a larger bespoke fume extraction cabinet was created to accommodate a large FDM printer and an SLA printer, which were used in other projects. Some post-processing of MSLA-printed parts was conducted here, due to the larger volume in comparison to the commercially made cabinet. A commercial fume extractor (BOFA AD Oracle iQ [32]) with pre, HEPA and active carbon filters were used to provide fume extraction. Both the commercial and bespoke extracted cabinets were assessed and

certified by ICL's Local Exhaust Ventilation team, with subsequent annual checks undertaken.

A designated chemical cabinet was used to safely store all necessary chemicals, including opened resin bottles. The fume cabinets and chemical cabinets were located directly adjacent to each other, as shown in Fig. 2.7.

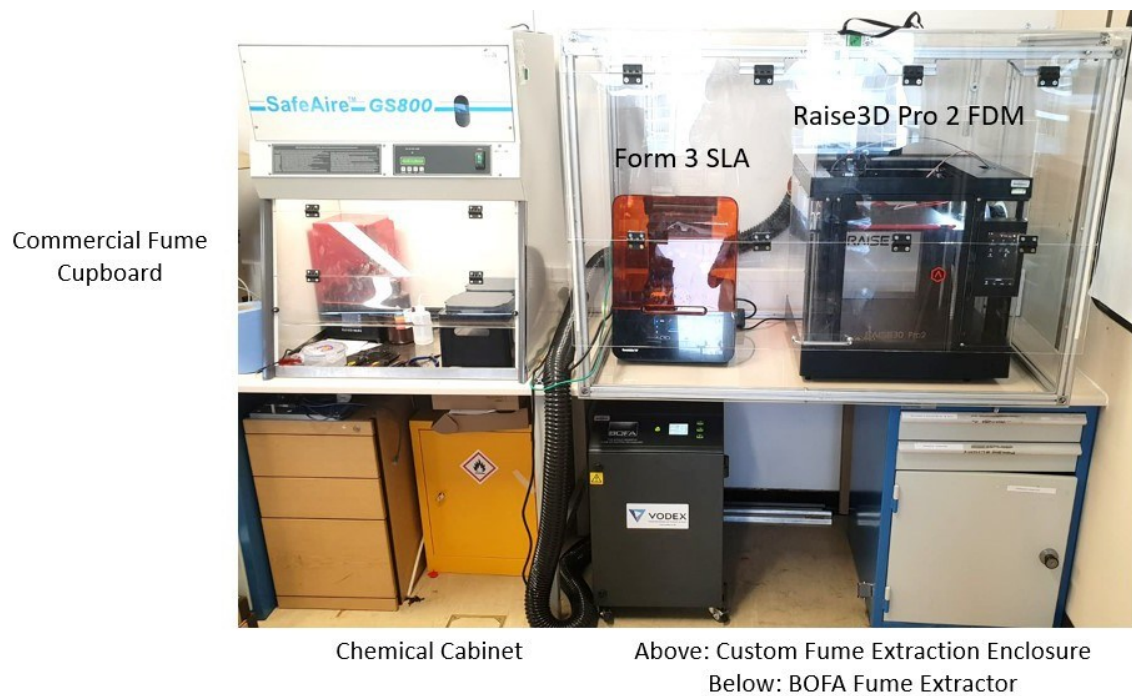


FIGURE 1.7: Photograph of 3-D printing and post-processing lab set-up.

Disposal of all waste resin and chemicals was undertaken through ICL's chemical waste management procedures. Resin-contaminated water was left to stand in ambient light for a day, after which most of the resin suspended in the water would float to the surface and cure with ambient UV light. The cured polymer is then removed from the water and disposed in a general waste bin. The remaining water is filtered before disposal into a sink, with the filter being disposed in a general waste bin.

1.7. Conclusion

In this chapter, an overview of the various polymer-based 3-D printing technologies is given, including examples of their use for manufacturing microwave and millimeter-wave MPRWGs. Of these technologies, VP printing is chosen, as it provides high resolution and high surface quality for a low retail cost. The cheapest VP technology is MSLA printing, which is rapidly gaining popularity for its substantially lower cost in comparison to SLA and DLP printers.

An outline of the 3-D printing procedure was given, which was ubiquitously employed. Two different MSLA printers were used: the Elegoo Mars and the Elegoo Mars 2 Pro. Also, two different plating technologies were employed: commercial copper electroplating and in-house silver electroless plating (i.e., chemical plating without the use of electrodes). Different combinations of printing technologies, plating techniques, and waveguide designs give rise to the four Generations of MPRWGs that were fabricated and measured. Finally, an explanation of the necessary health and safety precautions that were undertaken is given.

1.8. References

- [1] B. DeBoer, N. Nguyen, F. Diba and A. Hosseini, "Additive, subtractive, and formative manufacturing of metal components: a life cycle assessment comparison," *The International Journal of Advanced Manufacturing Technology*, vol. 115, p. 413–432, 2021.
- [2] F. J. Tischer, "Experimental attenuation of rectangular waveguides at millimeter wavelengths," *IEEE Trans. on Microw. Theory and Techn.*, vol. 27, no. 1, pp. 31-37, 1979.
- [3] B. Redwood, F. Schöffer, B. Garret, "The 3-D printing handbook", 1st ed., Amsterdam, The Netherlands: 3D Hubs B.V., 2018.
- [4] R. Payapulli, L. Zhu, S.-H. Shin, M. Stanley, N. M. Ridler and S. Lucyszyn, "Polymer-based 3-D printed 140 to 220 GHz metal waveguide thru lines, twist and filters," *IEEE Access*, vol. 11, pp. 32272-32295, Mar. 2023.
- [5] S.-H. Shin, R. Payapulli, L. Zhu, M. Stanley, X. Shang, N. M. Ridler, and S. Lucyszyn, "3-D printed plug and play prototyping for low-cost sub-THz subsystems," *IEEE Access*, vol. 10, pp. 41708-41719, Apr. 2022.
- [6] S.-H. Shin, X. Shang, N. M. Ridler, and S. Lucyszyn, "Polymer-based 3-D printed 140-220 GHz low-cost quasi-optical components and integrated subsystem assembly," *IEEE Access*, vol. 9, pp.28020-28038, Feb. 2021.
- [7] S. Lucyszyn, X. Shang, W. J. Otter, C. Myant, R. Cheng, and N. M. Ridler, "Polymer-based 3D printed millimeter-wave components for spacecraft payloads," *IEEE MTT-S International Microwave Workshop Series on Advanced Materials and Processes (IMWS-AMP)*, Ann Arbor, USA, Jul. 2018 (Invited).
- [8] D. M. Pozar, "Microwave engineering," 4th ed., Hoboken, New Jersey: John Wiley & Sons, Inc., 2012.
- [9] M. D'Auria, W. J. Otter, J. Hazell, B. T. W. Gillatt, C. Long-Collins, N. M. Ridler, and S. Lucyszyn, "3-D printed metal-pipe rectangular waveguides," *IEEE Trans. on Components, Packaging and Manufacturing Technology*, vol. 5, no. 9, pp. 1075- 1092, May 2006.

- [10] S.-H. Shin, D. Alyasiri, M. D'Auria, W. J. Otter, C. W. Myant, D. Stokes, Z. Tian, N. M. Ridler, and S. Lucyszyn, "Polymer-based 3-D printed Ku-band steerable phased-array antenna subsystem," *IEEE Access*, vol. 7, pp. 106662-106673, Aug. 2019.
- [11] E. Márquez-Segura, S.-H. Shin, A. Dawood, N. M. Ridler, and S. Lucyszyn, "Microwave characterization of conductive PLA and its application to a 12 to 18 GHz 3-D printed rotary vane attenuator," *IEEE Access*, vol. 9, pp. 84327-84343, 2021.
- [12] W. J. Otter and S. Lucyszyn, "Hybrid 3-D-printing technology for tunable THz applications," *Proc. of the IEEE*, vol. 105, no. 4, pp. 756-767, Apr. 2017.
- [13] W. J. Otter, N. M. Ridler, H. Yasukochi, K. Soeda, K. Konishi, J. Yumoto, M. Kuwata-Gonokami, and S. Lucyszyn, "3D printed 1.1 THz waveguides," *IET Electron Lett.*, vol. 53, no. 7, pp. 471-473, Mar. 2017.
- [14] I. Gibson, D. Rosen, B. Stucker, "Additive manufacturing technologies: 3D printing, rapid prototyping, and direct digital manufacturing", 2nd ed., New York, NY, USA: Springer Science and Business Media, 2015.
- [15] T. Hara, Y. Hosokawa, T. Matsunaga, and S.-S. Lee, "Fabrication and its characteristics of Ka-band electroplated 3D printed waffle type waveguide," *46th International Conference on Infrared, Millimeter and Terahertz Waves (IRMMW-THz)*, Chengdu, China, Sep. 2021.
- [16] I. Kauppila, "The best SLS 3D printers in 2023", (2023). All3DP. Accessed: Jan. 23, 2023. [Online]. Available: <https://all3dp.com/1/best-sls-3d-printer-desktop-industrial/>.
- [17] K. Fujiwara, R. Kobayashi, S. Kuwahara, S. Takemura, K. Takizawa, and Y. Watanabe, "3-D printed iris waveguide filter in W-band," *23rd International Microwave and Radar Conference (MIKON)*, Warsaw, Poland, Oct. 2020.
- [18] A. von Bieren, E. de Rijk, J.-P. Ansermet, and A. Macor, "Monolithic metal-coated plastic components for mm-wave applications," *39th International Conference on Infrared, Millimeter, and Terahertz waves (IRMMW-THz)*, Tuscon, USA, Sep. 2014.
- [19] F. Fischer, "FDM and PolyJet 3D printing," Eden Prairie, MN, USA, Stratasys

- Inc., White Paper, 2013. [Online].
- [20] W. J. Otter and S. Lucyszyn, “Hybrid 3-D-printing technology for tunable THz applications,” *Proc. of the IEEE*, vol. 105, no. 4, pp. 756-767, Apr. 2017.
- [21] Formlabs, “Form 3: industrial-quality desktop SLA 3-D printer”, (2023). Formlabs. Accessed: Jan. 23, 2023. [Online]. Available: <https://formlabs.com/eu/3d-printers/form-3/>.
- [22] Anycubic, “Anycubic Photon D2: consumer DLP 3-D printer | Anycubic 3-D printing”, (2022). Anycubic. Accessed: Jan. 23, 2023. [Online]. Available: <https://www.anycubic.com/products/photon-d2-dlp-3d-printer>.
- [23] Phrozen Technology, “Phrozen Sonic Mini 8K 3D Printer”, (2022). Anycubic. Accessed: Jan. 23, 2023. [Online]. Available: <https://phrozen3d.com/products/phrozen-sonic-mini-8k-resin-3d-printer?variant=43781374345403>.
- [24] F. Gehrke, “Anycubic Photon Ultra – what even is DLP?”, (2023). All3DP. Accessed: Jan. 23, 2023. [Online]. Available: <https://all3dp.com/4/anycubic-photon-ultra-what-even-is-dlp/#:~:text=In%20a%20nutshell%2C%20DLP%20is,through%20and%20blocking%20the%20rest>.
- [25] Elegoo Inc., “ELEGOO Mars UV photocuring LCD MSLA 3D printer,” 2021. Accessed: Jan. 07, 2023. [Online]. Available: <https://www.elegoo.com/collections/mars-series/products/elegoo-mars-lcd-3d-printer>.
- [26] Elegoo Inc., “Elegoo Mars 2 Pro mono LCD MSLA resin 3D printer,” 2021. Accessed: Jan. 07, 2023. [Online]. Available: <https://www.elegoo.com/products/elegoo-mars-2-pro-mono-lcd-3d-printer>.
- [27] Chitubox, “CHITUBOX, All-in-one SLA/DLP/LCD Slicer, 3D printing preprocessing software,” 2021. Accessed: Jan. 07, 2023. [Online]. Available: <https://www.chitubox.com/en/page/chitubox-free>.
- [28] K. Min et al. “3D printing-induced fine particle and volatile organic compound emission: an emerging health risk,” *Environmental Science & Technology*

Letters, vol. 8, no. 8, pp. 616-625, Jun. 2021.

- [29] E. Jacobsen et al. “Measuring and controlling emissions from polymer filament desktop 3D printers,” Health and Safety Executive, Derbyshire, United Kingdom, RR1146, 2017.
- [30] *Filter Selection Based On Chemical Hazard Analysis & Risk Assessment*, 1st ed., Gruppo Strola s.a.s., Torino, Italy, 2020, pp. 1-2.
- [31] *Gruppo Strola GS800 Bench-top filtration fume cupboard*, 1st ed., Gruppo Strola s.a.s., Torino, Italy, 2020, pp. 1-2.
- [32] BOFA AD Oracle iQ Extraction Unit (2021). Vodex. Accessed: Dec. 24, 2021. [Online]. [https://www.vodex.co.uk/product/bofa-ad-oracle-iq-extraction-unit//](https://www.vodex.co.uk/product/bofa-ad-oracle-iq-extraction-unit/).

2. Overview of Rectangular Waveguide and Network Theory

2.1. Introduction

Part of the content in this chapter (i.e., Chapter 3.4) was written in a research article by R. Payapulli et al., which was published in *IEEE Access* in March 2023 [1].

The theoretical operation of MPRWGs is based on the fundamentals of electromagnetism, with the behavior of electric and magnetic fields being described by Maxwell's equations. These are given below in differential form, with all fields assumed to be time-harmonic and with $e^{j\omega t}$ dependence [2]:

$$\nabla \cdot \mathbf{E} = \frac{\rho_v}{\epsilon_0}, \quad (2.1a)$$

$$\nabla \cdot \mathbf{B} = 0, \quad (2.1b)$$

$$\nabla \times \mathbf{E} = -\frac{\partial \mathbf{B}}{\partial t}, \quad (2.1c)$$

$$\nabla \times \mathbf{B} = \mu_0 \left(\mathbf{J} + \epsilon_0 \frac{\partial \mathbf{E}}{\partial t} \right), \quad (2.1d)$$

where ∇ , \mathbf{E} , \mathbf{B} , ρ_v , ϵ_0 , t , μ_0 , and \mathbf{J} refer to the nabla operator, vector electric field strength, vector magnetic field strength, charge density within the medium, permittivity of free space, time, permeability of free space, and the vector current density, respectively. In Chapter 3.2, the equations describing the operation of MPRWGs are given. In Chapter 3.3 and 3.4, the fundamentals of microwave and millimeter-wave network analysis and measurements are explained, which is necessary to interpret the results in this thesis.

2.2. Rectangular Waveguide Theory

The geometry of a rectangular waveguide is given in Fig. 3.1, with an aperture width a and aperture height b . The guided EM radiation propagates in the z -direction, with the x - y plane being the transverse plane. The permeability and permittivity of free space are represented by μ_0 and ϵ_0 , respectively.

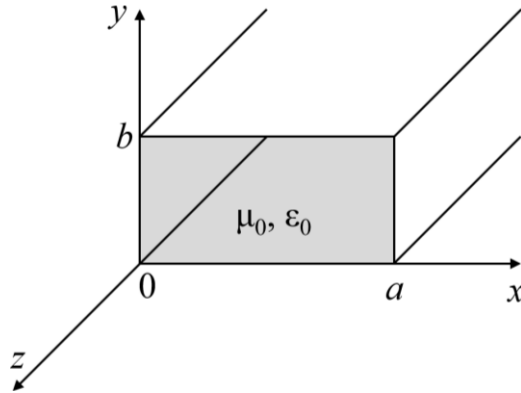


FIGURE 2.1: Geometry of an air-filled rectangular waveguide.

Assuming that the waveguide is source-free (i.e., $\rho_v = 0$), and wave propagation along the z -direction giving $e^{j\omega t}$ dependence for the electric and magnetic fields, (2.1c) and (2.1d) can be reduced to give the following four equations, which describe the transverse components of the electric and magnetic fields [2]:

$$E_x = -\frac{j}{k_c^2} \left(\beta \frac{\partial E_z}{\partial x} + \omega \mu_0 \frac{\partial H_z}{\partial y} \right), \quad (2.2a)$$

$$E_y = \frac{j}{k_c^2} \left(-\beta \frac{\partial E_z}{\partial y} + \omega \mu_0 \frac{\partial H_z}{\partial x} \right), \quad (2.2b)$$

$$H_x = \frac{j}{k_c^2} \left(\omega \epsilon_0 \frac{\partial E_z}{\partial y} - \beta \frac{\partial H_z}{\partial x} \right), \quad (2.2c)$$

$$H_y = -\frac{j}{k_c^2} \left(\omega \epsilon_0 \frac{\partial E_z}{\partial x} + \beta \frac{\partial H_z}{\partial y} \right), \quad (2.2d)$$

where $\omega = 2\pi f$ is the angular frequency, f is the linear frequency, $k_c^2 = k^2 - \beta^2$ is the cut-off wavenumber, and β is the propagation constant. These can be solved for Transverse Electric (TE) or Transverse Magnetic (TM) modes by setting $E_z = 0$ or $H_z = 0$, respectively, to obtain the general solution for each [2]. The TEM mode cannot propagate in waveguides, as they are made of a single conductor. The particular solution is then found by imposing the boundary conditions set by the waveguide geometry to give the internal field equations. Here, these are given for TE modes only, as all fabricated waveguides are designed to operate in the TE_{10} mode. Their full derivations are omitted, for brevity. Note that TEM modes, with $E_z = H_z = 0$, do not propagate in MPRWGs.

Equations (2.3), given below, describe the electric and magnetic fields in the transverse plane $E_{x,y}$ and $H_{x,y}$, and the magnetic field in the direction of propagation H_z , for TE_{mn} modes. Here, the linear frequency of the EM radiation is given by f , with angular frequency $\omega = 2\pi f$, and angular wavenumber $k = \omega\sqrt{\mu_0\varepsilon_0}$ [2]:

$$E_x = \frac{j\omega\mu_0n\pi}{k_c^2 b} A_{mn} \cos(k_x x) \sin(k_y y) e^{-j\beta z}, \quad (2.3a)$$

$$E_y = -\frac{j\omega\mu_0m\pi}{k_c^2 a} A_{mn} \sin(k_x x) \cos(k_y y) e^{-j\beta z}, \quad (2.3b)$$

$$H_x = \frac{j\beta m\pi}{k_c^2 a} A_{mn} \sin(k_x x) \cos(k_y y) e^{-j\beta z}, \quad (2.3c)$$

$$H_y = \frac{j\beta n\pi}{k_c^2 b} A_{mn} \cos(k_x x) \sin(k_y y) e^{-j\beta z}, \quad (2.3d)$$

$$H_z = A_{mn} \cos(k_x x) \cos(k_y y) e^{-j\beta z}, \quad (2.3e)$$

where: m and n are the mode numbers (with $m = 0, 1, 2, \dots$ and $n = 0, 1, 2, \dots$); $k_x = \frac{m\pi}{a}$ and $k_y = \frac{n\pi}{b}$ are angular wavenumber separation variables in the x - and y -directions, respectively; and A_{mn} is the TE_{mn} mode amplitude.

From these equations, we can see that all fields have a $e^{-j\beta z}$ component, giving a travelling wave field pattern in the z -direction, and sinusoidal components that give standing wave field patterns in the x - and y - directions (i.e., the transverse plane). This creates a TE mode pattern, which can be interpreted as the interference pattern formed by

the waves propagating by continually reflecting off the sidewalls.

It can be seen that, if $m = 0$ and $n = 0$, there is no propagation; therefore, the TE₀₀ mode does not exist. For the TE₁₀ mode with $m = 1$ and $n = 0$, $E_x = E_z = H_y = 0$, with E_y , H_x , and H_z all varying sinusoidally in the x -direction, with no variation in the y -direction for any field component.

The propagation constant is given by [3]:

$$\beta = \sqrt{k^2 - k_c^2} = \sqrt{k^2 - \left(\frac{m\pi}{a}\right)^2 - \left(\frac{n\pi}{b}\right)^2} \quad (2.4)$$

This is a real value when $k > k_c$, which results in wave propagation above a cut-off frequency for a given mode; therefore, waveguides can be considered as high-pass filters. For a source-free air-filled waveguide, this is given by:

$$f_{c,mn} = \frac{k_c}{2\pi\sqrt{\mu_0\varepsilon_0}} = \frac{1}{2\pi\sqrt{\mu_0\varepsilon_0}} \sqrt{\left(\frac{m\pi}{a}\right)^2 + \left(\frac{n\pi}{b}\right)^2} \quad (2.5)$$

For $a > b$, the lowest cut-off frequency exists for the TE₁₀ mode, with $f_{c,10} = \frac{c}{2a}$, with c being the speed of light in a vacuum. This is referred to as the dominant mode. Since standard millimeter-wave MPRWG aperture sizes have $a = 2b$, the next cut-off frequency will be for the TE₂₀ mode at $2f_{c,10}$. Therefore, for strict TE₁₀ mode operation, specified frequency ranges are typically from $\sim 1.2f_{c,10}$ to $\sim 1.9f_{c,10}$ [3].

Below the cut-off frequency, the propagation constant is purely imaginary. In this case, the propagation constant becomes $\alpha = \sqrt{k_c^2 - k^2}$, resulting in the fields exponentially decaying proportional to $e^{-\alpha z}$. This is known as an evanescent mode [2].

The free-space linear wavelength λ relates to the angular wavenumber by $k = 2\pi/\lambda$. Likewise, the guided wavelength relates to the waveguide propagation constant by $\lambda_g = 2\pi/\beta$. For the TE₁₀ mode, this gives [3]:

$$\lambda_g = \frac{\lambda}{\sqrt{1-\left(\frac{\lambda}{\lambda_c}\right)^2}} = \frac{c}{f} \cdot \frac{1}{\sqrt{1-\left(\frac{c}{2af}\right)^2}} \quad (2.6)$$

Given that λ is defined as the distance between two equal phase planes in free-space, λ_g can be interpreted as the distance between two equal phase planes in the z -direction along the waveguide. For propagating modes, this is always greater than the free-space wavelength, due to the sidewall reflections increasing the overall path length.

The phase velocity v_p is defined as the velocity of a fixed wave point on the wave, which is given by the rate of change in distance z with respect to time (i.e., $\frac{\partial z}{\partial t} = \frac{\omega}{\beta}$ for transmission lines and waveguides). In waveguides, this is faster than the speed of light. Group velocity v_g is defined as the velocity of the envelope of the signal, which is given by $\frac{\partial \omega}{\partial \beta}$. In waveguides, this is slower than the speed of light. It is associated with the group delay $\tau = \frac{l}{v_g}$, which is the time taken for information to propagate along a transmission medium of length l . For dispersive media, v_p and v_g vary with frequency and are not equal to each other, as β is a non-linear function of frequency. For air-filled rectangular waveguides, these quantities are given below, with $v_p v_g = c^2$ [2]:

$$v_p = \frac{\omega}{\beta} = \frac{c}{\sqrt{1 - \left(\frac{c}{2af}\right)^2}} \quad (2.7)$$

$$v_g = \frac{\partial \omega}{\partial \beta} = c \cdot \sqrt{1 - \left(\frac{c}{2af}\right)^2} \quad (2.8)$$

The power flow along a lossy transmission line with minimal reflections is given by $P(z) = P_0 e^{-2\alpha_C z}$, where P_0 is the power of the signal at the waveguide input and α_C is the TE₁₀ mode attenuation constant due to finite conductivity sidewalls. From this, the power loss per unit length in the z -direction due to finite conductivity of the sidewalls is given by $P_{loss} = \frac{\partial P(z)}{\partial z} = 2\alpha_C P(z)$, with α_C given by [2]:

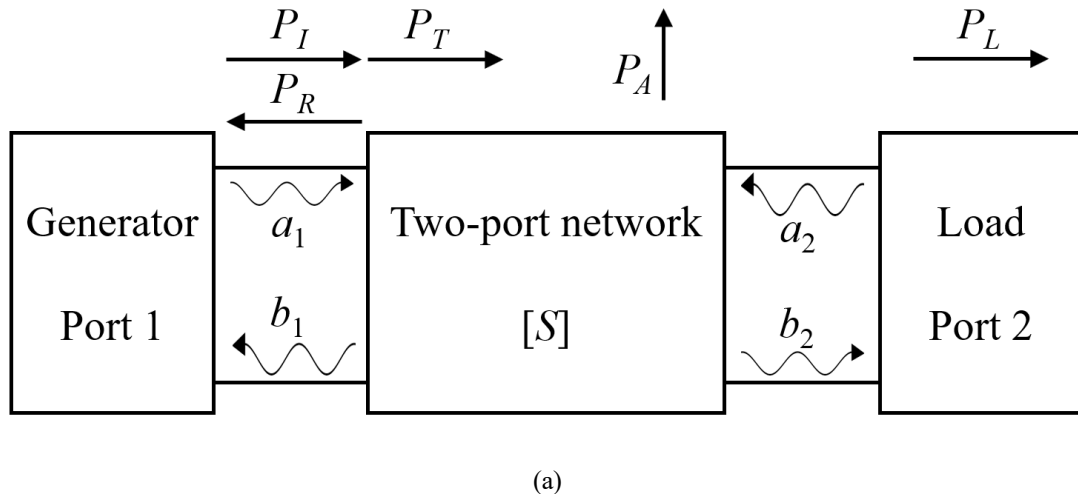
$$\alpha_C = \frac{P_{loss}(0)}{2P_0} = \frac{R_S}{\eta_0} \cdot \frac{2\pi^2 b + a^3 k_0^2}{a^3 b \beta k_0} \text{ [Np/m]} \quad (2.9)$$

where $R_S = \sqrt{\frac{\omega \mu_0}{2\sigma_0}}$ is the classical surface resistance of the conductor, σ_0 is the bulk DC conductivity of the conductor, and η_0 is the intrinsic wave impedance of free space. (2.9) is calculated by analyzing the current flow within the waveguide walls (omitted here).

2.3. Fundamentals of Microwave and Millimeter-Wave Network Analysis

Electrical network analysis for low-frequency circuits, using Kirchhoff's voltage and current laws, assume that there is negligible phase change across the circuit. As such, these techniques cannot be applied to microwave frequency circuits. Instead, we apply scattering (S-) parameters, which describes electrical networks in terms of the incident, transmitted, and reflected voltage waves at each port of the network [4].

S-parameters shall be explained here with respect to a two-port device-under-test (DUT), as this applies to all rectangular waveguides given in this thesis. In general, however, S-parameters can be defined for multiple-port networks. We define the problem according to Fig. 3.2. Here, the generator is the source of the applied signal power, which is incident onto the two-port network and is accepted by the load. The generator and load are assumed to be perfectly impedance matched, both having characteristic impedance Z_0 . The voltage waves incident on the network from Ports 1 and 2 are given by a_1 and a_2 , respectively. The voltage waves transmitted through / reflected from the network to Ports 1 and 2 are given by b_1 and b_2 , respectively. All voltage waves are represented by an amplitude and a phase. The power quantities P_- are defined later.



(a)

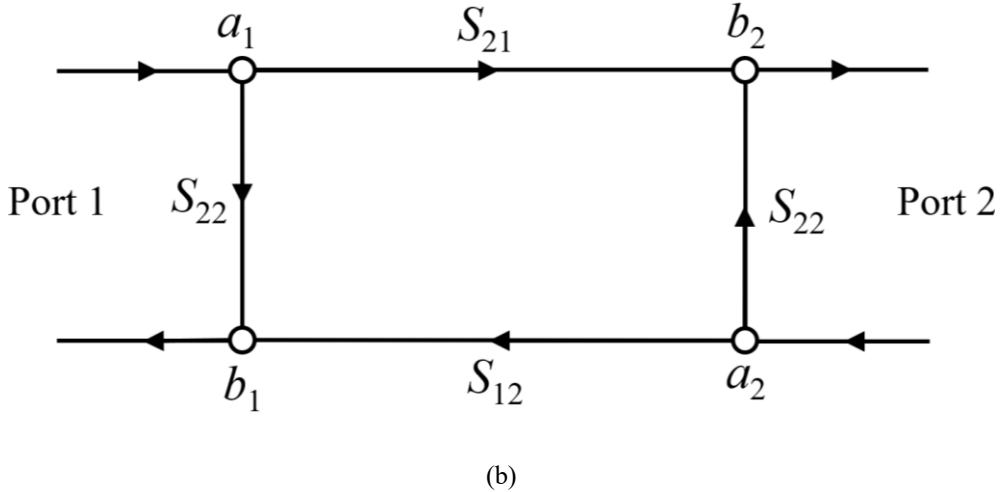


FIGURE 2.2: Representation of a two-port network: (a) definition of incident and reflected waves, and power delivered to each part of the network, with power quantities for Port 1 being driven; and (b) signal flow graph.

The scattering matrix, or $[S]$ matrix, of the network is given by [4]:

$$\begin{bmatrix} b_1 \\ b_2 \end{bmatrix} = \begin{bmatrix} S_{11} & S_{12} \\ S_{21} & S_{22} \end{bmatrix} \begin{bmatrix} a_1 \\ a_2 \end{bmatrix} \quad (2.10)$$

It can be seen that, by expanding this matrix equation, the S-parameter S_{ij} is found by driving the signal at Port j and measuring at the undriven Port i (i.e., $a_i = 0$). For example, to obtain S_{21} , Port 1 is driven and Port 2 is undriven ($a_2 = 0$), with the driven incident voltage wave a_1 and the measured transmitted voltage wave b_2 giving $S_{21} = b_2/a_1$. Note that all S-parameters will have amplitude and phase.

The signal flow graph in Fig. 3.2(b) is a graphical representation of the relationship between the S-parameters and the incident and transmitted/reflected voltage waves. For example, we can see that the voltage wave a_1 that is incident on the network splits into two waves: a reflected wave b_1 and a transmitted wave b_2 , with S_{11} and S_{21} representing their respective relationships with a_1 .

S_{11} and S_{22} are reflection coefficients at Ports 1 and 2, respectively, given that the other Port is not driven and is terminated with a matched load (i.e., no reflection from this port). S_{21} and S_{12} are transmission coefficients from Port 1 to Port 2 and from Port 2 to Port 1, respectively, with the non-driven Port again terminated with a matched load. Ideally, waveguides are passive, reciprocal, symmetrical and homogeneous devices, giving $S_{11} = S_{22}$ and $S_{21} = S_{12}$.

With Port 1 in Fig. 3.2(a) being driven, we obtain five power quantities [5]. These refer to the incident power of the signal P_I , the reflected power P_R , the transmitted power (which is delivered to the load) P_L , the true power delivered to the two-port network $P_T = P_I - P_R$, and the power absorbed/dissipated by the two-port network $P_A = P_T - P_L$. From the principle of conservation of energy, $P_I = P_L + P_R + P_A$.

The ratio of the transmitted power to the incident power is known as the transmittance, which is given by $\mathcal{T} = \frac{P_L}{P_I} = |S_{21}|^2$, for a passive, symmetrical, reciprocal, and homogenous device [4]. Likewise, the ratio of the reflected power to the incident power is known as the reflectance, which is given by $\mathcal{R} = \frac{P_R}{P_I} = |S_{11}|^2$. The ratio of the power absorbed by the two-port network to the incident power is known as the absorptance, which is given by $\mathcal{A} = \frac{P_A}{P_I} = \frac{P_I - P_R - P_L}{P_I} = 1 - |S_{11}|^2 - |S_{21}|^2$. From the principle of conservation of energy, $1 = \mathcal{T} + \mathcal{R} + \mathcal{A}$.

2.4. Measurements

Note that the definitions given here are for input loss/attenuation, with the driven signal incident on Port 1. For the output loss/attenuation, with the driven signal incident on Port 2, we simply substitute $|S_{11}|^2 \rightarrow |S_{22}|^2$ and $|S_{21}|^2 \rightarrow |S_{12}|^2$.

2.4.1 Insertion Loss

For the derivation of the insertion loss of a two-port network, we define a baseline case as being a perfectly matched and lossless generator and load, having zero power loss

when directly connected. After inserting the device-under-test (DUT), the input insertion loss (IL) is defined as the transmitted power loss normalized to the incident power [4]. This is also equivalent to the total attenuation α_T due to the two-port network, and is typically expressed in decibels (dB). The definition is given by:

$$IL = -10 \log_{10} \left(\frac{P_L}{P_I} \right) = -10 \log_{10} |S_{21}|^2 \quad (2.11)$$

Note that power loss and attenuation are conventionally defined as positive values; since $\frac{P_L}{P_I} \leq 1$, the negative of this logarithm is taken.

The ideal textbook transmittance (which assumes perfect wave impedance matching) and the corresponding insertion loss for an air-filled MPRWG is given by [2]:

$$|S_{21}|^2 = e^{-2\alpha_C L} \quad (2.12)$$

where L is the physical waveguide length. Substituting (2.12) into (2.11) gives an expression for the insertion loss for an ideal, perfectly matched waveguide.

$$IL|_{Ideal} = 8.686 \alpha_C L [\text{dB}] \quad (2.13)$$

2.4.2 Return Loss

For a two-port network, input return loss (RL) is defined as the ratio of the reflected power at Port 1 to the incident power [4]. It is typically expressed in decibels (dB). The definition is given by:

$$RL = -10 \log_{10} \left(\frac{P_R}{P_I} \right) = -10 \log_{10} |S_{11}|^2 [\text{dB}] \quad (2.14)$$

2.4.3 Mismatch Loss Attenuation

Input mismatch loss attenuation α_M is the ratio of the true power delivered to the network to the incident power [4]. This is exacerbated with a greater impedance mismatch as this increases the reflected power, causing a greater discrepancy between the true power and the incident power. This is given by:

$$\alpha_M = -10 \log_{10} \left(\frac{P_T}{P_I} \right) = -10 \log_{10} \left(\frac{P_I - P_R}{P_I} \right) = -10 \log_{10} (1 - |S_{11}|^2) \text{ [dB]} \quad (2.15)$$

2.4.4 Dissipative Attenuation

The total input power attenuation $\alpha_T = \alpha_M + L\alpha'_D = -10 \log_{10} |S_{21}|^2$ [dB]. Here, α'_D represents the input dissipative attenuation per unit length due to ohmic losses. This is defined as the ratio between the power delivered to the load P_L to the true power delivered to the two-port network P_T [6], [7]. This removes the effect of the reflected power loss P_R , thereby giving a quantity that describes the attenuation within the network due to ohmic losses. This quantity also scales with the physical length of a waveguide or transmission line L , and is given by:

$$\alpha'_D = -10 \log_{10} \left(\frac{P_L}{P_T} \right) = -\frac{10}{L} \log_{10} \left(\frac{|S_{21}|^2}{1 - |S_{11}|^2} \right) \text{ [dB/m]} \quad (2.16)$$

Since α_M does not contribute to the intrinsic transmission loss performance, only α'_D is considered in the measurements given in this thesis.

The ideal calculated dissipative attenuation $\alpha'_D|_{Ideal}$, with ideal cross-sectional dimensions to give perfect wave impedance matching ($|S_{11}| = 0$), can be calculated by substituting (2.12) into (2.16):

$$\alpha'_D|_{Ideal} = \frac{IL|_{Ideal}}{L} = 8.686 \alpha_C \text{ [dB/m]} \quad (2.17)$$

Therefore, $\alpha'_D|_{Ideal}$ corresponds to the attenuation constant, given by (2.9), converted from Np/m to dB/m. For resonators, dB/ λ_g may be a more useful unit of measurement, obtained simply by multiplying (2.16) and (2.17) by λ_g .

2.4.5 Time Domain Reflectometry (TDR)

Time-domain reflectometry (TDR) is a very sensitive tool for detecting impedance mismatches, with its transient responses, which may not be easily seen from steady-state frequency-domain responses. As such, TDR is useful for determining the quality of flange-to-flange wave impedance matching, at port-to-DUT and inter-component interconnects, and for performing a non-invasive test for physical deformation and surface defects within MPRWGs.

Within a VNA, a discrete inverse Fourier transform is applied to the frequency-domain return loss responses (S_{11} and S_{22}). Ideally, this is mathematically equivalent to launching a unit impulse into the DUT and measuring the corresponding reflected response [7]. The resulting TDR response is a series of return pulses, each corresponding to a discrete wave impedance discontinuity. Note that, for a band-pass frequency-domain operation having an ideal rectangular (also referred to as ‘boxcar’, ‘top hat’ or ‘brick-wall’) filtering function with a 3 dB bandwidth BW , the corresponding full-width at half-maximum (FWHM) values of the ‘synthetic-pulse’ for the time-domain impulse response is $t_{FWHM,R} = 1.2/BW = 15$ ps, using $BW = 80$ GHz for G-band operation [7]. Frequency-domain Kaiser-Bessel ($\beta_K = 6$) and Hanning window functions have impulse widths of $t_{FWHM,K} = 1.63 \times t_{FWHM,R} = 1.96/BW = 24.4$ ps [8] and $t_{FWHM,H} = 2/BW = 25$ ps, respectively [7]. A Hanning window reduces the sidelobes that would be apparent in TDR measurements if using a rectangular window, due to the avoidance of high frequency Fourier components.

The extracted physical distance d along a thru line between any two points on a TDR

trace and the corresponding two-port differential-phase group delay τ_g is given by [7]:

$$d \simeq v_g \Delta t / 2 \quad [\text{m}] \quad (2.18)$$

$$\tau_g = d/v_g \simeq \Delta t / 2 \quad [\text{s}] \quad (2.19)$$

where Δt refers to the round-trip time difference between any two points on the trace. Between the two main reflection pulse peaks, Δt should correspond to twice the flange-to-flange length L of a waveguide DUT, with v_g calculated at the mid-band frequency of 180 GHz.

It can be shown that, for normal passive homogeneous/uniform media (e.g., material samples or guided-wave structures under test) of infinite thickness/length, the peak of the ‘synthetic-pulse’ from the magnitude of the input voltage-wave reflection coefficient TDR ($|S_{11}|$) can be given by [9]:

$$|\rho_o|_{Peak,R} = \frac{Z-Z_0}{Z+Z_0} \quad (2.20)$$

where subscript ‘R’ refers to the use of the rectangular frequency-domain window function, ρ_o is the zeroth-order electric-field wave reflection coefficient, Z is the intrinsic impedance for a material sample or characteristic/wave impedance for a transmission line/waveguide under test, and Z_0 is the reference impedance; both impedances must be dispersionless (i.e., independent of frequency). For a Hanning frequency-domain window function, having subscript ‘H’, the peak is given by [9]:

$$|\rho_o|_{Peak,H} = \frac{|\rho_o|_{Peak,R}}{2} \quad (2.21)$$

With a medium of finite thickness/length, two dominant peaks will be seen. Given dispersionless impedances, the first peak is given by the following close approximation [9]:

$$|\rho_o|_{1st\ Peak,R} \cong \frac{Z-Z_0}{Z+Z_0} \quad (2.22)$$

For an ideal (lossless and dispersionless) medium it can be shown, using a simple heuristic engineering approach [9], that the second peak is given by the following approximation:

$$|\rho_o|_{2nd\ Peak,H} \cong \frac{(1-|\rho_o|_{1st\ Peak,R}^2) \cdot |\rho_o|_{1st\ Peak,R}}{2} \quad (2.23)$$

Equations (2.20)-(2.23) are quantitative for lossless and non-dispersive media. However, since waveguides are inherently highly frequency dispersive [10], (2.20)-(2.23) can only predict qualitative values, being of the same order of magnitude.

2.5. Conclusion

This chapter has covered the basics of rectangular waveguide theory, giving the key equations that describe the main operating principles, the fundamentals of S-parameters for two-port networks, and various power loss measurements. This provides all the necessary theoretical basis for the interpretation of the measured results given in this thesis.

2.6. References

- [1] R. Payapulli, L. Zhu, S.-H. Shin, M. Stanley, N. M. Ridler, and S. Lucyszyn, “Polymer-based 3-D printed 140 to 220 GHz metal waveguide thru lines, twist and filters,” *IEEE Access*, vol. 11, pp. 32272-32295, Mar. 2023.
- [2] D. M. Pozar, “Microwave engineering,” 4th ed., Hoboken, New Jersey: John Wiley & Sons, Inc., 2012.
- [3] N. Marcuvitz, “Waveguide handbook,” 2nd ed., London, U.K.: Peter Peregrinus Ltd., on behalf of The Institution of Electrical Engineers, 1986.
- [4] A. Coster, “Attenuation measurement”, Chapter 5 in *Microwave Measurements*, R. J. Collier and A. D. Skinner (Editors), 3rd Edition, London, U.K.: IET, Oct. 2007, pp. 91–119.
- [5] F. L. Warner, “Attenuation measurement,” Chapter 8 in *Microwave Measurements*, A. E. Bailey (Editor), 2nd Edition, London, U.K.: IEE, 1989, pp. 132–134.
- [6] M. D'Auria, W. J. Otter, J. Hazell, B. T. W. Gillatt, C. Long-Collins, N. M. Ridler, and S. Lucyszyn, “3-D printed metal-pipe rectangular waveguides,” *IEEE Trans. on Components, Packaging and Manufacturing Technology*, vol. 5, no. 9, pp. 1075- 1092, May 2006.
- [7] S. Lucyszyn, “RFIC and MMIC measurement techniques”, Chapter 11 in *Microwave Measurements*, R. J. Collier and A. D. Skinner (Editors), 3rd Edition, London, U.K.: IET, Oct. 2007, pp. 217–262.
- [8] A. H. Nuttall, “Some windows with very good sidelobe behavior,” *IEEE Trans. on Acoustics, Speech, and Signal Processing*, vol. 29, no. 1, pp. 84-91, Feb. 1981.
- [9] J. Sun, S. Lucyszyn, “Extracting complex dielectric properties from reflection-transmission mode spectroscopy”, *IEEE Access*, vol. 6, no. 1, pp.8302-8321,2018.
- [10] J. Sun, A. Dawood, W. J. Otter, N. M. Ridler, and S. Lucyszyn, “Microwave characterization of low-loss FDM 3-D printed ABS with dielectric-filled metal-pipe rectangular waveguide spectroscopy”, *IEEE Access*, vol. 7, pp. 95455-95486, Jul. 2019.

3. Trends on Polymer-Based 3-D Printing for Millimeter-wave MPRWGs

All of the content of this chapter is based on a research article by Payapulli et al., which was published in *IEEE Access* in March 2023 [1].

This unique and exhaustive up-to-date literature review has been undertaken for 3-D printed thru lines above 75 GHz, 90° twists above 8 GHz, and BPFs above 75 GHz, as these were the components that were manufactured here. To the best of our knowledge, all metal- and polymer-based exemplars have been included, giving valuable insight into the main design challenges for each component type.

3.1. Thru Lines

Thru lines are defined here as straight sections of waveguide, used as interconnects between two other components. They are the simplest MPRWG structure, representing a useful benchmark for assessing performance. Upper- and sub-millimeter-wave (300 GHz to 3 THz) COTS waveguides are generally precision-machined with two split-block parts that are joined through brazing.

From an exhaustive search, sixteen examples of 3-D printed thru lines operating above 75 GHz were found in the open literature; all references published since 2015. A summary is given in Table 1.1, where α'_D and RL refer to the respective average dissipative attenuation per unit length and worst-case return loss across its waveguide band. The former enables a direct comparison between thru lines with the same waveguide band, and is discussed further in Chapters 3 and 4. In addition, nine COTS thru lines are included, for comparison.

The submillimeter seamless (single-block) waveguide product range from Flann Microwave Ltd. includes low loss COTS thru line components operating up to 1.1 THz [2]. The nominal insertion loss, measured at the lower band-edge frequency f_L , is shown

in Table 1.1. Either copper or nickel is electroformed (a type of formative manufacturing) to create the MPRWG, having a quoted internal mean profile surface roughness of $R_a < 0.2 \mu\text{m}$. The performance is commensurate with commercially machined waveguides having a split-block construction [2]. Further analysis of these Flann waveguides is given in Chapter 7.

Silicon micromachining has also been shown to produce upper-millimeter-wave waveguides with high accuracy and precision. This technology enables easy integration of waveguide components with active MMICs using a split-block construction. For example, Pursula et al. have demonstrated a 10 mm-long 220 GHz to 325 GHz (WR-3) thru line, exhibiting a mid-band insertion loss of 2.3 dB ($\alpha'_D = 230 \text{ dB}$) and a worst-case return loss of 24 dB [3]. This represents a significantly higher attenuation when compared with EM simulations and with rectangular waveguide thru lines at the same frequency band, as shown in Table 1.1. The authors of this publication have identified the cause of the additional attenuation as EM radiation leakage through gaps in the split-block structure, which occurred due to over-etching. This approach may benefit from the “trough-and-lid” assembly solution that is presented later in this thesis.

Single-block metal-based 3-D printed thru lines have been demonstrated at D-band and J-band (220 to 325 GHz) by Zhang and Zirath, using selective laser melting (SLM) [4]. No additional plating was required, as the SLM printer uses a copper alloy powder. The reported measured α'_D values are 19 dB/m and 121 dB/m for 50 mm long thru lines at D- and J-bands, respectively; these are 10 dB/m and 88 dB/m for their respective COTS counterparts.

The difference in α'_D , between those from metal-based 3-D printed and COTS thru lines, can be attributed to ohmic losses, principally due to poor intrinsic bulk DC conductivity of the metal alloy powders, and high surface roughness. Also, due to the high costs associated with metal-based 3-D printers, fabrication may employ outsourcing services.

Polymer-based 3-D printing has been shown to produce low loss upper-millimeter-wave and THz thru lines, as demonstrated by von Bieren et al. at J-band, using a single-block design [5]. Fabrication was undertaken using a high-resolution stereolithographic

apparatus (SLA) printer, providing dimensional accuracy to within only $\pm 10 \mu\text{m}$, followed by their custom-developed copper plating process. The measured α'_D is only 13 dB/m; an order of magnitude improvement (in dB/m) over the previous metal-based exemplar [4], due to the substantially higher metal conductivity.

ICL previously demonstrated polymer-based 3-D printed thru lines above G-band, using two different high-cost manufacturing techniques. First, single-block 500 to 750 GHz (WM-380) and 750 GHz to 1.1 THz (WM-250) exemplars were fabricated using the University of Tokyo's experimental ultra-high-resolution RECILS 3-D printer [6] and a commercial electroless plating process [7]. With the former the mid-band α'_D is 240 dB/m, which is significantly poorer than the COTS counterpart, having 65 dB/m. Second, a 325 to 500 GHz split-block thru line was fabricated by outsourcing high-resolution polymer-jet (Polyjet) 3-D printing, with 500 nm thick copper sputter coating; the average α'_D is 440 dB/m. Radiation leakage from the split is believed to be the major loss mechanism. This is caused by a break in the transverse current path, due to a physical gap between assembled parts. Neither of these exemplars can be considered low loss MPRWG components.

An example of low-cost manufacturing (i.e., with total manufacturing costs being low in comparison to the retail costs of typical COTS counterparts) uses a desktop polymer-based SLA printer and a simple silver-copper electroless plating process [8], [9]. This was used to produce a D-band single-block 25.4 mm long thru line [10], with an average measured α'_D of 26 dB/m (comparable to a COTS thru line).

Until now, at G-band, ICL reported the only previous example of a low-cost 3-D printed thru line, employing a traditional symmetrical E-plane split-block design and a desktop SLA printer [11]. This first attempt demonstrated a high α'_D of 59 dB/m, due to radiation leakage from the split. It will be shown in this paper that low loss can be achieved with our unconventional H-plane split-block design and a low-cost MSLA printer.

TABLE 3.1: Millimeter-wave 3-D printed and COTS thru lines.

(EP = electroplating, ELP = electroless plating, *nominal worst-case insertion loss found at the lower band-edge frequency f_L and †COTS components were measured by me or ICL)

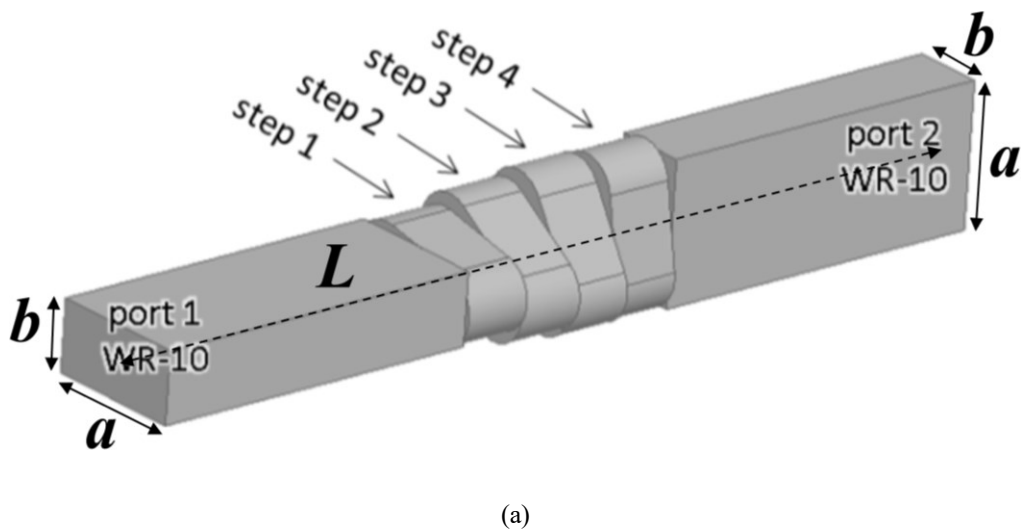
Frequency Range (GHz) [Waveguide Band]	α'_D (dB/m)	RL (dB)	Length (mm)	Split-Block	Manufacturing Technology	Plating	Year	Ref.
65-90 [WR-12]	7.5	10	50		SLM (Cu-15Sn)	None	2016	[4]
	4.3†	25†	50		COTS (Al)	Au	2022	[12]
	5.5	25	100	No	Proprietary Cu plating		2017	[13]
	6.3	17	25.4		Ag and Cu ELP		2017	[10]
	8.3	18	100	E-plane symmetrical	MLS (AlSi10Mg)	None	2017	[13]
	11	20	60		SLA	30 µm Cu EP	2015	[14]
	14.0	21	25.4		DLP	Ag ELP	2016	[9]
	11.5*	-	100		COTS	Au	2023	[2]
	19	20	50		SLM (Cu-15Sn)	None	2016	[4]
75-110 [WR-10]	25.6	-	25.4	No	SLA	Ag and Cu ELP	2017	[10]
	9.4†	27†	50.8		COTS (Al)	Au	2022	[15]
	9.9†	28†	25.4	H-plane <i>a</i> -edge				
	12.7	15	7.4		MSLA	50 µm Cu EP	2022	This work
	13.7	14	10.4	No	COTS	Au	2023	[2]
	17*	-	100		SLA	20 µm Cu EP	2018	[11]
	59	6	50.8	E-plane symmetrical				
	13	-	25		SLA	Custom- developed Cu plating	2014	[13]
110-170 [WR-6]	31*	-	100		COTS	Au	2023	[2]
	120	12	50		SLM (Cu-15Sn)	None	2016	[4]
	230	24	10		Si micromachining	Au	2017	[3]
	36	-	25.4	No	RECILS	3.6 µm Ni, Cu and Au ELP	2022	[16]
140-220 [WR-5]	61*	-	100		COTS	Au	2023	[2]
	440	-	25		Polyjet	500 nm Cu sputter coating	2017	[17]
	115*	-	100	E-plane symmetrical	COTS	Au	2023	[2]
220-325 [WR-3]	240	7	5		RECILS	1 µm Ag electroplating	2017	[7]
	230*	-	100		COTS	Au	2023	[2]
325-500 [WM-570]	1,400	6	5	No	RECILS	1 µm Ag electroplating	2017	[7]
500-750 [WM-380]								
750-1100 [WM-250]								

3.2. 90° Twists

Quasi-optical and waveguide integrated subsystems often utilize polarization splitting. This will lead to the use of orthogonally polarized waveguide ports. To connect these ports together, or to restore equal alignment between them, a physical rotation of 90° can be employed. This is known as a waveguide twist. At upper-millimeter-wave frequencies, commercial twists are normally realized by forced mechanical rotation of a straight MPRWG thru line about its longitudinal axis [18], resulting in a smooth transition. This may cause internal physical defects and poor structural rigidity; the end result being even more expensive than the original thru line.

Alternatively, 90° twists can also be manufactured through precision-machining, by using novel designs. Examples include a stepped rotation twist at W-band [19], shaped channel transition at J-band [20] and a rectangular-square-rectangular transition at WM-380 [21]. However, their multiple wave impedance discontinuities, which are inherent with these full waveguide band transitions, will result in a degraded return loss performance and, therefore, higher insertion loss when compared with smooth transitions.

Images of a stepped twisting transition and a smooth twisting transition are given in Fig. 3.1, showing the internal geometry of these components.



(a)

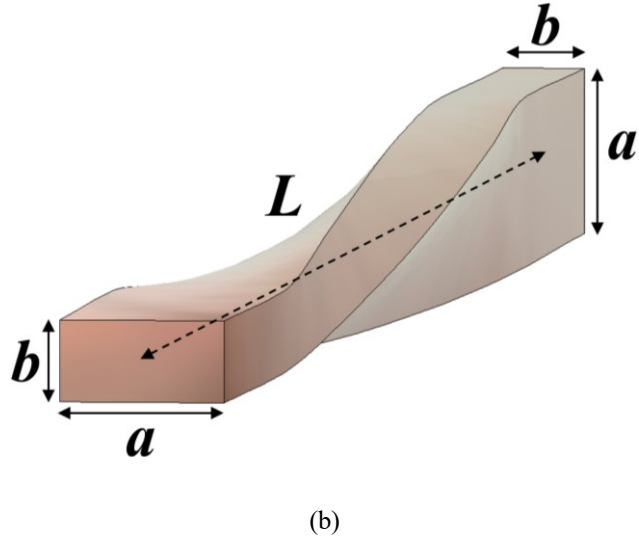


FIGURE 3.1: Internal geometry of a 90° twist: (a) stepped transition, designed by Al-Tarifi and Filipovic [19]; and (b) smooth transition, as used in this thesis.

From an exhaustive literature review, seventeen 3-D printed 90° twists were found in the open literature, with a summary given in Table 1.2. Here, IL refers to the average insertion loss for the discrete twist across the waveguide band. ‘Rotational Smoothness’ refers to the degree of rotation per λ_{gL} for smooth twists, where λ_{gL} is the guided wavelength at the lower band-edge frequency (having the worst-case attenuation), or step length per λ_{gL} for stepped twists. As can be seen for the WR-10 COTS twists, in Table 1.2, a lower value of rotational smoothness gives a better return loss, but at the expense of a degraded insertion loss.

The majority of the examples are integrated with one or more functionalities, as a single component or within a multi-component subsystem. This demonstrates the capability of 3-D printing for manufacturing complex waveguide geometries, avoiding the need for inter-stage flange-to-flange coupling and, therefore, reducing wave impedance mismatch losses. With all integrated twists, IL and RL measurements were not available for the discrete component.

Zhang et al. demonstrated the integration of two functionalities into a single component at Ka-band (26.5 to 40 GHz): a 90° twist and a 4th order Chebyshev diaphragm inductive iris-coupled BPF [22]. Fabrication involves SLA printing and copper

electroplating. Measured results show 0.8 dB average passband insertion loss and 0.4% frequency down-shifting from the designed BPF center frequency. Peverini et al. demonstrated the integration of three functionalities into a single component at Ku-band: a 90° twist, a low-pass filter and a 90° bend [23]. Measured results exhibit 0.1 dB average passband insertion loss and greater than 60 dB stopband rejection.

With multi-component subsystems, Dimitriadis et al. demonstrated a fixed Ka-band single-block 2×2 conical horn antenna array, with a waveguide feeding network consisting of three 3 dB power splitters, two smooth transition 90° twists, two smooth 90° bends and four 90° miter bends [24], using an SLA printer and electroless copper plating. Measured results show an antenna gain of 19-23 dBi across Ka-band.

More recently, ICL demonstrated the first fully 3-D printed tunable microwave subsystem, consisting of 26 circuit elements, creating a Ku-band steerable 4-element phased array antenna [25]. The main MPRWGs were fabricated using Polyjet and copper electroplating. The subsystem integrated three 3 dB power splitters, four dielectric-insert tunable phase shifters, four smooth transition 90° twists and four H-plane sectoral horn antennas. The total measured beam steering angle is approximately ±27° at 15 GHz and 17 GHz.

In summary, polymer-based 3-D printed 90° twists have already been demonstrated up to 110 GHz. It will be shown here that a G-band 90° twist can be realized by modifying the design of a low loss thru line.

TABLE 3.2: Microwave and mm-wave 3-D printed 90° twists operating above 8 GHz.
(*measured step length/ λ_{gL} and †COTS components that I measured),

Frequency Range [Waveguide Band]	IL (dB)	RL (dB)	Total Length (mm)	Twist Type	Rotational Smoothness (°/ λ_{gL})	Integration	Split-Block	Manufacturing Technology	Plating	Year	Ref.
8-12 [WR-90]	-	-	109		54	BPF			Cu electroplating	2021	[26]
	-	-	-		-	Power splitter, 90° bends, BPFs, horn antenna array	No	SLA	20 µm Cu and Sn electroplating	2019	[27]
12-18 [WR-62]	-	-	-		-	Power splitters, 90° bends, phase shifters, horn antenna array	H-plane symmetrical	Polyjet	20 µm Cu electroplating	2019	[25]
15-22 [WR-51]	-	-	63	Smooth	58	90° bend, BPF		SLA	Cu	2022	[28]
	-	-	47, 63, 79		60, 45, 36	90° bend, BPF		SLM (AlSi10Mg)		2018	[23]
	-	-	-		-	Orthogonal Mode Transducer (OMT)		MLS (AlSi10Mg)	None	2019	[29]
	-	-	-		-	90° bend, OMT, slotted antenna			5 µm Cu electroless	2017	[30]
	-	-	-		-	Power splitters, 90° bends, horn antenna array			Cu electroless	2017	[24]
26.5-40 [WR-28]	-	-	20.6	Stepped	0.28*		No	SLA	11 µm Cu and Ag electroplating	2020	[31]
	-	-	44.3			BPF			11 µm Cu and Ag electroplating	2019	[22]
	-	-	-	Smooth	-	Power splitters, turnstile junction, OMT		MLS (AlSi10Mg)	None	2022	[32]
	-	-	-		-	Diplexer, OMT		DLP	Ag electroless	2020	[33]
75-110 [WR-10]	0.10†	25†	31.75		31			COTS (Al)	Ag	-	[34]
	0.21	26.4	42		20		None		Au	2022	[35]
	0.21	22	4.7	Stepped	0.18*			MLS (Stainless steel)	None	2016	[19]
140-220 [WR-5]	0.62	13.2	31.75		18		H-plane a-edge	MSLA	50 µm Cu electroplating	2022	This work
	0.62†	12.9†	31.75	Smooth	18		No	COTS (Cu)	Au	-	[36]

3.3. Bandpass Filters

Waveguide bandpass filters (BPFs) are constructed from cavity resonators, which are partially enclosed waveguide structures that support standing waves at particular resonant frequencies for any given mode [37]. These typically have a length of $\lambda_g/2$. Cavity resonators are connected using coupling elements, which enable resonant electromagnetic energy within one cavity to be coupled into an adjacent cavity. These are typically shunt inductive discontinuities, such as symmetrical diaphragm inductive irises or transverse offset inductive irises (both of which shall be introduced in Chapter 6). The coupling coefficients of these elements determine the 3-dB bandwidths of each of the resonators, with a greater coupling coefficient (achieved with greater iris aperture widths) giving a larger bandwidth. The overall filter response is determined by the electrical lengths of the cavity resonators and the coupling coefficients of their adjacent coupling elements. This produces a transmission passband response; ideally, all frequencies within the passband are transmitted without attenuation, and all frequencies outside the passband are completely rejected. Practical waveguide filters always display some passband attenuation, which reduces for higher unloaded quality (Q-)factor resonators, a transition band roll-off, and a non-zero stopband rejection.

The two most common types of bandpass filter design are the Butterworth and Chebyshev [38]. The former has a maximally flat response within the passband (i.e., no passband ripple), since all return loss zeros are situated at the center frequency. In contrast, Chebyshev filters exhibit a passband ripple due to having return loss zeros spaced evenly across the passband. They have a comparatively steeper roll-off than Butterworth filters, but are more susceptible to passband distortion due to manufacturing inaccuracies.

The ability to realize very high Q-factor cavity resonators using MPRWGs enables higher performance BPFs when compared to planar transmission lines. Examples of the latter were reported by Robertson, Katehi, and Rebeiz, who designed and manufactured silicon micromachined planar 95 GHz (W-band) BPFs using a membrane-supported structure [39]. These exemplars displayed superior performance to W-band BPFs using conventional substrate-supported circuits, such as coplanar waveguide or microstrip, with an average insertion loss of 3.6 dB. The loss is attributed primarily to conductor ohmic

losses within the planar transmission lines. Since the conduction current density within waveguide sidewalls is comparatively much lower than in planar transmission lines, insertion losses are typically lower, with 3-D printed W-band MPRWG BPFs exhibiting an average of around 1.2 dB insertion loss, as shown in Table 1.3.

This makes waveguide BPFs essential for any mm-wave subsystem that requires strict frequency selection. For example, passive radiometry requires the selection of specific frequency ranges that are allocated for Earth observation purposes, thereby reducing out-of-band noise from commercial, industrial, medical, and scientific RF usage to acceptable levels. As they are required to fulfil a design specification, BPFs are generally custom designed.

At microwave (0.3 to 30 GHz) and lower-millimeter-wave frequencies (30 to *ca.* 100 GHz), the associated linear dimensions (i.e., lengths and widths of both the cavities and their coupling irises) are significantly larger than the minimum feature size of most manufacturing technologies, even with low-cost printers. However, for a constant bandwidth, higher operational frequency BPFs require higher loaded Q-factors (Q_L) and smaller dimensions. Therefore, the range of suitable printer technologies is further limited. Poor manufacturing accuracy can result in significant frequency shifting, primarily due to errors in cavity dimensions. Moreover, significant changes in the bandwidth can be found, primarily due to errors in iris dimensions. In extreme cases, the desired filter response can be distorted beyond acceptable limits.

As a result, almost all sub-THz (*ca.* 100 to 300 GHz) MPRWG BPFs reported in the open literature employ high-accuracy micromachining technologies, achieving close agreement with design specifications. Examples include CNC milling [40] and laser micromachining [41] at W-band, SU8 micromachining at J-band [42] and deep reactive-ion etching (DRIE) at WM-250 [43]. A full literature review of micromachined sub-THz COTS MPRWG BPFs has already been published [44].

From an exhaustive literature review, twelve examples of 3-D printed BPFs operating above 75 GHz were found. A summary is given in Table 1.3; all references published since 2015. Here, f_0 , BW , and FBW refer to the center frequency, 3 dB bandwidth and fractional bandwidth, respectively. Note that $FBW = BW/f_0$ is based on designed

values, while ‘Measured Q_L ’ is based on the measured 3 dB fractional bandwidth. With the exception of our chained-function BPF [44], all other filters were Chebyshev. In all cases, TE₁₀₁ mode rectangular cavity resonators were employed, with the majority using symmetrical diaphragm inductive irises. Three exceptions use either transverse offset inductive irises [44], asymmetrical diaphragm capacitive irises [45], or symmetrical capacitive stubs [46].

Metal-based 3-D printed examples include shaped rectangular and slotted spherical resonator BPFs at X-band [47]-[48], depressed super-ellipsoid resonator BPFs at Ku-band [49] and rectangular cavity resonator BPFs at W-band [50], G-band [51] and J-band [45]. As expected, higher insertion loss is measured when compared to machined BPFs, due to lower effective bulk DC conductivity and larger surface roughness.

Polymer-based printing has also been widely employed, with examples including slotted dual-mode circular waveguide resonator BPFs at X-band [52], gap waveguide BPFs at Ka-band [53], and rectangular cavity resonator BPFs at W-band [9]. As expected, passband insertion loss is lower than exemplars that use metal-based printing. However, in general, greater center frequency shifting occurs due to lower manufacturing accuracy.

Furthermore, several types of manufacturing accuracy limitations with polymer-based printing do not exist in metal-based technologies. These include: (i) pixel quantization errors, associated with MSLA printing [44]; (ii) significant iris corner rounding (ICR), due to either material erosion or resin residues; (iii) warping, due to uneven cooling-based contraction; and (iv) shrinkage during UV post-curing.

For BPFs, manufacturing accuracy limitations can be divided into two categories: dimensional and geometrical. The former refers to discrepancies between the designed and manufactured linear dimensions. The latter refers to changes in resonator and iris geometries. ICL have previously developed a pre-distortion technique for pixel quantization errors, associated with MSLA printing, being one type of dimensional inaccuracy [44]. With the latter, addressed in this paper, ICR is the main type of geometrical inaccuracy found with low-cost polymer-based printers. Here, the resulting passband frequency shifting is investigated. It will be shown that good results can be achieved using our new ICR compensation technique, when applied to G-band BPFs.

TABLE 3.3: Millimeter-wave 3-D printed MPRWG BPFs.

(EP = electroplating, ELP = electroless plating, * ICL's previously reported transverse offset iris

†Chebyshev and ‡chained-function BPFs [44]).

f_0 (GHz)	FBW (%)	Waveguide Band [Filter Order]	IL (dB)	RL (dB)	Measured Q_L	Split-Block	Manufacturing Technology	Plating	f_0 Shift (%)	BW Shift (%)	Coupling	Year	Ref.
83.5	6.0	WR-12 [11]	3.0	9	14.5		SLM	None	+4.2	+20		2015	[54]
90	11.1		0.4	18	6.7	No	SLA	10 μm Cu EP	-2.8	+10		2016	[41]
90	11.1	WR-10 [5]	1.0	15	7.3		MLS (Stainless steel)	5 μm Cu EP	-1.0	-0.1	Symmetrical Diaphragm	2019	[50]
			1.9	18	7.0			None	-1.8	+0.7	Inductive Iris		
91.3	7.8	WR-10 [4]	1.4	7.6	12.2		SLS (Polyamide)	Cu EP	-3.8	+1.4		2020	[55]
100	10	WR-10 [6]	1.0	11	15.8	E-plane symmetrical	SLA	30 μm Cu EP	+7.2	-32		2015	[9]
100	10	WR-10 [4]	0.3	17	9.0		MSLA	Cu EP	+1.1	+12	Symmetrical Capacitive Stub	2021	[46]
155		WR-05	0.5	10	11.2				+2.3	-8.4			
175	10	[5]	0.4	13	11.5	H-plane <i>a</i> -edge	MSLA	50 μm Cu EP	+0.5	+13	Symmetrical Diaphragm Inductive Iris	2022	This work
180	11		2.9	18	7.2	No	MLS (Stainless steel)	None	-1.4	+21			
		WR-5 [5]	3.0	18	7.1				-1.5	+21	Symmetrical Diaphragm Inductive Iris	2020	[51]
183	9.3		0.6†	6†	7.7†	H-plane <i>a</i> -edge	MSLA	50 μm Cu EP	-3.3†	+11†	Transverse Offset Inductive Iris	2022	[44]*
			0.6‡	13‡	5.8‡				-0.9‡	+15‡			
300	10.5	WR-3 [5]	1.1	10	8.0	E-plane symmetrical	MLS (Stainless steel)	3 μm Au ELP	-1.2	+6.8	Asymmetrical Diaphragm Capacitive Iris	2021	[45]

3.4. Conclusion

Here, a unique and exhaustive up-to-date literature review for 3-D printed MPRWG thru lines, twists and BPFs has been given for all work prior to that undertaken by me and my colleagues at ICL.

3-D printed thru lines have been demonstrated up to 1.1 THz, using an experimental, ultra-high-resolution 3-D printer; losses were significantly high, which was likely to be due to under-plating within the channel. For low loss implementations, the highest frequency example was demonstrated at 220 GHz to 325 GHz (WR-3) by von Bieren et

al. using an ultra-high-resolution SLA 3-D printer [5]. For implementations that are both low cost and low loss, the highest frequency achieved thus far was demonstrated at W-band by Shen et al. using a low-cost DLP printer and a custom-developed electroless plating process.

3-D printed 90° twists have been demonstrated at up to 110 GHz, using both stepped and smooth transition designs. These have often been integrated along with other functionalities (e.g., bandpass filtering) or within integrated subsystems.

3-D printed BPFs have been demonstrated up to 110 GHz with polymer-based 3-D printing. With metal-based 3-D printing, the highest reported center frequency BPF is 300 GHz, by Skaik et al.. The greater accuracy in linear BPF dimensions, less significant geometrical inaccuracies, and rigidness of the structures after printing has enabled this WR-3 BPF using metal-based printing; for the time being, this frequency band is beyond the capabilities of polymer-based printing.

In summary, this timely review reveals three main challenges that have precluded the realization of G-band split-block waveguides: (i) EM radiation leakage loss; (ii) assembly part alignment; and (iii) manufacturing accuracy limitations.

3.5. References

- [1] R. Payapulli, L. Zhu, S.-H. Shin, M. Stanley, N. M. Ridler and S. Lucyszyn, "Polymer-based 3-D printed 140 to 220 GHz metal waveguide thru lines, twist and filters," *IEEE Access*, vol. 11, pp. 32272-32295, Mar. 2023.
- [2] Flann Microwave. (2022). Flann Microwave. Accessed: Jan. 07, 2023. [Online]. Available: <https://flann.com/wp-content/uploads/2022/03/Sub-Millimetre-Seamless-Waveguide-Datasheet-Revision-3.pdf>.
- [3] P. Pursula, A. Lamminen, M. Kantanen, J. Saarilahti and V. Ermolov, "Sub-THz micromachined waveguides for wafer level integration of MMICs," *47th European Microwave Conference (EuMC)*, Nuremberg, Germany, 2017, pp. 1061-1064.
- [4] B. Zhang and H. Zirath, "Metallic 3-D printed rectangular waveguides for millimeter-wave applications," *IEEE Trans. on Components, Packaging and Manufacturing Technology*, vol. 6, no. 5, pp. 796-804, May 2016.
- [5] A. von Bieren, E. de Rijk, J.-P. Ansermet, and A. Macor, "Monolithic metal-coated plastic components for mm-wave applications," *39th International Conference on Infrared, Millimeter, and Terahertz waves (IRMMW-THz)*, Tuscon, USA, Sep. 2014.
- [6] H. Yasukochi, "Three-dimensional modeling apparatus, object, and method of manufacturing an object," US Patent Appl. US20120045617A1, Feb. 23, 2012.
- [7] W. J. Otter, N. M. Ridler, H. Yasukochi, K. Soeda, K. Konishi, J. Yumoto, M. Kuwata-Gonokami, and S. Lucyszyn, "3D printed 1.1 THz waveguides," *IET Electron Lett.*, vol. 53, no. 7, pp. 471-473, Mar. 2017.
- [8] J. Shen and D. Ricketts, "Additive manufacturing of complex millimeter-wave waveguides structures using digital light processing," *IEEE Trans. on Microwave Theory and Techniques*, vol. 67, no. 3, pp. 883-895, Mar. 2019.
- [9] J. Shen, M. Aiken, C. Ladd, M. D. Dickey, and D. S. Ricketts, "A simple electroless plating solution for 3D printed microwave components," *Asia-Pacific Microwave Conference (APMC)*, New Delhi, India, Dec. 2016.
- [10] J. Shen, M. W. Aiken, M. Abbasi, D. P. Parekh, X. Zhao, M. D. Dickey, and D. S. Ricketts, "Rapid prototyping of low loss 3D printed waveguides for millimeter-

- wave applications,” *IEEE MTT-S International Microwave Symposium (IMS)*, Honolulu, USA, Jun. 2017.
- [11] S. Lucyszyn, X. Shang, W. J. Otter, C. Myant, R. Cheng, and N. M. Ridler, “Polymer-based 3D printed millimeter-wave components for spacecraft payloads,” *IEEE MTT-S International Microwave Workshop Series on Advanced Materials and Processes (IMWS-AMP)*, Ann Arbor, USA, Jul. 2018 (Invited).
 - [12] *N5250C PNA Series Microwave Network Analyzer System*, 1st ed., Keysight Technologies, Inc., Santa Rosa, CA, USA, 2017.
 - [13] S. Verploegh, M. Coffey, E. Grossman, and Z. Popovic, “Properties of 50–110-GHz waveguide components fabricated by metal additive manufacturing,” *IEEE Trans. on Microwave Theory and Techniques*, vol. 65, no. 12, pp. 5144-5153, Dec. 2017.
 - [14] M. D'Auria, W. J. Otter, J. Hazell, B. T. W. Gillatt, C. Long-Collins, N. M. Ridler, and S. Lucyszyn, “3-D printed metal-pipe rectangular waveguides,” *IEEE Trans. on Components, Packaging and Manufacturing Technology*, vol. 5, no. 9, pp. 1075-1092, May 2006.
 - [15] Virginia Diodes, “Straight Waveguides, Tapers, Horn Antennae,” 2022. Accessed: Jan. 07, 2023. [Online]. Available: <https://www.vadiodes.com/en/products/straight-waveguides-tapers-horn-antenna-directional-couplers>.
 - [16] K. Soeda, K. Naganuma, K. Konishi, H. Tamaru, N. Mio, H. Ito, and J. Yumoto, “3D-printed waveguide for 220 GHz - 325 GHz band,” *47th International Conference on Infrared, Millimeter and Terahertz Waves (IRMMW-THz)*, Delft, Netherlands, Sep. 2022.
 - [17] W. J. Otter and S. Lucyszyn, “Hybrid 3-D-printing technology for tunable THz applications,” *Proc. of the IEEE*, vol. 105, no. 4, pp. 756-767, Apr. 2017.
 - [18] A. A. Kirilenko, D. Y. Kulik, and L. A. Rud, “Compact 90° twist formed by a double-corner-cut square waveguide section,” *IEEE Trans. on Microwave Theory and Techniques*, vol. 56, no. 7, pp. 1633-1637, Jul. 2008.
 - [19] M. A. Al-Tarifi and D. S. Filipovic, “Design and fabrication of a full W-band multi-step waveguide 90° twist,” *IEEE Microwave and Wireless Components Lett.*, vol. 26, no. 11, pp. 903-905, Nov. 2016.

- [20] G. Chattopadhyay, J. S. Ward, N. Llombert, and K. B. Cooper, "Submillimeter-wave 90° polarization twists for integrated waveguide circuits," *IEEE Microwave and Wireless Components Lett.*, vol. 20, no. 11, pp. 592-594, Nov. 2010.
- [21] J.-Q. Ding, Y. Zhao, and S.-C. Shi, "A full WR-3 band and low-loss 90° waveguide twist based on CNC," *IEEE Transactions on Terahertz Science and Technology*, vol. 10, no. 1, pp. 903-905, Jan. 2020.
- [22] Y. Zhang, J. Xu, F. Zhang, X. He, X. Li, Y. Sun, and S. Xu, "A 3-D printed Ka-band twisted waveguide filter with filtering and polarization rotation," *IEEE International Symposium on Antennas and Propagation and USNC-URSI Radio Science Meeting*, Atlanta, USA, Jul. 2019.
- [23] O. A. Peverini, M. Lumia, G. Addamo, F. Paonessa, G. Virone, R. Tascone, F. Calignano, G. Cattano, and D. Manfredi, "Integration of an H-plane bend, a twist, and a filter in Ku/K-band through additive manufacturing," *IEEE Trans. on Microwave Theory and Techniques*, vol. 9, pp. 2210-2219, May 2018.
- [24] A. I. Dimitriadis, T. Debogović, M. Favre, M. Billod, L. Barloggio, J.-P. Ansermet, and E. de Rijk, "Polymer-based additive manufacturing of high-performance waveguide and antenna components," *Proc. of the IEEE*, vol. 105, no. 4, pp. 668-676, Apr. 2017.
- [25] S.-H. Shin, D. Alyasiri, M. D'Auria, W. J. Otter, C. W. Myant, D. Stokes, Z. Tian, N. M. Ridler, and S. Lucyszyn, "Polymer-based 3-D printed Ku-band steerable phased-array antenna subsystem," *IEEE Access*, vol. 7, pp. 106662-106673, Aug. 2019.
- [26] C. Bartlett, D. Miek, F. Kamrath, D. Bruhn, and M. Höft, "X-band 3D-printed metal-insert twist-component for bandpass filter applications," *IEEE MTT-S International Microwave Filter Workshop (IMFW)*, Perugia, Italy, Nov. 2019.
- [27] F. Le Borgne, G. Cochet, J. Haumont, D. Diedhiou, K. Donnart, and A. Manchec, "An integrated monobloc 3D printed front-end in Ku-band," *49th European Microwave Conference (EuMC)*, Paris, France, Oct. 2019.
- [28] Q. Liu, Y. Zhang, F. Zhang and J. Xu, "A 3D printed waveguide hybrid bandpass filter integrated with twisting and bending functionalities," *IEEE International Symposium on Antennas and Propagation and USNC-URSI Radio Science Meeting (AP-S/URSI)*, Denver, CO, USA, Jul. 2022.

- [29] G. Addamo, O. A. Peverini, D. Manfredi, F. Calignano, F. Paonessa, M. Lumia, and G. Virone, “Electromagnetic and mechanical analyses of a 3D-printed Ka-band integrated twist and orthomode transducer,” *IEEE MTT-S International Microwave Workshop Series on Advanced Materials and Processes for RF and THz Applications (IMWS-AMP)*, Bochum, Germany, Jul. 2019.
- [30] M. García-Vigueras, E. Menargues, T. Debogovic, E. de Rijk, and J. R. Mosig, “Cost-effective dual-polarised leaky-wave antennas enabled by three-dimensional printing,” *IET Microw. Antennas Propag.*, vol. 11, no. 14, pp. 1985-1991, Sep. 2017.
- [31] Y. Zhang, F. Zhang, Y. Gao, J. Xu, C. Guo, and X. Shang, “3D printed waveguide step-twist with bandpass filtering functionality,” *IET Electron Lett.*, vol. 11, no. 56, pp. 527-528, 2020.
- [32] S. Chen, J. Li, Z. Xu and T. Yuan, “A Ka-band wideband monolithically metallic 3-D printed turnstile junction orthomode transducer with shaped internal profile,” *IEEE/MTT-S International Microwave Symposium*, Denver, CO, USA, Jun. 2022.
- [33] J. Shen and D. S. Ricketts, “Compact W-band “swan neck” turnstile junction orthomode transducer implemented by 3-D printing,” *IEEE Trans. on Microwave Theory and Techniques*, vol. 68, no. 8, pp. 3408-3417, May 2020.
- [34] Millimeter Wave Products Inc., “Product catalog: microwave & millimeter wave components & sub-assemblies,” St Petersburg, FL, U.S.A.: MIWV.com, 2023, p. 78.
- [35] Flann Microwave Ltd., “Waveguide Twists: Series 450,” Flann.com. Accessed: Jan. 07, 2023. [Online]. Available: <http://flann.com/wp-content/uploads/2015/04/Series-450.pdf>
- [36] Pasternack Enterprises Inc., “WR-5 90 Degree Right-hand Waveguide Twist,” 2022. Accessed: Jan. 07, 2023. [Online]. Available: <https://www.pasternack.com/wr-5-90-waveguide-twist-ug387mod-140-220-ghz-pew5tw0002-p.aspx>.
- [37] I. Hunter, “Theory and design of microwave filters,” 1st ed., London, U.K.: The Institution of Engineering and Technology, 2001.
- [38] R. J. Cameron, C. M. Kudsia, and R. R. Mansour, “Microwave filters for communication systems: fundamentals, design and applications,” 2nd ed., Hoboken, New Jersey: John Wiley & Sons, Inc., 2018.

- [39] S. V. Robertson, L. P. B. Katehi, and G. M. Rebeiz, "Micromachined W-band filters," *IEEE Transactions on Microwave Theory and Techniques*, vol. 44, no. 4, pp. 598–606, Apr. 1996.
- [40] X. Shang, M. Lancaster, and Y.-L. Dong, "W-band waveguide filter based on large TM₁₂₀ resonators to ease CNC milling," *Electronics Lett.*, vol. 53, no. 7, pp. 488–490, Mar. 2017.
- [41] X. Shang, P. Penchev, C. Guo, M. J. Lancaster, S. Dimov, Y. Dong, M. Favre, M. Billod, and E. de Rijk, "W-band waveguide filters fabricated by laser micromachining and 3-D printing," *IEEE Transactions on Microwave Theory and Techniques*, vol. 64, no. 8, pp. 488–490, Aug. 2016.
- [42] H. Yang, Y. Dhayalan, X. Shang, M. J. Lancaster, B. Liu, H. Wang, M. Henry, and P. G. Huggard, "WR-3 waveguide bandpass filters fabricated using high precision CNC machining and SU-8 photoresist technology," *IEEE Trans. on Terahertz Science and Technology*, vol. 8, no. 1, Jan. 2018.
- [43] J. Hu, S. Liu, Y. Zhang, and R. Xu, "Micromachined terahertz waveguide bandpass filters," *IEEE MTT-S International Microwave Symposium (IMS)*, Honolulu, USA, Jun. 2017.
- [44] L. Zhu, R. Payapulli, S.-H. Shin, M. Stanley, N. M. Ridler, and S. Lucyszyn, "3-D printing quantization predistortion applied to sub-THz chained-function filters," *IEEE Access*, vol. 10, pp. 38944-38963, Mar. 2022.
- [45] T. Skaik, M. Salek, P. Hunyor, H. Wang, P. G. Huggard, T. Starke, M. Attallah, and R. Martinez, "A 3D printed 300 GHz waveguide cavity filter by micro laser sintering," *IEEE Trans. Terahertz Sci. Technol.*, vol. 12, no. 3, pp. 274-281, May 2022.
- [46] C. Bartlett, J. Bornemann and M. Höft, "3-D-printing and high-precision milling of W-band filter components with admittance inverter sequences," *IEEE Trans. on Components, Packaging and Manufacturing Technology*, vol. 11, no. 12, pp. 2140-2147, Sep. 2021.
- [47] J. A. Lorente, M. M. Mendoza, A. Z. Petersson, L. Pambaguián, A. A. Melcon, and C. Ernst, "Single part microwave filters made from selective laser melting," *European Microwave Conference (EuMC)*, Rome, Italy, Oct. 2009.

- [48] F. Zhang, S. Gao, J. Li, Y. Yu, C. Guo, S. Li, M. Attallah, X. Shang, Y. Wang, M. J. Lancaster, and J. Xu, “3-D printed slotted spherical resonator bandpass filters with spurious suppression,” *IEEE Access*, vol. 7, pp. 128026 - 128034, Sep. 2019.
- [49] P. Booth and E. Valles Lluch, “Enhancing the performance of waveguide filters using additive manufacturing,” *Proc. of the IEEE*, vol. 105, no. 4, pp. 613 - 619, Apr. 2017.
- [50] M. Salek, X. Shang, R. C. Roberts, M. J. Lancaster, F. Boettcher, D. Weber, and T. Starke, “W-band waveguide bandpass filters fabricated by micro laser sintering,” *IEEE Transactions on Circuits and Systems II: Express Briefs*, vol. 66, no. 1, pp. 61-65, Jan. 2019.
- [51] T. Skaik, M. Salek, Y. Wang, M. J. Lancaster, T. Starke, and F. Boettcher, “180 GHz waveguide bandpass filter fabricated by 3D printing technology,” *2020 13th UK-Europe-China Workshop on Millimetre-Waves and Terahertz Technologies (UCMMT)*, pp. 1-3, 2020.
- [52] C. Guo, J. Li, J. Xu, and H. Li, “An X-band lightweight 3-D printed slotted circular waveguide dual-mode bandpass filter,” *IEEE International Symposium on Antennas and Propagation & USNC/URSI National Radio Science Meeting*, San Diego, USA, Jul. 2017.
- [53] B. Al-Juboori, J. Zhou, Y. Huang, M. Hussein, A. Alieldin, W. J. Otter, D. Klugmann, and S. Lucyszyn, “Lightweight and low-loss 3-D printed millimeter-wave bandpass filter based on gap-waveguide,” *IEEE Access*, vol. 7, pp. 2624 - 2632, Dec. 2018.
- [54] B. Zhang and H. Zirath, “3D printed iris bandpass filters for millimetre-wave applications,” *Electronics Lett.*, vol. 51, no. 22, pp. 1791–1793, Oct. 2015.
- [55] K. Fujiwara, R. Kobayashi, S. Kuwahara, S. Takemura, K. Takizawa, and Y. Watanabe, “3-D printed iris waveguide filter in W-band,” *23rd International Microwave and Radar Conference (MIKON)*, Warsaw, Poland, Oct. 2020.

4. G-Band Polymer-Based 3-D Printed MPRWG Standard Designs and Thru Lines

4.1 Introduction

A significant part of the content in this chapter (i.e., Chapters 4.4 and 4.5) is based on a research article by R. Payapulli et al., which was published in *IEEE Access* in March 2023 [1].

Standard WM-1295 [2] MPRWGs have internal cross-sectional dimensions of only $1,295 \mu\text{m} \times 647.5 \mu\text{m}$ for G-band operation (equivalent to WR-5), with the flange design based on IEEE standard specifications [3]. All 3-D computer-aided design (CAD) was undertaken using Autodesk Fusion 360.

Thru lines are used to provide a benchmark level of performance for a given MPRWG design. This design can then be adapted to produce more geometrically complex MPRWG components. In Chapters 5 and 6, these thru line designs are adapted to produce 90° twists and BPFs.

Measurements are provided for all fabricated thru lines to demonstrate their respective performances. A detailed analysis of measurements is undertaken for the successfully performing 4th Gen. components. Measurements for 1st, 2nd, and 3rd Gens. are used to provide insight on design flaws to be corrected for subsequent Gens.; as such, a less detailed analysis in comparison to that of the 4th Gen. measurements is given.

4.2 1st Generation

4.2.1 Design

1st Gen. thru lines were not manufactured due to a lack of available time. Instead, 90° twists and BPFs were used as a proof-of-concept for the 1st Gen. design, which shall be presented in Chapters 5 and 6. Nevertheless, the design that was employed shall be

introduced here, as this provides context for the development of subsequent component Gens..

A split-block design was employed, as this provides plating fluids with improved internal access to the waveguide, ensuring sufficient metalization even with conventional copper electroplating. In theory, a conventional symmetrical E-plane split (i.e., made at the center of the broad wall, with the split parallel to the narrow wall) will have less loss attributed to radiation leakage with high quality manufactured waveguides, as no transverse currents flow across the center of the broad wall with TE_{10} mode propagation. Therefore, this split orientation is adopted here.

For the BPFs, the split is constructed such that it avoids the large screw-holes on each flange. This is referred to here as a ‘deviating split’. This is done because the large clamping force from the screws that fit through these holes, which are used to assemble the waveguide to the measurement setup, may begin to push apart the assembled waveguide. For this reason, previous split-block waveguide thru lines have also employed this principle [4].

In addition, to mitigate against EM radiation leakage from the split, a radio-frequency (RF) choke is employed. The design was introduced by Lewis et al. [5] for CNC machined J-band waveguides, which is shown in Fig. 4.1. The operation principle is similar to that of a waveguide choke flange, which is commonly used to prevent damage at the outer flange edges due to the high surface current densities across flange-to-flange connections [6]. In Lewis’s RF choke, two quarter-wavelength waveguide lengths are employed within a symmetrical E-plane split. These function as impedance inverters, transforming the short-circuit connection at ‘A’ on Fig. 4.1(a) to an open-circuit connection at ‘B’, which in turn transforms to a short-circuit connection at the junction between the waveguide channel and the split ‘C’. A good electrical connection at ‘A’ is required for a short-circuit; it is easier to achieve a good connection here than at ‘C’, where several factors (e.g., edge rounding, edge defects, assembly part misalignment, and dirt and debris) can add electrical resistance. Therefore, radiation leakage is mitigated, and the dimensional tolerances and manufacturing accuracy requirements are reduced.

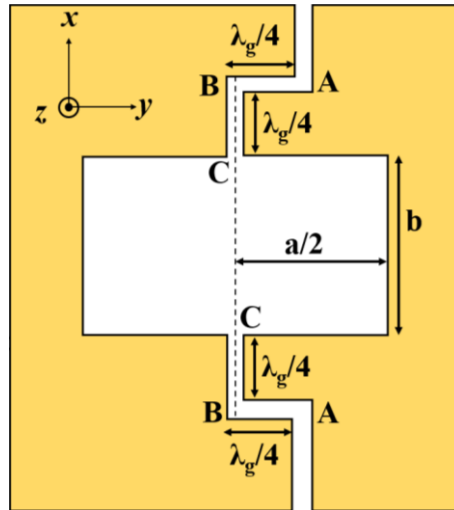


FIGURE 4.1: Schematic of the RF choke design from Lewis et al. [5].

This RF choke design was employed in the 1st Gen. BPFs, as shown in Fig. 4.2. There appears to be a large gap between the assembled split-block parts; this is partially due to a shadow cast by rounded edges, but a physical gap is also present. The effects of this gap on measured results shall be briefly discussed in Chapter 4.2.2. Note that the twist employs a very similar structure, which will be explained in Chapter 5.2.1.

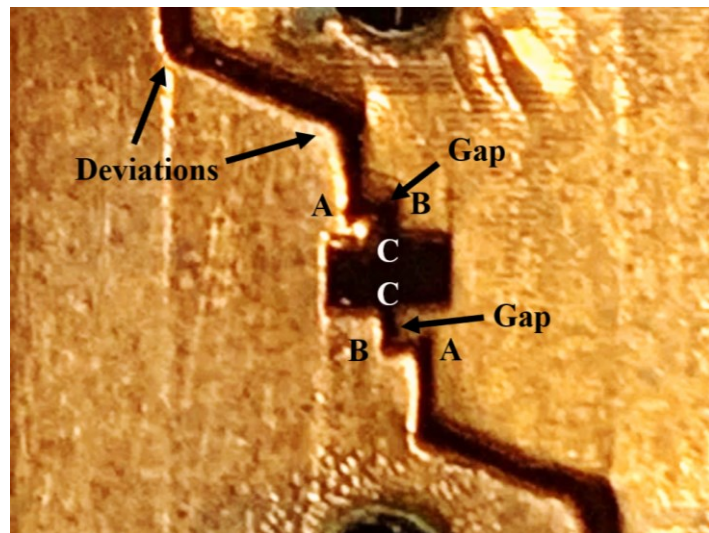


FIGURE 4.2: Close-up of the 1st Gen. MPRWG BPF aperture, showing RF choke and a deviating symmetrical E-plane split.

4.2.2 Measurements

1st Gen. MPRWG 90° twists and BPFs exhibited a very high insertion loss and return loss. These results are given in Chapters 5 and 6, respectively. This is due to the gap between the assembled parts causing EM radiation leakage from the split; the required short-circuit connection at ‘C’ on Fig. 4.1 was not achieved with the 3-D printed component. Indeed, this gap was exacerbated by the RF choke and the deviating split, particularly after copper electroplating, as these design features made tight assembly very difficult. A physical gap between assembly parts is more likely to occur with polymer-based printing at G-band when compared to CNC machining (which was employed by Lewis et al. [5]), due to poorer dimensional accuracy and geometric changes from warping (particularly at the extremities of printed parts) and shrinkage. Furthermore, even a minor misalignment between assembled split-block parts caused significant cross-sectional distortion (i.e., the waveguide aperture not being rectangular), which was also exacerbated by the RF choke and deviating split after plating. This also degrades the return loss, as there will be a large wave impedance mismatch between the measurement ports and the waveguide. Both the gap at the split and assembly part misalignment can be observed in Fig. 4.2.

4.3 2nd Generation

4.3.1 Design

The 2nd Gen. components used a single-block design. Here, the waveguide is printed as a single contiguous piece. As there is no split and no part assembly is required, this mitigates against the radiation leakage and assembly part misalignment found with the 1st Gen. components. This approach has been previously employed by ICL for thru lines operating up to 1.1 THz using ultra-high-resolution RECILS 3-D printing [7] and a commercial, custom-developed electroless plating process.

The main design challenge for single-block is metalization. The process that is employed is given in Chapter 4.3.2.

4.3.2 Fabrication

The Elegoo Mars 3-D printer was employed for fabrication, using the Elegoo Water Washable Rapid Resin (Ceramic Grey).

In the Chitubox slicer software, the broad wall of the waveguide is oriented such that it is parallel to the build plate, as shown in Fig. 4.3. This orientation was found to optimize dimensional accuracy and produces the sharpest edge and corner features. Printing time was 2h per component.

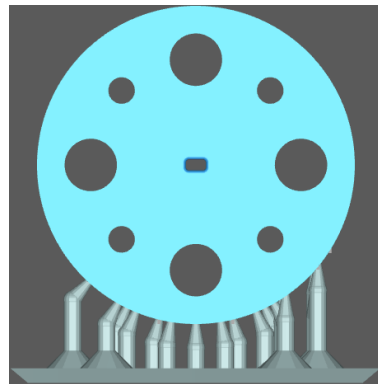


FIGURE 4.3: Flange view of the print orientation in Chitubox, showing support structures.

For electroplating, a seed layer of nickel is usually deposited first through electroless plating. This makes all surfaces conductive, enabling the part to function as the cathode during electroplating. However, narrow internal waveguide channels are unlikely to be plated due to two factors. First, the channel is unlikely to be sufficiently metalized during nickel electroless plating, as plating fluid will have limited access to the internal channel. Second, even with sufficient internal plating, the narrow channel profile in comparison to the rest of the part will cause a relatively higher conduction current density there, and therefore a higher electrical resistance, during electroplating, which will result in minimal internal electroplating.

Therefore, electroplating is not a suitable candidate metalization technique for single-block waveguides. However, an electroless plating procedure may be feasible, with

vigorous agitation being required for plating fluid to continually flow within the channel. This has been achieved for D-band polymer-based 3-D printed waveguides, having an aperture width of 1.65 mm, by Shen et al. [8]. Their custom-developed silver electroless plating process was used as a seed layer for an additional copper electroless plating process. The former process has been shown to adhere well to non-conductive UV-cured photopolymer surfaces, as explained in detail and demonstrated by their silver-plated W-band waveguides [9]. Therefore, this process was employed for our G-band single-block waveguides. All edges and corners were rounded to provide a greater surface area for metal adhesion during plating.

Only 10.4 mm-long thru lines were printed and plated. The final components weighed only 10.5 g; one of these is shown in Fig. 4.4. Three different thru lines were measured; for two, a single layer of plating was applied, with two layers of plating being applied for the third.

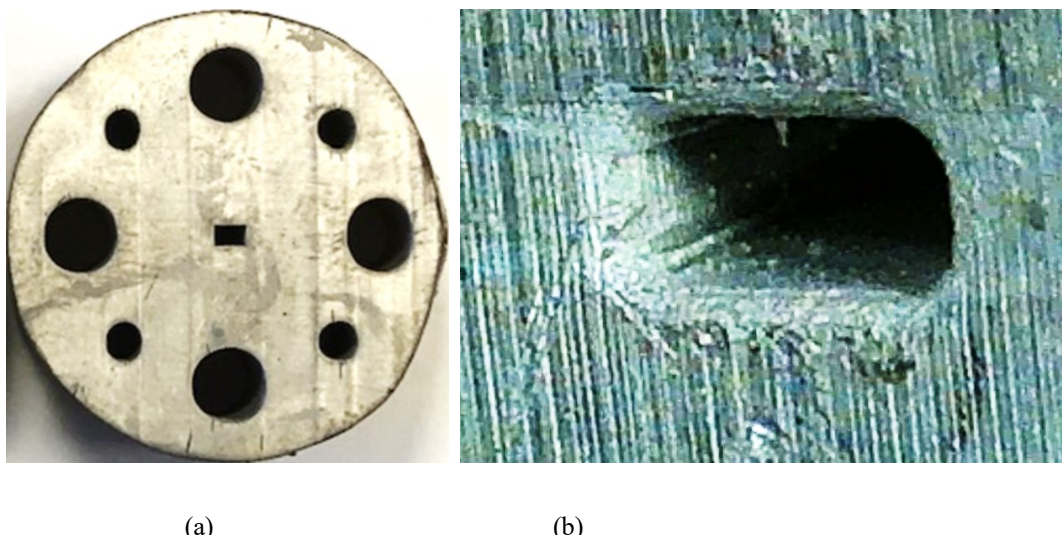


FIGURE 4.4: Flange view images of the single-block 10.4 mm MPRWG thru line: (a) full component; and (b) close-up of channel.

4.3.3 Measurements

All scattering (S-)parameter measurements in this thesis were undertaken at the U.K.'s National Physical Laboratory, using their Keysight Technologies PNA-X N5247B vector network analyzer (VNA) [10], with VDI WR-5.1 frequency extender heads [11].

Calibration is required for all VNAs before undertaking measurements; this is a process that compensates for systematic errors within the instrument hardware (such as different losses within directional couplers that sense the incident, reflected and transmitted waves at each port, or differences in the receivers at each port), and can also correct for additional hardware that is used to enable specific measurement types [12]. Thru-Reflect-Line (TRL) calibration was undertaken prior to these measurements, with reference planes at the VNA frequency extension heads. Here, three different calibration standards are employed: (i) thru (i.e., the two ports connected together) as a transmission standard; (ii) a short circuit for both ports, as a reflection standard; and (iii) a 1-inch thru line, as a phase standard [13]. The two-port device under test (DUT) is assembled and placed between the two measurement reference planes, as shown in Fig. 4.5. One-port measurements are undertaken by connecting the DUT to Port 1, with Port 2 left open.

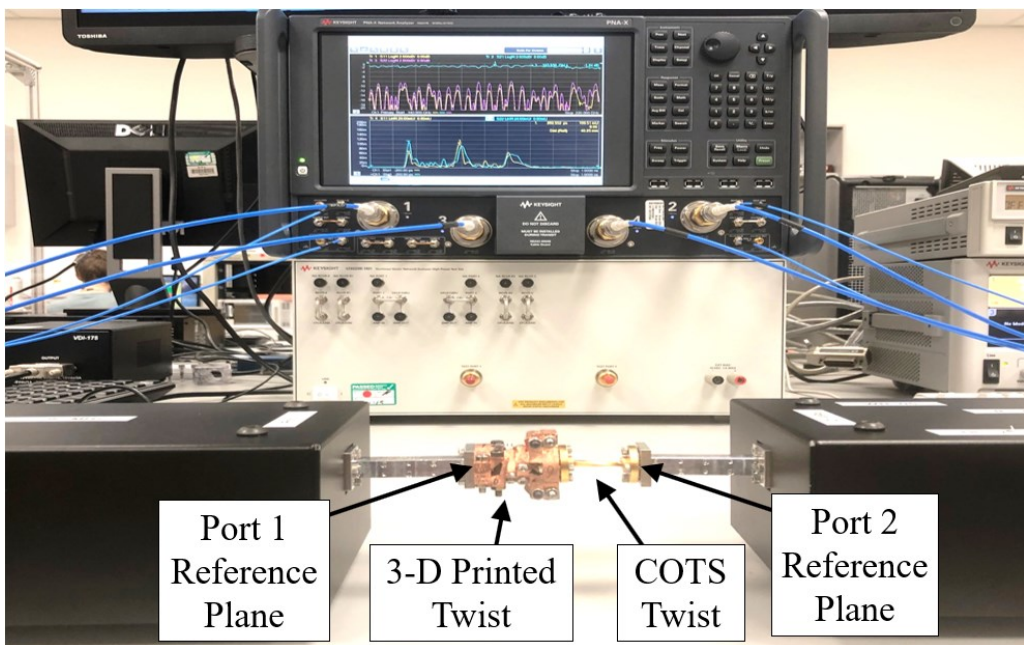


FIGURE 4.5: Two-port waveguide measurement setup, with VNA screen displaying the frequency-domain response (top panel) and time-domain response (bottom panel). The DUT here is a 3-D printed 90° twist connected to a COTS 90° twist.

In this Section, the three plated and measured 10.4 mm thru lines shall be referred to in the following order: (i) single layer plated #1, (ii) single layer plated #2, and (iii) double layer plated.

All responses that are referred to here as ‘EM simulated’ adopt the ideal dimensions and smooth rectangular walls in Ansys High-Frequency Structure Simulator (HFSS), which is a commercial 3-D full-wave EM simulation software package [14].

Figure 4.6 shows the reflection measurements for the 10.4 mm 3-D printed thru lines across G-band. The S_{11} and S_{22} responses are not in good agreement, indicating asymmetry in all waveguides. This is believed to be due to non-uniform plating. With the surface of the unplated internal channel being rough, due to the pixelation effect evident in the surface of MSLA-printed parts, a very thin internal deposition of silver is likely to leave areas (e.g., grooves between pixels) that remain un-plated, which will cause EM radiation leakage. Furthermore, even if the entire channel is uniformly plated, a thin layer of plating will cause a high insertion loss due to the high conduction current densities within the waveguide walls (which are induced by the guided EM energy).

Note that it was not possible to measure radiation leakage during measurements. Verification of internal plating thickness would require destructive analysis, which was not performed.

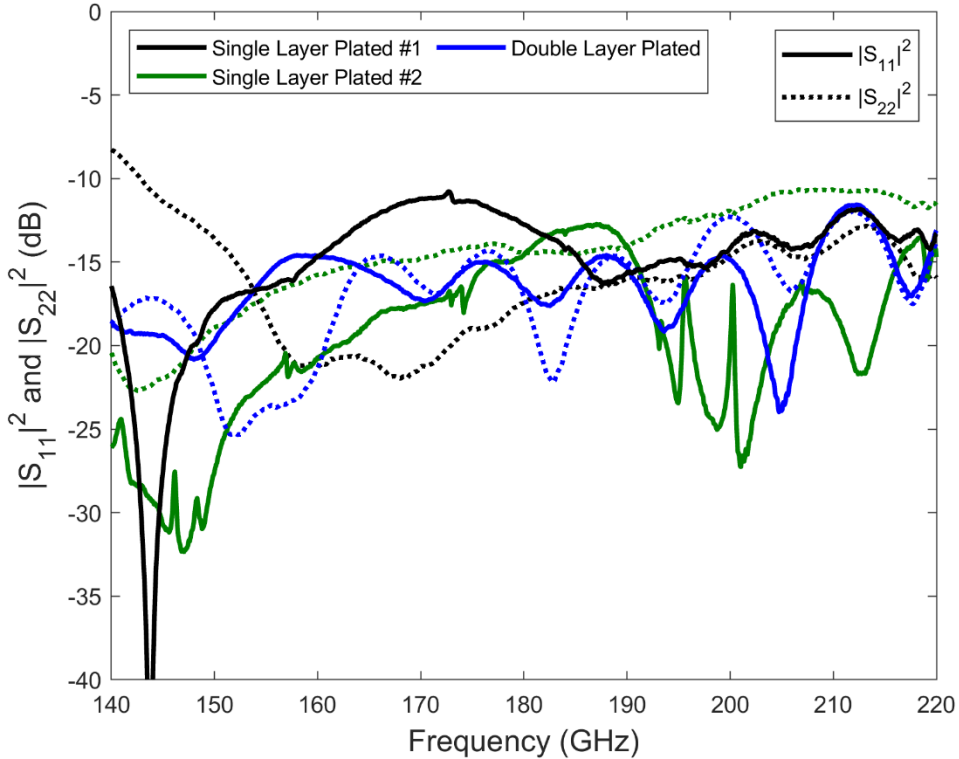


FIGURE 4.6: Reflection measurements for the 3-D printed 10.4 mm thru lines.

The worst-case return losses across G-band are: (i) 8.3 dB, (ii) 10.7 dB, and (iii) 11.6 dB. The poor return losses are likely to be due to poor overall waveguide transmission performances, which give a significant change in wave impedance between the port and the waveguide, dimensional inaccuracy, and the corner rounding that was designed into each waveguide.

Figure 4.7 shows transmission measurements across G-band, with the average insertion loss across G-band being: (i) 9.6 dB, (ii) 11.2 dB, and (iii) 4.7 dB. In addition, the ideal calculated (using Equation (2.17)) and EM simulated responses for both thru lines are included, for which a close-up shown in the inset. Both are in good agreement, with an average insertion loss across G-band of 0.08 dB.

There is a huge discrepancy between the measured and the calculated/simulated results, which is believed to be due to insufficient internal plating thickness. This would explain why the double plated waveguide exhibits a lower insertion loss in comparison to the single plated waveguides.

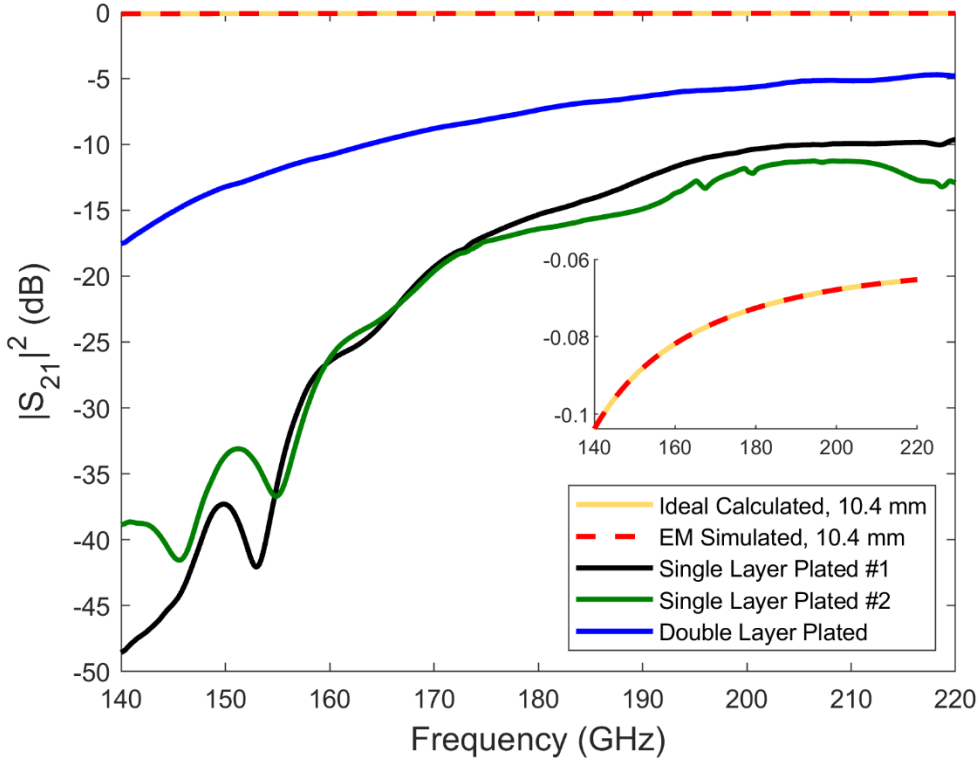


FIGURE 4.7: Transmission results for the 3-D printed 7.4 mm and 10.4 mm thru lines (close-up of ideal calculated and EM simulated responses in the inset).

Figure 4.8 shows the ideal calculated (using Equation (2.17)), EM simulated and measured dissipative attenuation α'_D across G-band (using Equation (2.16)). The measured α'_D values, averaged across G-band, are: (i) 4,600 dB/m, (ii) 4,000 dB/m, and (iii) 1,700 dB/m. The ideal calculated and EM simulated responses for both thru lines are also included, for which a close-up is shown in the inset. Both are in good agreement, with an average α'_D across G-band of 7.6 dB/m.

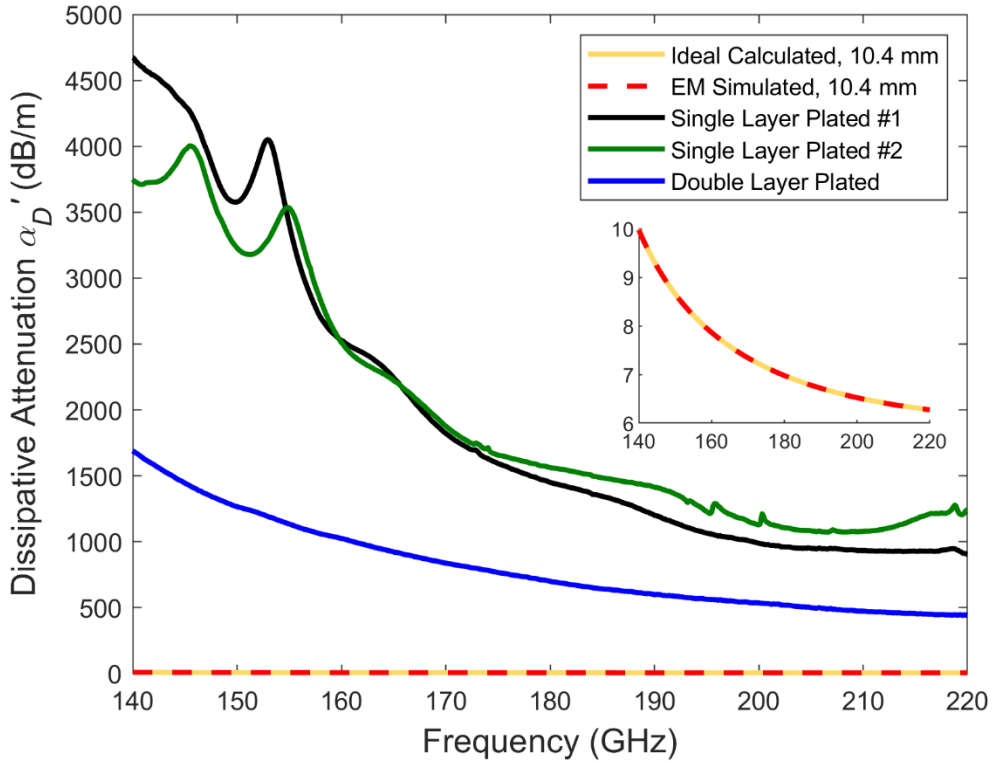


FIGURE 4.8: Dissipative attenuation for the 3-D printed 7.4 mm and 10.4 mm thru lines: (a) per meter; and (b) per guided wavelength.

As a lower insertion loss is achieved with the double layer plated exemplar, a potential solution for realizing low insertion loss waveguides (e.g., below an average of 0.5 dB for a 10.4 mm thru line) would be to apply multiple plating layers. This was not possible due to a lack of available time, which was primarily due to COVID-19 lab access restrictions that were instituted in 2021; these included time restrictions and the requirement for PhD supervisors to be present in the lab when using hazardous chemicals.

Another potential solution would be to pump plating fluid directly into the channel, thus ensuring a consistent supply of silver ions to internal surfaces, which would result in a more uniform internal metalization. This could be achieved using a microfluidic pump, such as a bi-directional peristaltic pump, as previously demonstrated by Bal et al. for V-band 3-D printed waveguides [15]. Again, this was not investigated here due to a lack of available time.

4.4 3rd Generation

4.4.1 Design

As discovered with the 2nd Gen. components, the small aperture dimensions for WR-5 MPRWGs makes conventional electro- or electroless plating impractical.

The 1st Gen. design, using a conventional symmetrical E-plane split, was also found to be impractical. However, there are a number of improvements that can be made to mitigate against radiation leakage and part misalignment.

Firstly, the RF choke is removed, and the deviating split is replaced with a straight planar split. This enabled contact between the two assembly parts at the channel. The assembled parts must be as tight as possible to ensure that they are not pushed apart when fixed to the measurement setup. However, this design was still susceptible to a small gap at the split and minor part misalignment, which are still likely to cause significant radiation leakage and return loss degradation.

Against conventional wisdom, the 3rd Gen. MPRWGs are constructed by printing the waveguide and all internal features on the bottom part, with the split made along the broad sidewall, as a solution to avoid assembly part misalignment. This is referred to here as an ‘H-plane *a*-edge’ split; the nomenclature is derived from Stil et al. [16], where an E-plane split along the narrow sidewall is defined as ‘*b*-edge’. Further advantages for this construction include the easier removal of resin residue, easier integration of external components and the ability to inspect and measure complete waveguide features (as discussed in Chapter 6). Note that H-plane *a*-edge splits have already been reported in 3-D printed MPRWGs at S-band [17], X-band [18], Ka-band [19], D-band [20], G-band [4] and WM-570 band [21], with four of these examples integrating external components.

To mitigate against radiation leakage, candidate techniques from subtractive manufacturing include brazing, RF chokes [5], pin wall joints [22] and photonic crystal joints [23]. These are unsuitable here, due to the polymer’s inability to withstand high temperatures, its inherent softness, and post-production warping. Instead, our design employs ‘lips’ that form part of the sidewalls, to connect with the upper wall. These reduce the contact area between the top and bottom part, enabling a good electrical/EM

seal with tight assembly. This is illustrated in Fig. 4.9, with a and b referring to the internal aperture width and height, respectively. The lip width W and lip height H are set to 400 μm and 200 μm , respectively. The full split-block structure is referred to here as the ‘trough-and-lid’ assembly.

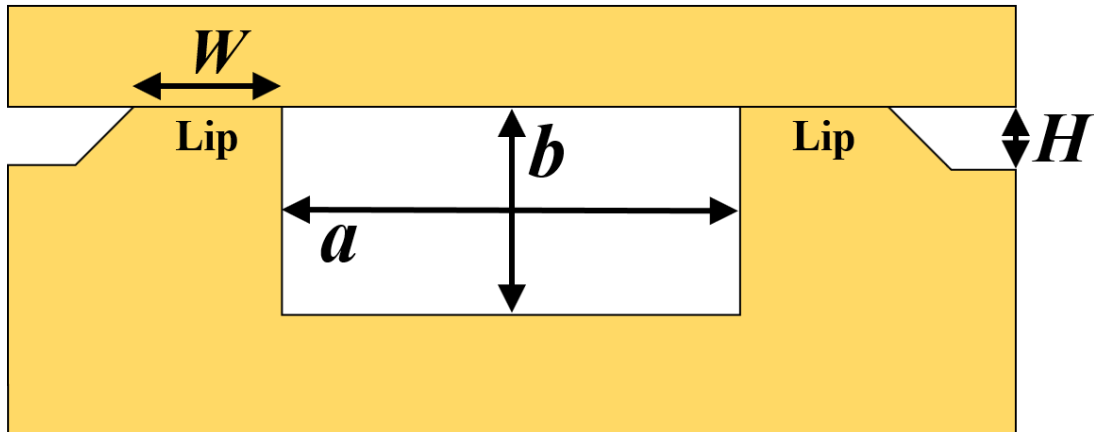


FIGURE 4.9: Flange view illustration of the trough-and-lid assembly, showing lips in contact with the flat top part.

While having been developed independently for 3-D printing by myself, a recent online search found a similar approach with commercially-available machined mixers at W-band [24] and G-band [25]. Since machined parts are very rigid, any significant inaccuracy may result in a gap occurring between the lips and the lid, resulting in radiation leakage. In contrast, with polymer-based printing, there is some degree of malleability that helps to close small gaps.

Finally, to advance the technology readiness level of polymer-based printing for aerospace applications, all MPRWG components have an improved structural rigidity in comparison to previous designs (this is referred to here as ruggedization). Two lengths of 3-D printed thru line are manufactured and measured: 7.4 mm and 10.4 mm.

4.4.2 Fabrication

The Elegoo Mars 3-D printer was used for fabrication. In Chitubox, the broad wall of the waveguide is oriented such that it is parallel to the build plate, as with previous Generations. This is shown in Fig. 4.10.

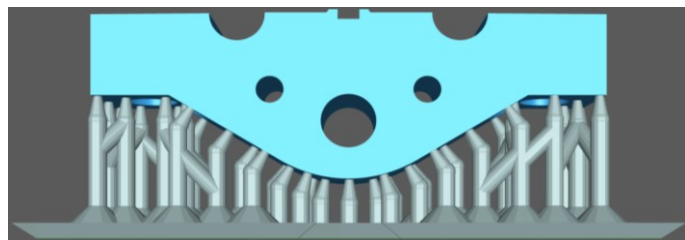


FIGURE 4.10: Flange view of print orientations in Chitubox, showing support structures.

With the commercial copper electroplating process, a thin electroless-plated nickel seed layer is first deposited, followed by a 50 μm thick layer of electroplated copper, corresponding to 283 skin depths at 140 GHz. This guarantees a minimum thickness at corners and edges. Finally, an anti-tarnishing treatment is applied. This avoids the oxidation of plated copper, which may detrimentally affect measured results. The effects of copper oxidation over time were not considered here.

Printing time was 1h20m per component. Two components each were printed for the 7.4 mm and 10.4 mm lengths, with measurements of the marginally better performing components presented. After 3-D printing and electroplating, and prior to full assembly, the 7.4 mm and 10.4 mm thru lines weigh 4.7 g and 6.6 g, respectively.

Two pairs of stainless steel screws, nuts and washers are used for assembly. Alignment between the two ruggedized parts is further improved by using two pairs of stainless steel dowel pins, which ensure flat flange interfaces. The fully assembled 3-D printed 10.4 mm thru line is shown in Fig. 4.11.

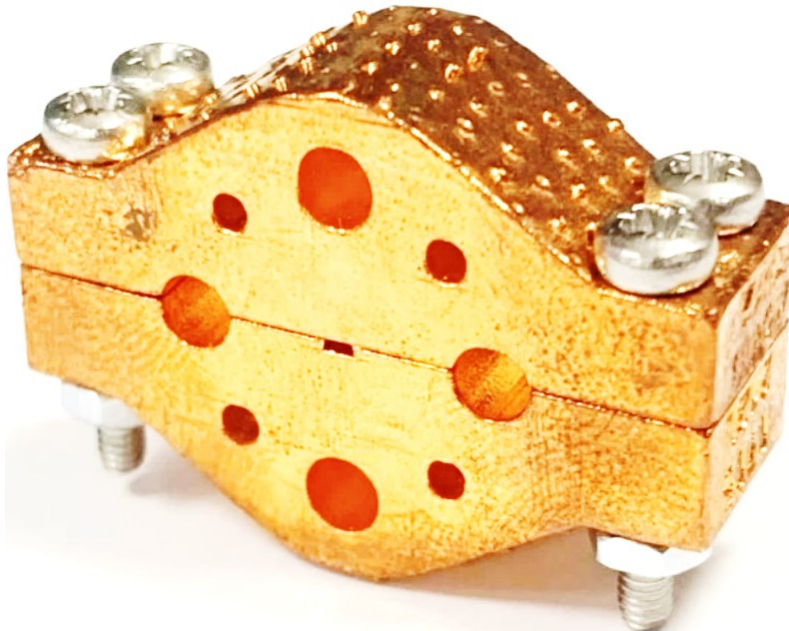


FIGURE 4.11: Fully assembled 3rd Gen. WR-5 MPRWG thru lines after copper plating.

Although using metal fasteners is a useful approach for prototyping, components that are designed for practical applications may use solutions such as 3-D printed or plastic fasteners or conductive epoxy glue.

Overtightening was avoided, as this can cause rectangular-to-trapezoidal cross-sectional distortion. Although this distortion has an effect on the measured results of these 3rd Gen. thru lines, only a brief qualitative analysis is provided here. A more detailed analysis of this effect is given in Chapter 4.5.3. In future, a torque spanner could be used for reliable and repeatable tightening, with the appropriate torque applied to ensure good contact between the top and bottom parts.

Each 3-D printed component costs approximately \$0.20 to print, while the additional commercial copper electroplating costs approximately \$82 (depending on the total surface area). Table 4.1 shows a more accurate cost comparison for G-band COTS thru lines and 90° twists, all sourced from the US (Pasternack Enterprises Inc., Fairview Microwave Inc., and Hasco Components Inc.). The cost ratio is defined here as the purchase cost of the COTS component per unit length divided by total cost per unit length of our 3-D printed counterpart.

Note that retail costs include several additional costs, such as marketing and profit, so this can only be considered as a maximum cost saving. Furthermore, a performance comparison was not given here as ICL do not own these components. The prices of measured COTS thru lines were only available through a confidential quote.

TABLE 4.1: Comparative costs (at the time of writing) for G-band thru lines with COTS components and their 3-D printed counterparts (*costs available online).

COTS Manufacturer	Cost (\$)*	Length (mm)	Cost per unit length (\$/mm)	Cost ratio	Ref.
Pasternack	456	25.4	18	2.4	[26]
Fairview	429	25.4	17	2.3	[27]
Hasco	259	25.4	10	1.4	[28]
ICL (3-D printed)	78	10.4	8	-	This work

4.4.3 Measurements

The 7.4 mm and 10.4 mm 3-D printed thru lines are measured. Copper (with bulk DC conductivity of 5.8×10^7 S/m) is used for all COTS thru line theoretical calculations and EM simulations.

Figure 4.12 shows the reflection measurements for the 7.4 mm and 10.4 mm 3-D printed thru lines across G-band. The S_{11} and S_{22} responses are in good agreement, indicating that these waveguides are symmetric. The worst-case return loss is 17.0 dB and 11.2 dB for the 7.4 mm and 10.4 mm 3-D printed thru lines, respectively. Return loss is primarily the result of aperture size and spatial orientation discrepancies at the flange interfaces between the waveguide extender heads (defining the calibrated reference planes) and the DUT. This is exacerbated with 3-D printed thru lines, due to four factors:

- (i) poorer dimensional accuracy of rectangular apertures; (ii) rounded edges and corners;
- (iii) rectangular-to-trapezoidal cross-sectional distortion, due to lip bending; and (iv) 3-D misalignment between extender heads and DUT apertures.

Nevertheless, the return loss obtained here is greater than 10 dB. Furthermore, the current results compare favorably to those from the previously reported G-band thru line [18], which had a worst-case return loss of 6 dB. This is due to assembly part misalignment being avoided, which is more likely to occur with the traditional symmetrical E-plane split block approach.

At 218 GHz, the 7.4 mm thru line has a spurious response, which indicates the excitation of a higher-order mode. The TE₂₀ is the next higher order mode; from (2.5), this is excited at $f_{c,20} = \frac{c}{a} = 230$ GHz, for a channel aperture width $a = 1,295$ μm . Excitation of this mode at a lower frequency may be caused by an effective increase in a to approximately 1,380 μm due to rounding at the lips or insufficient contact between the top and bottom parts.

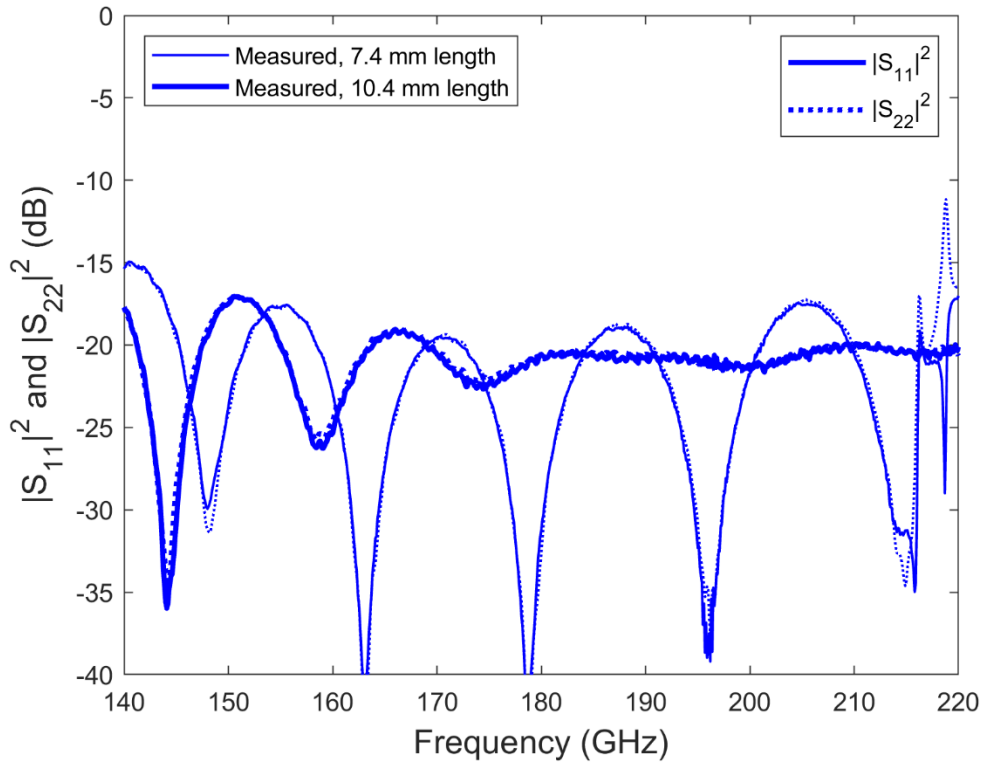


FIGURE 4.12: Reflection measurements for the 3-D printed 7.4 mm and 10.4 mm thru lines.

Figure 4.13 shows transmission measurements across G-band for the 7.4 mm and the 10.4 mm thru lines, with the ideal calculated (using (2.13)) and EM simulated responses for both thru lines also included. The average insertion loss across G-band is 0.15 dB and 0.14 dB for the 7.4 mm and the 10.4 mm thru lines, respectively. This compares reasonably well with the calculated and EM simulated responses. The spurious response above 210 GHz for the 7.4 mm thru line is evident here.

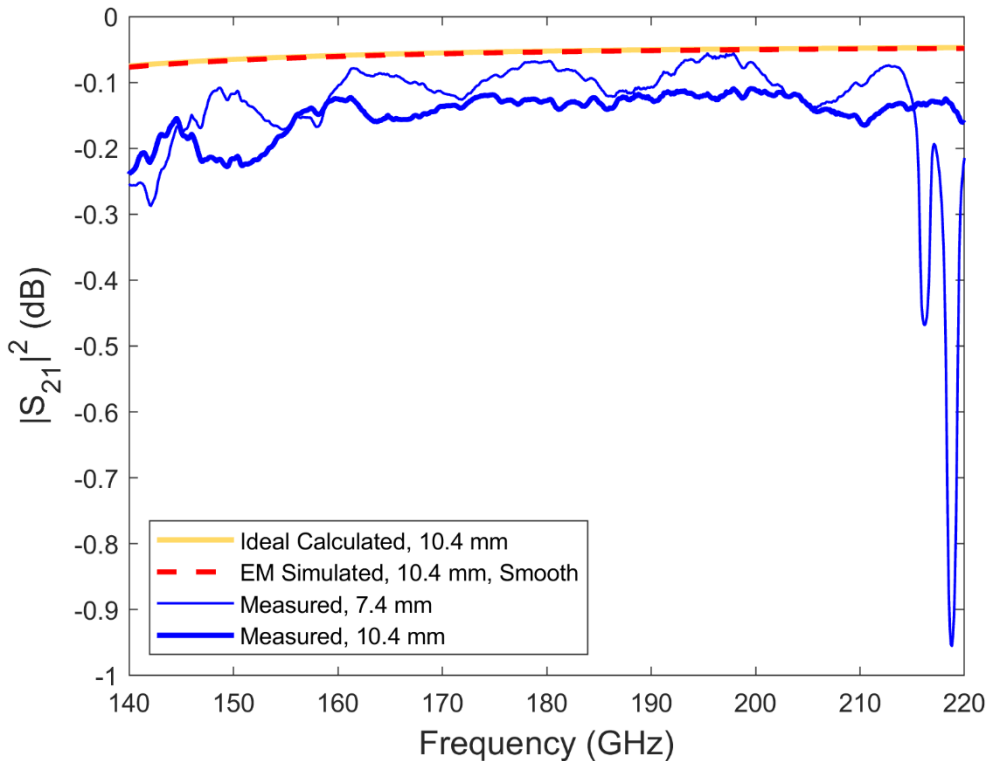


FIGURE 4.13: Transmission results for the 3-D printed 7.4 mm and 10.4 mm thru lines.

Figure 4.14 shows the calculated, EM simulated and measured α'_D across G-band. Both EM simulated responses are in good agreement with the ideal calculated results. The measured α'_D , averaged across G-band, is 13.0 dB/m and 10.5 dB/m for the 7.4 mm and 10.4 mm 3-D printed thru lines, respectively.

Scanning electron microscope (SEM) images were not taken for any 3rd Gen. components (printed using the Elegoo Mars). Therefore, the surface roughness of these

parts was not characterized, so it will not be included in these measurements.

Additional attenuation due to cross-sectional distortion is not characterized here; this will be investigated in Chapter 4.5.3. However, due to prioritizing the avoidance of over-tightening, only minor cross-sectional distortion occurred, which is likely to be the cause of the slightly higher attenuation at the lower-band frequencies.

Nevertheless, these reflection, transmission and dissipative attenuation measurements strongly suggest that the trough-and-lid assembly is suitable for the realization of low-cost and low loss 3-D printed G-band thru lines.

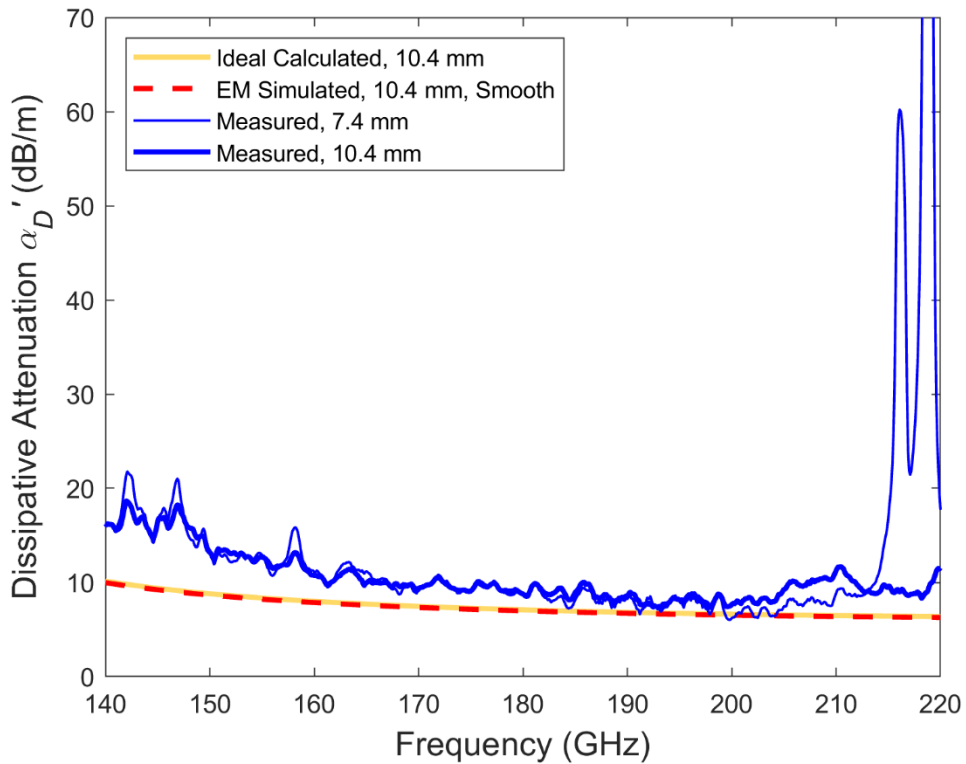


FIGURE 4.14: Dissipative attenuation for the 3-D printed 7.4 mm and 10.4 mm thru lines: (a) per meter; and (b) per guided wavelength.

4.5 4th Generation

4.5.1 Design

The design of 4th Gen. thru lines was almost identical to that of the 3rd Gen. thru lines. The lip width W was increased to 550 μm to improve its robustness, as tighter assembly would be employed to avoid the spurious response seen previously.

4.5.2 Fabrication

In contrast to the 3rd Gen. thru lines, 3-D printing is undertaken using the low-cost (\$230) Elegoo Mars 2 Pro was used for 3-D printing, with the Elegoo Water Washable Rapid Resin (Ceramic Grey). The printing orientation is identical to that shown by Fig. 4.10.

The new MSLA 3-D printer enabled sharper corner and edge features than the older Elegoo Mars, as shown in Fig. 4.15.

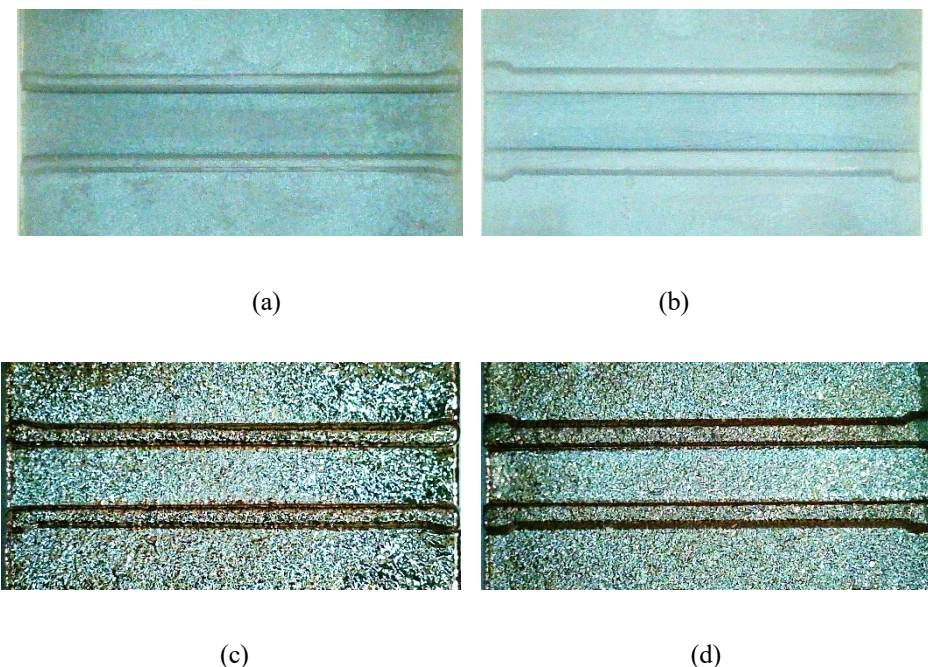


FIGURE 4.15: Comparison between 3rd and 4th Gen. 3-D printed MPRWG thru lines: (a) 3rd Gen. 3-D printed 10.4 mm thru line, bottom part, before plating; (b) 4th Gen. 3-D printed 10.4 mm thru line, bottom part, before plating; (c) 3rd Gen., after plating; and (d) 4th Gen., after plating.

This is expected to result in a lower return loss, as a more rectangular cross-section with less edge rounding should provide a better wave impedance matching with the ports. This may also remove the spurious response for the 7.4 mm thru line.

A 50 μm copper electroplating process was again employed, with an added anti-tarnishing treatment. For the 4th Gen. thru lines, it was found that metalization caused a narrowing of internal waveguide dimensions, which is compensated for in the CAD drawing. Initially, a standard 50 μm deposition in the trough was assumed. However, the plating thickness here was found to be only 35 μm . This underplating is believed to be the result of having a narrow trough (with higher conduction current density during electroplating). Subsequent waveguides were re-designed to account for the 35 μm thickness within the trough when using the standard 50 μm process. Printing time was 1h20m per component. Two components each were printed for the 7.4 mm and 10.4 mm lengths, with measurements of the marginally better performing components presented.

After 3-D printing and electroplating, these 4th Gen. thru lines weigh the same as their corresponding 3rd Gen. thru line lengths. The disassembled 3-D printed 10.4 mm thru line, before and after electroplating, is shown in Figs. 4.16(a) and 4.16(b).



(a)

(b)

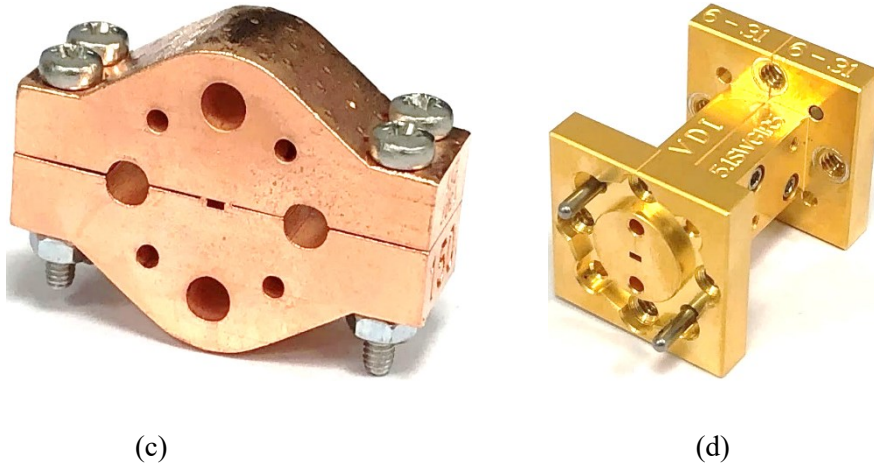


FIGURE 4.16: 4th Gen. WR-5 MPRWG thru lines: (a) disassembled 3-D printed 10.4 mm thru line, before plating; (b) disassembled, after plating, showing stainless steel dowel pins; (c) fully assembled 3-D printed 10.4 mm thru line, after plating; and (d) 25.4 mm COTS counterpart from VDI [29].

As with the 3rd Gen. thru lines, two pairs of stainless steel screws, nuts and washers are used for assembly. Alignment between the two ruggedized parts is further improved by using two pairs of stainless steel dowel pins, which ensure flat flange interfaces, as shown in Fig. 4.16(b). The fully assembled 3-D printed 10.4 mm thru line is shown in Fig. 4.16(c). A 25.4 mm thru line COTS counterpart, from Virginia Diodes Inc. (VDI) [29], is shown in Fig. 4.16(d), which appears to have a textbook symmetrical E-plane split. This was used as a measured comparative reference.

The trough-and-lid assembly for a thru line is shown in Fig. 4.17, where a_{min} and a_{max} refer to the minimum and maximum trough widths, respectively. It was found that overtightening has caused rectangular-to-trapezoidal cross-sectional distortion, with $\sim 9^\circ$ of lip bending, shown in Fig. 4.17. Due to tighter assembly, this was more significant for the 4th Gen. thru lines in comparison to their 3rd Gen. counterparts. The effect of this deformation on measured performance will be discussed in Chapter 4.5.3.

The printing and plating costs for these thru lines are equivalent to those given in Table 4.1, in Chapter 4.4.2.

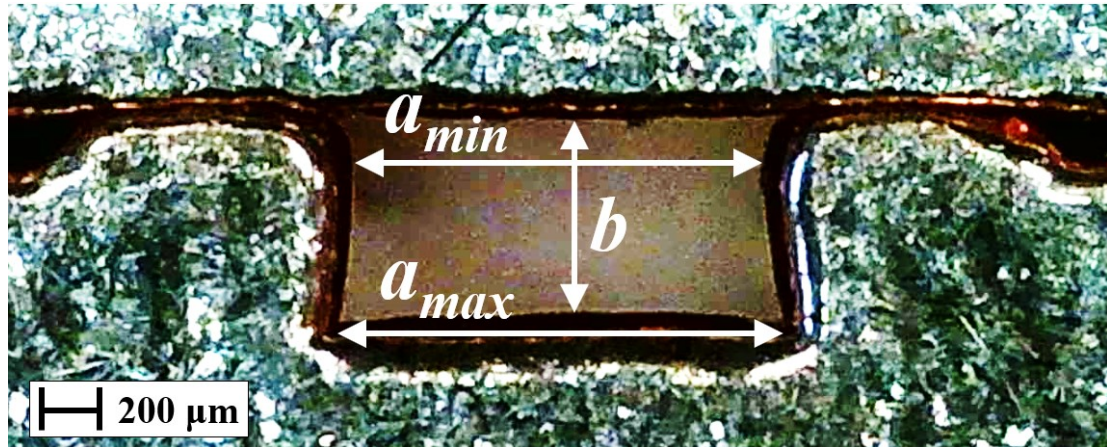


FIGURE 4.17: Flange view microphotograph of the trough-and-lid assembly for a thru line, showing lips in contact with the flat top part.

4.5.3 Measurements

The 7.4 mm and 10.4 mm 3-D printed thru lines are measured. In addition, two VDI WR-5 thru line counterparts, of lengths 25.4 mm and 50.8 mm, are included for comparison. The measured aperture dimensions [a_{min} , a_{max} , b] for the 3-D printed thru lines are [1,010 μm , 1,320 μm , 680 μm] and [1,000 μm , 1,290 μm , 690 μm] for the 7.4 mm and 10.4 mm thru lines, respectively. The COTS thru lines are machined from aluminium alloy 6061-T6, with quoted cross-sectional aperture dimensions being ideal [1,295 μm , 1,295 μm , 647.5 μm] [30]. Gold (with bulk DC conductivity of $4.1 \times 10^7 \text{ S/m}$) is used for all COTS thru line theoretical calculations and EM simulations, since the machined parts are gold plated. Copper is used for all 3-D printed counterparts. All COTS components are assumed to be smooth internally.

Additional loss due to surface roughness is applied to EM simulations by multiplying the simulated dissipative attenuation α'_D by a factor of K . For the Extended and Huray-Hemispherical roughness models, which have been shown to be appropriate for these copper electroplated parts, $K = 1.32$ and 1.28 , respectively, at the mid-band frequency of 180 GHz. The calculations for these values are obtained in Chapter 7.

Figure 4.18 shows the reflection measurements for all thru lines across G-band. The S_{11} and S_{22} responses are in good agreement, indicating a similar wave impedance mismatch at both ports. The worst-case return loss is 14.9 dB and 14.1 dB for the 7.4 mm and 10.4 mm 3-D printed thru lines, respectively. In comparison, they are 27.8 dB and 26.5 dB for the 25.4 mm and 50.8 mm COTS thru lines, respectively. Again, the poorer return loss for the 3-D printed components is primarily the result of aperture size and spatial orientation discrepancies at the flange interfaces between the waveguide extender heads and the DUT, as explained in Chapter 4.4.3. In comparison, the COTS thru lines exhibit high dimensional accuracy in all aspects.

Nevertheless, the return loss is still greater than 10 dB. In comparison with the 3rd Gen. thru lines, the measured return loss is slightly greater (if omitting the spurious response observed above 210 GHz for the 3rd Gen. 7.4 mm part) due to overtightening causing rectangular-to-trapezoidal cross-sectional distortion. These results compare favorably to those from the previously reported G-band thru line [18], with a worst-case return loss of 6 dB, due to misalignment between parts being avoided.

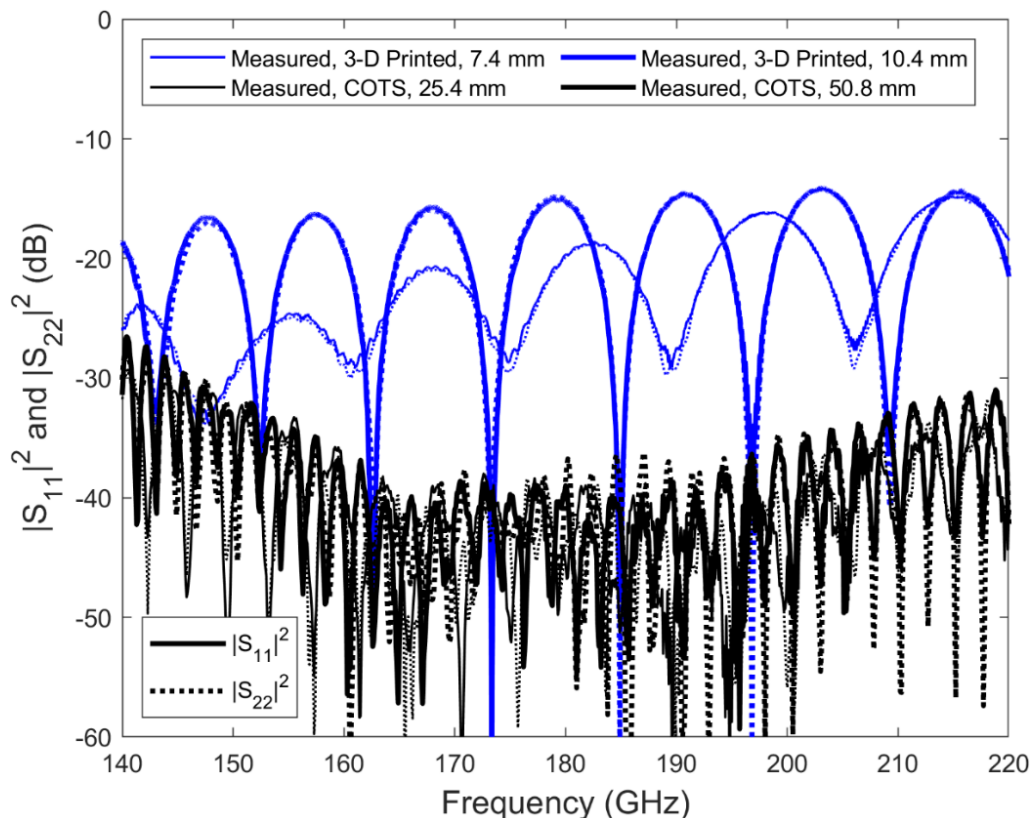


FIGURE 4.18: Reflection measurements of the 3-D printed and COTS thru lines.

Fabry-Pérot ripples are evident in the frequency responses, caused by wave impedance mismatches located at both ports. These have frequency period Δf , correspond to standing-wave reflections between two spatial boundaries that are separated by waveguide length $L \approx v_g(180 \text{ GHz})/\Delta f$, where $v_g(180 \text{ GHz}) = 2.30 \times 10^8 \text{ m/s}$ is the theoretical mid-band group velocity of the waveguide. With $\Delta f = 29.8, 22.3 \text{ GHz}$, the extracted value for $L \approx 7.7, 10.3 \text{ mm}$, corresponding to the exact length $L = 7.4, 10.4 \text{ mm}$ between ports.

Figure 4.19 shows transmission measurements across G-band, as well as the ideal calculated, EM simulated and EM re-simulated responses for a 7.4 mm thru line. The average insertion loss across G-band is 0.14 dB and 0.22 dB for the 7.4 mm and the 10.4 mm thru lines, respectively.

All responses that are referred to in this paper as ‘EM re-simulated’ adopt measured dimensions in HFSS, giving a more accurate characterization of the real component. For example, here, the measured effective mean aperture width $a_{mean} = (a_{min} + a_{max})/2 \cong 1,150 \mu\text{m}$ is applied to account for rectangular-to-trapezoidal cross-sectional distortion. The re-simulated S-parameters are then used to calculate α'_{DS} in Equation (7.1). In addition, surface roughness losses are included, using the Extended/Huray-Hemispherical model $K(180 \text{ GHz})$ values calculated previously. The results match closely with the measured data for the 7.4 mm thru line.

In comparison with the 3rd Gen. thru lines, the average insertion loss is slightly greater, particularly for the 10.4 mm thru line. The greater dissipative attenuation due to cross-sectional distortion is believed to be the main cause, as explained later.

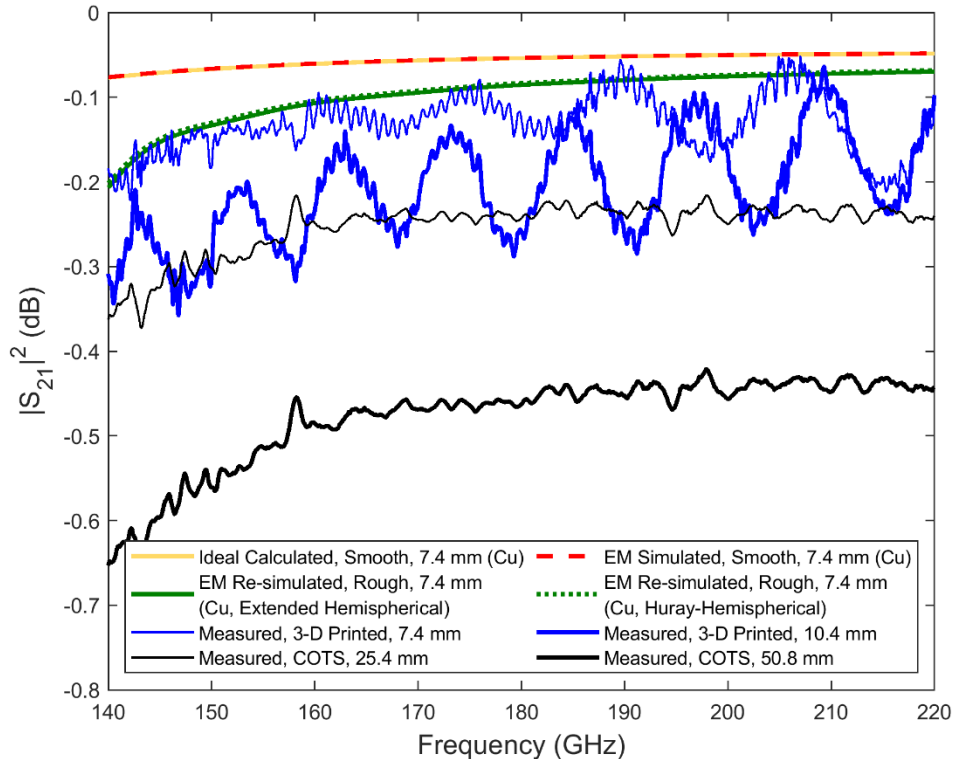
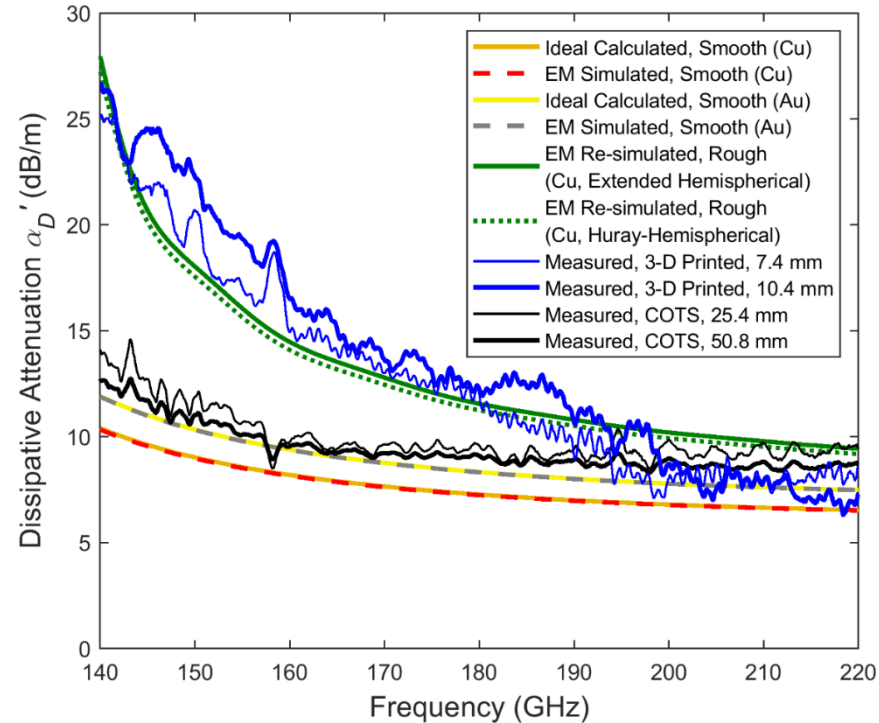


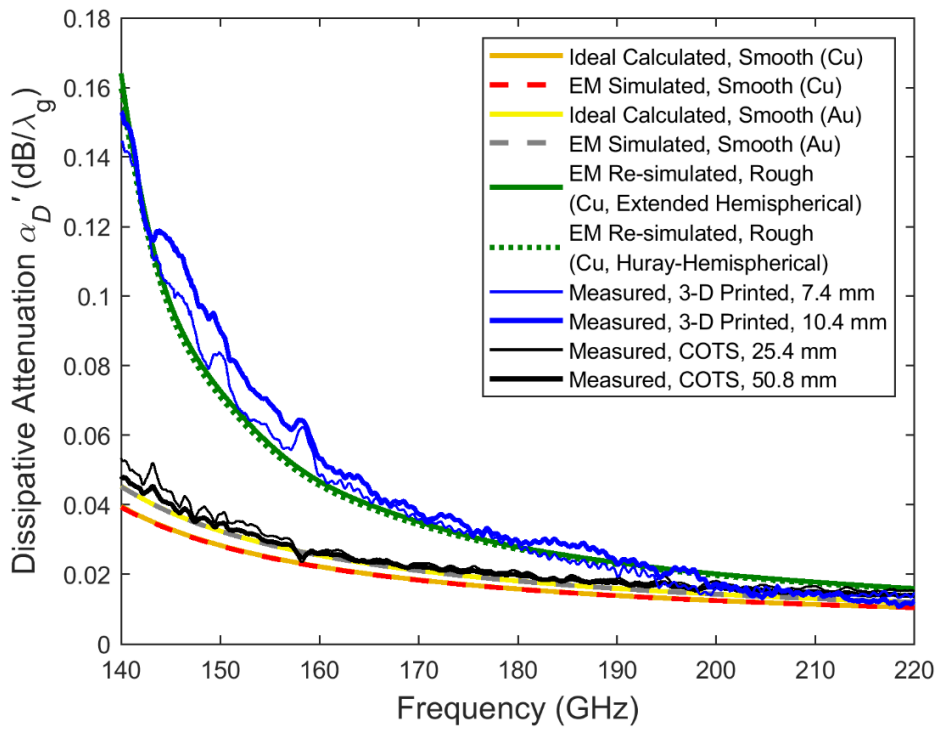
FIGURE 4.19: Transmission results for the 3-D printed and COTS thru lines.

With the Fabry-Pérot ripples, observed in both reflection and transmission frequency responses, the peaks in the transmission responses (corresponding to the troughs in the reflection responses) approach the EM re-simulated curves.

Figure 4.20 shows the calculated, EM simulated, measured and EM re-simulated α'_D across G-band. Both EM simulated responses are in good agreement with the ideal calculated results, with both modelling scenarios having smooth rectangular walls and perfect wave impedance matching. The measured α'_D , averaged across G-band, is 12.7 dB/m (0.032 dB/ λ_g) and 13.7 dB/m (0.035 dB/ λ_g) for the 7.4 mm and 10.4 mm 3-D printed thru lines, respectively.



(a)



(b)

FIGURE 4.20: Dissipative attenuation for the 3-D printed 7.4 mm and 10.4 mm thru lines: (a) per meter; and (b) per guided wavelength.

In comparison, these measurements are 9.9 dB/m ($0.024 \text{ dB}/\lambda_g$) and 9.4 dB/m ($0.022 \text{ dB}/\lambda_g$) for the 25.4 mm and 50.8 mm COTS thru lines, respectively, comparing well with both ideal calculated and EM simulations.

With reference to Fig. 4.20, between *ca.* 200 and 220 GHz, the 3-D printed and COTS thru line performances are commensurate.

EM re-simulations agree closely with the measurements, with effective mean aperture width $a_{mean} \approx 1,150 \mu\text{m}$ and the Extended/Huray-Hemispherical model $K(180 \text{ GHz})$ values being applied. Surface roughness adds approximately 2-3 dB/m of additional attenuation across G-band. The degraded performance for the 3-D printed thru lines below *ca.* 200 GHz can be mainly attributed to the rectangular-to-trapezoidal cross-sectional distortion. The narrower effective mean aperture width shifts the TE_{10} mode cutoff frequency from 116 GHz up to 130 GHz, dramatically increasing the attenuation at the lower band edge frequency for G-band. It is worth noting that detailed re-simulations were also undertaken with a trapezoidal cross-section, using measured values for a_{min} and a_{max} , with very similar results to the narrowed rectangular cross-section.

In comparison with the 3rd Gen. thru lines, average α'_D is slightly greater, which is again due to cross-sectional distortion.

Our previously reported 3-D printed thru line exhibits an average α'_D of 59 dB/m at G-band [18]. D- and J-band metal-based MLS 3-D printed 50 mm thru lines reported by Zhang and Zirath exhibit an average α'_D of 19 dB/m and 120 dB/m, respectively [31]. Table 1.1 shows that our current results compare favorably with all 3-D printed D-band thru lines, and are even commensurate with some 3-D printed W-band thru lines, despite having a higher theoretical minimum attenuation due to the smaller aperture dimensions. This provides a robust proof-of-concept for the split-block trough-and-lid assembly.

Emulated TDR ($|S_{11}|$ and $|S_{22}|$) measurements have been undertaken in the VNA by applying a discrete inverse Fourier transform is applied to the frequency-domain return loss responses (S_{11} and S_{22}), as explained in Chapter 3.4.5. A Kaiser-Bessel window function (with $\beta_K = 6$, which closely approximates a Hanning window function) is applied to the frequency-domain measurements, across G-band with 5,001 data points,

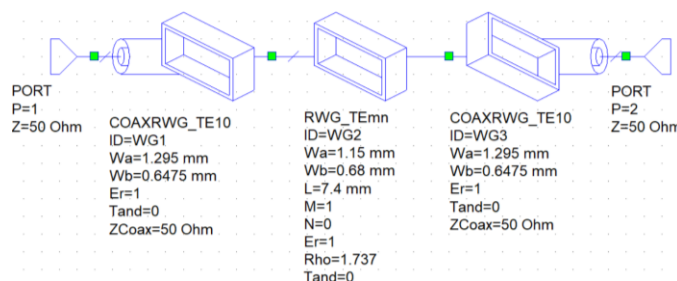
before undertaking the inverse Fourier transform using the PNA-X Band Pass Impulse transform mode. From observation, the arithmetic mean reflected impulse width for the EM (re-)simulated and measured TDR data is ≈ 24 ps.

Using (2.18), with $v_g(180\text{ GHz}) = 2.07 \times 10^8\text{ m/s}$ calculated using $a \rightarrow a_{mean}$, the second pulse is predicted to arrive at ~ 72 ps and ~ 101 ps for the 7.4 mm and 10.4 mm 3-D printed thru lines, respectively.

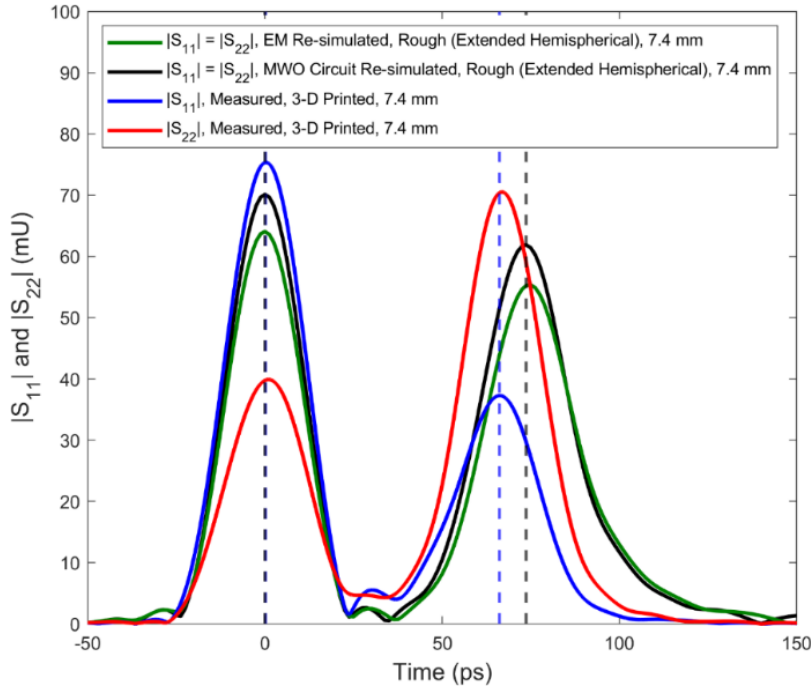
Emulated TDR $|S_{11}|$ measurements can also be created from frequency-domain EM (re-)simulations, by importing a Touchstone data file into AWR's Microwave Office® (MWO). Here, $|\text{TDR_BPI}(1,1,0,10,4,0)|$ calculates the time-domain, Band-Pass Impulse (BPI) response for a linear, time-invariant network. In addition, MWO can emulate TDR measurements from simple circuit elements; as shown in Fig. 4.21(a) with $a \rightarrow a_{mean}$. Re-simulations apply $K(180\text{ GHz}) = 1.32$ and 1.28 to give effective bulk DC conductivity values for rough copper of $3.34 \times 10^7\text{ S/m}$ and $3.54 \times 10^7\text{ S/m}$; these, in turn, give the corresponding MWO circuit simulator ‘metal bulk resistivity normalized to copper’ values (Rho) of 1.737 and 1.638. The results from both the Extended and Huray-Hemispherical roughness models are almost identical, so only the former is shown.

In order to match with PNA-X TDR measurements, MWO must employ a Hanning window, with a Time Resolution Factor of 10 (to apply sufficient zero-padding in the frequency-domain to increase the time resolution) and an amplitude scaling factor of $\times 2$ (to account for the one-sided frequency-domain spectrum).

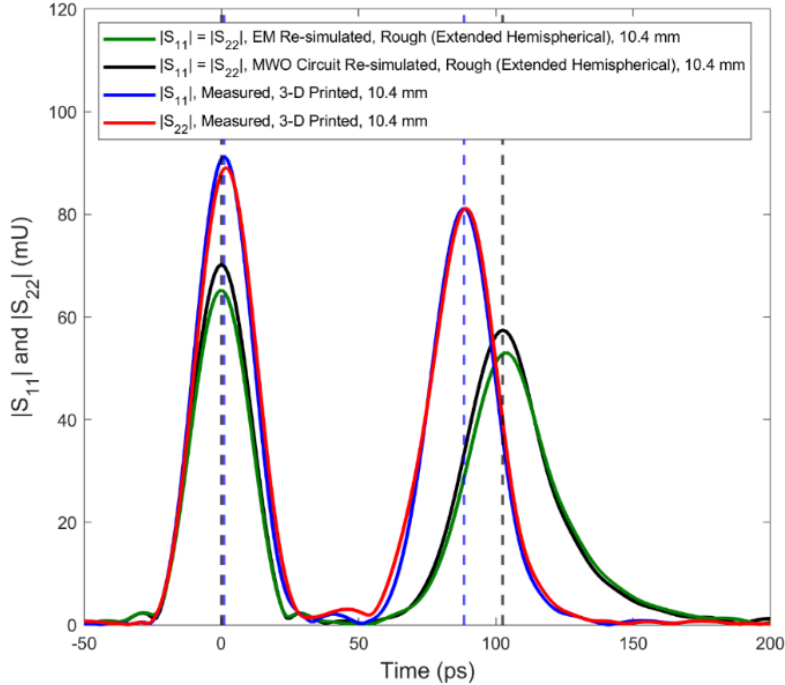
With reference to Fig. 4.21(b) and 4.21(c), the straight vertical blue and black dashed lines indicate the timings of reflected pulse peaks from the measured S_{11} (blue trace) and MWO circuit re-simulation $|S_{11}| = |S_{22}|$ (black trace), respectively.



(a)



(b)



(c)

FIGURE 4.21: Emulated TDR re-simulations and measurements for the 3-D printed thru lines:
 (a) MWO re-simulated setup for the reduced width 7.4 mm thru line; (b) 7.4 mm thru line traces;
 and (c) 10.4 mm thru line traces.

The second reflected pulses for the respective 7.4 mm and 10.4 mm 3-D printed thru lines arrive at 74 ps and 104 ps in EM re-simulations and at 73 ps and 102 ps in MWO circuit re-simulations. There is good agreement between the re-simulated values and those previously calculated (~ 72 ps and ~ 101 ps, respectively). However, as shown in Fig. 4.21, there is a slight discrepancy with the measured results, as the second pulses arrive at 67 ps and 92 ps for the 7.4 mm and 10.4 mm 3-D printed thru lines, respectively. This is believed to be mainly due to mechanical compression of the copper-plated polymer-based thru lines (in the longitudinal direction) with our measurement setup. As a result, from both MWO re-simulations and (2.18), the respective reduction in lengths are believed to be approximately 0.5 mm (6.8%) and 0.9 mm (9.1%).

Figure 4.21 qualitatively shows the measured levels of wave impedance mismatching at both ports. From Fig. 4.21(b) and 4.21(c), the two dominant peaks are evident. The first peak in $|S_{11}|$ represents the wave impedance mismatch reflection from the unit impulse incident at Port 1 and the second peak corresponds to the reflection at Port 2. Similarly, the first peak in $|S_{22}|$ represents the wave impedance mismatch reflection from the unit impulse incident at Port 2 and the second peak corresponds to the reflection at Port 1.

As a useful reference, where there is an equal wave impedance mismatch at both ports, the MWO re-simulations results show that the second peak will be lower than the first, mainly due to the product of the two complex Fresnel transmission coefficients at the incident port being less than unity. From this simulation benchmark, we can establish which port has the worst wave impedance mismatch. For example, with reference to Fig. 4.21(b), the 7.4 mm thru line has the worse wave impedance mismatch at Port 1, when compared to Port 2. Conversely, with reference to Fig. 4.21(c), the 10.4 mm thru line has the worse wave impedance mismatch at Port 2, when compared to Port 1.

4.6 Conclusion

This chapter explains the four Gens. of design iterations that have been employed in the research of low-cost and low loss G-band MPRWGs. 1st Gen. thru lines were not manufactured; nevertheless, the design is explained here, as it informed subsequent designs. 90° twists and BPFs served as benchmarks for this design, with both exhibiting a very high insertion loss due to radiation leakage from the large gap at the split, and a poor return loss due to both the physical gap and misalignment between assembly parts.

2nd Gen. thru lines employed single-block designs, with the internal channel plating using a silver electroless plating technique. If successful, a single-block design would avoid the previously mentioned issues with the 1st Gen. design. However, measured insertion loss was poor; this is believed to be due to insufficient plating thickness. In future, either multiple plating applications or a custom-developed plating technique to selectively metalize the channel would be necessary to realize G-band single-block thru lines.

For the 3rd Gen., we investigated the design and application of a ‘trough-and-lid’ assembly solution, using an H-plane a-edge split and lips that extend beyond the sidewalls to connect with the upper wall. This was to provide a solution for the radiation leakage and assembly part misalignment, which was evident in the 1st Gen. design. Fabrication was undertaken using an ultra-low-cost desktop MSLA 3-D printer. Our outsourcing plating costs are high, when compared to the 3-D printing, but the overall cost is still low. In-house plating would dramatically reduce this cost. An average α'_D across G-band of 13.0 dB/m for the 7.4 mm exemplar and 10.5 dB/m for the 10.4 mm exemplar was demonstrated, which compares well with all previously reported D- and G-band 3-D printed thru lines.

4th Gen. thru lines adopted the same trough-and-lid assembly approach and plating procedure as the 3rd Gen. thru lines, but the more up-to-date Elegoo Mars 2 Pro was used for 3-D printing. 3-D printed thru line measurements demonstrate an average α'_D across G-band of 12.7 dB/m ($0.032 \text{ dB}/\lambda_g$) for the 7.4 mm exemplar and 13.7 dB/m ($0.035 \text{ dB}/\lambda_g$) for the 10.4 mm exemplar, which compares well with all previously reported D- and G-band 3-D printed thru lines. Commensurate performance to the COTS counterparts

is achieved above ca. 200 GHz. However, below ca. 200 GHz, rectangular-to-trapezoidal cross-sectional distortion (due to lip bending) causes additional attenuation. This was confirmed with EM re-simulations, by applying the measured effective mean aperture width $a_{mean} < a$; the resulting increase in the TE10 mode cut-off frequency, from 116 GHz to 130 GHz, significantly increases the level of attenuation in the lower-half of the band. A more robust lip design should be investigated, having a reduced height and increased width, to mitigate lip bending.

Surface roughness modeling was also applied to the 4th Gen. thru lines, using the Extended/Huray-Hemispherical models with $K(180 \text{ GHz}) = 1.32$ and 1.28 , respectively, adding approximately 2-3 dB/m of additional attenuation across G-band. This is the first example of their use with 3-D printed MPRWGs.

A detailed TDR analysis has confirmed that the flange-to-flange interfaces are the main source of reflections, with a qualitative comparison made between port wave impedance matching. Moreover, when tightly fixed to the measurement setup, the 3-D printed components are mechanically compressed in the longitudinal direction; by approximately 0.5 mm (6.8%) and 0.9 mm (9.1%) for the 7.4 mm and 10.4 mm thru lines, respectively.

4.7 References

- [1] R. Payapulli, L. Zhu, S.-H. Shin, M. Stanley, N. M. Ridler, and S. Lucyszyn, “Polymer-based 3-D printed 140 to 220 GHz metal waveguide thru lines, twist and filters,” *IEEE Access*, vol. 11, pp. 32272-32295, Mar. 2023.
- [2] IEEE standard for rectangular metallic waveguides and their interfaces for frequencies of 110 GHz and above – part 1: frequency bands and waveguide dimensions, IEEE Standard 1785.1-2012, 2012.
- [3] IEEE standard for rectangular metallic waveguides and their interfaces for frequencies of 110 GHz and above – part 2: waveguide interfaces, IEEE Standard 1785.2-2016, 2016.
- [4] S. Lucyszyn, X. Shang, W. J. Otter, C. Myant, R. Cheng, and N. M. Ridler, “Polymer-based 3D printed millimeter-wave components for spacecraft payloads,” *IEEE MTT-S International Microwave Workshop Series on Advanced Materials and Processes (IMWS-AMP)*, Ann Arbor, USA, Jul. 2018 (Invited).
- [5] S. M. Lewis, E. A. Nanni and R. J. Temkin, “Direct machining of low-loss THz waveguide components with an RF choke,” *IEEE Microwave and Wireless Components Letters*, vol. 24, no. 12, pp. 842-844, Dec. 2014
- [6] B. Pyne, R. Naruse, H. Saito, J. Hirokawa, V. Ravindra and P. R. Akbar, “Robust contactless noncircular choke flange for wideband waveguide applications,” *IEEE Transactions on Microwave Theory and Techniques*, vol. 67, no. 3, pp. 861-867, Mar. 2019.
- [7] W. J. Otter, N. M. Ridler, H. Yasukochi, K. Soeda, K. Konishi, J. Yumoto, M. Kuwata-Gonokami, and S. Lucyszyn, “3D printed 1.1 THz waveguides,” *IET Electron Lett.*, vol. 53, no. 7, pp. 471-473, Mar. 2017.
- [8] J. Shen, M. W. Aiken, M. Abbasi, D. P. Parekh, X. Zhao, M. D. Dickey, and D. S. Ricketts, “Rapid prototyping of low loss 3D printed waveguides for millimeter-wave applications,” *IEEE MTT-S International Microwave*

Symposium (IMS), Honolulu, USA, Jun. 2017.

- [9] J. Shen, M. Aiken, C. Ladd, M. D. Dickey, and D. S. Ricketts, “A simple electroless plating solution for 3D printed microwave components,” *Asia-Pacific Microwave Conference (APMC)*, New Delhi, India, Dec. 2016.
- [10] N. Shoaib, N. M. Ridler, and M. J. Salter, “Commissioning of the NPL WR-05 waveguide network analyser system for S-parameter measurements from 140 GHz to 220 GHz,” NPL Report TQE 12, National Physical Laboratory, Teddington, UK, Mar. 2015.
- [11] A. Rumiantsev and N. Ridler, “VNA calibration,” *IEEE Microwave Magazine*, vol. 9, no. 3, pp. 86-99, June 2008.
- [12] I. Instone, “Calibration of automatic network analysers”, Chapter 12 in *Microwave Measurements*, R. J. Collier and A. D. Skinner (Editors), 3rd Edition, London, U.K.: IET, Oct. 2007, pp. 263–290.
- [13] Ansys Inc., “Ansys HFSS | 3D High Frequency Simulation Software”, 2023.
Accessed: Apr. 07, 2023. [Online]. Available:
<https://www.ansys.com/en/products/electronics/ansys-hfss>.
- [14] Virginia Diodes Inc., “VNA Extender - VDI Model: WR5.1-VNAX”, 2022.
Accessed: Jan. 07, 2023. [Online]. Available:
<https://www.vadiodes.com/index.php/en/products/vector-network-analyzer?id=853>.
- [15] A. Bal, D.G. Carey, F.A. Espinal and G.H. Huff, “Electroless silver plating of 3D printed waveguide components by peristaltic pump driven system,” *Electronics Letters*, vol. 5, no. 2, pp. 100-102, Jan. 2019.
- [16] I. Stil, A.L. Fontana, B. Lefranc, A. Navarrini, P. Serres, and K.F. Schuster, “3-D printed iris waveguide filter in W-band,” *22nd International Symposium on Space Terahertz Technology*, Tokyo, Japan, Apr. 2012.
- [17] A. Pons, J. M. García, F. D. Quesada, A. Alvarez-Melcon, A. Romera, J. Hinojosa, M. Guglielmi, V. E. Boria, and L. Arche-Andradas, “Evanescent mode filters composed of dielectric parts built using 3D-printing methods,” *IEEE MTT-S International Microwave Filter Workshop (IMFW)*, Perugia,

Italy, Nov. 2021.

- [18] M. V. Mrvić, M. M. Potrebić, and D. V. Tošić, “Compact H-plane dual-band bandstop waveguide filter,” *Journal of Computational Electronics*, vol. 16, pp. 939–951, Jun. 2017.
- [19] X. Shang, P. Klasmann, and M. J. Lancaster, “A compact Ka-band waveguide orthomode transducer fabricated by 3-D printing,” *46th European Microwave Conference (EuMC)*, London, UK, Jan. 2017.
- [20] L. Zhu, S.-H. Shin, R. Payapulli, T. Machii, M. Motoyoshi, N. Suematsu, N. M. Ridler, and S. Lucyszyn, “3-D printed rectangular waveguide 123-129 GHz packaging for commercial CMOS RFICs,” *IEEE Microwave and Wireless Component Letters*, vol. 33, Jan. 2023, DOI: 10.1109/LMWT.2022.3220364.
- [21] S. Lucyszyn, X. Shang, W. J. Otter, C. Myant, R. Cheng, and N. M. Ridler, “Polymer-based 3D printed millimeter-wave components for spacecraft payloads,” *IEEE MTT-S International Microwave Workshop Series on Advanced Materials and Processes (IMWS-AMP)*, Ann Arbor, USA, Jul. 2018 (Invited).
- [22] N. Jastram, M. A. Al-Tarifi, L. Boskovic, and D. S. Filipovic, “On the split-block realization of millimeter-wave ridge waveguide components,” *IEEE Microwave and Wireless Components Letters*, vol. 28, no. 4, pp. 296-298, Apr. 2018.
- [23] J. Hesler, “A photonic crystal joint (PCJ) for metal waveguides,” *2001 IEEE MTT-S International Microwave Symposium Digest*, Phoenix, USA, May 2001.
- [24] Microwaves101, “Waveguide Construction,” 2022. Accessed: Jan. 07, 2023. [Online]. Available: <https://www.microwaves101.com/encyclopedia/waveguide-construction>.
- [25] Millimeter Wave Products Inc., “75 GHz to 110 GHz, Harmonic Mixer,” 2022. Accessed: Jan. 07, 2023. [Online]. Available: <https://www.miww.com/920w-387-harmonic-mixer-f-frequency-range-75-ghz-to-110-ghz-lo-frequency-range-2-ghz-to-20-ghz-lo-drive-level-10-dbm/>
- [26] Pasternack Enterprises Inc., “WR-5 Straight Waveguide Section 1 Inch Length,

- UG-387/U-Mod Round Cover Flange from 140 GHz to 220 GHz”, 2022. Accessed: Jan. 07, 2023. [Online]. Available: <https://www.pasternack.com/wr-5-straight-waveguide-section-ug387-mod-round-pew05s000-1-p.aspx>.
- [27] Fairview Microwave Inc., “WR-5 Waveguide Section 1 Inch Straight Length with UG-387/U-Mod Round Cover Flange from 140 GHz to 220 GHz,” 2022. Accessed: Jan. 07, 2023. [Online]. Available: <https://www.fairviewmicrowave.com/wr-5-waveguide-section-straight-ug387-mod-round-fmw05s000-1-p.aspx>.
- [28] Hasco Components Inc., “Waveguide, WR-5, 1-inch Straight Section, 140 GHz to 220 GHz, G-Band,” 2022. Accessed: Jan. 07, 2023. [Online]. Available: <https://www.hasco-inc.com/waveguide-components/wr-5-millimeter-waveguide-1-inch-straight-section-140-ghz-to-220-ghz-g-band/>.
- [29] Virginia Diodes, “Straight Waveguides, Tapers, Horn Antennae,” 2022. Accessed: Jan. 07, 2023. [Online]. Available: <https://www.vadiodes.com/en/products/straight-waveguides-tapers-horn-antenna-directional-couplers>.
- [30] R. Wenger, “1-inch self-symmetric straight”, Virginia Diodes Inc., Charlottesville, VA, USA, May 2014.
- [31] B. Zhang and H. Zirath, “Metallic 3-D printed rectangular waveguides for millimeter-wave applications,” *IEEE Trans. on Components, Packaging and Manufacturing Technology*, vol. 6, no. 5, pp. 796-804, May 2016.

5. G-band Polymer-Based 3-D Printed MPRWG 90° Twists

5.1 Introduction

A significant part of the content in this chapter (i.e., Section 5.3) is based on a research article by R. Payapulli et al., which was published in *IEEE Access* in March 2023 [1].

1st Gen. twists were fabricated and measured, in addition to successful 4th Gen. twists using the trough-and-lid assembly. Measurements of the former are briefly presented, with analysis on the main design flaws and suggestions for improvements given. For the latter, a detailed analysis is given, including TDR measurements.

2nd and 3rd Gen. twists were not fabricated. For the former, their respective thru line components exhibited poor performance. For the latter, the design and performance would be similar to 4th Gen. twists.

5.2 1st Generation

5.2.1 Design

G-band COTS 90° twists, manufactured by Pasternack Enterprises Inc., have a flange-to-flange component length of 1.25 inches (31.75 mm), which includes 0.25 inch (6.35 mm) thru lines within each flange. This results in a twist length of exactly $5\lambda_{gL}$, having a rotational smoothness of $18^\circ/\lambda_{gL}$. Any evanescent mode excitation at one port will have significantly decayed over a distance of $5\lambda_{gL}$, avoiding interactions with the other port and, thus, avoiding additional insertion loss. Our two ruggedized 3-D printed counterparts have the same flange-to-flange component length of 31.75 mm. This design employs a twisting E-plane symmetrical split (i.e., the split twists along the length of the component such that it is constantly E-plane symmetrical with respect to the waveguide channel).

The smooth twisting transition was created using the *Sweep* function in Autodesk

Fusion 360. The 3-D CAD layout for the internal 90° twist geometry, along with that of a thru line, is shown in the inset of Fig. 5.1. Here, L indicates the same total length for both components, and the cross-sectional waveguide dimensions are fixed along this length.

Simulations are performed using HFSS. Here, the internal MPRWG walls are represented by copper, having a bulk DC conductivity of 5.8×10^7 S/m. The simulated band-average insertion loss and worst-case return loss for a perfectly matched twist are 0.28 dB and 17.2 dB, respectively. Also included in Fig. 5.1 are the simulation results for a 31.75 mm thru line; degraded performance can be inferred by the introduction of the twist. Local maxima and minima in the transmission response correspond to local minima (nulls) and maxima in the reflection response, respectively.

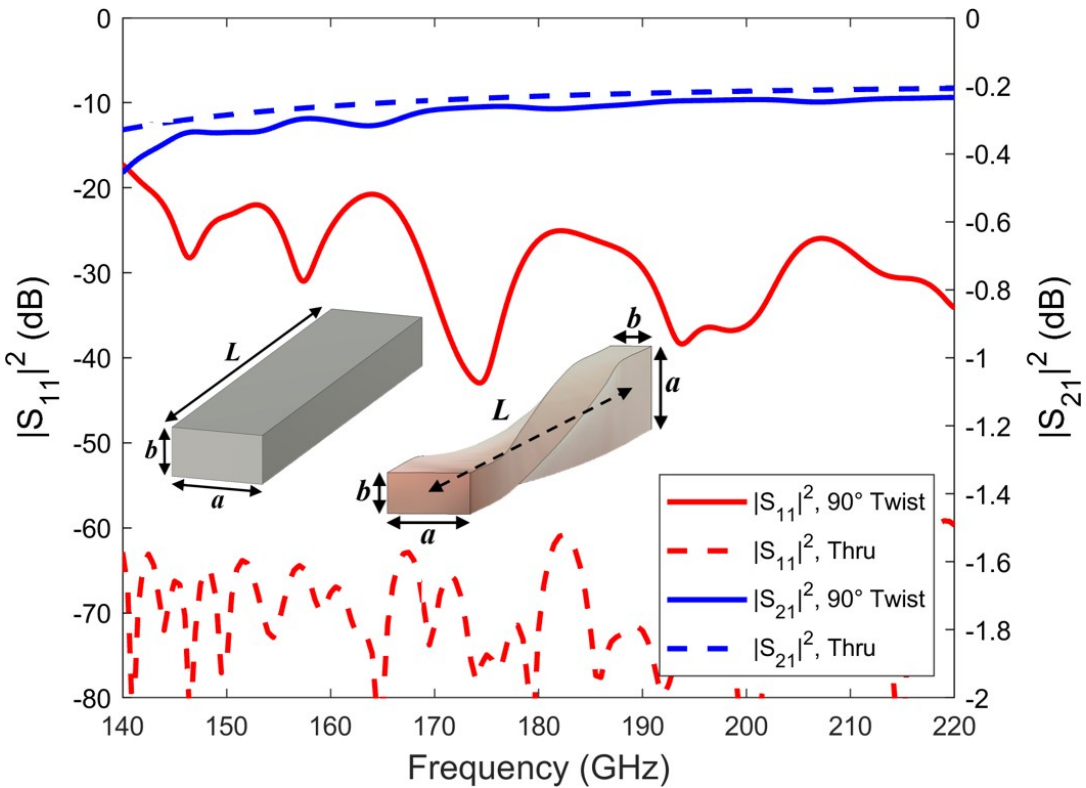


FIGURE 5.1: HFSS simulation results for the WR-5 thru and 90° twist (insets show internal CAD layouts of the components) having length $L = 31.75$ mm.

5.2.2 Fabrication

The Elegoo Mars printer was used here for fabrication, with metalization outsourced to a commercial service provider. As before, a 50 μm plating thickness is used, with an expected 35 μm plating thickness in the channel.

The 1st generation 90° twists were printed with the broad wall parallel to the build plate at one port and perpendicular to the build plate at the other port, as shown in Fig. 5.2. This avoids stepped sidewalls due to sloping orientations at each port.

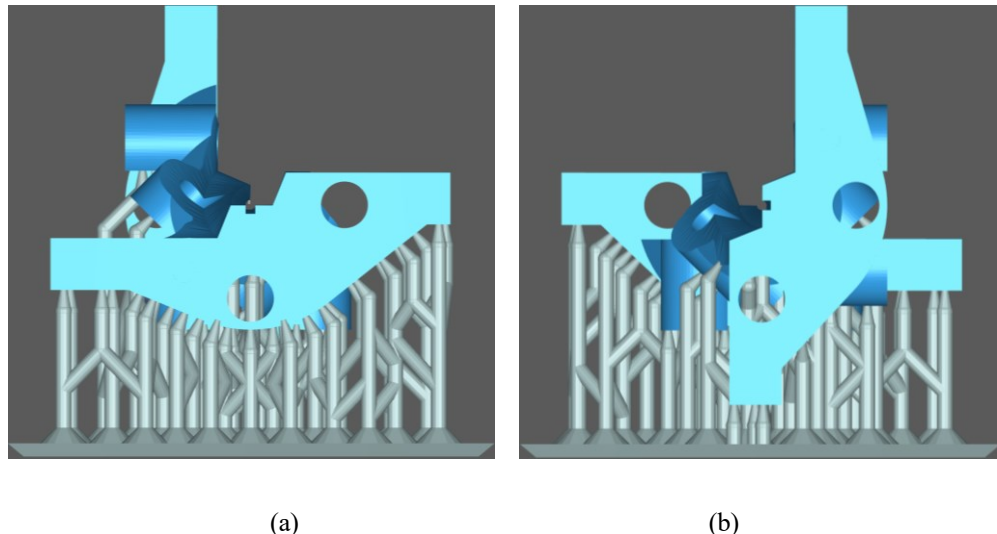


FIGURE 5.2: Flange view of the Chitubox print orientation for the 1st Gen. twist, showing support structures: (a) port aligned with broad wall perpendicular to the build plate; and (b) other port aligned with broad wall parallel to the build plate.

After 3-D printing and electroplating, and prior to full assembly, the 90° twists weigh 15.8 g. Assembly of the ruggedized parts is achieved using five pairs of screws, nuts, and washers and four pairs of stainless steel dowel pins. Images of the disassembled and assembled 3-D printed twists are shown in Fig. 5.3. Note that the copper plating has tarnished, due to the length of time between plating and the photograph being taken.



FIGURE 5.3: 1st Gen. WR-5 MPRWG 31.75 mm 90° twists: (a) disassembled 3-D printed and copper electroplated split-block parts; and (b) two fully assembled 90° twists in cascade.

5.2.3 Measurements

Quantitative two-port measurements of a 90° twist require one of the frequency extender heads to be rotated by 90°. However, at such high millimeter-wave frequencies, the resulting phase mismatch in the associated feed coaxial cable could introduce a significant post-calibration measurement error. Instead, two-port measurements can be undertaken by cascading two 90° twists together. Here, the two 3-D printed twists are employed, giving a qualitative insertion loss for each individual component.

Figure 5.4 shows two-port reflection measurements across G-band for the two 3-D

printed twists connected in cascade. The worst-case return loss across G-band is 6.6 dB. The poor return loss is the result of three wave impedance mismatches (i.e., at both port flanges and the inter-twist flange interfaces), and is exacerbated by assembly part misalignment, edge rounding, dimensional inaccuracy, and aperture height reduction (which will be explained later). The Fabry-Pérot ripples in the frequency responses are characteristic of multi-stage reflections.

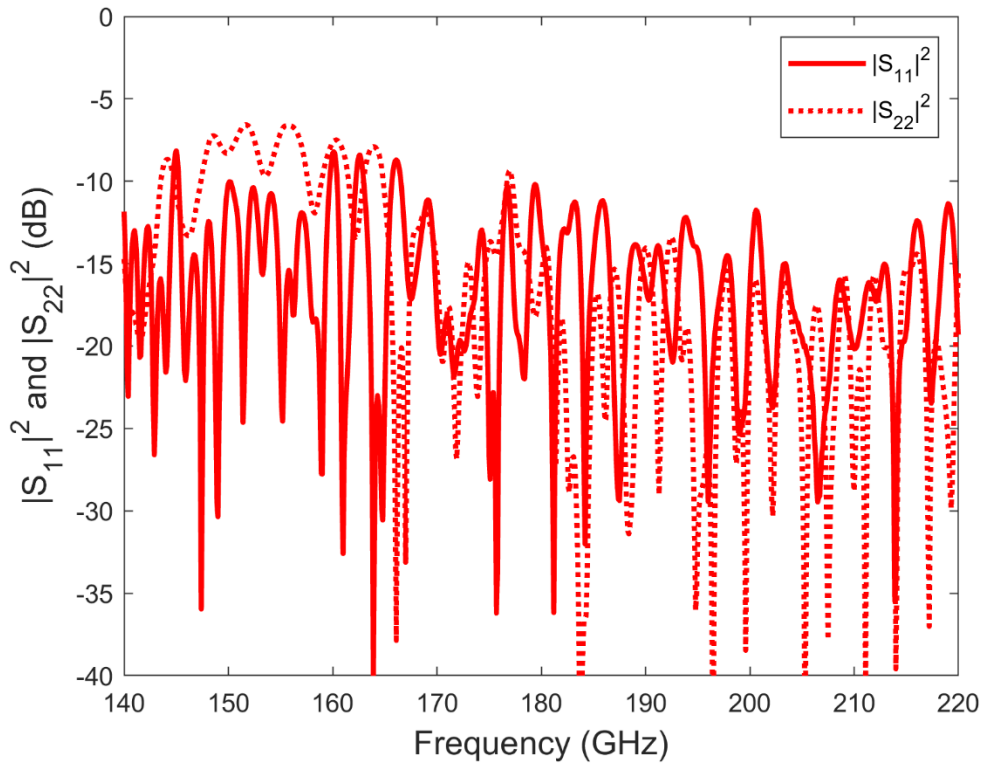


FIGURE 5.4: Reflection measurements for a cascade connection of two 1st Gen. 3-D printed 90° twists.

Figure 5.5 shows two-port transmission measurements across G-band for two 3-D printed twists connected in cascade. Below 160 GHz, the response demonstrates a sharp roll-off, with the insertion loss being around 70 dB below 150 GHz. This is characteristic of a waveguide with a cut-off frequency of around 160 GHz.

For both twists, the port apertures have an average measured width of 1.14 mm. This

corresponds to a cut-off frequency of $f_{c,10} = c/2a_{measured} = 132$ GHz. Although this is narrower than the ideal aperture width of $a = 1.295$ mm, the up-shifted cut-off frequency of 160 GHz would require an aperture width of ~ 0.93 mm. This may be the result of an aperture width reduction within the twisting transition, as the changing orientation of the waveguide with respect to the build plate may cause changes in the manufactured dimensions of key features. It is not possible to verify this using our measurement technique, as the aperture width within the twisting transition of an E-plane symmetrical split waveguide cannot be directly observed by an optical microscope.

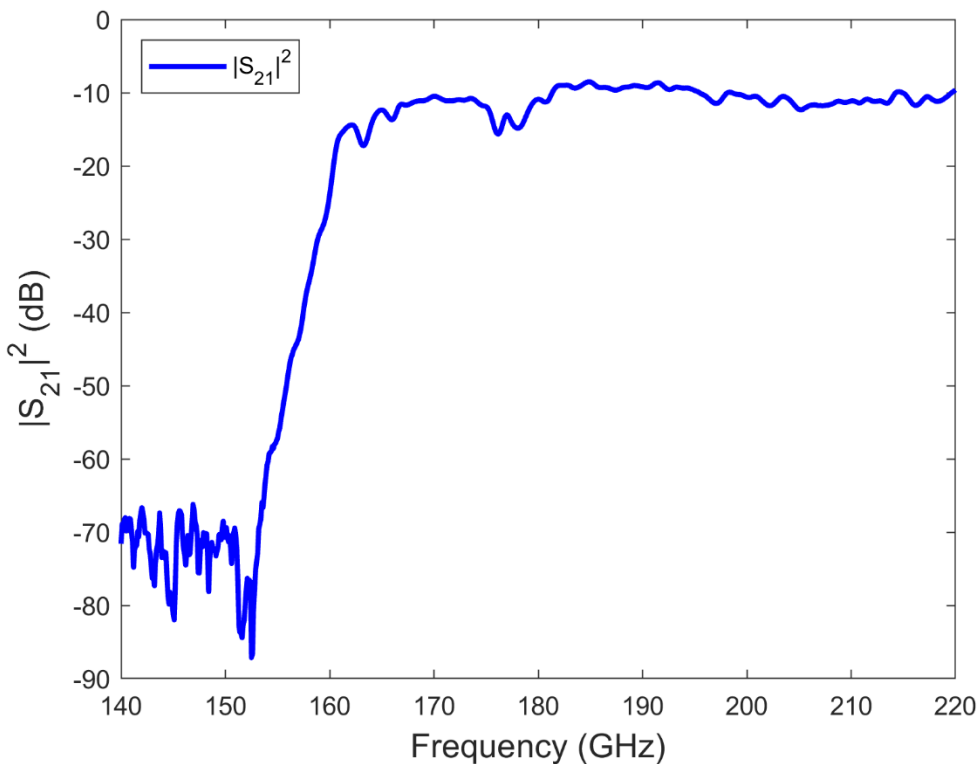


FIGURE 5.5: Transmission measurements for a cascade connection of two 1st Gen. 3-D printed 90° twists.

For both twists, the average measured narrow wall dimension is found to be $b_{meas} = 0.53$ mm, which is narrower than the ideal of 0.648 mm. This is due to the upper sidewall being an unsupported overhang with this printing orientation, resulting in sagging and thus an aperture height reduction. Note that this does not have an effect on the cut-off

frequency for TE₁₀ mode operation, but will cause a return loss degradation.

Above the cut-off frequency, the average insertion loss is 10.9 dB. Therefore, the qualitative average insertion loss for a single 3-D printed twist is approximately 5.5 dB. As discussed in Chapter 4.2.3, this high insertion loss is due to EM radiation leakage from the split, as a gap between the assembly parts occurs. This is further exacerbated by significant edge rounding at the junction between the waveguide channel and split, as shown in Fig. 5.6, which will further increase this gap.



FIGURE 5.6: Close-up of the 1st Gen. 90° twist channel, showing edge rounding.

5.3 4th Generation

5.3.1 Design

Our 4th Gen. 3-D printed twist has a length of 31.75 mm (i.e., equal to the length of the 1st Gen. 3-D printed twists and the COTS twists). The transition was created in CAD using the same method as for the 1st Gen. twists. In addition, to avoid the cut-off frequency up-shift observed for the 1st Gen. components, the aperture width of the twisting transition was increased by 0.1 mm (this is an arbitrary increase that was decided on from prior 3-D printing experience). The trough-and-lid assembly approach has been adopted for these components, which has been shown to mitigate against EM radiation leakage in thru lines.

The major design challenges emerge due to the twisting transition. To preserve the operating principle of the proposed split-block design, the split must be H-plane a -edge, with lips adjacent to the channel, along the entirety of the component. Therefore, the split must twist along with the waveguide channel, with the top piece becoming a twisting lid. This complex geometry is easily realized with additive manufacturing, which is further evidence of its utility.

Due to their irregular shapes and post-production warping, the split-block 90° twist pieces are unlikely to fit together as tightly as the thru line. This is solved by designing as many screw-holes as possible along the channel (six pairs in total, with screw-holes positioned closer to the channel towards the middle of the part), ensuring that the lips maintain good electrical contact with the top piece along the entire length of the 90° twist. Four pairs of steel dowel pins are used for alignment along the length of the component. Structural ruggedization is performed by thickening the screw-holes and reinforcing the middle; this also enables tight clamping without deforming the parts.

5.3.2 Fabrication

The Elegoo Mars 2 Pro was used for 3-D printing, which produces parts with less edge and corner rounding than the previous Elegoo Mars model. Dimensional analysis was also undertaken to ensure that the port aperture dimensions were reasonably accurate.

50 μm copper electroplating was employed, with an assumed internal plating thickness of 35 μm (as found in Chapter 4.5.2). To avoid the aperture height reduction observed in the 1st Gen. twists, these 90° twists were rotated by 45° such that the two waveguide ports are at $\pm 45^\circ$, as shown in Fig. 5.7. This orientation was found to optimize dimensional accuracy and minimize sidewall overhang, with the caveat being the introduction of stepped sidewalls at the ports due to their sloped orientations. Printing time was 3h30m per component.

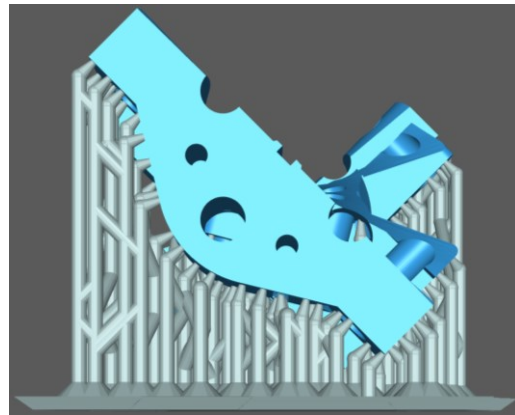
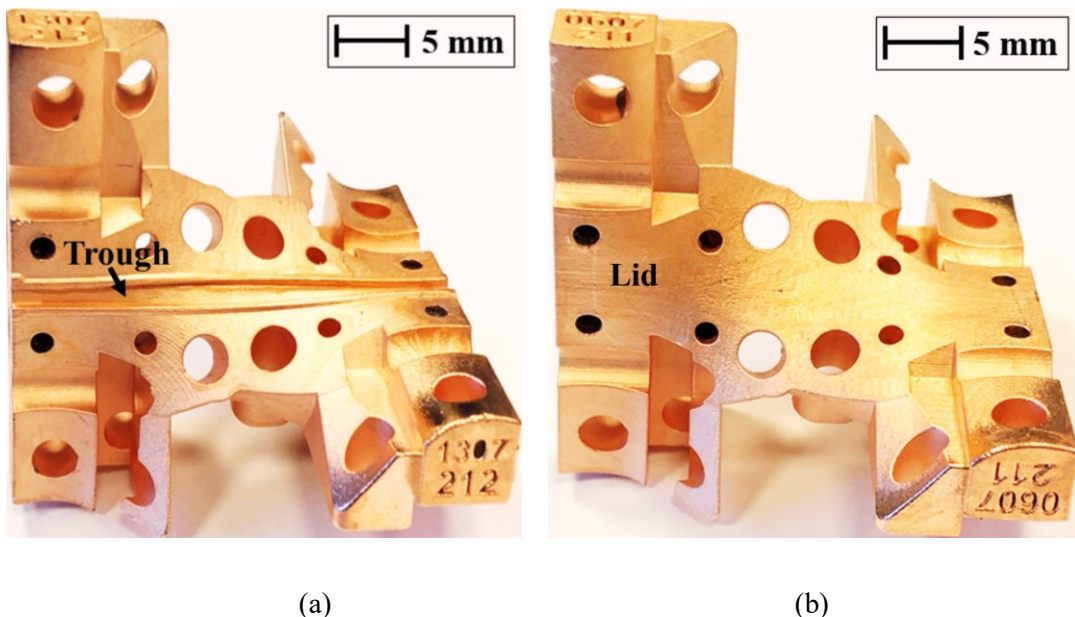


FIGURE 5.7: Flange views of print orientations in Chitubox for the 4th Gen. twist, showing support structures.

Images of a disassembled and assembled 3-D printed twist, along with its COTS counterpart, are shown in Fig. 5.8. Unlike the thru lines, it was found that a tight assembly did not introduce significant cross-sectional distortion. This is likely due to the distributed forces being exerted in different directions along the waveguide length. It can be seen in Fig. 5.8(a) that there are imperfections in the floor of the trough.



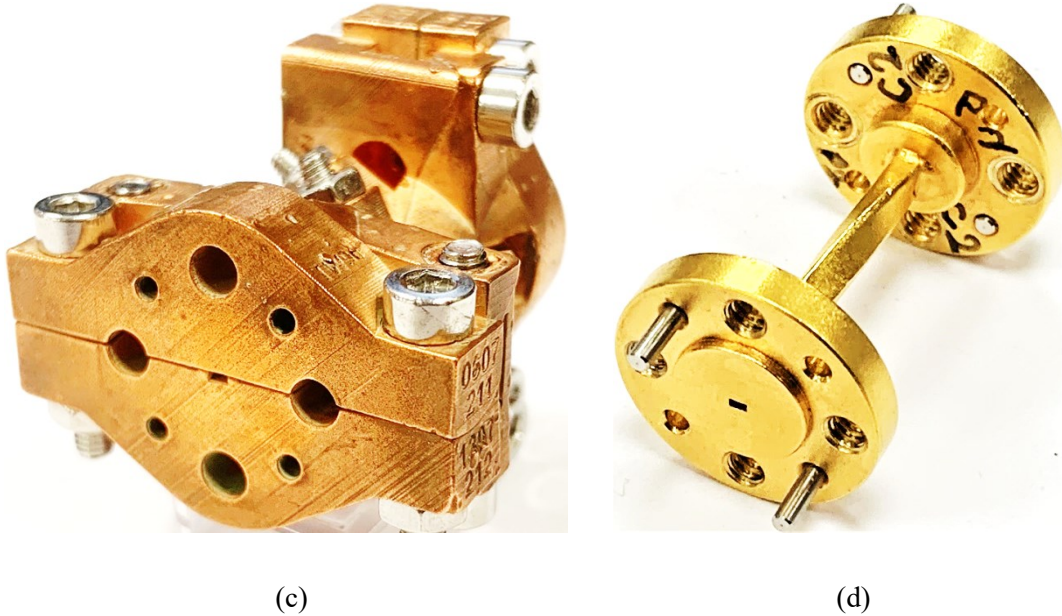


FIGURE 5.8: 4th Gen. WR-5 MPRWG 31.75 mm 90° twists: (a) disassembled 3-D printed and copper electroplated bottom part (twisting trough); (b) disassembled top part (twisting lid); (c) fully assembled; and (d) COTS counterpart from Pasternack [2].

Six 90° twists were fabricated in total, with all exhibiting a similar S-parameter performance. A detailed analysis of the exemplar that exhibited the lowest insertion loss is given here.

Each 3-D printed component costs approximately \$0.20 to print, while the additional commercial copper electroplating costs approximately \$82 (depending on the total surface area). Table 5.1 shows a more accurate cost comparison for G-band COTS 90° twists, all sourced from the US (Pasternack Enterprises Inc., Fairview Microwave Inc., and Hasco Components Inc.). The cost ratio is defined here as the purchase cost of the COTS component per unit length divided by total cost per unit length of our 3-D printed counterpart. A larger cost reduction is found with the twist than the thru lines, which was given in Table 4.1 (Chapter 4.4.2), due to the extra processing steps needed in commercial machining. Clearly, 3-D printing can be employed to produce more geometrically complex components at little to no extra cost. It will be seen, in Section 5.3.3, that the measured performance of our 3-D printed twist is commensurate with the Pasternack COTS counterpart.

TABLE 5.1: Comparative costs (at the time of writing) for G-band 90° twists with COTS components and their 3-D printed counterparts (*costs available online).

Component Type	COTS Manufacturer	Cost (\$) *	Length (mm)	Cost per length (\$/mm)	Cost ratio	Insertion loss (dB)	Ref.
90° Twist	Pasternack	735	31.75	23	8.5	0.62	[2]
	Fairview	414	31.8	13	4.8		[3]
	Hasco	407	25.4	16	5.9		[4]
	ICL (3-D printed)	86	31.8	3	-	0.62	This work

5.3.3 Measurements

Two-port measurements, with two twists connected in cascade, are given here. As an alternative, quantitative one-port measurements were undertaken by connecting one end of a 90° twist to the Port 1 frequency extender head, with the other end connected to a termination.

Here, a high quality commercial wave impedance matched load, manufactured by VDI, was used as the termination. Ideally, if the matched load is connected directly to the measurement port (i.e., no twist inserted), all the incident power at the matched load will be dissipated, resulting in a zero reflection coefficient at this termination. With the twist inserted, the measured reflectance $|S_{11}|^2$ will then represent the reflection response of the individual twist, thereby giving quantitative values for the return loss of the individual component.

Note that qualitative insertion loss for an individual twist component can be achieved by undertaking one-port transmission measurements with a 90° twist connected to a high-quality wave impedance short-circuit. This terminates the waveguide with a solid metal boundary, with the quantitative insertion loss being half the measured value (also assuming reflected power is insignificant in comparison to the transmitted power). However, it was found that a good flange-to-flange connection between the 3-D printed twist and a commercial VDI short-circuit component was not possible, as the latter did not conform well to the surface of the 3-D printed part due to warping at the edges of the 3-D printed part. This caused significant flange leakage loss, which meant that these one-

port measurements did not provide a quantitative insertion loss.

Three components are used in the following measurements: the 3-D printed 90° twist and two brand-new commercial 90° twists (referred to here as COTS #1 and COTS #2). The mean measured aperture dimensions $[a, b]$ for these three twists are $[1,270 \mu\text{m}, 580 \mu\text{m}]$, $[1,250 \mu\text{m}, 720 \mu\text{m}]$ and $[1,260 \mu\text{m}, 710 \mu\text{m}]$, respectively, at both ends. None of the three components meet the WM-1295 standard of $[a, b] = [1,295 \mu\text{m}, 647.5 \mu\text{m}]$, with the 3-D printed twist having a better dimensional match when compared to COTS #1. Moreover, COTS #1 and COTS #2 have very similar dimensions, while COTS #2 was found to have a visible aperture defect at one of its flanges.

Figure 5.9 shows one-port reflection measurements across G-band for the individual 3-D printed and COTS #1 twists, connected to a wave impedance matched load termination. The COTS #2 twist was not included here, as its flange aperture defect results in poorer reflection measurements when compared to those from the COTS #1 twist.

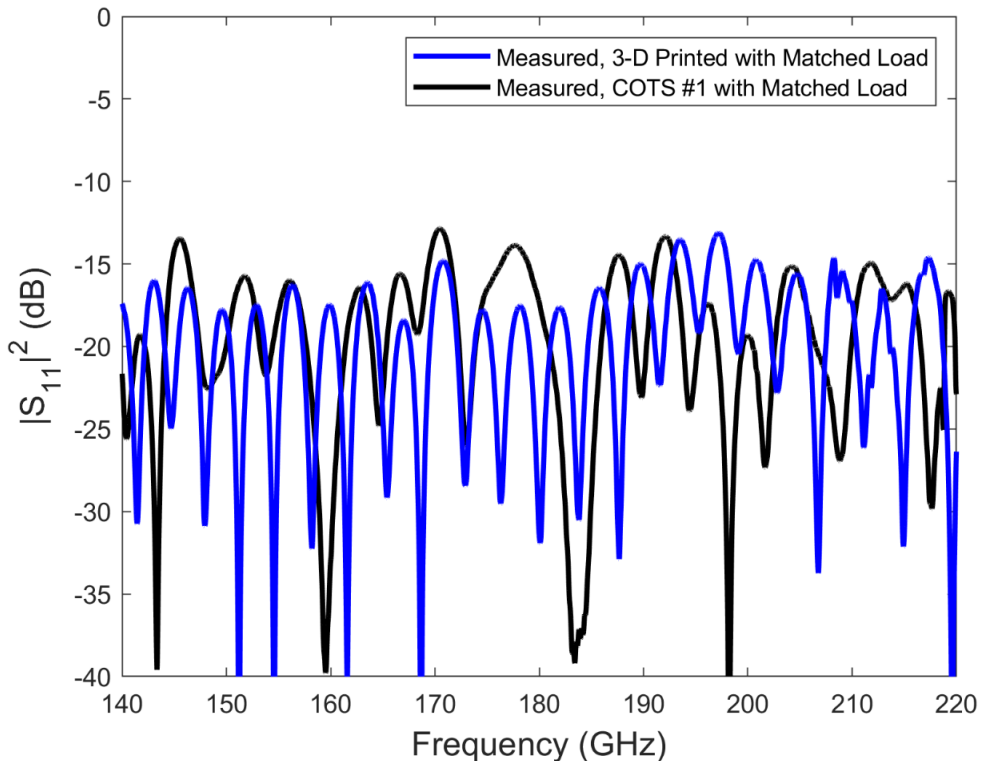
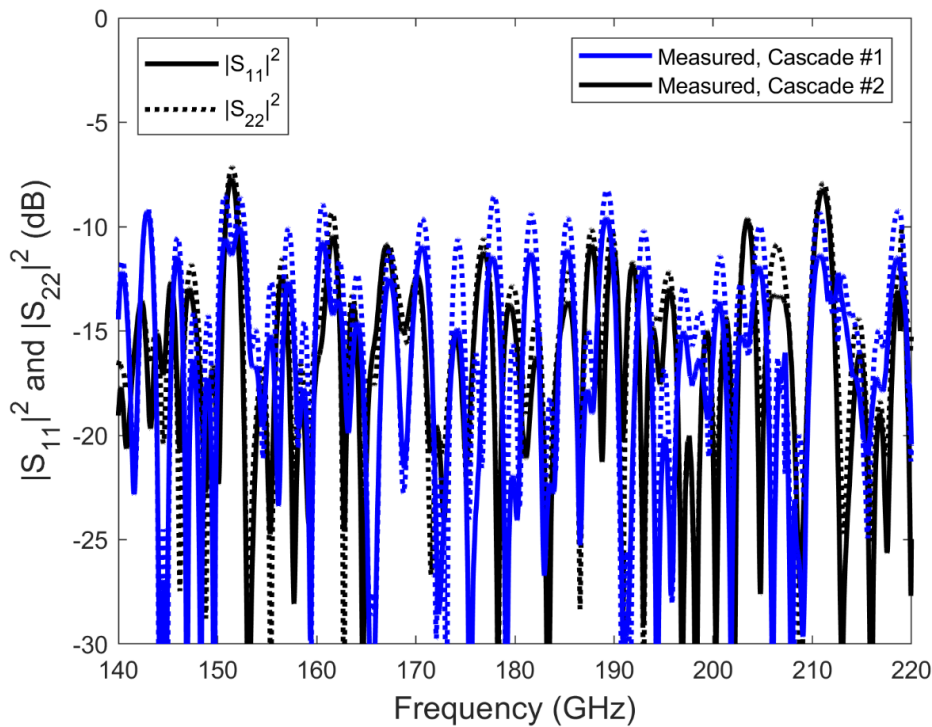


FIGURE 5.9: One-port reflection measurements for the 3-D printed and COTS #1 twists (terminated with a wave impedance matched load).

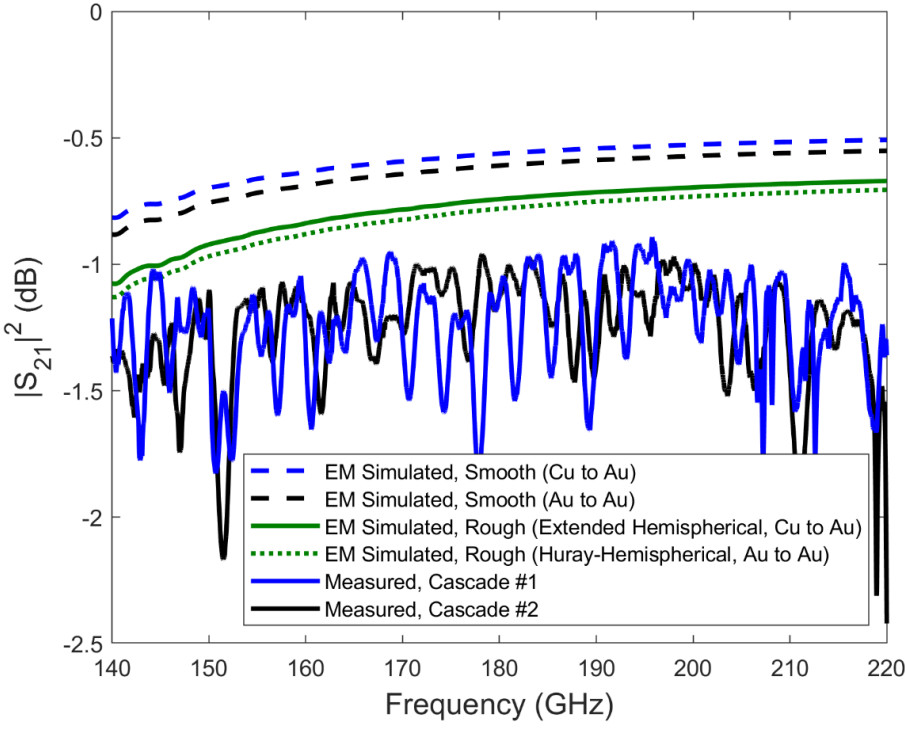
The worst-case return loss across G-band is 13.2 dB for the 3-D printed 90° twist, while that for the COTS #1 twist is 12.9 dB. The return loss for the 3-D printed twist is generally greater than 15 dB across G-band. In general, our 3-D printed twist has a measured return loss that is commensurate with its brand-new commercial counterpart.

For two-port measurements, two cascade combinations were employed: (i) the 3-D printed twist (at Port 1) connected to COTS #1 (at Port 2), and (ii) COTS #1 (at Port 1) connected to COTS #2 (at Port 2). These shall be referred to here as Cascades #1 and #2, respectively. As the COTS twists are manufactured from gold-plated oxygen-free hard copper [2], associated theoretical calculations and EM (re-)simulations are undertaken using the bulk DC conductivity of gold.

Figure 5.10(a) shows two-port reflection measurements across G-band for Cascades #1 and #2. The worst-case return loss across G-band is 8.3 dB and 7.2 dB for Cascades #1 and #2, respectively. The 1.1 dB improvement in the worst-case return loss with Cascade #1 can be attributed to the aperture dimensions of the 3-D printed twist being closer to the ideal dimensions, when compared to that for COTS #1 or #2.



(a)



(b)

FIGURE 5.10: Two-port EM simulations and measurements for Cascades #1 and #2: (a) reflection; and (b) transmission.

The poor overall return loss is the result of three wave impedance mismatches (i.e., at both port flanges and the inter-twist flange interfaces). The Fabry-Pérot ripples in the frequency responses are characteristic of multi-stage reflections.

Figure 5.10(b) shows two-port transmission measurements for Cascades #1 and #2, across G-band, demonstrating an average insertion loss of 1.24 dB for both cascade scenarios. The qualitative average insertion loss for a single twist is approximately 0.62 dB, given that all twists have similar return loss performances. This suggests a commensurate insertion loss performance between the 3-D printed twist and the COTS counterparts.

The EM simulated transmission responses for two ideal cascaded twists (having perfect wave impedance matching) exhibit significantly lower loss when compared to Cascades #1 and #2. When surface roughness losses are applied, using the

Extended/Huray-Hemispherical model $K(180 \text{ GHz})$ values, the results are closer to our measurements. However, there is still a significant discrepancy due to the 3-D printed-to-COTS inter-twist mismatch (also found with Cascade #2). Moreover, any intra-waveguide defects, which could be introduced by the respective manufacturing techniques of either twist, may cause significant reflections. For example, within the 3-D printed twist, this would be associated with layer-by-layer defects due to changing printing orientation and by defects seen in Fig. 5.8(a).

It should be noted that α'_D cannot be investigated with Cascades #1 and #2. This is because Equation (2.16) is no longer valid, as the wave impedance mismatch reflections from the 3-D printed-to-COTS #1 twist flange interface and intra-waveguide defects result in a non-homogeneous DUT.

Using the mean measured aperture widths of $a = 1.27 \text{ mm}$ and 1.25 mm for the single 3-D printed and COTS #1 twists, respectively, the corresponding calculated mid-band group velocities are $v_g(180 \text{ GHz}) = 2.26 \times 10^8$ and $2.24 \times 10^8 \text{ m/s}$. By applying these to Equation (2.18), the respective second pulses in TDR measurements are predicted to arrive at 281 ps and 284 ps . With Cascade #1, the time of the second pulse for $|S_{11}|$ is equal to that for the one-port 3-D printed twist, with the second pulse for $|S_{22}|$ corresponding to that for one-port COTS #1 twist. The third pulse is predicted to arrive at $281 + 284 = 565 \text{ ps}$, with both $|S_{11}|$ and $|S_{22}|$ responses.

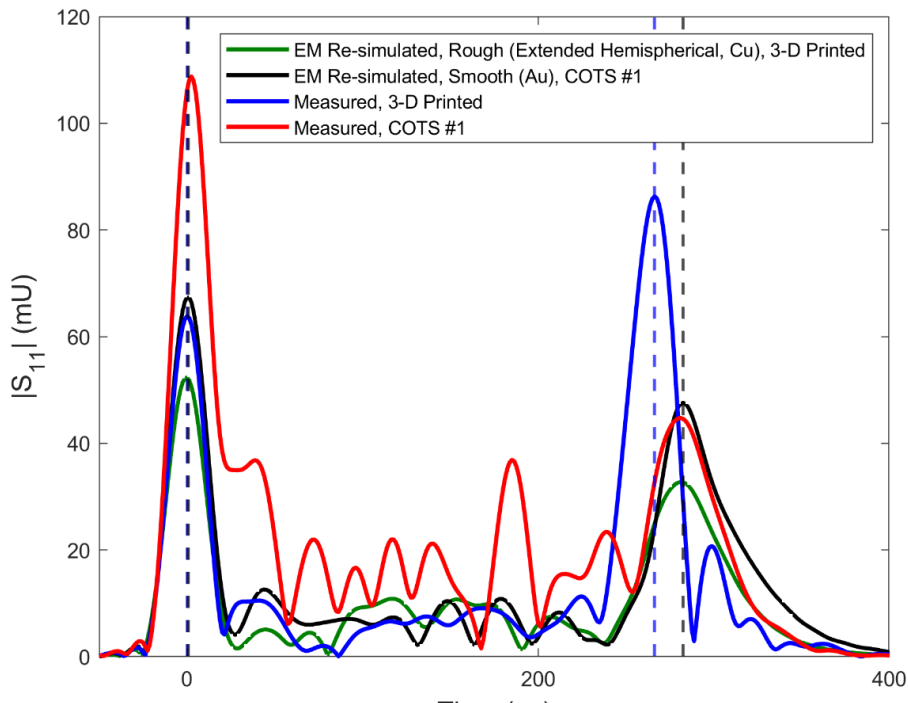
Figure 5.11(a) shows one-port TDR traces for the 3-D printed and COTS #1 twists, with Fig. 5.11(b) showing two-port TDR traces for Cascade #1. VNA measurements and EM re-simulations (with only the Extended-Hemispherical model shown) are given. In Fig. 5.11(a), two major reflections are observed, corresponding to the interface flanges at the measurement port and at the matched load. In Fig. 5.11(b), three major reflections are observed, corresponding to the flange interfaces at the two measurement ports and between the twists.

With reference to Fig. 5.11(a) and 5.11(b), the second reflected pulses arrive at 267 ps and 281 ps in the measurements and at 281 ps and 283 ps in the EM re-simulations, for the 3-D printed and COTS #1 twists, respectively. It should be noted that the previously calculated single-twist arrival time predictions are for a 31.75 mm thru line, using

Equation (2.18), which gives almost identical values with EM re-simulations for the 31.75 mm long twists. With reference to Fig. 5.11(b), the third reflected pulses arrive at 525 ps and 539 ps for the corresponding S_{11} and S_{22} measurements and at 553 ps and 565 ps in the EM re-simulations.

The slight discrepancy between measured and calculated/re-simulated results is due to mechanical compression of the 3-D printed twist in the longitudinal direction with our measurement setup. The reduction in the 3-D printed twist lengths, calculated using Equation (2.18) with the timings of the second pulses in Fig. 5.11(a) and 5.11(b), is approximately 1.6 mm (5.0%).

Overall, the 3-D printed twist has a better wave impedance match, when compared to COTS #1. With reference to Fig. 5.11(a), it can be seen that the 3-D printed twist has a worse wave impedance mismatch at Port 2, when compared to Port 1. Conversely, COTS #1 has a worse wave impedance mismatch at Port 1, when compared to Port 2.



(a)

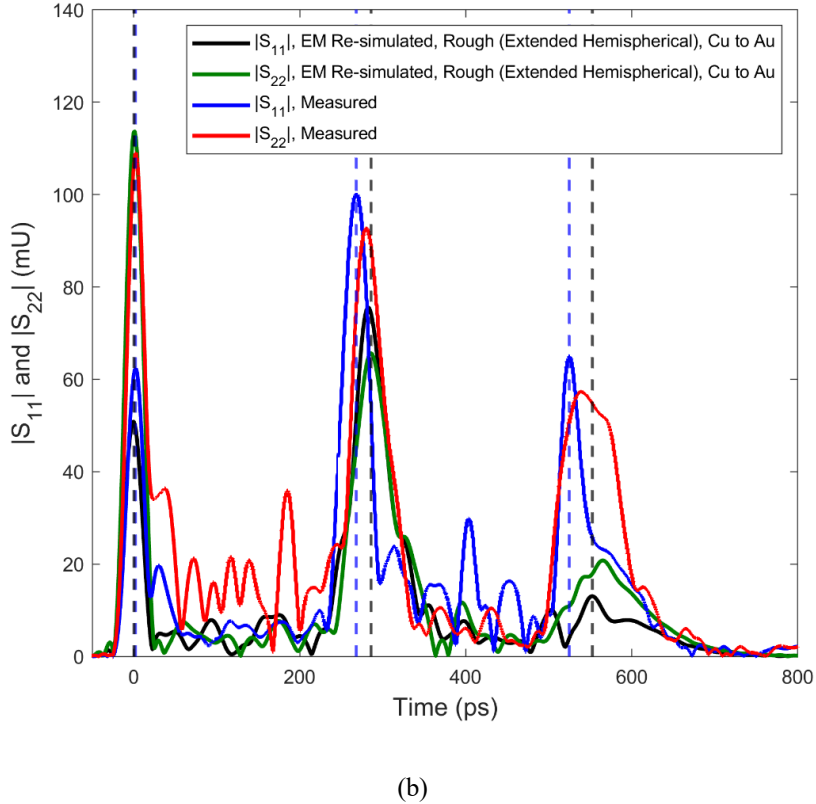


FIGURE 5.11: TDR measurements and EM re-simulations: (a) one-port for the 3-D printed and COTS #1 twists terminated with a VDI matched load; and (b) two-port for Cascade #1.

Between the main reflections, smaller pulses can also be seen in Fig. 5.11, both in the measurements and re-simulations. The latter are consistent in magnitude with both the 3-D printed and COTS #1 twists. These are believed to be due to distributed reflections from the twisting transition.

Moreover, these re-simulated smaller pulse amplitudes agree with those measured for the 3-D printed twist. However, the commercial twist exhibits significant smaller pulses, which are much greater in magnitude than those predicted through re-simulations. Since internal discontinuities are not included in the re-simulations, and also because of the short time intervals between the smaller pulses, it is believed that they are due to internal defects seen in the measured results. These may have occurred due to forced mechanical rotation during manufacture. Note that this cannot be verified without destructive visual inspection.

5.4 Conclusion

The 1st Gen. 90° twists were designed using a twisting symmetrical E-plane split. The worst-case return loss across G-band is 6.6 dB, which is exacerbated by assembly part misalignment, edge rounding, dimensional inaccuracy, and aperture height reduction inherent to the printing orientation. A significant up-shift in cut-off frequency is observed in the transmission response, from 116 GHz to 160 GHz, which is believed to be due to aperture width reduction within the twisting transition. Furthermore, above the measured cut-off frequency, the average insertion loss is 10.9 dB. This is due to EM radiation leakage from the split, which is exacerbated by edge rounding.

For the 4th Gen. twists, the trough-and-lid assembly, which was successfully employed to realize low-cost and low loss thru lines, was used to produce six 90° twists, all exhibiting a similar S-parameter performance. These are the first polymer-based 3-D printed 90° twists operating at above 110 GHz. A detailed analysis has been undertaken for one of these components. This design mitigates EM radiation leakage, while increasing the aperture width at the twisting transition to avoid cut-off frequency up-shifting.

The 3-D printed and COTS #1 90° twists exhibit commensurate quantitative worst-case return losses of 13.2 dB and 12.9 dB, respectively. Furthermore, from two-port measurements, both exhibit commensurate qualitative average insertion losses, being approximately 0.62 dB. Surface roughness modeling was again used to predict additional attenuation. The discrepancy between the insertion loss of EM simulations with roughness correction applied and that of Cascade #1 is due to dimensional inaccuracy and the large reflection from the inter-component connection. The retail cost of the measured COTS counterpart is a factor of $\times 8.5$ greater than the manufacturing cost of our ruggedized 3-D printed/plated 90° twist.

A detailed TDR analysis confirms that the flange-to-flange interfaces are the main source of reflections, with a qualitative comparison made between port wave impedance matching given. Similar to the thru line, when tightly fixed to the measurement setup, the 3-D printed twist is mechanically compressed in the longitudinal direction by approximately 1.6 mm (5.0%). TDR suggests that there is a significant return loss

contribution from internal defects in COTS #1, which cannot be verified without destructive visual inspection. This was not evident in 3-D printed twist.

As the dimensional accuracy and surface quality of MSLA 3-D printing improves, the S-parameter performance of trough-and-lid 90° twists is expected to improve.

5.5 References

- [1] R. Payapulli, L. Zhu, S.-H. Shin, M. Stanley, N. M. Ridler, and S. Lucyszyn, “Polymer-based 3-D printed 140 to 220 GHz metal waveguide thru lines, twist and filters,” *IEEE Access*, vol. 11, pp. 32272-32295, Mar. 2023.
- [2] Pasternack Enterprises Inc., “WR-5 90 Degree Right-hand Waveguide Twist,” 2022. Accessed: Jan. 07, 2023. [Online]. Available: <https://www.pasternack.com/wr-5-90-waveguide-twist-ug387mod-140-220-ghz-pew5tw0002-p.aspx>.
- [3] Fairview Microwave Inc., “WR-5 90 Degree Waveguide Right-hand Twist Using a UG-387/U-Mod Flange and a 140 GHz to 220 GHz Frequency Range,” 2022. Accessed: Jan. 07, 2023. [Online]. Available: <https://www.fairviewmicrowave.com/wr-5-90-waveguide-twist-ug387mod-140-220-ghz-fmw5tw0002-p.aspx>.
- [4] Hasco Components Inc., “Waveguide Section, 90 Degree Twist, 1-Inch Section, 140 GHz to 220 GHz, G-Band,” 2022. Accessed: Jan. 07, 2023. [Online]. Available: <https://www.hasco-inc.com/waveguide-components/wr-5-millimeter-waveguide-90-degree-twist-1-inch-section-140-ghz-to-220-ghz-g-band/>.

6. Design, Optimization, and Fabrication of MSLA-Printed G-band MPRWG BPFs

6.1 Introduction

A significant part of content in this chapter (i.e., Sections 6.3 and 6.4) is based on research articles by Shin et al., for which I was the 2nd author [1], and Payapulli et al. [2], which was published in *IEEE Access* in March 2023.

1st Gen. G-band symmetrical diaphragm inductive iris(SDII)-coupled BPFs, using an RF choke and a symmetrical E-plane split, are presented. The design specification is given by the allocated bands of scientific interest within G-band [3]. Here, the inherent design flaws of these components result in a poor performance; this is used to inform the subsequent designs. For the 4th Gen. components, the trough-and-lid assembly is employed, with transverse offset inductive irises (TOII) being initially used. Despite all components producing bandpass filter transmission responses, all TOII-coupled BPFs exhibit center frequency down-shifting, and the 150 GHz BPF exhibited severe passband distortion.

The main cause of frequency down-shifting and bandwidth-increasing is identified as iris corner rounding (ICR). Here, a systematic compensation procedure to correct these effects is presented. This is successfully applied to 4th Gen. SDII-coupled BPFs, with the design specification being a modification of that which was previously applied.

Measurements of the 1st Gen. BPFs and 4th Gen. TOII-coupled BPFs are presented, with a brief analysis of these results and the causes of additional insertion loss or frequency shifting. A more detailed analysis is given for the 4th Gen. SDII-coupled filter measurements, including the effects of ICR and its compensation.

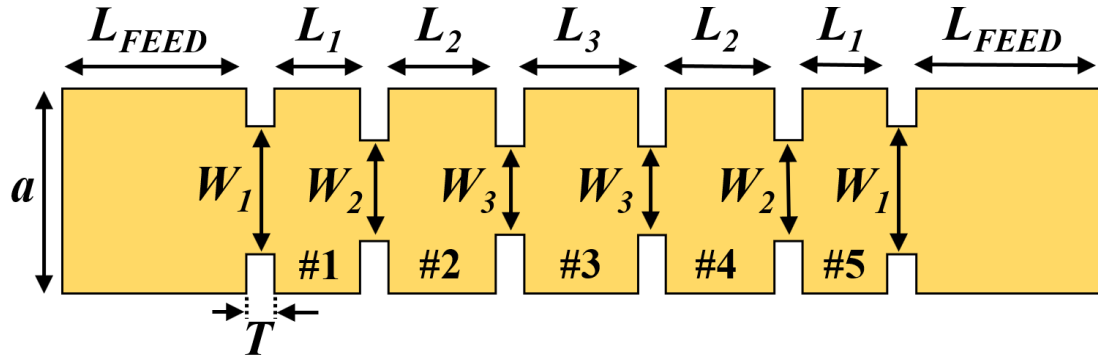
2nd and 3rd Gen. BPFs were not fabricated and measured. The former exhibited a poor S-parameter performance with proof-of-concept thru lines. The latter were 3-D printed but not plated or measured, which will be explained in Section 6.3.2.

6.2 Standard BPF Design Procedure

As explained in Chapter 3.3, a waveguide bandpass filter is constructed of coupled cavity resonators. The center frequency and bandwidth of the transmission passband are determined by the waveguide dimensions, as these determine the electrical lengths of the resonators, the inter-resonator coupling coefficients, and the external Q-factors (i.e., coupling to the input and output feed lengths).

An illustration of a 5th order symmetrical diaphragm inductive iris (SDII)-coupled waveguide BPF is shown in Fig. 6.1(a). Each resonator is labelled #*i* ($i \in [1, 2, 3, 4, 5]$). L_{FEED} is the length for both the input and output feed lines and L_i is the length of resonator #*i*, with symmetrical construction such that $L_1 = L_5$ and $L_2 = L_4$. The aperture width of the *j*th iris is denoted by W_j ($j \in [1, 2, 3, 4, 5, 6]$), with $W_1 = W_6$, $W_2 = W_5$, and $W_3 = W_4$.

Furthermore, an illustration of a 5th order transverse offset inductive iris (TOII)-coupled waveguide BPF is shown in Fig. 6.1(b), with variables retaining the same meaning as from Fig. 6.1(a). As illustrated here, the TOIIs are realized by connecting cavity resonators together with an offset in the *x*-direction.



(a)

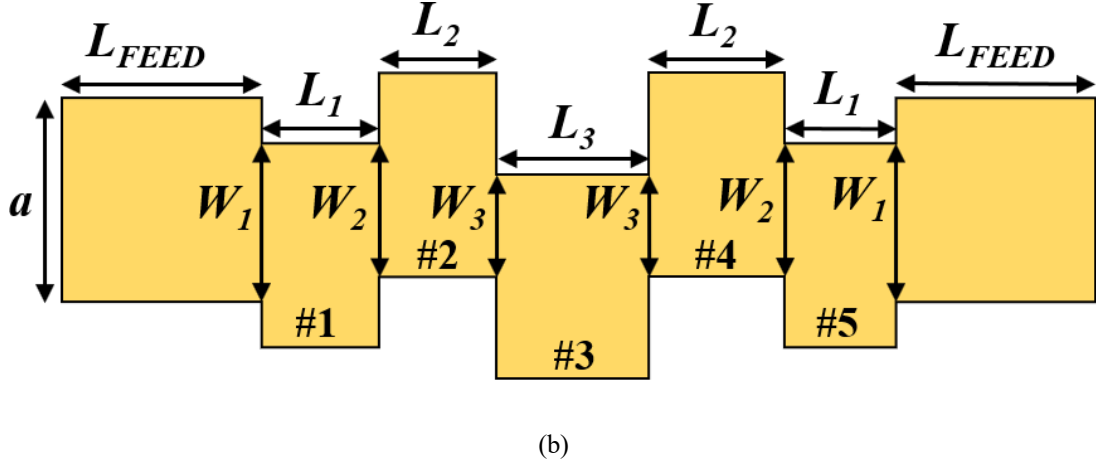


FIGURE 6.1: Plan view illustration of a symmetrical 5th order waveguide BPF, showing ideal rectangular geometries: (a) SDII-coupled; (b) TOII-coupled.

The cavity resonator lengths and iris aperture widths for both designs are obtained by calculating the external quality factors Q_{e1} , Q_{eN} and inter-resonator coupling coefficients $M_{k,k+1}$ (for $k = 1, \dots, N - 1$), which can be achieved for an N^{th} order BPF [4]. The normalized quantities are given by [4]:

$$q_{e1} = g_0 \cdot g_1, \quad q_{eN} = g_N \cdot g_{N+1}, \quad m_{k,k+1} = \frac{1}{\sqrt{g_k \cdot g_{k+1}}} \quad (6.1)$$

where g_0 , g_1 , ..., g_{N+1} are referred to as the lowpass prototype elements. For Butterworth filters, these are given by [5]:

$$g_0 = g_{N+1} = 1, \quad g_k = 2 \sin \left[\frac{(2k-1)\pi}{2n} \right] \quad (\text{for } k = 1, \dots, N - 1) \quad (6.2)$$

For Chebyshev filters, these are given by [5]:

$$g_0 = 1, \quad g_1 = \frac{2a_1}{\gamma}, \quad g_k = \frac{4a_{k-1}a_k}{b_{k-1}g_{k-1}} \quad (\text{for } k = 2, \dots, N)$$

$$g_{N+1} = \begin{cases} 1 & \text{for } N \text{ odd} \\ \coth^2 \left(\frac{\beta}{4} \right) & \text{for } N \text{ even} \end{cases} \quad (6.3)$$

where $a_k = \sin \left[\frac{(2k-1)\pi}{2n} \right]$ and $b_k = \gamma^2 + \sin^2 \left[\frac{k\pi}{n} \right]$ (for $k = 1, \dots, N$), $\gamma = \sinh \left[\frac{\beta}{2n} \right]$,

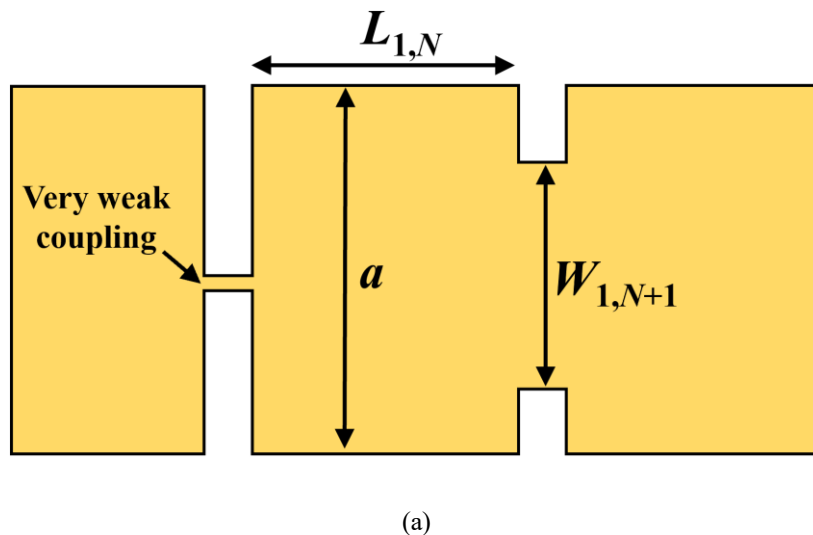
$\beta = \ln \left[\coth \left(\frac{L_{AR}}{17.37} \right) \right]$, and L_{AR} is the ripple level of the Chebyshev filter.

The external Q-factors and inter-resonator coupling coefficients are then denormalized, as given below [5]:

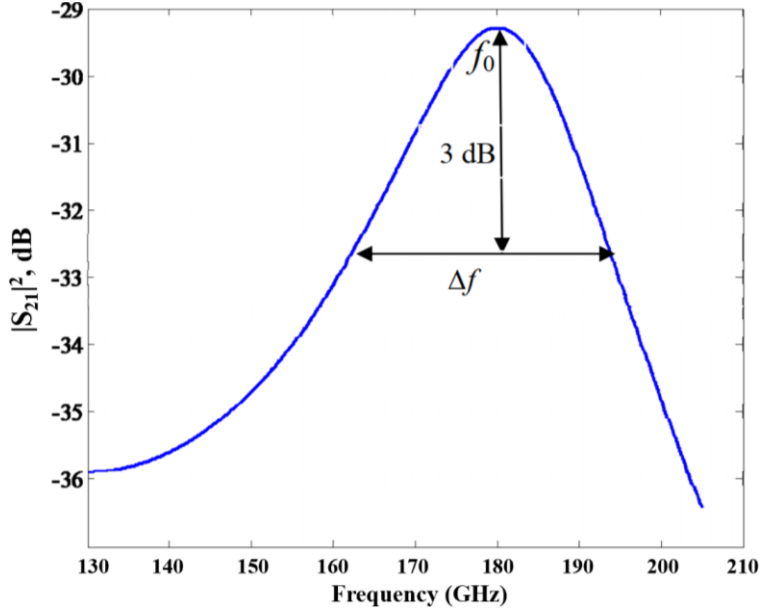
$$Q_{e1} = \frac{q_{e1}}{FBW}, \quad Q_{eN} = \frac{q_{eN}}{FBW}, \quad M_{k,k+1} = FBW \cdot m_{k,k+1} \quad (6.4)$$

where $FBW = f_0/BW$ is the fractional bandwidth, f_0 is the filter's center frequency, and BW is the filter's 3-dB bandwidth.

The physical dimensions of the input and output resonator lengths and iris aperture widths are calculated by simulating the waveguide resonator structure shown in Fig. 6.2(a). Here, the resonator is very weakly coupled to the left hand side, such that the predominant effect on the transmission response comes from the coupling to the right hand side. The cavity resonator length $L_{1,N}$ and iris aperture width $W_{1,N+1}$ are varying using parametric sweeps until the center frequency of the transmission plot is at the specified filter center frequency and the Q-factor of the resonator is equal to the calculated external Q-factors: $\frac{f_0}{\Delta f} = Q_{e1,N}$. The transmission response is shown in Fig. 6.2(b).



(a)



(b)

FIGURE 6.2: EM simulations for obtaining input/output resonator and iris dimensions: (a) plan view of simulated structure; and (b) transmission results, showing center frequency and 3-dB bandwidth.

Figure 6.3(a) shows an illustration of the simulated structure for the calculation of the internal resonator lengths and iris aperture widths. Starting with the input and output cavity resonator connections, with the lengths L_1 and L_N determined from the previous step, parametric sweeps are performed on the lengths L_2 and L_{N-1} and the widths W_2 and W_N . The resulting transmission results, shown in Fig. 6.3(b), should exhibit two resonance frequencies f_1 and f_2 . These frequencies are varied until the following relationships are satisfied [5]:

$$\frac{f_2^2 - f_1^2}{f_2^2 + f_1^2} = M_{k,k+1} \quad (\text{for } k = 1, \dots, N-1) \quad (6.4a)$$

$$\frac{f_1 + f_2}{2} = f_0 \quad (6.4b)$$

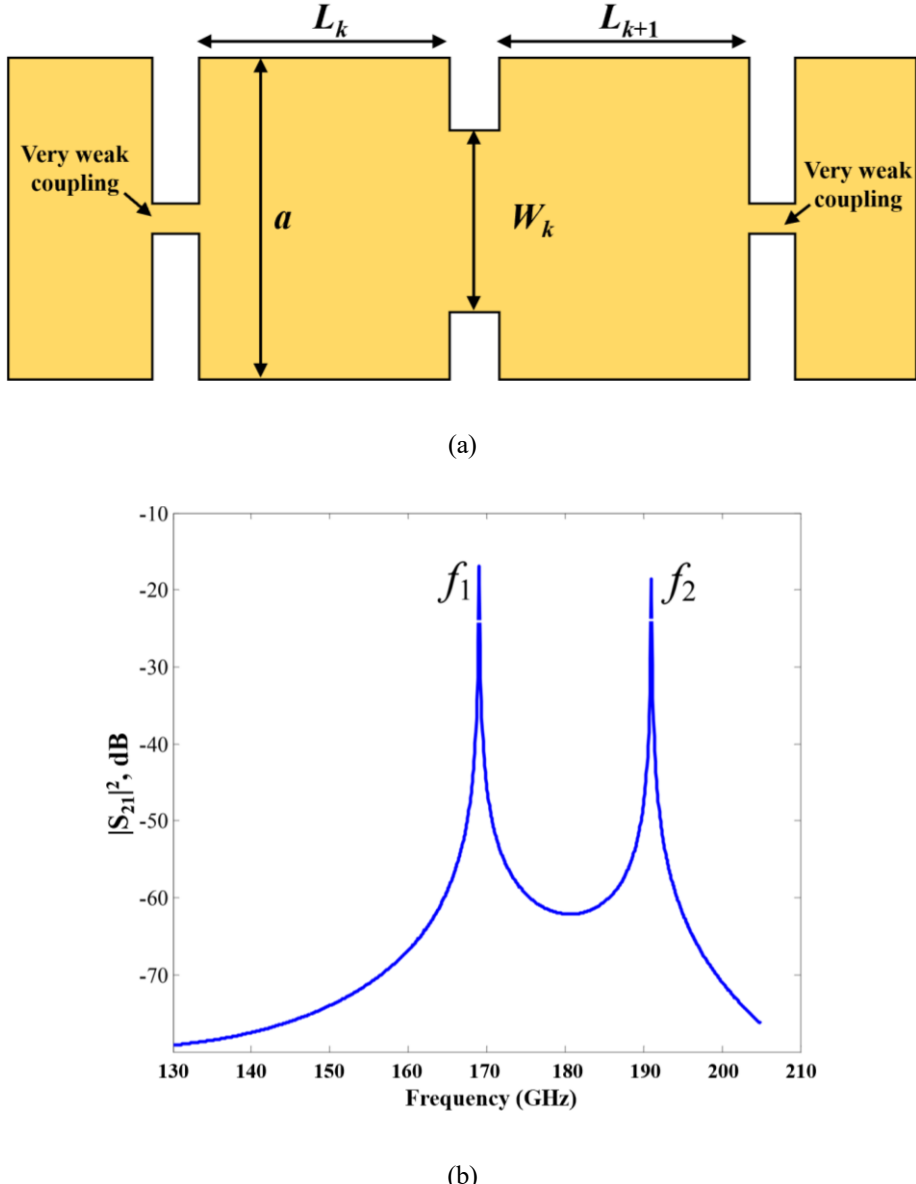


FIGURE 6.3: EM simulations for obtaining internal resonator and iris dimensions: (a) plan view of simulated structure; and (b) transmission results, showing two resonance frequencies.

This step is repeated for the next resonator cascade combination, with the lengths of L_2 and L_{N-1} obtained from the previous repetition. This is continued until all cavity resonator lengths and iris aperture widths are obtained. A final tuning and optimization can be conducted in HFSS to better match the ideal filter specifications.

To obtain the resonator lengths and iris aperture widths for a TOII-coupled BPF, these

simulations must be undertaken using TOII-coupling for the waveguide structures shown in Figs. 6.2(a) and 6.3(b).

The unloaded Q-factor $Q_{u,\text{TE}101}$ for an air-filled rectangular TE_{101} mode cavity resonator with width a and height b , assuming negligible dielectric losses, is given by [6]:

$$Q_{u,\text{TE}101} = \frac{\pi\eta_0}{4R_s} \left[\frac{2b(a^2+l^2)^{\frac{3}{2}}}{al(a^2+l^2)+2b(a^3+l^3)} \right] \quad (6.5)$$

where $\eta_0 = \sqrt{\frac{\mu_0}{\epsilon_0}}$ is the intrinsic impedance of air, $R_s = \sqrt{\frac{\omega\mu_0}{2\sigma_0}}$ is the classical surface resistance of the metal sidewalls, σ_0 is the DC bulk conductivity of the sidewalls, and l is the length of the cavity.

For smooth copper with $\sigma_0|_{Smooth} = 5.8 \times 10^7$ S/m, we obtain a value of $Q_{u,\text{TE}101}|_{Smooth} \cong 2000$, with relatively insignificant variation across G-band. The effective DC bulk conductivity of the rough electroplated copper on 4th Gen. components is $\sigma_0|_{Rough} = 3.4 \times 10^7$ S/m, with $K \cong 1.3$ using the Hemispherical model as discussed in Chapter 7. From this, we obtain a value of $Q_{u,\text{TE}101}|_{Rough} \cong 1500$, again with relatively insignificant variation across G-band.

6.3 1st Generation

6.3.1 Design

The structural design of the 1st Gen. split-block MRPWGs is presented in Chapter 4.2.1, employing a deviating symmetrical E-plane split and an RF choke. For these BPFs, all irises have a thickness $T = 400 \mu\text{m}$.

These waveguide BPFs employ a Chebyshev (Type I) approximation design, due to their steeper transition band roll-off and superior stop-band rejection characteristics when compared to Butterworth approximation filters.

With a view to applying these BPFs to radiometer front-end subsystems, the design

specification was based on the allocated frequency bands of scientific interest for satellite-based passive remote sensing, as determined by the World Meteorological Organization (WMO) and the International Telecommunications Union (ITU) [3]. Three BPFs are designed to exactly comply with the allocated bands given in Table 6.1.

TABLE 6.1: Allocated frequency bands of scientific interest for satellite passive remote sensing within G-band (140 to 220 GHz) [3].

Center frequency (GHz)	Allocated Bandwidth (GHz)	Primary Earth observation measurements
150	2.5	N ₂ O, Earth surface temperature, cloud parameters, reference window for temperature soundings
183.3	17	N ₂ O, Water vapor profiling, O ₃
204.5	9	N ₂ O, ClO, water vapor, O ₃

The ideal linear BPF dimensions (i.e., cavity resonators lengths and iris aperture widths) are calculated using standard textbook filter synthesis explained in Chapter 6.2, with minor tuning undertaken in HFSS. Note that Chebyshev BPF upper and lower passband edge frequencies, and consequently the bandwidth, are defined by the 20 dB return loss edge frequencies (not the 3 dB additional insertion loss frequencies).

A feed length $L_{FEED} \approx \lambda_{gL}/2$ is used; this would exactly correspond to lengths of 1.57 mm, 1.06 mm, and 0.89 mm for the 150 GHz, 183.3 GHz, and 204.5 GHz BPFs, respectively. Here, we use $L_{FEED} = 1.638$ mm, 1.221 mm, and 0.980 mm, giving respective flange-to-flange lengths of exactly 12 mm, 8 mm, and 7.5 mm for the 150 GHz, 183.3 GHz, and 204.5 GHz BPFs. All linear BPF dimensions are given in Table 6.2.

Note that EM simulations using these dimensions approximate the ideal Chebyshev filter, but are not in exact agreement, as this would require a more accurate synthesis process.

TABLE 6.2: Ideal designed linear BPF dimensions for the SDII-coupled 150 GHz, 183.3 GHz, and 204.5 GHz BPFs, with bandwidths of 2.5 GHz, 17 GHz, and 9 GHz, respectively.

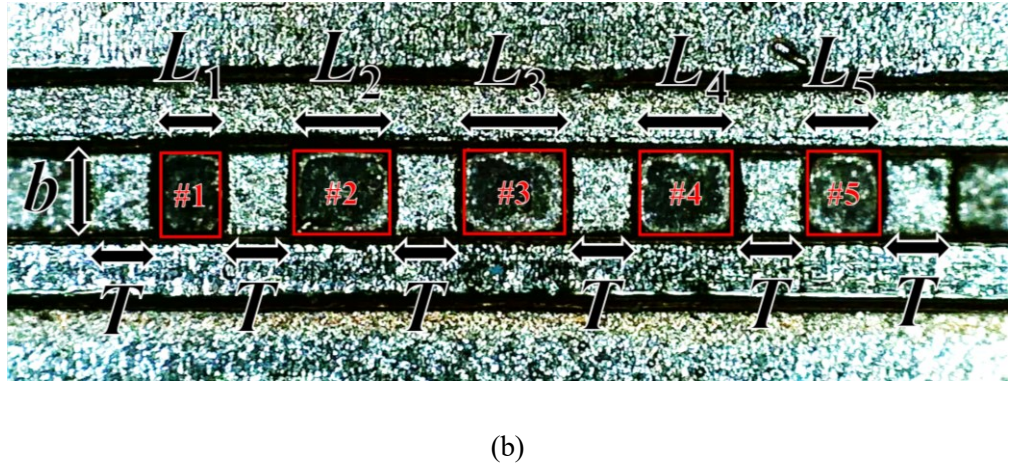
Linear BPF Dimensions	Ideal Designed Dimensions (μm)		
	$f_0 = 150 \text{ GHz}$	$f_0 = 183.3 \text{ GHz}$	$f_0 = 204.5 \text{ GHz}$
L_{FEED}	1,638	1,221	980
L_1	1,156	531	544
L_2	1,331	688	678
L_3	1,350	721	697
W_1	851	889	730
W_2	639	729	569
W_3	600	686	533
T	400	400	400

6.3.2 Fabrication

As with all 1st Gen. components, the Elegoo Mars printer was used for fabrication, with the Elegoo Water Washable Rapid Resin (Ceramic Grey), and with metalization outsourced to a commercial service provider (50 μm plating thickness, with 35 μm in the channel). The printing time was 1h20m per component. Only one components was manufactured for each BPF. The orientation of each part on the printer's build plate in Chitubox is the same as that given in Fig. 4.10. The full component and internal geometry is shown in Fig. 6.4.



(a)



(b)

FIGURE 6.4: 3-D printed and copper electroplated 5th order Chebyshev SDII-coupled BPFs: (a) full component; and (b) microphotograph of the internal structure for one split-block part of the 183.3 GHz exemplar, with key linear BPF dimensions labelled and feed lengths omitted; red rectangles highlight the peripheries of the cavities.

Note that, as the split is E-plane symmetrical, Fig. 6.4 is a view of the channel's narrow sidewall; cavity resonator lengths are visible, but iris aperture widths are not.

6.3.3 Measurements

Figure 6.5 shows the S-parameter responses for the 150 GHz BPF, showing EM simulated and measured results.

It can be seen that bandpass filtering is not achieved, as there is no transmission passband. This can be attributed to the very narrow designed fractional bandwidth of 1.7%, to agree with the specification given in Table 6.1. To achieve a good bandpass filter response, the chosen manufacturing technology would require very strict dimensional tolerances to achieve excellent accuracy in the linear BPF dimensions, in addition to minimal geometric inaccuracy (e.g., negligible iris corner rounding). An example of such a technology would be high accuracy CNC machining. Furthermore, from Table 1.3, it can be seen that this designed fractional bandwidth is significantly lower than any reported 3-D printed BPFs. Therefore, with the current state of polymer-based 3-D printing technology, it is not possible to produce a BPF for the WMO-ITU allocated frequency band at 150 GHz.

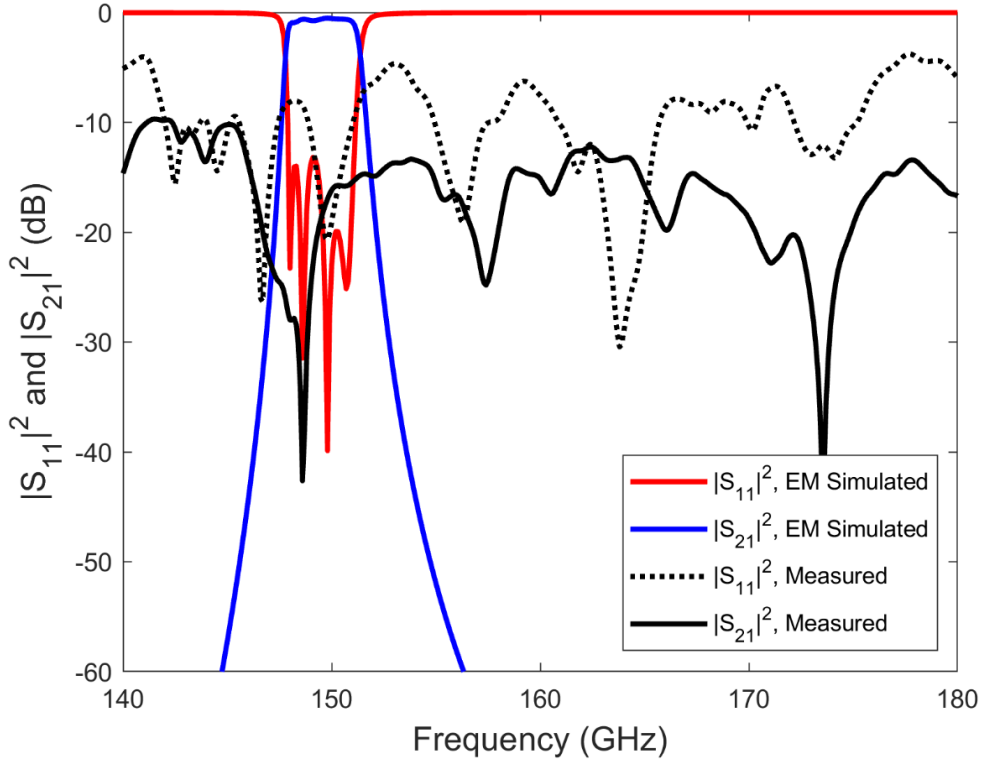


FIGURE 6.5: EM simulated and measured two-port S-parameter G-band responses for the 1st Gen. SDII-coupled 150 GHz BPF.

Figure 6.6 shows the S-parameter responses for the 183.3 GHz BPF, showing EM simulated and measured results. In contrast to the 150 GHz filter, an observable bandpass filter transmission response is obtained. However, due to significant EM radiation leakage, there is a very high insertion loss. The cause of this leakage was explained in Chapter 4.2.3 (i.e., a physical gap at the split between the two assembly parts, which was exacerbated by the RF choke and deviating split).

The minimum measured insertion loss is 6.8 dB at 189.3 GHz. The measured center frequency is 190 GHz, corresponding to an up-shift of 6 GHz, with a 3 dB bandwidth of 13.4 GHz. Passband frequency shifting can be explained by manufacturing inaccuracies. A detailed analysis is omitted for these measurements, but has been provided for the 4th Gen. SDII-coupled BPFs.

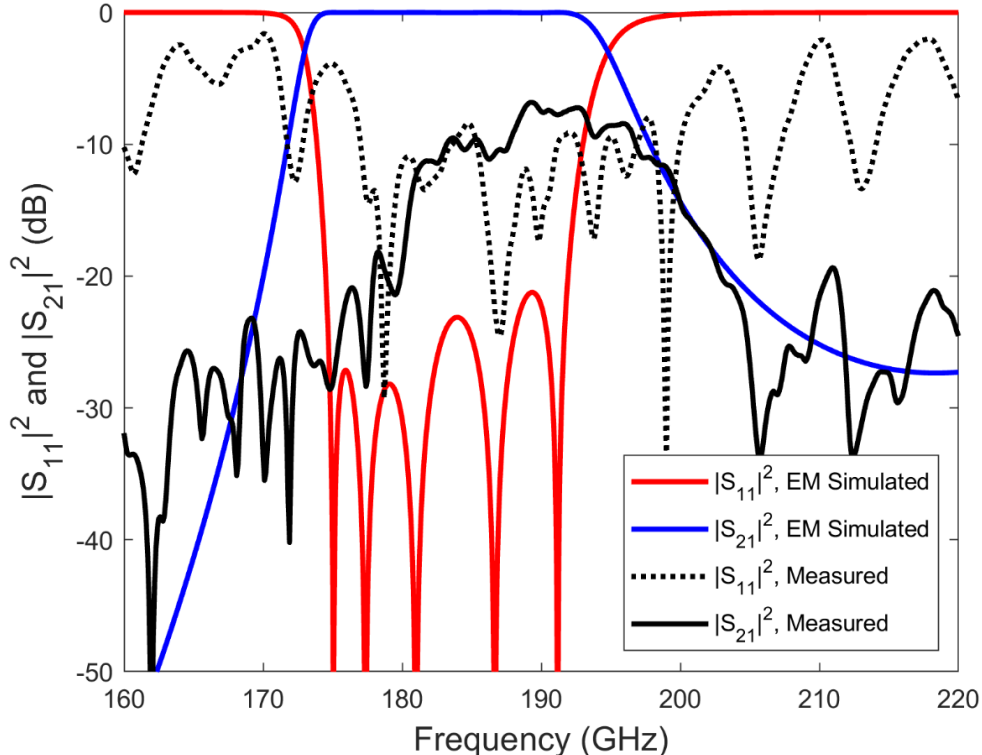


FIGURE 6.6: EM simulated and measured two-port S-parameter G-band responses for the 1st Gen. SDII-coupled 183.3 GHz BPF.

Figure 6.7 shows the S-parameter responses for the 204.5 GHz BPF, showing EM simulated and measured results. Again, despite there being an observable bandpass filter transmission response, there is a very high insertion loss due to EM radiation leakage.

The minimum measured insertion loss is 7.0 dB at 200.7 GHz. The measured center frequency is 204.5 GHz, giving a center frequency shift of 0.0 GHz, with a 3 dB bandwidth of 14.8 GHz.

In summary, for the production of low-cost and low loss BPFs, significant improvements in the mitigation of EM radiation leakage and passband frequency shifting must be made. Moreover, the 150 GHz filter specifications must be relaxed, with a higher fractional bandwidth.

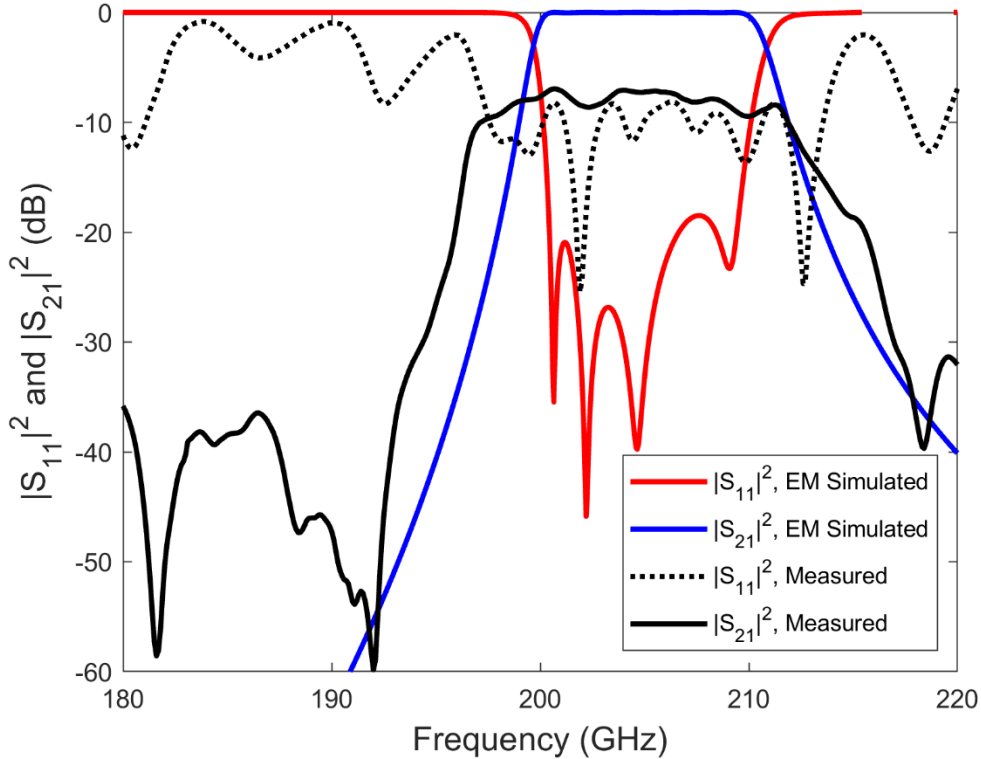


FIGURE 6.7: EM simulated and measured two-port S-parameter G-band responses for the 1st Gen. SDII-coupled 204.5 GHz BPF.

6.4 4th Generation TOII-coupled BPFs

6.4.1 Design

All 4th Gen. components employ the trough-and-lid assembly, which has demonstrated low-cost and low loss thru lines and 90° twists. The H-plane *a*-edge split provides a complete internal plan view of the trough, enabling the detection of visual defects and allowing dimensional characterization. This is not possible with a symmetrical E-plane split or single-block designs, with non-destructive testing.

Similar to the 1st Gen. BPFs, three filters are initially designed, manufactured, and measured, with center frequencies of 150 GHz, 183.3 GHz, and 204.5 GHz. The latter two maintain the same bandwidths that were previously employed. The specification of the 150 GHz BPF is relaxed by increasing the bandwidth to 6 GHz. This gives $Q_L = 25$

(a reduction) and $FBW = 4\%$ (an increase); this is approximately equal to the previous 204.5 GHz filter, which exhibited a bandpass filter transmission response.

For these filters, transverse offset inductive irises (TOIIs) are employed to couple adjacent rectangular TE_{101} mode cavity resonators together; an illustration of a 5th order TOII-coupled waveguide BPF was given in Fig. 6.1(b).

The advantage of this design is that the 3-D printing of thin and potentially fragile SDIIs is avoided. This simplifies post-processing, which should result in less edge and corner rounding. Moreover, the dimensional inaccuracies of these small features will exacerbate frequency shifting.

As mentioned previously, waveguide BPFs typically use a Chebyshev (Type I) approximation design. However, these are more sensitive to manufacturing accuracy limitations than Butterworth approximation filters, as their return loss zeros should be precisely distributed across the passband. Indeed, this was confirmed by the relatively poor passband transmission response of ICL's G-band Chebyshev BPF [7] and all filters from Chapter 6.2. Therefore, Butterworth approximation designs are employed here, having all return loss zeros located at the center frequency. Note that, for Butterworth BPFs, the passband edge frequencies are defined at the 3 dB additional insertion loss points (thus giving a 3 dB bandwidth).

Again, the ideal linear BPF dimensions are calculated using the standard textbook filter synthesis, with minor tuning performed in HFSS. An arbitrary feed length $L_{FEED} \approx 1.5$ mm is used, which is slightly greater than $\lambda_{gL}/2$ for each center frequency. This gives respective flange-to-flange lengths of 10.4 mm, 7.4 mm and 7.1 mm for the 155 GHz, 175 GHz, and 200 GHz BPFs. Note that the two fabricated thru lines have the same flange-to-flange lengths as the 150 GHz and 183.3 GHz BPFs, to establish a baseline insertion loss for comparison. A 7.1 mm thru line was not fabricated, as its performance would be similar to that of the 7.4 mm exemplar. The final linear BPF dimensions are given in Table 6.3. Note that EM simulations using these dimensions approximate the design specification, but are not in exact agreement.

TABLE 6.3: Ideal designed linear BPF dimensions for the TOII-coupled 150 GHz, 183.3 GHz, and 204.5 GHz BPFs, with bandwidths of 6 GHz, 17 GHz, and 9 GHz, respectively.

Linear BPF Dimensions	Ideal Designed Dimensions (μm)		
	$f_0 = 150 \text{ GHz}$	$f_0 = 183.3 \text{ GHz}$	$f_0 = 204.5 \text{ GHz}$
L_{FEED}	1,732	1,518	1,524
L_1	1,274	765	745
L_2	1,453	932	850
L_3	1,483	971	862
W_1	888	890	695
W_2	664	670	480
W_3	587	570	420

6.4.2 Fabrication

For all 4th Gen. BPF components, Elegoo Mars 2 Pro was used for 3-D printing, with the Elegoo Water Washable Rapid Resin (Ceramic Grey). The orientation of each part on the printer's build plate in Chitubox, is exactly the same as that of all thru lines (i.e., with the broad wall parallel to the build plate). For brevity, this figure is omitted here.

Though the LCD pixel size of this 3-D printer is slightly larger than that of the previous Elegoo Mars model, which was used for all 3rd Gen. components, manufacturing accuracy is significantly improved. This is shown in Fig. 6.8.

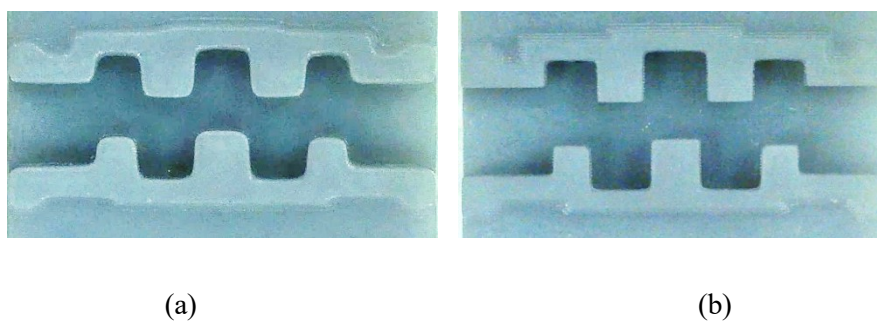


FIGURE 6.8: Comparison between different Generations of 3-D printed transverse offset inductive iris-coupled (TOII) BPFs (before plating, bottom parts only): (a) 3rd Gen., using the Elegoo Mars; and (b) 4th Gen., using the Elegoo Mars 2 Pro.

Iris corner rounding, edge rounding, and non-horizontal/vertical sidewalls are observed with the older printer, with these being significantly reduced in the newer model. This is due to a sturdier construction and an upgraded LCD screen in the newer model, though degradation of mechanical components and of the LCD screen for the older model also influence these inaccuracies.

Metalization is undertaken using the same commercial copper electroplating process as with all 4th Gen. components, accounting for a 35 μm plating thickness within the trough when using the standard 50 μm process. Two components each were printed for each BPF, with measurements of the marginally better performing components presented.

The internal waveguide features for the mid-band 183.3 GHz TOII-coupled BPF is shown in Fig. 6.9 (with feed lengths omitted). Images of the other filters are omitted, for brevity. Post-assembly cross-sectional distortion was negligible; this is likely to be due to the TOIIs providing lateral reinforcement.

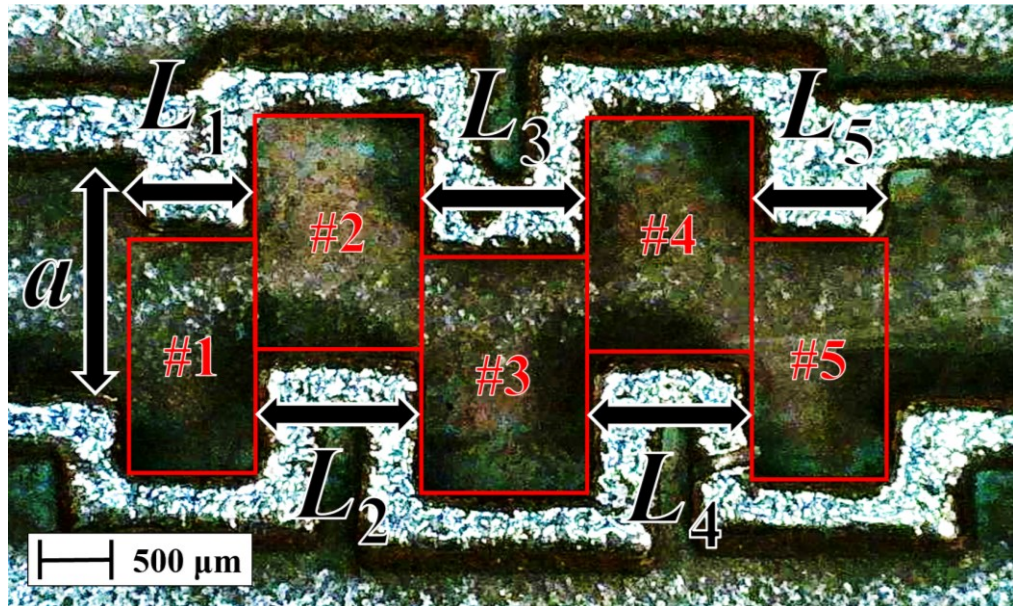


FIGURE 6.9: Plan view microphotograph of the internal structure for a 3-D printed and copper electroplated 5th order Butterworth 183.3 GHz TOII-coupled BPF, with cavity resonators labelled and feed lengths omitted. Red rectangles highlight the peripheries of the cavities.

Note that the H-plane a -edge split now enables a clear plan view of the channel, including cavity resonator lengths and iris aperture widths.

A cost comparison for G-band BPFs are not included, as these components have bespoke specifications that require a quote from the manufacturer.

6.4.3 Measurements

Figure 6.10 shows the S-parameter responses for the 150 GHz BPF, showing EM simulated and measured results. EM re-simulations, which use the real linear BPF dimensions, ICR, and surface roughness modelling, are not included here. These will be included for the 4th Gen. SDII-coupled BPFs. It can be seen that the BPF almost preserves the typical Butterworth approximation, having the characteristic mid-band single return loss zero. However, severe passband distortion is evident.

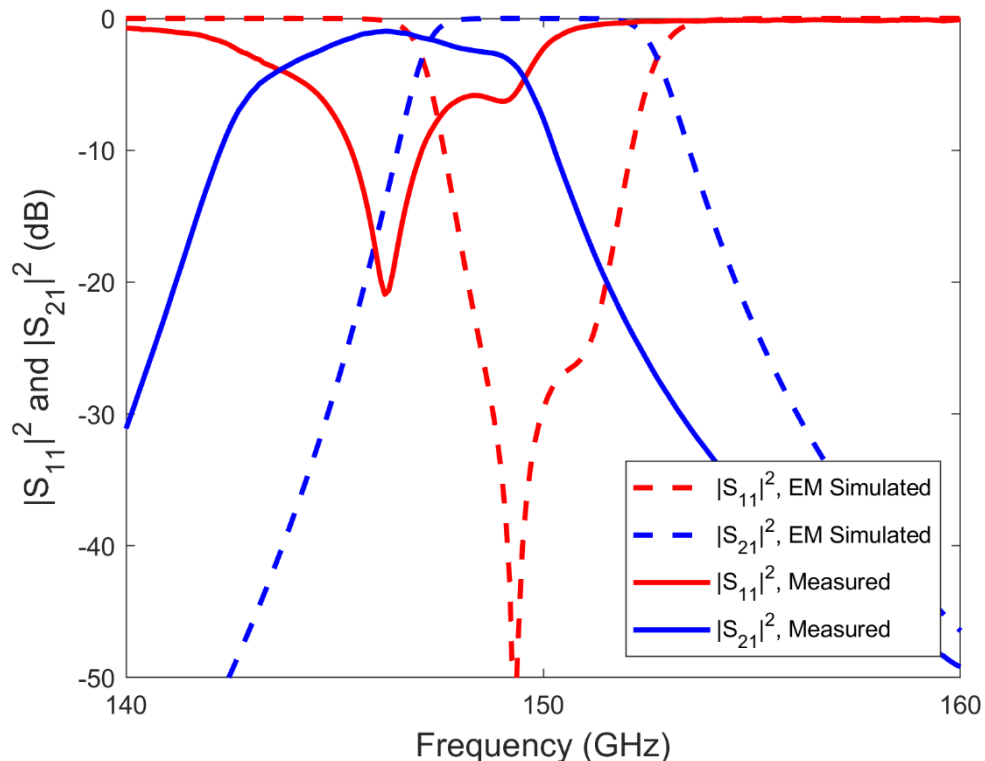


FIGURE 6.10: EM simulated and measured two-port S-parameter G-band response for the 7.4 mm long TOII-coupled 150 GHz BPF.

Insertion loss degradation within the passband is due to resonator detuning, as this also distorts the reflection response such that the filter's return loss zeroes (situated at the center frequencies of each resonator) will not be situated precisely at the overall BPF center frequency.

The minimum measured insertion loss is 1.0 dB at 146.2 GHz. The measured center frequency is 146.5 GHz, corresponding to a down-shift of 2.3% (3.5 GHz). The measured 3 dB bandwidth is 5.8 GHz, corresponding to a decrease of 3.3% (0.2 GHz), and thereby increasing Q_L from the target value of 25 to the measured value of 25.3.

Again, passband frequency shifting and distortion can be explained by manufacturing inaccuracies, of which the two primary types are the discrepancies between the ideal and real linear BPF dimensions and ICR, with compensation not being applied to these filters. Due to a lack of available time, a detailed analysis is omitted for these measurements, but is provided for the 4th Gen. SDII-coupled BPFs in Chapter 6.4.3.

Figure 6.11 shows the S-parameter responses for the 183.3 GHz BPF, showing EM simulated and measured results.

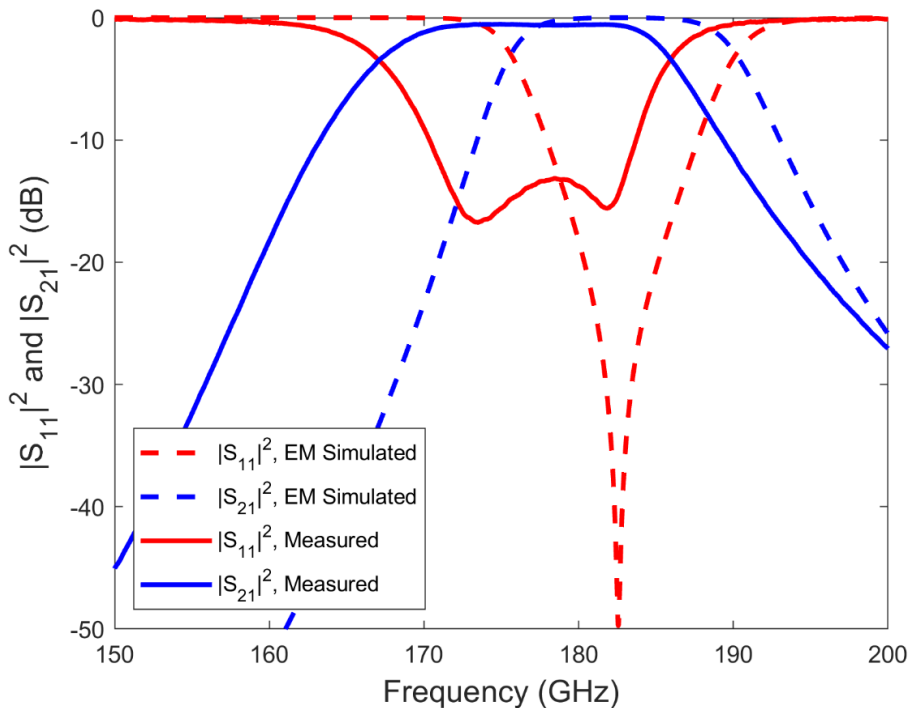


FIGURE 6.11: EM simulated and measured two-port S-parameter G-band response for the 7.4 mm long TOII-coupled 183.3 GHz BPF.

It can be seen that the typical Butterworth approximation is not preserved. Nevertheless, bandpass filtering is achieved, with a relatively undistorted passband transmission response due to the higher fractional bandwidth (9.3%) when compared to the 150 GHz BPF.

The minimum measured insertion loss is 0.5 dB at 174.9 GHz. The measured center frequency is 176.6 GHz, corresponding to a down-shift of 3.7% (6.8 GHz). The measured 3 dB bandwidth is 19 GHz, corresponding to an increase of 3.3% (2 GHz), and thereby decreasing Q_L from the target value of 10.8 to the measured value of 9.3.

As ICR is known to cause down-shifting, and has not been compensated for here, this suggests that it is a factor in the observed frequency shifting. Another potential factor is reduced resonator lengths and wider iris aperture widths.

Figure 6.12 shows the S-parameter responses for the 204.5 GHz BPF, showing EM simulated and measured results.

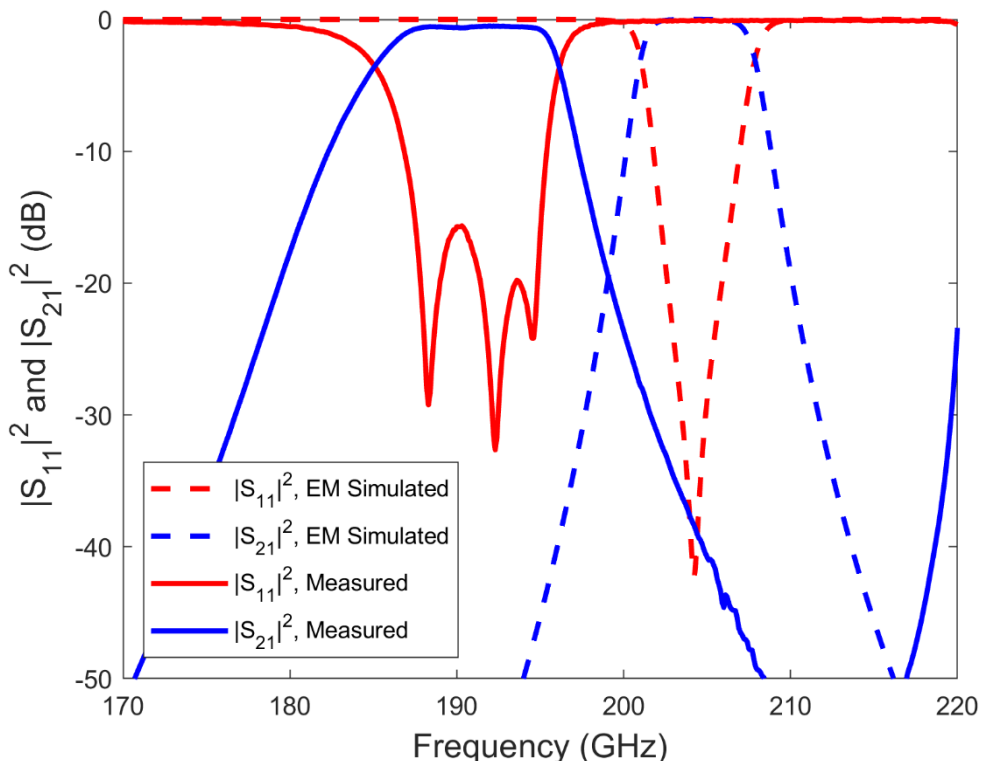


FIGURE 6.12: EM simulated and measured two-port S-parameter G-band response for the 7.1 mm long TOII-coupled 204.5 GHz BPF.

It can be seen that the typical Butterworth approximation is not preserved. Nevertheless, bandpass filtering is achieved, with a relatively undistorted passband transmission response.

The minimum measured insertion loss is 0.5 dB at 192 GHz. The measured center frequency is 190.6 GHz, corresponding to a down-shift of 6.8% (13.9 GHz). The measured 3 dB bandwidth is 11.0 GHz, corresponding to an increase of 22.2% (2 GHz), and thereby decreasing Q_L from the target value of 22.7 to the measured value of 17.3.

This is a significant passband frequency shift, which would be due to the aforementioned manufacturing inaccuracies.

In summary, despite producing two successful G-band BPFs, mechanical inaccuracies leading to resonator detuning have resulted in center frequency down-shifting and bandwidth increasing. As this has occurred for all filters, it is likely to be the result of a systematic error; ICR is believed to be one of the causes, as this occurs on all printed and plated parts and was not compensated for here. Linear BPF dimensions must also be reasonably accurate.

The components in this section were briefly presented in a separate research article in *IEEE Access* [1], without a detailed discussion or analysis.

6.5 4th Generation SDII-coupled BPFs

6.5.1 Design

A second batch of 4th Gen. BPFs were designed, with the specifications relaxed such that all BPFs have $FBW = 10\%$, which is comparable to previous successful BPFs. The 150 GHz and 204.5 GHz center frequencies are shifted to 155 GHz and 200 GHz, respectively, such that their EM simulations exhibit at least 20 dB insertion loss at the G-band edge frequencies. The 183.3 GHz center frequency is shifted to 175 GHz, such that its passband approximately bisects that of the two other filters. This gives 3 dB bandwidths of 15.5

GHz, 17.5 GHz, and 20 GHz for the BPFs centered at 155 GHz, 175 GHz, and 200 GHz, respectively. Further improvements to the accuracy of MSLA technology must be made before BPFs with narrower fractional bandwidths can be realized at G-band, enabling compliance with WMO-ITU allocated frequency bands [3].

For this second batch, SDIIs are employed to couple adjacent rectangular TE₁₀₁ mode cavity resonators together. This was to contrast with our research group's TOII-coupled Chebyshev and chained-function filters [7], which were being manufactured concurrently. As SDII-coupling is the conventional waveguide BPF implementation, this would demonstrate that our trough-and-lid assembly solution enables standard designs at G-band, thus avoiding the need to discover novel solutions. An illustration of the internal geometry was given in Fig. 6.1, with symmetry. For these 4th Gen. BPFs, all SDIIs have a thickness $T = 270 \mu\text{m}$.

Moreover, further investigation is undertaken into the frequency shifting effects of manufacturing inaccuracies. First, linear BPF dimensions are measured after printing, with more accurate parts being chosen for plating. Systematic errors in linear BPF dimensions are not compensated for; this is the subject of a separate research article, which introduced a pre-distortion technique for pixel quantization in MSLA-printing [7]. Instead, iris corner rounding (ICR) is investigated.

As before, the first design step is to calculate the ideal linear BPF dimensions using the standard textbook filter synthesis, with minor tuning performed in HFSS. Respective flange-to-flange lengths of 10.4 mm, 7.4 mm and 7.1 mm are used for the 155 GHz, 175 GHz, and 200 GHz BPFs, to enable a direct insertion loss comparison with the previous TOII-coupled BPFs.

The second design step is to characterize all forms of geometrical inaccuracy, which are evident on 3-D printed parts as different types of corner rounding, as illustrated in Fig. 6.13. Rounding at the bottom and top of the trough or iris is referred to here as floor and ceiling rounding, respectively. However, EM simulations have shown that both these types of rounding exhibit a negligible influence on passband performance. Moreover, negligible floor rounding is found in practice.

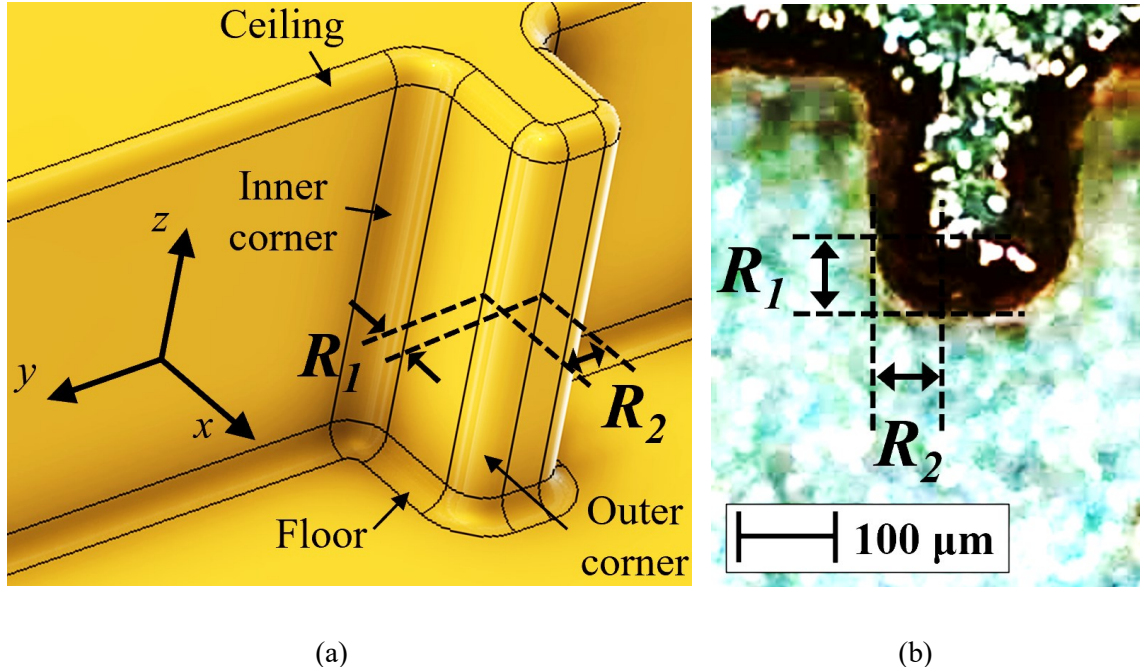


FIGURE 6.13: All types of rounding occurring on an SDII: (a) CAD isometric representation; and (b) 3-D printed and copper electroplated, plan view microphotograph.

However, ceiling rounding is significant, due to erosion during post-print cleaning. As shown in Fig. 6.13(b), significant ceiling rounding does not reflect the incident light (projected from an elevated position) and is observed as a dark rim.

Only inner and outer ICR is considered. The former results from an excess resin residue, due to insufficient post-print cleaning. The latter is mainly due to erosion during post-print cleaning, prior to full UV curing, as well as pixelation and UV light dispersion. Rounding radii are best measured at the mid-point of the internal sidewalls, to avoid any contributions from the floor and ceiling rounding. Iris corner rounding is found to be elliptical, rather than circular, giving two ICR radii per corner (R_1 and R_2), as illustrated in Fig. 6.13(b) for outer rounding. Similar variables can also be assigned to inner rounding, although their sizes will be approximately similar to the outer rounding. It has been found here, from preliminary printed and plated filter implementations (without any compensation), that the arithmetic mean value for all ICR radii $R \approx 100 \mu\text{m}$ for ten samples. As a result, this single value is used in our rounded BPF designs as a means of compensation.

Our final design step is to implement ICR compensation. Figure 6.14 illustrates the non-rounded and rounded single resonator geometries used in simulations, for both TOII- and SDII-coupling. Rounded corners in CAD are achieved by employing the ‘Fillet tool’ in Fusion 360. The cavity has two adjacent inductive irises, with L_{FEED} , L_{AB} , T and $W_{A,B}$ corresponding to the feed length, cavity length, iris thickness and iris aperture widths, respectively. With the rounded case, circular radius R is applied to both irises, effectively increasing the iris width. This results in a 3 dB bandwidth increase, due to an increase in the coupling coefficients [5]. Moreover, the cavity’s effective electrical length increases, due to an increase in the effective iris electrical length, resulting in a resonator center frequency down-shift. With every iris corner being rounded by the same amount in the simulations, the full BPF frequency response also has a 3 dB bandwidth increase and a center frequency down-shift.

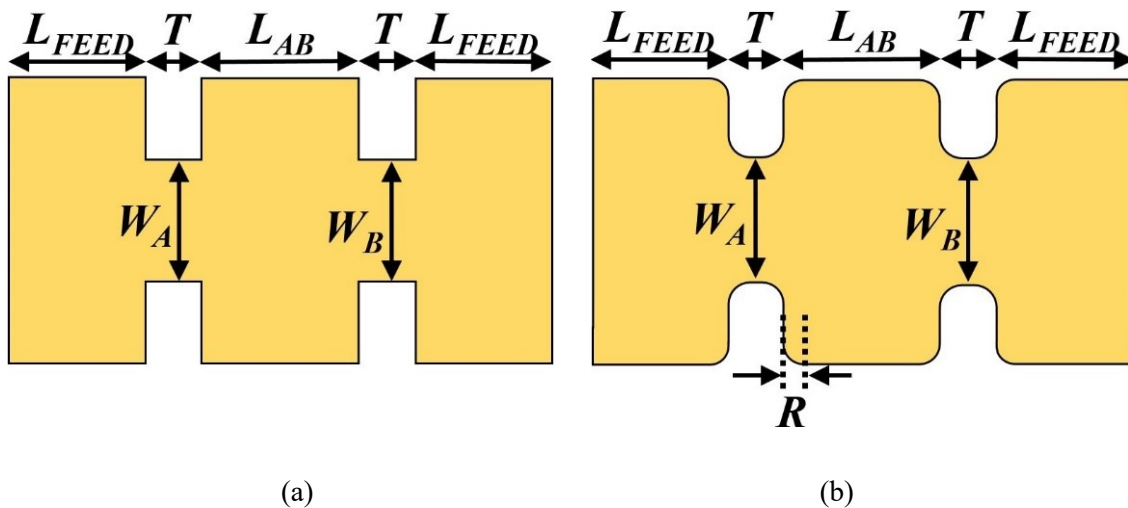


FIGURE 6.14: Plan view illustration of a single cavity resonator, having two inductive irises: (a) non-rounded; and (b) rounded.

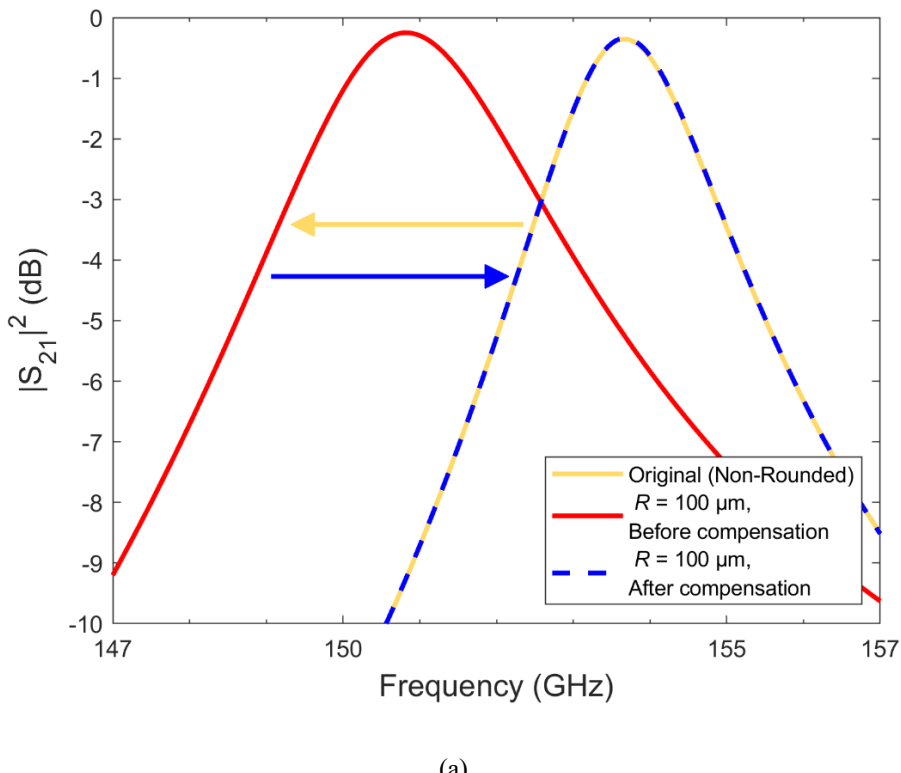
Simulations are first undertaken with the non-rounded cavity resonator, giving target values for the center frequency and 3 dB bandwidth. Then, with the pre-determined value of R , parametric sweeps of L_{AB} and $W_{A,B}$ are applied to tune the rounded cavity resonator to the fixed target values for center frequency and bandwidth from the non-rounded case.

With the symmetrical 5th order BPF, as illustrated in Fig. 6.1, the individual cavity resonators are treated independently, as shown in Fig. 6.14(a) and 6.14(b). Cavities #1 and #5 and Cavities #2 and #4 are identical. The full ICR compensation procedure is detailed below; after compensation, L_i' and W_j' refer to the length of the i^{th} rounded cavity resonator ($i \in [1, 2, 3, 4, 5]$) and the aperture width of the j^{th} rounded iris ($j \in [1, 2, 3, 4, 5, 6]$), respectively:

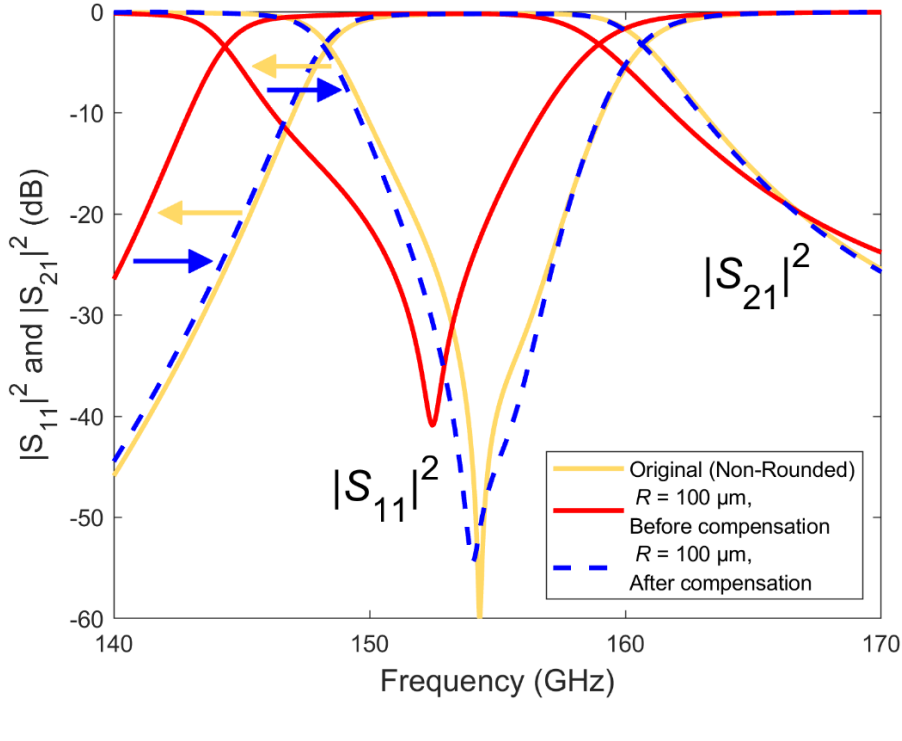
- (i) With the design parameters calculated using the standard filter synthesis procedure, simulate each single resonator with its two non-rounded adjacent irises. Record the center frequencies and -3 dB bandwidths.
- (ii) Apply the measured average iris corner rounding R to all single resonator models.
- (iii) Simulate rounded Resonator #3, noting the shifted center frequency and -3 dB bandwidth. Conduct a parametric sweep on the resonator length and iris aperture widths, L_3 and $W_3 = W_4$, until the original non-rounded center frequency and -3 dB bandwidth is obtained. Record the new dimensions as L_3' and $W_3' = W_4'$.
- (iv) Conduct step (iii) with rounded Resonator #2, with L_2 and W_2 as the swept variables and W_3' fixed as the aperture width of Iris #3. Record the new dimensions as L_2' ($= L_4'$) and W_2' ($= W_5'$).
- (v) Conduct step (iii) with rounded Resonator #1, with L_1 and W_1 as the swept variables and W_2' fixed as the aperture width of Iris #2. Record the new dimensions as L_1' ($= L_5'$) and W_1' ($= W_6'$).
- (vi) Using the new set of dimensions obtained in the previous steps, simulate the full rounded BPF.
- (vii) Conduct minor tuning, if required.

Figure 6.15(a) shows the results of ICR compensation when applied to Cavity #3 for the 155 GHz SDII-coupled BPF. The yellow and blue arrows indicate the down- and up-shifting due to ICR and its compensation, respectively. It can be seen that, with $R = 100 \mu\text{m}$, ICR causes a center frequency down-shift of 2.0% (3.0 GHz) and a 3 dB bandwidth increase of 40% (1.0 GHz). After compensation, the non-rounded response is almost fully restored. It should be noted that Cavity #3 has the highest loaded Q-factor and, therefore, has greatest sensitivity to rounding, when compared to the other cavity resonators.

The simulation results for the complete rounded BPF are shown in Fig. 6.15(b). It can be seen that, with $R = 100 \mu\text{m}$, ICR causes a center frequency down-shift of 1.8% (2.8 GHz) and a 3 dB bandwidth increase of 14.2% (2.2 GHz). After compensation, the non-rounded response is almost fully restored, with the small differences being attributed to the cumulative effect from reconstructing the complete BPF. The final linear BPF dimensions are given in Table 6.4. Note that EM simulations using these dimensions approximate the design specification, but are not in exact agreement.



(a)



(b)

FIGURE 6.15: ICR compensation simulations applied to the 155 GHz SDII-coupled BPF, with yellow and blue arrows indicating frequency shifting due to detuning and compensation, respectively: (a) Cavity #3 only; and (b) complete BPF.

TABLE 6.4: Non-rounded and compensated linear BPF dimensions for the SDII-coupled 155 GHz, 175 GHz, and 200 GHz BPFs, with bandwidths of 15.5 GHz, 17.5 GHz, and 20 GHz, respectively.

Linear Dimensions	$f_0 = 155 \text{ GHz}$		$f_0 = 175 \text{ GHz}$		$f_0 = 200 \text{ GHz}$	
	Non-rounded (μm)	$R = 100 \mu\text{m}$, Compensated (μm)	Non-rounded (μm)	$R = 100 \mu\text{m}$, Compensated (μm)	Non-rounded (μm)	$R = 100 \mu\text{m}$, Compensated (μm)
L_{FEED}	1849	1873	919	1023	1,170	1,242
L_1	870	863	672	635	528	500
L_2	1093	1082	851	807	682	653
L_3	1156	1144	896	851	721	690
W_1	1000	979	905	880	820	795
W_2	790	746	700	680	625	600
W_3	690	645	625	605	550	525
T	270	270	270	270	270	270

6.5.2 Fabrication

The 3-D printing and metalization process for these SDII-coupled BPFs is identical to that of the TOII-coupled components.

The internal waveguide features for the mid-band 175 GHz SDII-coupled BPF are shown in Fig. 6.16 (both with feed lengths omitted). Images of the other filters are omitted, for brevity. Note that post-assembly cross-sectional distortion was negligible; this is likely to be due to the irises providing lateral reinforcement.

Two components each were printed for each BPF, with measurements of the marginally better performing components presented.

A cost comparison for G-band BPFs are not included, as these components have bespoke specifications that require a quotation.

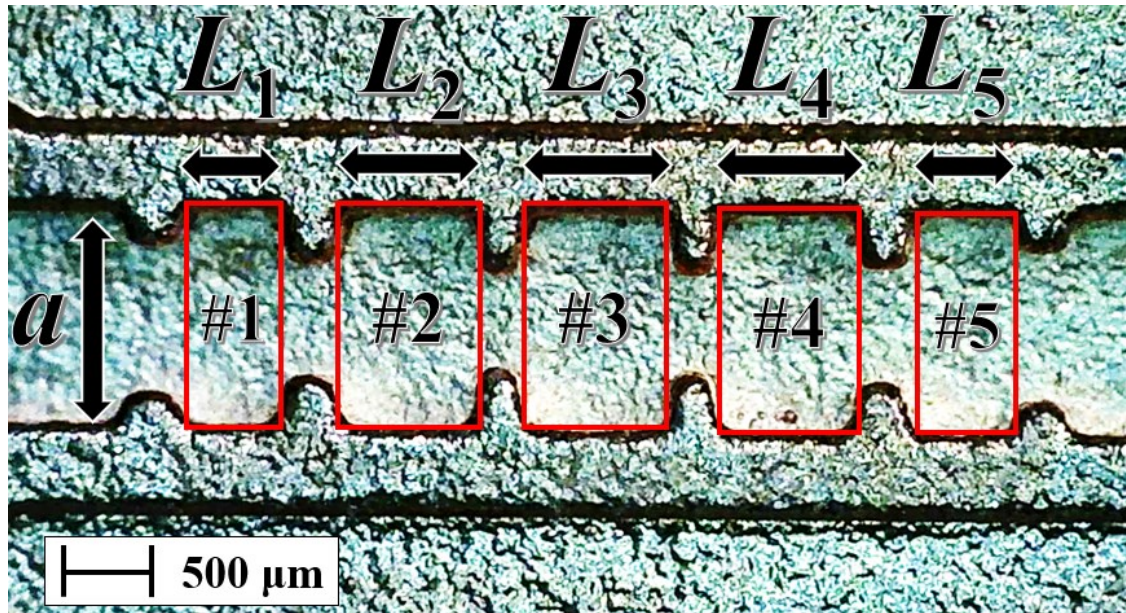


FIGURE 6.16: Plan view microphotographs of the internal structure for 3-D printed and copper electroplated 5th order Butterworth 175 GHz SDII-coupled BPFs, with ICR compensation. Cavity resonators are labelled, and feed lengths are omitted. Red rectangles highlight the peripheries of the cavities.

6.5.3 Measurements

Figure 6.17 shows the S-parameter responses for the 155 GHz BPF, showing EM simulated, measured and EM re-simulated results (i.e., using measured dimensions and iris corner rounding). As with the thru lines and twists, surface roughness is included in the EM re-simulations, with the Extended- and Huray-Hemispherical models; the latter not being visible in Fig. 6.17(a). The measured and re-simulated responses agree well, suggesting that the linear BPF dimensions were accurately measured. For the close-up transmission passband response shown in Fig. 6.16(b), the measured 10.4 mm thru line is also included as a comparative reference.

It can be seen from Fig. 6.17 that the BPF almost preserves the typical Butterworth approximation, having the characteristic mid-band single return loss zero. In contrast, our previously published G-band 5th order Chebyshev filter [7] lost its characteristic return loss zero passband distribution, mainly due to not incorporating ICR compensation.

At the center frequency, the measured insertion losses for this 10.4 mm long BPF and reference 10.4 mm thru line are 0.47 dB and 0.24 dB, respectively, giving a minimum discrepancy of only 0.23 dB at 155 GHz. With both the BPF and thru line there is a good impedance match at 155 GHz, with return losses at 20 dB. It is evident that surface roughness and resonator detuning (due to manufacturing inaccuracy) are the main contributors to insertion loss (i.e., there is insignificant radiation leakage).

There is a slight center frequency up-shift of 2.3% (3.6 GHz) and an 8.4% (1.3 GHz) decrease in 3 dB bandwidth, increasing Q_L from the target value of 10 to the measured value of 11.2. Passband frequency shifting can be explained by measuring the linear BPF dimensions and ICR. The former were found to be a good fit to its predicted compensation values. However, the measured average ICR radius is 75 μm , compared to the predicted compensation value of $R = 100 \mu\text{m}$. Since ICR compensation results in a center frequency up-shift and a 3 dB bandwidth narrowing, this suggests that over-compensation has occurred. A more accurate R value may be obtained by taking more samples, obtaining specific R values for each BPF design, and by controlling environmental factors to produce more reliable prints.

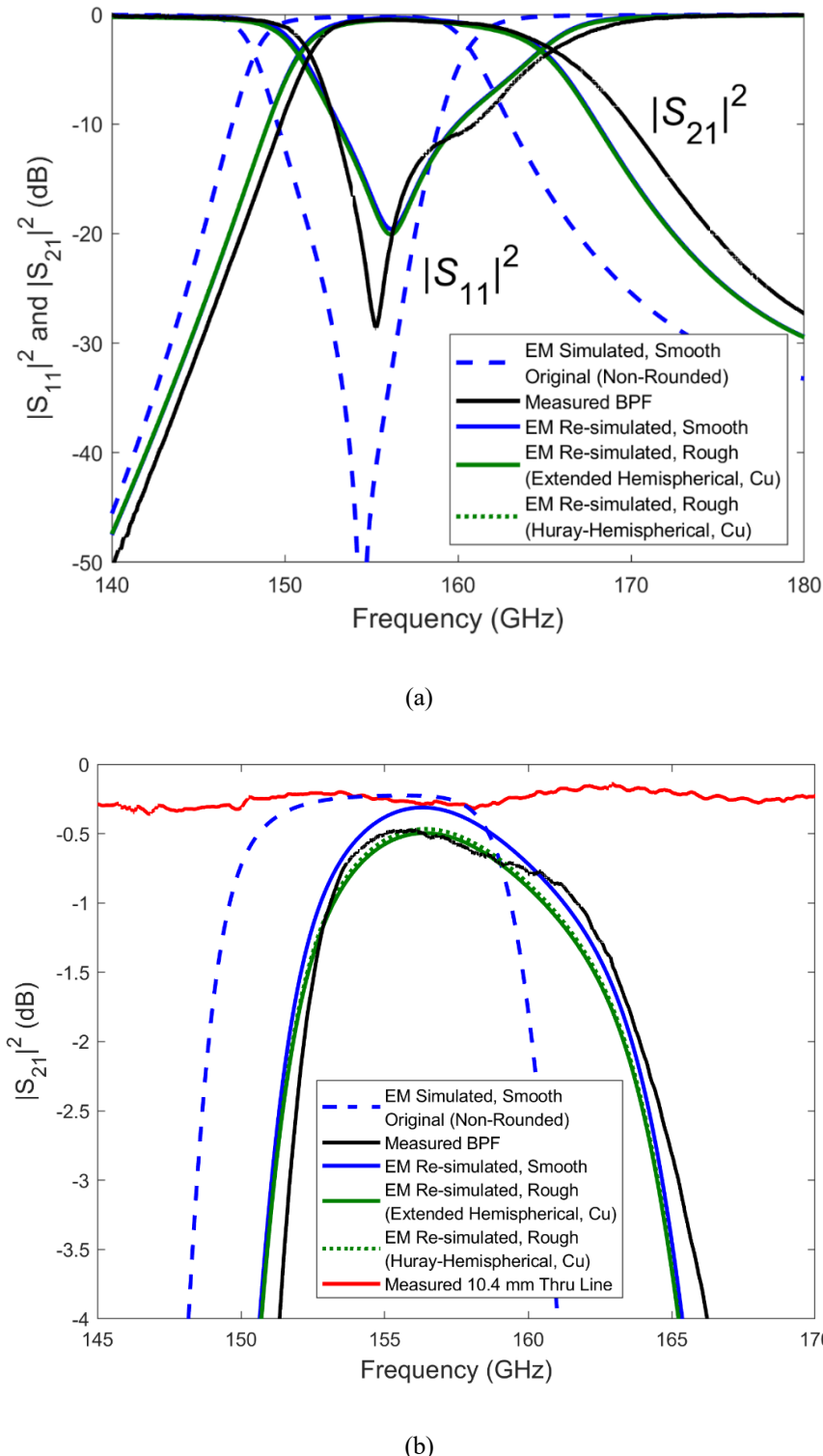


FIGURE 6.17: EM simulated, measured and EM re-simulated two-port S-parameter responses for the 10.4 mm long SDII-coupled 155 GHz BPF, with ICR compensation applied: (a) full G-band responses; and (b) close-up passband transmission responses, with the 10.4 mm reference thru line included.

Figure 6.18 shows the S-parameter responses for the 175 GHz BPF, showing EM simulated, measured and EM re-simulated results. Surface roughness, with the Extended and Huray-Hemispherical models, is again included in the EM re-simulations; the latter not being clearly visible in Fig. 6.18(a). The measured and re-simulated responses agree well, suggesting that the linear BPF dimensions were accurately measured. For the close-up transmission passband response shown in Fig. 6.18(b), the measured 7.4 mm thru line is also included as a comparative reference.

It can be seen from Fig. 6.18 that the measured and re-simulated responses for our G-band 5th order filter do not preserve the typical Butterworth approximation, mainly due to underestimating the level of reduction in the iris width values associated with the predicted compensation. Nevertheless, bandpass filtering is achieved.

The minimum insertion loss for this 7.4 mm long BPF is 0.44 dB, at 180 GHz. At this frequency, the reference 7.4 mm thru line has an insertion loss of 0.13 dB, giving a minimum discrepancy of only 0.31 dB when compared with the BPF. With both the BPF and thru line there is a good impedance match at 180 GHz, with return losses better than 20 dB.

There is a slight center frequency up-shift of only 0.5% (0.9 GHz) and a 12.7% (2.2 GHz) increase in 3 dB bandwidth, increasing Q_L from the target value of 10 to the measured value of 11.5.

The minimal passband frequency shifting can be explained by the good fit of the measured cavity lengths and ICR to its predicted compensation values. Here, the measured average ICR radius is 95 μm , compared to the predicted compensation value of $R = 100 \mu\text{m}$. Choosing an accurate R value can be difficult, due to the several factors that influence ICR (discussed previously). Nevertheless, compensation with an R value that approximates the real values is sufficient to reduce frequency shifting.

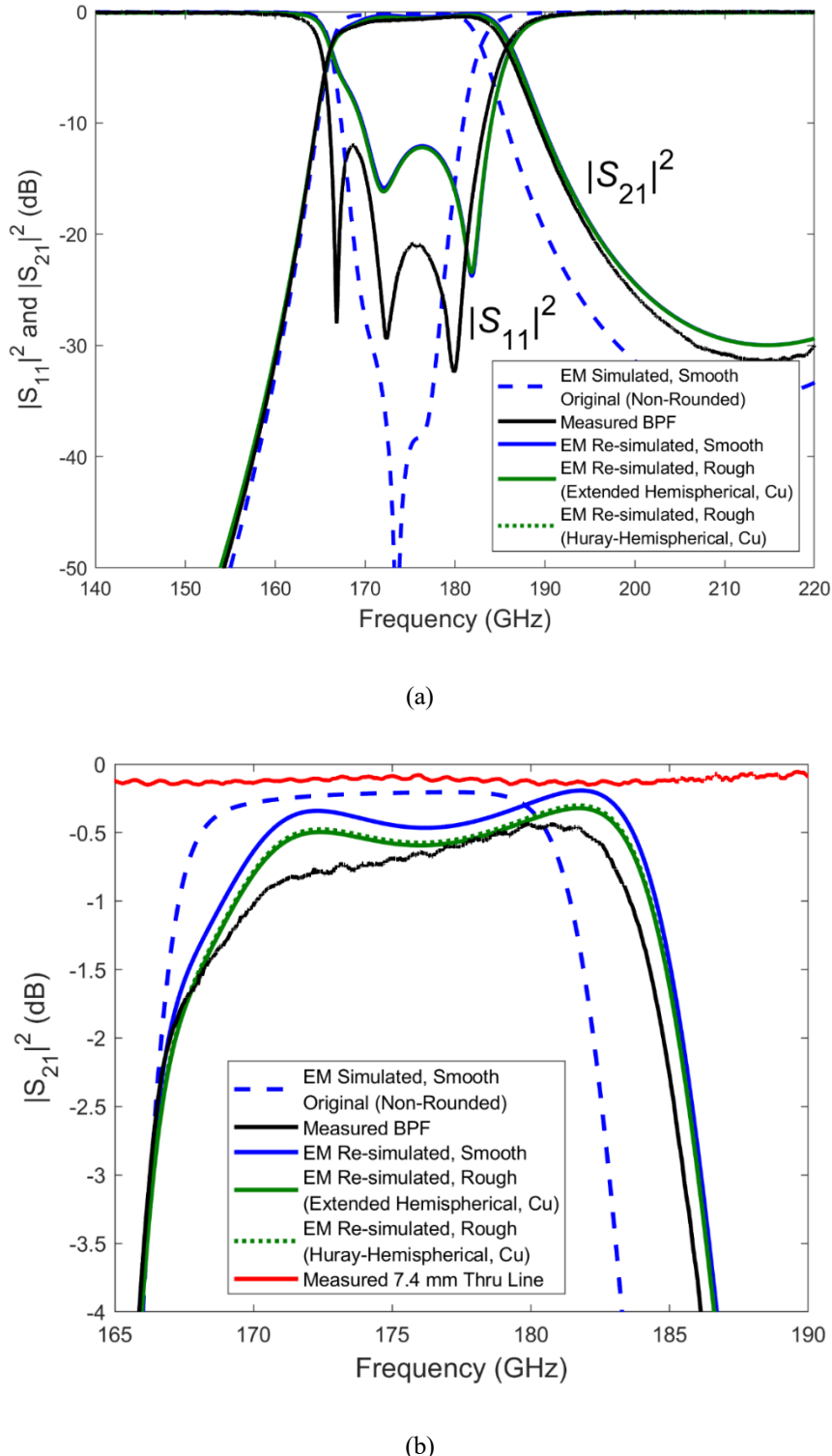


FIGURE 6.18: EM simulated, measured and EM re-simulated two-port S-parameter responses for the 7.4 mm long SDII-coupled 175 GHz BPF, with ICR compensation applied: (a) full G-band responses; and (b) close-up passband transmission responses, with the 7.4 mm reference thru line included.

Figure 6.19 shows the S-parameter responses for the 200 GHz BPF, showing EM simulated, measured and EM re-simulated results. Surface roughness, with the Extended and Huray-Hemispherical models, is again included in the EM re-simulations; the latter not being clearly visible in Fig. 6.19(a). The measured and re-simulated responses agree well, suggesting that the linear BPF dimensions were accurately measured. For the close-up transmission passband response shown in Fig. 6.19(b), the measured 7.4 mm thru line is also included as a comparative reference. Despite the BPF having a length of 7.1 mm, this thru line will provide a reasonable comparative reference, as the difference in insertion loss between a 7.4 mm and a 7.1 mm thru line is relatively insignificant in comparison to the measured BPF insertion loss.

It can be seen from Fig. 6.19 that the measured and re-simulated responses for our G-band 5th order filter do not preserve the typical Butterworth approximation. Indeed, there appears to be a splitting of the return loss zeroes in the reflection response. This has resulted in a worst-case return loss of 7.5 dB at 199 GHz. This in turn has caused passband distortion, with an insertion loss of 1.8 dB at this frequency.

The minimum insertion loss for this 7.1 mm long BPF is 0.67 dB, at 209.1 GHz. At this frequency, the 7.4 mm thru line has an insertion loss of 0.09 dB, giving a minimum discrepancy of 0.58 dB when compared with the BPF. With both the filter and thru line there is a good impedance match at 209.1 GHz, with return losses better than 20 dB.

There is a center frequency up-shift 2.9% (5.7 GHz) and a 2.4% (0.5 GHz) increase in 3 dB bandwidth, increasing Q_L from the target value of 10 to the measured value of 10.1.

The average measured iris thicknesses and iris widths approximate the design values reasonably well. However, on average, the resonator lengths are narrower by approximately 30 μm , thereby resulting in the observed frequency up-shift and return loss splitting. Moreover, at these higher operational frequencies, any given manufacturing inaccuracy will cause a relatively greater shifting of cavity resonator center frequencies and 3 dB bandwidths.

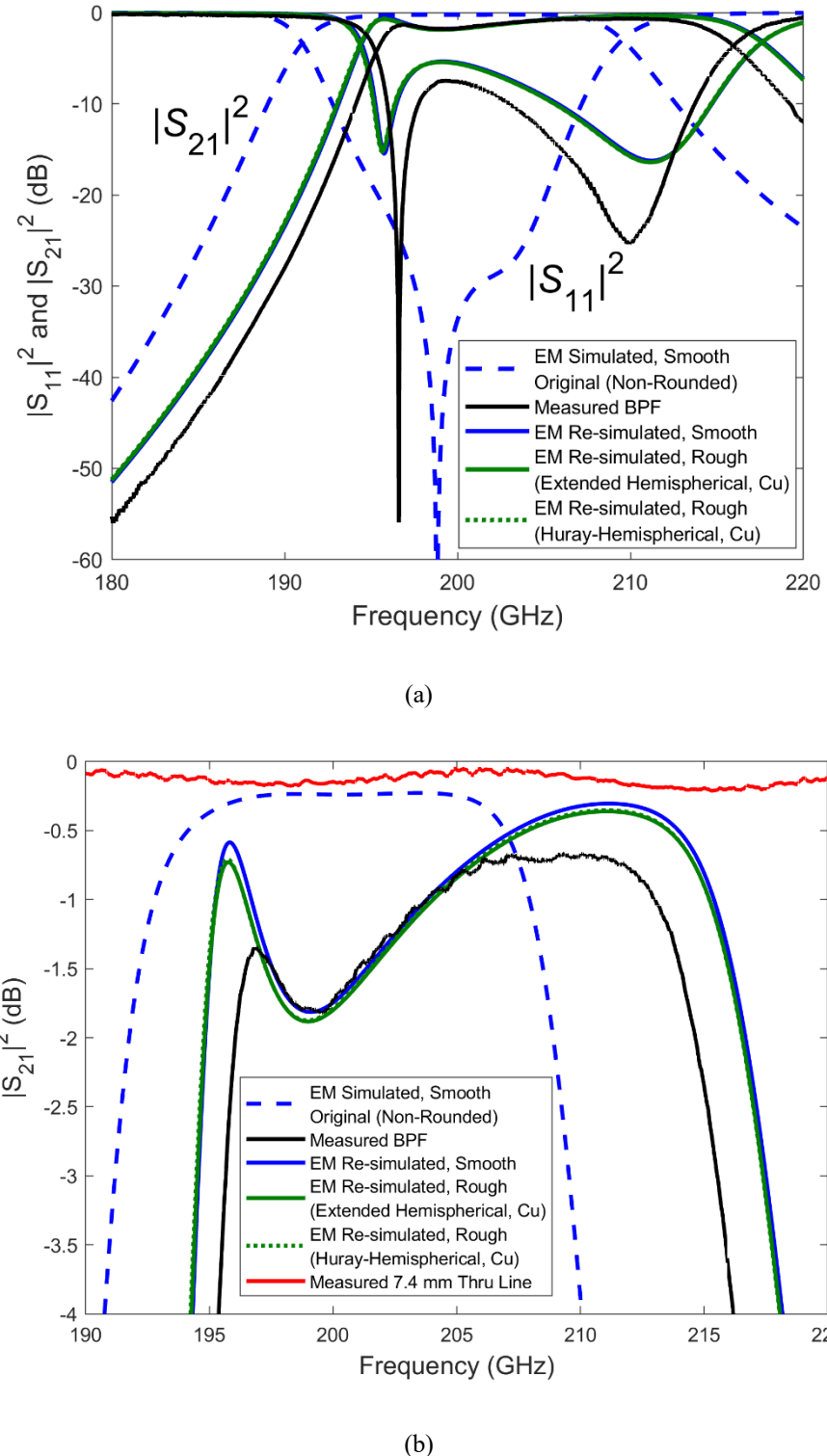


FIGURE 6.19: EM simulated, measured and EM re-simulated two-port S-parameter responses for the 7.1 mm long SDII -coupled 200 GHz BPF, with ICR compensation applied: (a) full G-band responses; and (b) close-up passband transmission responses, with the 7.4 mm reference thru line included.

The measured average iris corner rounding radius for this specific part is 105 μm , so CRC has applied a slight under-compensation that in turn causes a passband down-shift. This was not enough to counteract the aforementioned up-shifting effects.

The 155 GHz and 175 GHz BPF were reported in a recently published paper in *IEEE Access* [2], with the 200 GHz BPF being omitted due to its distorted passband. Filters operating at 200 GHz or above will require polymer-based 3-D printers with better dimensional accuracy; with the rapid pace of technological development in this area, these components can be expected soon.

As shown in Table 1.3, both of the reported SDII-coupled BPFs compare well with W-band polymer-based 3-D printed symmetrical diaphragm inductive iris BPFs, in terms of passband insertion loss and center frequency shift, despite the higher operational frequencies.

At G-band, our reported filters demonstrate a comparable frequency shift, and a ~ 2.5 dB insertion loss improvement, when compared to the higher-accuracy metal laser sintered (MLS) 180 GHz BPF [8]. In contrast to our previously reported 183.3 GHz 5th order chained-function filter [7], having a measured minimum insertion loss of 0.55 dB, our new 175 GHz 5th order Butterworth filter exhibits a slightly lower loss of 0.44 dB. Moreover, for the previous chained-function filter, Q_L significantly decreased from the target value of 10.8 to the measured value of 5.8, while our new 175 GHz filter increased from the target value of 10.0 to the measured value of 11.5. The levels of frequency shift were -0.9% with the previous filter and +0.5% with the new 175 GHz filter.

Furthermore, ICR compensation and selection of parts with relatively accurate 3-D printed linear BPF dimensions has resulted in significantly reduced passband frequency shifting in comparison to the TOII-coupled BPFs.

6.6 Conclusion

For the 1st Gen. components, a split-block approach is employed, with a symmetrical E-plane deviating split and an RF choke. The filters were designed to comply with the WMO-ITU allocated frequency bands of scientific interest [3]. As a result, due to its very narrow designed fractional bandwidth of 1.7%, the 150 GHz filter did not exhibit any transmission passband. Having larger fractional bandwidths of 9.3% and 4.4%, respectively, the 183.3 GHz and 204.5 GHz filters did exhibit a transmission passband. However, these components had a very high insertion loss due to radiation leakage from the split. Significant passband frequency shifting was also observed.

For the 4th Gen. components, the trough-and-lid assembly approach is employed, which was shown to mitigate radiation leakage and assembly part misalignment with thru lines and 90° twists. Initially, three 5th order TOII-coupled BPFs were designed. A similar specification was adopted, with a wider 6 GHz bandwidth for the 150 GHz filter, giving a fractional bandwidth of 4%. The 183.3 GHz and 204.5 GHz BPFs exhibited a good passband transmission response, but manufacturing inaccuracies cause significant frequency shifting. The two main types are found to be discrepancies in linear BPF dimensions and ICR compensation.

For the second batch of BPFs, these manufacturing inaccuracies were investigated in detail, with a unique, systematic ICR compensation technique been applied to three SDII-coupled 3-D printed BPFs. The 155 GHz and 175 GHz exemplars, which were reported in a recently submitted research article [2], exhibit a low minimum passband insertion loss of 0.47 dB and 0.44 dB, with center frequency up-shifting of only 2.3% and 0.5%, respectively. Further improvement can be expected with: (i) close visual inspection and early part selection/rejection during manufacture; (ii) improved manufacturing process characterization and control; (iii) design iteration; and (iv) the additional application of pixel quantization pre-distortion for MSLA printers (which was beyond the scope of this paper).

6.7 References

- [1] S.-H. Shin, R. Payapulli, L. Zhu, M. Stanley, X. Shang, N. M. Ridler, and S. Lucyszyn, “3-D printed plug and play prototyping for low-cost sub-THz subsystems,” *IEEE Access*, vol. 10, pp. 41708-41719, Apr. 2022.
- [2] R. Payapulli, L. Zhu, S.-H. Shin, M. Stanley, N. M. Ridler, and S. Lucyszyn, “Polymer-based 3-D printed 140 to 220 GHz metal waveguide thru lines, twist and filters,” *IEEE Access*, vol. 11, pp. 32272-32295, Mar. 2023.
- [3] Use of Radio Spectrum for Meteorology: Weather, Water and Climate Monitoring and Prediction. WMO-ITU, 2017, p. 75.
- [4] J. Hong and M. Lancaster, “Microstrip filters for RF/microwave applications,” 1st ed., Hoboken, New Jersey: John Wiley & Sons, Inc., 2001.
- [5] R. J. Cameron, C. M. Kudsia, and R. R. Mansour, “Microwave filters for communication systems: fundamentals, design and applications,” 2nd ed., Hoboken, New Jersey: John Wiley & Sons, Inc., 2018.
- [6] S. Ramo, J. R. Whinnery, and T. van Duzer, “Fields and waves in communications electronics,” 3rd ed., Hoboken, New Jersey: John Wiley & Sons, Inc., 1994.
- [7] L. Zhu, R. Payapulli, S.-H. Shin, M. Stanley, N. M. Ridler, and S. Lucyszyn, “3-D printing quantization predistortion applied to sub-THz chained-function filters,” *IEEE Access*, vol. 10, pp. 38944-38963, Mar. 2022.
- [8] T. Skaik, M. Salek, Y. Wang, M. J. Lancaster, T. Starke, and F. Boettcher, “180 GHz waveguide bandpass filter fabricated by 3D printing technology,” *2020 13th UK-Europe-China Workshop on Millimetre-Waves and Terahertz Technologies (UCMMT)*, pp. 1-3, 2020.

7. Additional Attenuation due to Conductor Surface Roughness in MPRWGs

7.1 Introduction

All of the content in this chapter is based on a research article by Payapulli et al., which was published in *IEEE Access* in March 2023 [1].

A conductor with a rough surface has additional losses, due to localized EM wave scattering from and power dissipation within microscopic surface defects [2]. Both become more significant at higher frequencies, as the dimensions of these defects become more significant when compared to the wavelength and classical skin depth, respectively. For example, ICL previously measured the root mean square (RMS) profile roughness $R_q = 1.16 \mu\text{m}$ for electroplated copper on an SLA-printed MPRWG [3]. By comparison, the classical skin depths for copper are $0.18 \mu\text{m}$ and $0.14 \mu\text{m}$ at 140 GHz and 220 GHz, respectively. As a result, surface roughness is expected to be an important contributor to insertion loss at G-band.

Surface roughness models generally relate either the power dissipated P_{DR} or dissipative attenuation α'_{DR} for rough conductors normalized to smooth conductors (P_{DS} or α'_{DS}), using a frequency-dependent roughness coefficient K [4]:

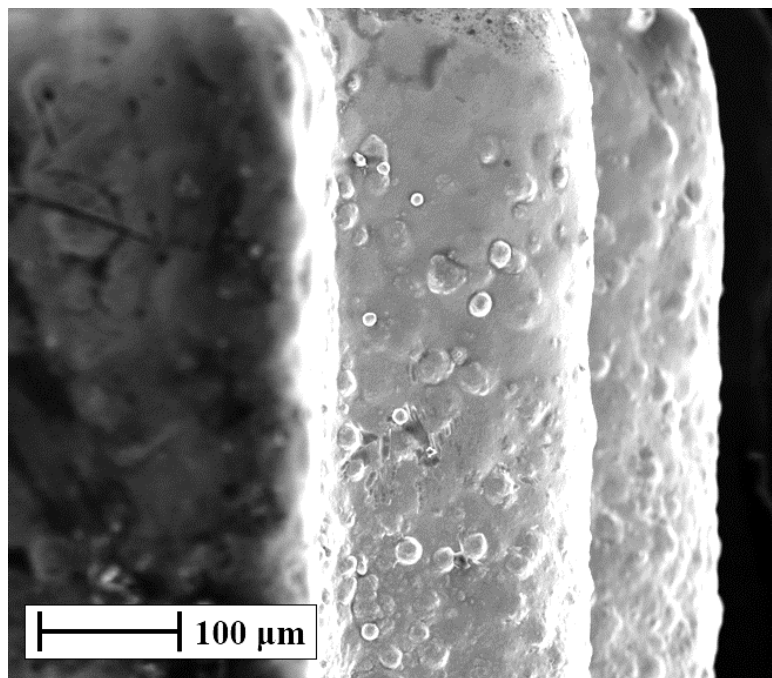
$$K = P_{DR}/P_{DS} = \alpha'_{DR}/\alpha'_{DS} \quad (7.1)$$

Using (7.1), most models fall into one of two categories: (i) phenomenological models, which fit empirical equations to α'_D measurements; and (ii) physical models, which apply analytical (Maxwell's) equations with boundary conditions set by the specific surface structures. With the former, the most commonly used examples are the Hammerstad-Jensen (HJ) model [4] and the Groiss model [5]. However, their roughness coefficients asymptotically approach $K = 2$ at relatively low frequencies (*ca.* 5 GHz), even with sub-micron values for R_q , making them unsuitable for G-band applications. With the latter,

the most commonly used examples are the Hemispherical model [6], which considers hemispherical protrusions on a flat plane, and the Huray model [2], which considers pyramidal protrusions of stacked spheres. The appropriate choice of physical model is dependent on the geometries of the surface defects observed on fabricated components.

7.2 Surface Roughness of 3-D Printed Components

Images of the iris sidewalls and the bottom of the MPRWG trough for the plated 155 GHz BPF are shown in Fig. 7.1, taken using a Zeiss LEO 1450VP scanning electron microscope (SEM). The surface roughness is representative of all plated parts. The main surface defects are approximately hemispherical, suggesting that the Hemispherical model is appropriate. Based on analyzing the microphotographs in Fig. 7.1, the average hemispherical radius r_{base} and separation distance between adjacent protrusions d_{peaks} are found to be $3.7 \mu\text{m}$ and $17 \mu\text{m}$, respectively. This corresponds to an effective value of $R_q = 1.41 \mu\text{m}$, by measuring the RMS height at the peaks of the hemispheres, which agrees well with our previous measurement of $R_q = 1.16 \mu\text{m}$.



(a)

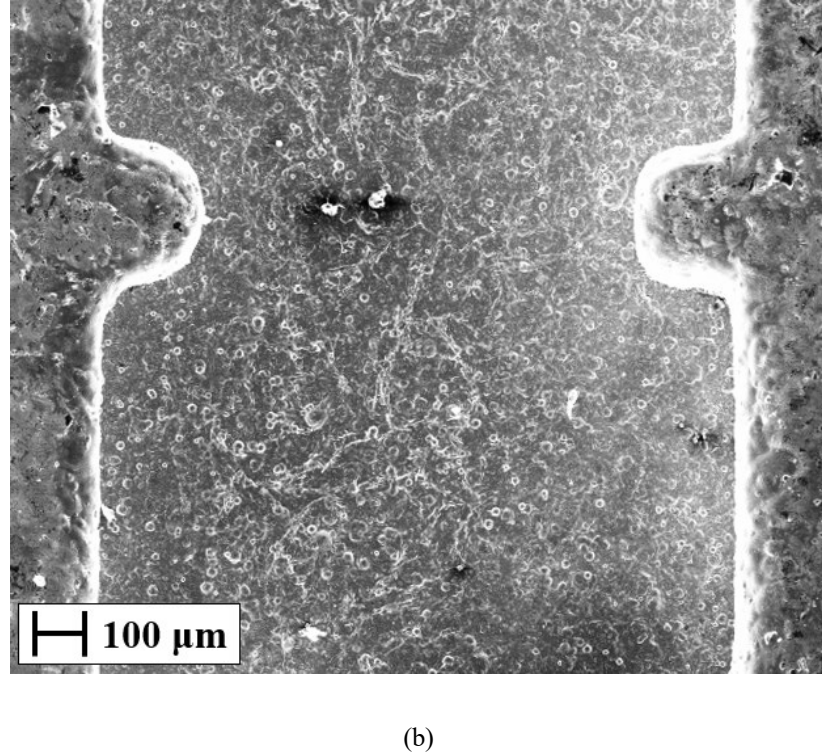


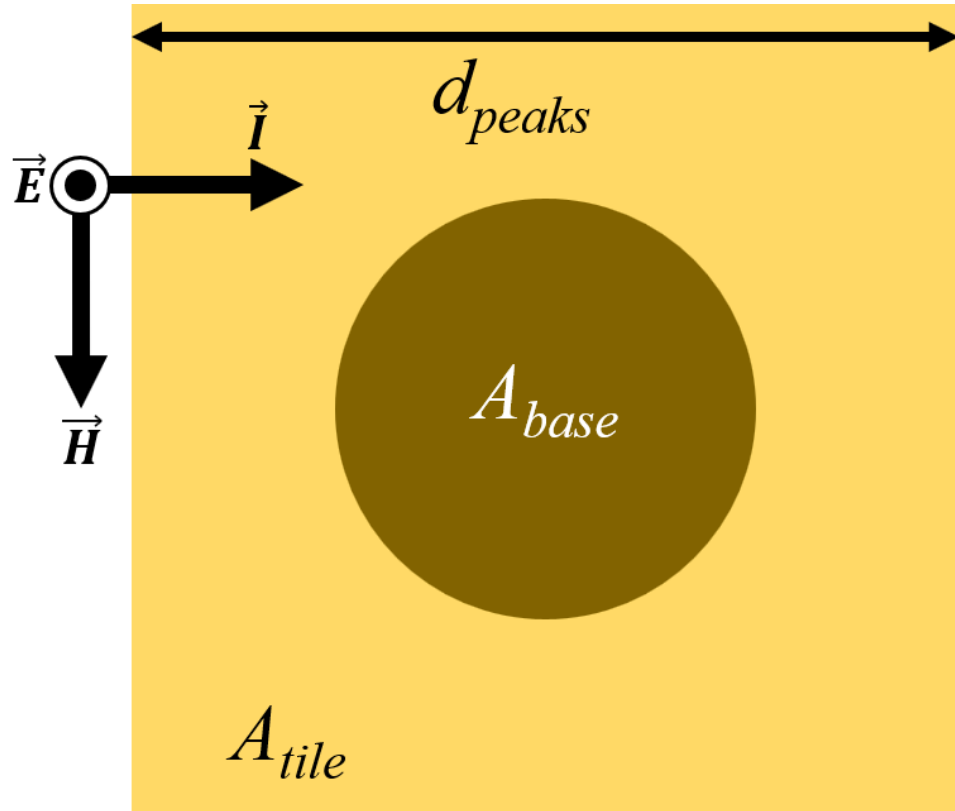
FIGURE 7.1: SEM images for the 155 GHz BPF: (a) iris sidewalls; and (b) plan view of the bottom of the MPRWG trough and one iris aperture.

Simulation-based techniques represent another surface roughness model category [7]-[8]; these were not considered, as the observed surface defects strongly suggest that the Hemispherical model is appropriate.

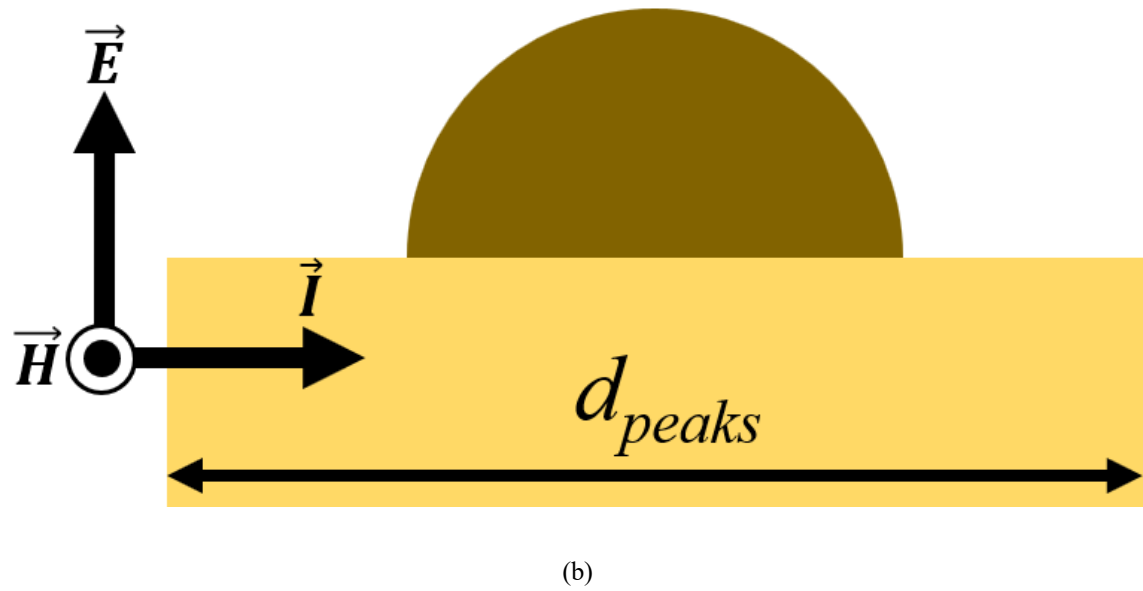
Figure 7.2 illustrates a single cell for the Hemispherical model, which is assumed to extend periodically in the longitudinal and transverse directions, across the entire conductor surface. A transverse electromagnetic (TEM) plane wave is applied, with electric field \vec{E} normal to the flat plane and the magnetic field \vec{H} being tangential, with the direction of propagation from left to right in Fig. 7.2. The dimensions A_{base} and A_{tile} refer to the areas of the hemisphere base and flat tile, respectively [6]. These can be related to the average physical dimensions, obtained from SEM images, as:

$$A_{base} = \pi r_{base}^2 \quad [\text{m}^2] \quad (7.2a)$$

$$A_{tile} = d_{peaks}^2 \quad [\text{m}^2] \quad (7.2b)$$



(a)



(b)

FIGURE 7.2: The Hemispherical surface roughness model, represented by a single hemispherical protrusion positioned on a flat plane, with incident plane wave propagating parallel to the flat surface: (a) plan view; and (b) side view [9].

A simplified equation for the Hemispherical model [6] roughness coefficient is:

$$K = \frac{\eta_0}{2R_S} \cdot \frac{\sigma_t}{A_{tile}} + \frac{A_{tile} - A_{base}}{A_{tile}} \quad (7.3)$$

where $\eta_0 = \sqrt{\frac{\mu_0}{\epsilon_0}}$ and $R_S = \sqrt{\frac{\omega\mu_0}{2\sigma_0}}$ are the intrinsic impedance of free space and classical surface resistance for a smooth conductor (calculated using bulk DC conductivity σ_0), respectively. The total cross-section σ_t , is the sum of the power dissipated and scattered by a conducting sphere positioned in free space divided by the incident flux (power surface density) [10]. Here, the dissipated and scattered fields are solved analytically, with the latter being derived from spherical Bessel functions [10] to give:

$$\sigma_t = \sigma_{dissipated} + \sigma_{scattered} \quad [\text{m}^2] \quad (7.4a)$$

$$\sigma_t = \frac{2\pi}{k_0^2} \sum_1^i \frac{(k_0 r_{base})^{2i+1}}{[(2i-1)!!]^2} \cdot \text{Im}\{\alpha_i + \beta_i\} \quad [\text{m}^2] \quad (7.4b)$$

where $\sigma_{dissipated}$ and $\sigma_{scattered}$ are the dissipated and scattered cross-sections, $k_0 = 2\pi/\lambda_0$ is the angular wavenumber, α_i and β_i are dimensionless scattering coefficients and i is a summation term. For $k_0 r_{base} \ll i$, the following long-wavelength approximations are given as [10]:

$$\alpha_i \simeq \frac{k_0 r_{base} - j(i+1)Z_S/\eta_0}{k_0 r_{base} + jiZ_S/\eta_0} \quad (7.5a)$$

$$\beta_i \simeq \frac{k_0 r_{base} - j(i+1)\eta_0/Z_S}{k_0 r_{base} + ji\eta_0/Z_S} \quad (7.5b)$$

The conventional Hemispherical model employs only the first term ($i = 1$) and is quoted as being valid up to 30 GHz [6]. However, to provide better accuracy for G-band, σ_t is calculated up to $i = 5$. This is referred to here as the Extended-Hemispherical model.

The conventional Huray model calculates $\sigma_t = \sigma_{dissipated}$, with $\sigma_{scattered}$ being omitted, using a different equation for the roughness coefficient (i.e., not employing (7.3)). Moreover, instead of using (7.4b) and any long-wavelength approximations, the 1st order Born approximation for the amplitude of the scattered fields is employed in (7.4a) with [10]:

$$\sigma_{dissipated} \simeq \frac{3\pi k_0 r_{base}^2 \delta_o}{1 + \frac{\delta_o}{r_{base}} + \frac{1}{2} \left(\frac{\delta_o}{r_{base}} \right)^2} \quad [\text{m}^2] \quad (7.6a)$$

$$\sigma_{scattered} \simeq \frac{10}{3} \pi k_0^4 r_{base}^6 \left[1 + \frac{2}{5} \cdot \frac{\delta_o}{r_{base}} \right] \quad [\text{m}^2] \quad (7.6b)$$

where $\delta_o = 1/\sigma_o R_S$ refers to the classical skin depth of the conductor, calculated using bulk DC conductivity. By including the $\sigma_{scattered}$ term in (7.6b), giving better accuracy for G-band, and adopting the Hemispherical model roughness coefficient equation in (7.3), this is referred to here as the Huray-Hemispherical model [2]. To the best of our knowledge, these Extended/Huray-Hemispherical models have not been previously applied to MPRWG applications.

With a perfectly smooth surface, A_{base} and σ_t are both zero, and so $K = 1$. The application of $K > 1$ to EM simulations was introduced previously in Chapters 4, 5 and 6. Using the values of r_{base} and d_{peaks} obtained from SEM images, the calculated mid-

band values are $K(180 \text{ GHz}) = 1.32$ and 1.28 for the Extended- and Huray-Hemispherical models, respectively, with minimal variation across the band. The calculated K values are multiplied by the calculated/simulated α'_{DS} to obtain α'_{DR} , as given by (7.1).

7.3 Surface Roughness of Commercial Waveguides

An example of a phenomenological model for the roughness coefficient can be seen in Fig. 7.3. Here, Fig. 7.3(a) shows the measured total attenuation, $\alpha_{TR} = -10 \log_{10} |S_{21}|^2$, for 100 mm long Flann Microwave Ltd COTS sub-millimeter seamless MPRWG thru lines [11], previously introduced in Chapter 1. Their current catalog covers eleven waveguide bands, ranging from WR-8 (with $f_L = 90 \text{ GHz}$) to WR-1 (with $f_L = 750 \text{ GHz}$). A close fit (derived empirically) to the measurements is found with $\alpha_{TR} \cong 7.1 \times 10^{-4} \cdot f_L(\text{GHz})^{1.5669}$, having a coefficient of determination $R^2 = 0.9986$, shown in Fig. 7.3(a). In addition, Fig. 7.3(a) also includes the dissipative attenuation for 100 mm long smooth thru lines α_{DS} , calculated at f_L . Equation (2.17) is used to calculate the dissipative attenuation for an ideal, perfectly-matched waveguide using the bulk DC conductivity for gold (since all the thru lines are gold-plated). A close fit (derived empirically) to the calculated results is found with $\alpha_{DS} \cong 9.2 \times 10^{-4} \cdot f_L(\text{GHz})^{1.4452}$, having a coefficient of determination $R^2 = 0.9980$, shown in Fig. 7.3(a).

For these COTS thru lines, the effective roughness coefficients $K_{eff}(f_L) = \alpha_{TR}/\alpha_{DS}$, with results given in Fig. 7.3(b). Using the previously derived empirical fits, effective $K_{eff}(f_L) \sim 0.77 \cdot f_L(\text{GHz})^{0.1217}$. These values will be an overestimation, as the total attenuation is increased by the contribution from the wave impedance mismatch reflection.

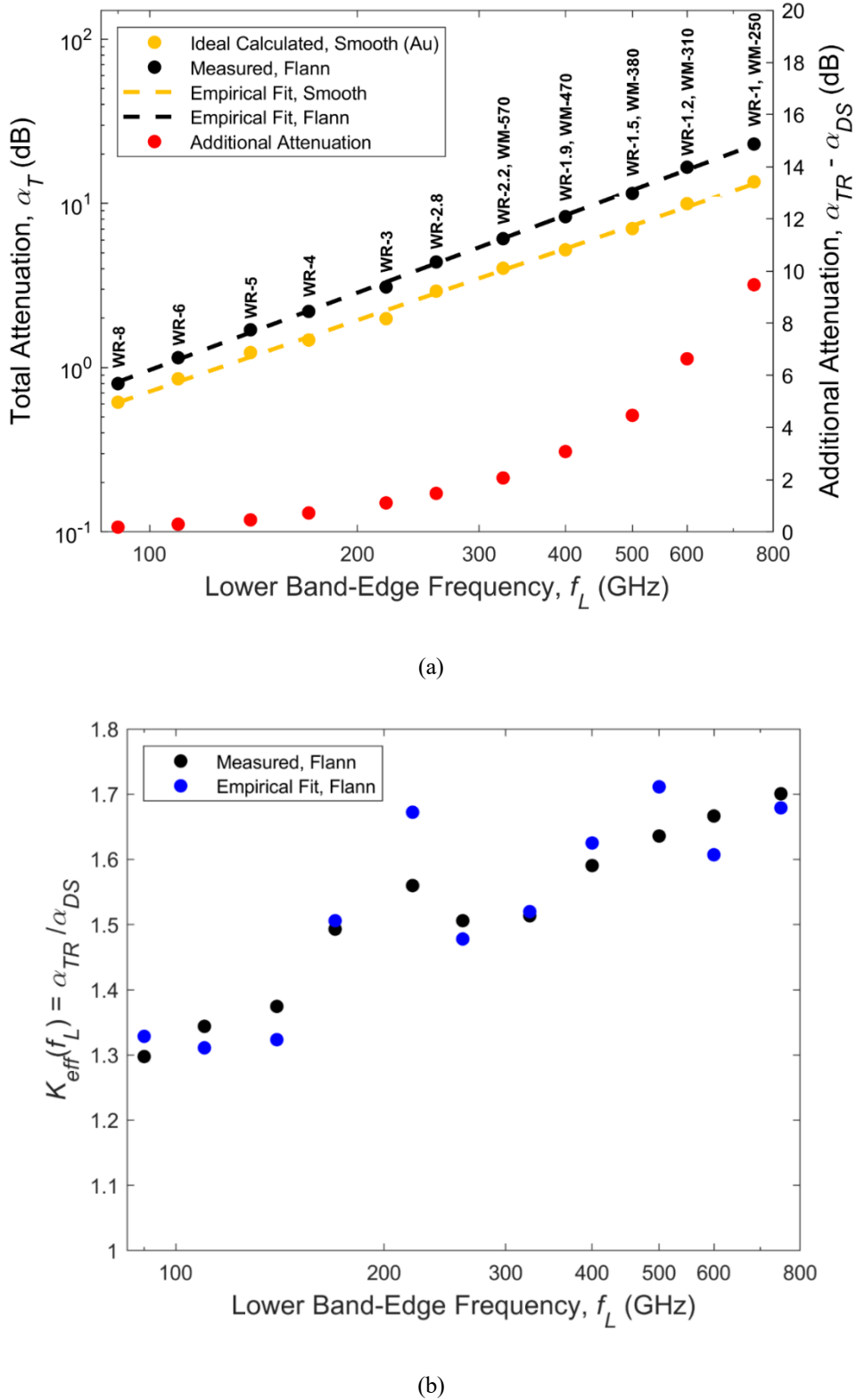


FIGURE 7.3: Flann submillimeter seamless waveguides: (a) total attenuation measurements, with ideal calculated values and COTS thru line measurements; and (b) effective roughness coefficient $K_{eff}(f_L)$.

7.4 Conclusion

This chapter has introduced and discussed the additional insertion loss due to conductor surface roughness that is exhibited in fabricated waveguide components. The Hemispherical physical surface roughness model is used here, as SEM images show that the surface defects are approximately hemispherical in nature. In addition, two modifications of the Hemispherical model are applied, which provide greater accuracy at these upper millimeter-wave frequencies.

7.5 References

- [1] R. Payapulli, L. Zhu, S.-H. Shin, M. Stanley, N. M. Ridler, and S. Lucyszyn, “Polymer-based 3-D printed 140 to 220 GHz metal waveguide thru lines, twist and filters,” *IEEE Access*, vol. 11, pp. 32272–32295, Mar. 2023.
- [2] P. G. Huray, O. Oluwafemi, J. Loyer, E. Bogatin, and X. Ye, “Impact of copper surface texture on loss: A model that works,” *DesignCon*, vol. 1, pp. 462–483, Jun. 2010.
- [3] M. D'Auria, W. J. Otter, J. Hazell, B. T. W. Gillatt, C. Long-Collins, N. M. Ridler, and S. Lucyszyn, “3-D printed metal-pipe mrectangular waveguides,” *IEEE Trans. on Components, Packaging and Manufacturing Technology*, vol. 5, no. 9, pp. 1075- 1092, May 2006.
- [4] E. Hammerstad and Ø. Jensen, “Accurate models for microstrip computer aided design,” in *IEEE MTT-S Int. Microw. Symp. Dig.*, May 1980, pp. 407–409.
- [5] S. Groiss, I. Bardi, O. Biro, K. Preis, and K. R. Richter, “Parameters of lossy cavity resonators calculated by the finite element method,” *IEEE Trans. Magn.*, vol. 32, no. 3, pp. 894–897, May 1996.
- [6] S. Hall, S. G. Pytel, P. G. Huray, D. Hua, A. Moonshiram, G. A. Brist, and E. Sijercic, “Multigigahertz causal transmission line modelling methodology using a 3-D hemispherical surface roughness approach,” *IEEE Trans. Microw. Theory Techn.*, vol. 55, no. 12, pp. 2614–2624, Dec. 2007.
- [7] Q. Chen, H. W. Choi and N. Wong, “Robust simulation methodology for surface-roughness loss in interconnect and package modelings,” *IEEE Trans. on Computer-Aided Design of Integrated Circuits and Systems*, vol. 28, no. 11, pp. 1654–1665, Nov. 2009.
- [8] S. Bakirtzis, X. Zhang, and C. D. Sarris, “Stochastic modeling of wave propagation in waveguides with rough surface walls,” *IEEE Trans. on Microwave Theory and Techniques*, vol. 69, no. 1, pp. 500–508, Jan. 2021.
- [9] S. H. Hall and H. L. Heck, “Advanced signal integrity for high-speed digital

- designs,” 1st ed., Hoboken, New Jersey: John Wiley & Sons, Inc., 2009.
- [10] J. D. Jackson, “Classical electrodynamics,” 3rd ed., Hoboken, New Jersey: John Wiley & Sons, Inc., 1999.
- [11] Flann Microwave. (2022). Flann Microwave. Accessed: Jan. 07, 2023. [Online]. Available: <https://flann.com/wp-content/uploads/2022/03/Sub-Millimetre-Seamless-Waveguide-Datasheet-Revision-3.pdf>.

8. Applications of MPRWGs in Millimeter-Wave Radiometer Front-End Subsystems

8.1 Introduction

Part of the content in this chapter (i.e., Chapter 8.4.2) is based on a research article by S.-H. Shin et al., for which I was the 2nd author [1].

As discussed in Chapter 1, waveguides are suitable for applications that require the receiving of very low power EM radiation (in addition to applications that require high power transmission, such as synthetic aperture radar), due to their significantly lower dissipative attenuation when compared to other transmission line technologies. Therefore, they are often employed in radiometers; these are instruments that measure the ‘noise’-like thermal radiation that is emitted by any object above absolute zero Kelvin [2].

Radiometers are often deployed on satellites for the measurement of thermal radiation emitted by the Earth, which enables the extraction of information about the Earth’s physical, chemical, and biological systems [3]. This is known either as ‘satellite-based remote-sensing’ or ‘satellite-based Earth observation’ [4].

As the demand for this information increases, the need for satellite payloads with lower mass and lower cost becomes more important, as this would significantly reduce the total cost of satellite-based Earth observation missions. Therefore, polymer-based 3-D printing is being presented as an alternative to machined waveguides for this application.

Here, the design of a polymer-based 3-D printed millimetre-wave front-end subsystem is presented, which is based on the design of existing radiometers. The design and manufacturing of the quasi-optical components, the manufacturing of the subsystem, and the final subsystem measurements at NPL were undertaken by S.-H. Shin; as such, these aspects will not be explained in detail. This demonstrates the integration of a waveguide BPF with a quasi-optical network, which represents a major step towards the use of 3-D printed waveguides for satellite-based applications. Note that waveguides could also potentially be employed in aircraft-, balloon-, and ground-based radiometers.

8.2 Radiometer Design

A radiometer measures the power of random broadband noise (due to thermal emission) from a receiving antenna [5]. The purpose of this measurement is to obtain an accurate measurement of the antenna temperature T_A , which relates to the brightness temperature T_B of the object being observed. According to the Rayleigh-Jeans law [6], these equivalent temperatures can be used to represent the power of the received signal using $P_A = kT_A B$, where Boltzmann's constant $k = 1.38 \times 10^{-23} \text{ J}\cdot\text{K}^{-1}$, and B is the bandwidth of the bandpass filter that is used to select a specific range of frequencies [7].

The received power is subsequently amplified by a low noise amplifier having gain G , and then filtered by the pre-detection band-pass filter with 3 dB bandwidth B . A square-law detector is used to produce an output voltage that is proportional to the input noise power P_A . To improve accuracy, the measured noise power is averaged over an integration time τ , as the mean received noise power is approximately constant over time [5].

The output noise power measurement is dependent on the stability of the receiver gain G and the antenna noise temperature T_N ; since these parameters are highly susceptible to drifting, this may result in an unstable measurement. This is typically mitigated by using a Dicke radiometer, as shown in Fig. 8.1 [6]. Here, a Dicke switch is employed immediately after the antenna to switch between T_A and a known reference temperature T_R , typically with a switching frequency of 1 kHz [6], with the output being proportional to the difference between T_A and T_R . This significantly reduces the contribution from T_N and reduces sensitivity to G .

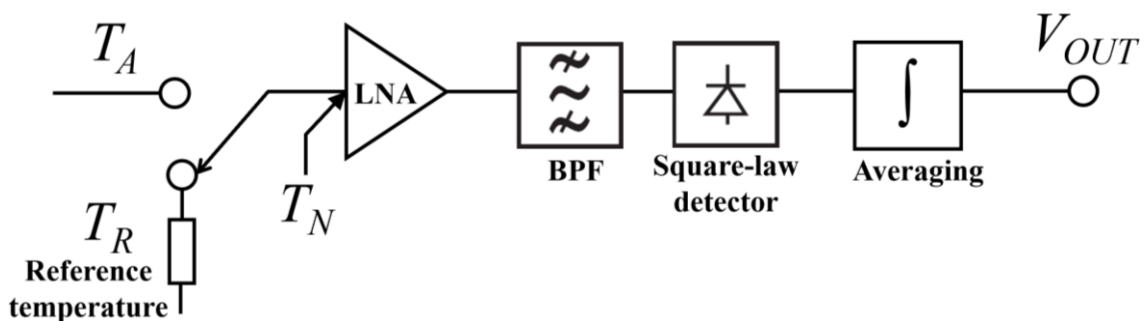


FIGURE 8.1: A Dicke radiometer block diagram.

Many spaceborne radiometers additionally switch to a ‘cold-sky’ reference, which is a view of the cosmic microwave background (CMB) in deep space (away from the Sun and Earth), having a known physical temperature of 2.73 K.

8.3 Current Implementations

Examples of operational satellite-borne radiometers that employ waveguides in their front-ends are given here:

National Aeronautics and Space Administration (NASA), United States

- ‘Microwave Radiometer (MWR)’ on the ‘Juno’ satellite [8]
- ‘Microwave Limb Sounder’ (MLS) on the ‘Aura’ satellite [9]
- ‘Advanced Microwave Scanning Radiometer-EOS’ (AMSR-E) on the ‘Aqua’ satellite [10]
- ‘Advanced Microwave Sounding Unit’ (AMSU) on the ‘Aqua’ satellite [11]

National Oceanic and Atmospheric Administration (NOAA), United States

- ‘Advanced Technology Microwave Sounder (ATMS)’ on the ‘Suomi NPP’ and ‘Joint Polar Satellite System (JPSS)’ satellites [12]

European Space Agency (ESA), European Union

- ‘Microwave Radiometer (MWR)’ on the ‘Sentinel-3’ satellite [13]

Swedish Space Corporation (SSC), Sweden

- ‘Submillimeterwave Radiometer (SMR)’ on the ‘Odin’ satellite [14]

An overview of the final example is given below, as its system design was reported in detail in the open literature.

8.3.1 ‘Submillimeter-wave Radiometer (SMR)’ on ‘Odin’

This radiometer operates onboard SSC’s Odin satellite and was optimized for observations of spectral lines in the (sub-)millimetre-wave region for detecting the oxygen, ozone, nitrogen dioxide, chlorine monoxide, nitric acid, and water vapor absorption lines.

Figure 8.2 shows a block diagram of the complete SMR system [14]. In this diagram, candidate components that can currently be realized using polymer-based 3D-printing are highlighted by solid red boxes. Dashed red boxes indicate more demanding higher frequency candidates, and dotted red boxes represent advanced hybrid active/passive solutions; these are both beyond the current capabilities of polymer-based 3-D printing.

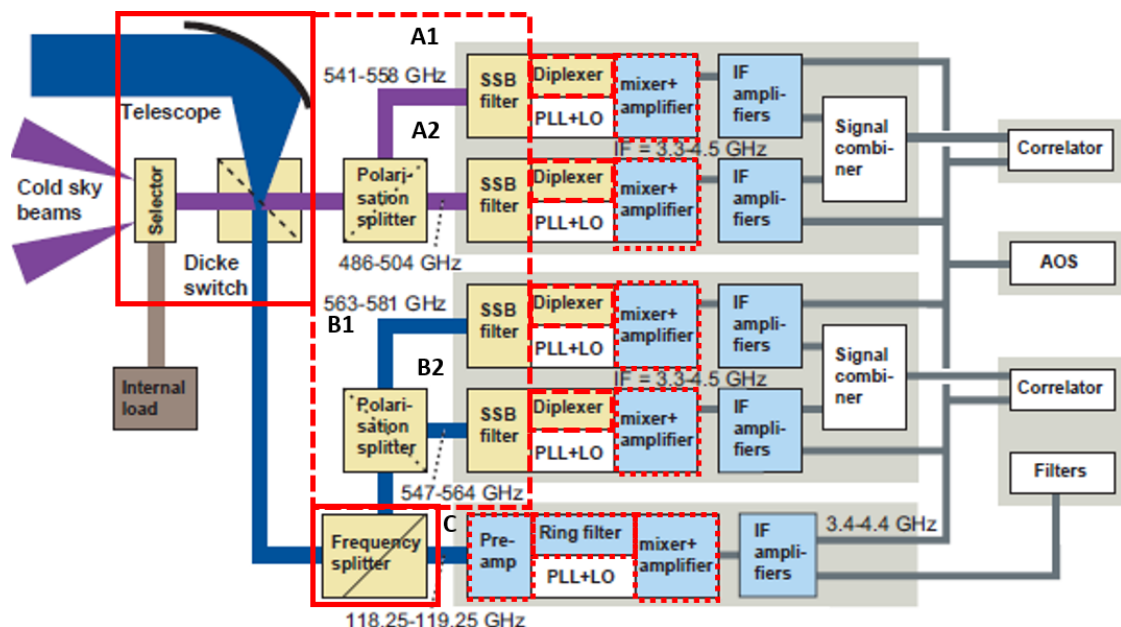


FIGURE 8.2: Block diagram of the SMR on the Odin satellite, adapted from Frisk et al. [14]. Red boxes indicate passive components that can currently be realized using 3-D printing, dashed red boxes indicate more demanding higher frequency candidates, and dotted red boxes represent advanced hybrid active/passive solutions.

The incoming radiation is observed through an antenna, which mechanically scans across the entire field of view, and is directed by a moving mirror (Dicke switch) to either receivers ‘A1’ / ‘A2’ or receivers ‘B1’ / ‘B2’ and ‘C’. This layout avoids the complete loss of all receivers during a mechanical failure of the Dicke switch. The antenna is a 1.1 m dual-reflector offset Gregorian reflecting telescope, with reflectors made from carbon-fiber-reinforced-plastic (CFRP) face sheets on CFRP honeycomb. The front surfaces are metalized with vacuum-deposited aluminium. This gives the antenna structural rigidity, whilst maintaining a low weight and low cost. An off-axis parabolic mirror, which has a similar function to the SMR antenna, has been previously reported by ICL [15].

The separation between the millimetre-wave channel ‘C’ and the THz channels ‘B1’ and ‘B2’ is achieved with a frequency-splitting dichroic filter (or diplexer); with 3-D printing at G-band, this would be achieved through a frequency selective surface (FSS). Within the THz blocks, the signals are split by polarization. This is done to provide redundancy; a mechanical or electrical failure with one polarization can be tolerated, as readings can still be taken using the other polarization. Wire-grid polarization splitters are a candidate analogue for these components.

Martin–Puplett interferometers are employed to provide single sideband filtering. This can also be achieved using 3-D printed waveguide bandpass filters. The received signal and local oscillator are fed into a diplexer, where they injected into the fixed-tuned mixers (these are waveguide-mounted Schottky diodes). The output intermediate frequency (IF) signal is then amplified, and the two polarizations are fed into a signal combiner. Such active component integration has not yet been achieved with polymer-based 3-D printed G-band waveguides, due to the lack of a suitable split-block assembly solution. However, given the success of the trough-and-lid assembly and the rapid rate of research in this field, this can be expected in the near future.

8.4 3-D Printed Millimeter-Wave Subsystem

8.4.1 HITRAN on the Web simulations

First, the center frequencies of the radiometer channels must be determined, with the selected frequency bands being of scientific interest. ‘HITRAN on the Web’ (HotW), which utilizes the ‘HITRAN’ spectral line database, can be used to provide spectral plots of atmospheric absorption lines, using line-by-line calculations to plot the absorption function (absorptance) A . This is a dimensionless quantity that represents the fraction of the radiative power that is absorbed, such that $A = P_{absorbed}/P_{incident} = 1 - P_{transmitted}/P_{incident} = 1 - T$, where T is transmittance [7]. Note that attenuation due to scattering can be ignored for interaction between gases and EM radiation at millimeter-wave and THz frequencies, which gives reflectance $R \approx 0$. Specific attenuation, which represents the gradient of attenuation with path length (usually represented in dB/km), can be calculated as $-10 \log_{10}\{T\} = -10 \log_{10}\{1 - A\}$ for a simulated/measured path length of 1 km. However, since HotW gives $A = 1$ for a path length of 1 km (resulting in infinite attenuation), the reference path length was chosen to be $L_{REF} = 0.1$ km. Since specific attenuation in dB per unit length scales linearly with path length, simulated results are scaled simply by multiplying by a factor of 10 [7].

Figure 8.3 shows the results of HotW simulations for five different atmospheric models, each representing the gaseous atmospheric mixture present at sea level for different latitudes and times of the year. In addition, simulations for dinitrogen monoxide (N_2O) and chlorine monoxide (ClO) in isolation are shown in the inset, exhibiting absorption lines at 150 GHz and 204.5 GHz, respectively. N_2O and ClO are released from fertilizers and chlorofluorocarbons (CFC), respectively. Both are major contributors to ozone depletion, with the former also being an important greenhouse gas [2]. The 150 GHz, 183.3 GHz, and 204.5 GHz absorption lines shown in Fig. 8.3 give the three center frequencies of the allocated frequency bands of scientific interest from the WMO-ITU [2].

Note that the variation in the specific attenuation observed at the H_2O spectral line is due to the variation in the water vapor content for each atmospheric model, with the greatest attenuation being the model of a tropical atmosphere.

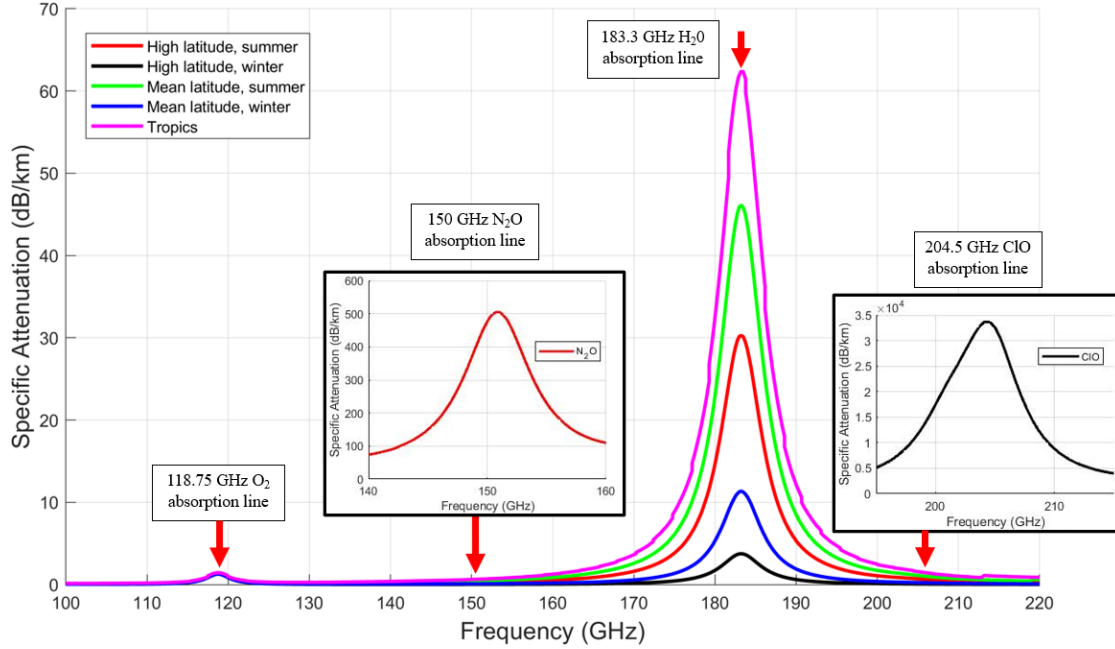


FIGURE 8.3: HotW simulations showing specific attenuation for five different sea-level atmospheric models; the absorption lines for N₂O and ClO are shown in the inset.

8.4.2 Subsystem Design

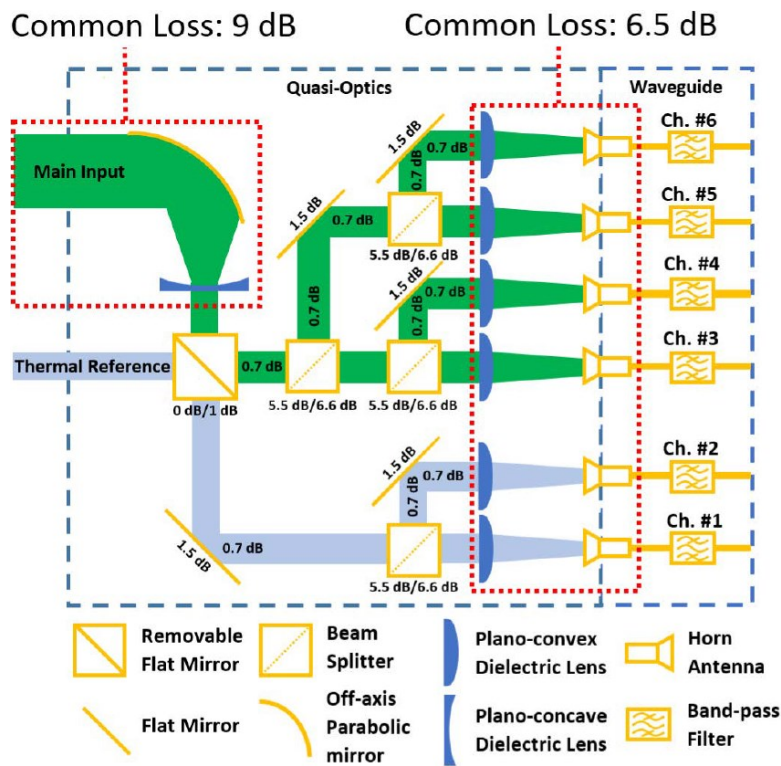
A block diagram overview of the subsystem is illustrated in Fig. 8.4(a), showing associated beam paths for each of the six channels. The design was based on that of the Odin SMR, as discussed in Chapter 8.3.1. This subsystem is designed for the three aforementioned allocated frequency bands (at 150 GHz, 183.3 GHz, and 204.5 GHz), with two orthogonally polarized channels per band (to provide redundancy for mechanical or electrical failure).

The main antenna for this subsystem is an off-axis parabolic mirror, which reflects the observed radiation onto a plano-concave lens, to give a collimated beam that can be manipulated quasi-optically. A removable planar mirror is employed for mechanically switching to a reference temperature, which functions similarly to the Dicke switch in the Odin SMR. When inserted, Channels #1 and #2 detect the reference temperature, with Channels #3 to #6 detecting the antenna temperature. When removed, Channels #1 and

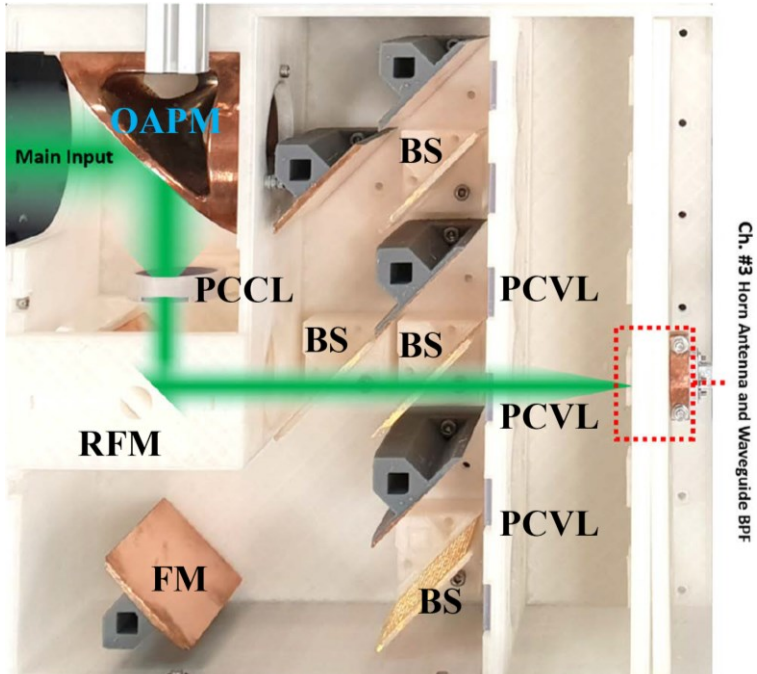
#2 detect the antenna temperature, with Channels #3 to #6 detecting the reference temperature. For application in an operational radiometer subsystem, this removable mirror must be automated to enable rapid switching.

Frequency- and polarization-splitting are performed using quasi-optical FSS high-pass filters and wire-grid polarizers, respectively. In future, MPRWG orthogonal mode transducers (OMTs) can be expected to perform polarization splitting at G-band.

The transition from the quasi-optical network to the waveguide network is achieved using feed horn antennas, with plano-convex lenses used to focus radiation into them. Subsequently, waveguide BPFs are used for frequency selection. These were reported in Chapter 6.3 and 6.4, with the transverse offset inductive iris-coupled 183.3 GHz BPF (introduced in Chapter 6.3.1) shown integrated into the subsystem in Fig. 8.4(b). In this diagram, the signal source is the VNA output connected to a horn antenna.



(a)



(b)

FIGURE 8.4: 3-D printed sub-THz subsystem: (a) block diagram overview of design; and (b) plan view photograph, with the 183.3 GHz BPF integrated.

In principle, most G-band MPRWG component types can be integrated into the waveguide network. In particular, 90° twists are necessary to ensure that the orthogonally polarized waveguide ports are restored to equal orientation with their adjacent channels. However, it was not possible to assemble the waveguide twists and BPFs together with sufficient tightness, which caused radiation leakage from the flange-to-flange connection. In future, this can be avoided by integrating these components together in 3-D printing.

S-parameter transmission and reflection results for the subsystem are given in Fig. 8.5. Channel #1 exhibited the lowest transmission loss of 21 to 24 dB across G-band, due to having the fewest components in its path. With the 183.3 GHz BPF integrated into Channel #1, a relatively insignificant additional loss is observed; this corresponds with the BPF's transmission response, as shown in Fig. 6.10, having a minimum insertion loss of 0.5 dB. The integrated measurements show that the filter's transmission and reflection characteristics are maintained.

OAPM = off-axis parabolic mirror

RFM = removable flat mirror

FM = flat mirror

PCCL = plano-concave lens

PCVL = plano-convex lens

BS = beam splitter

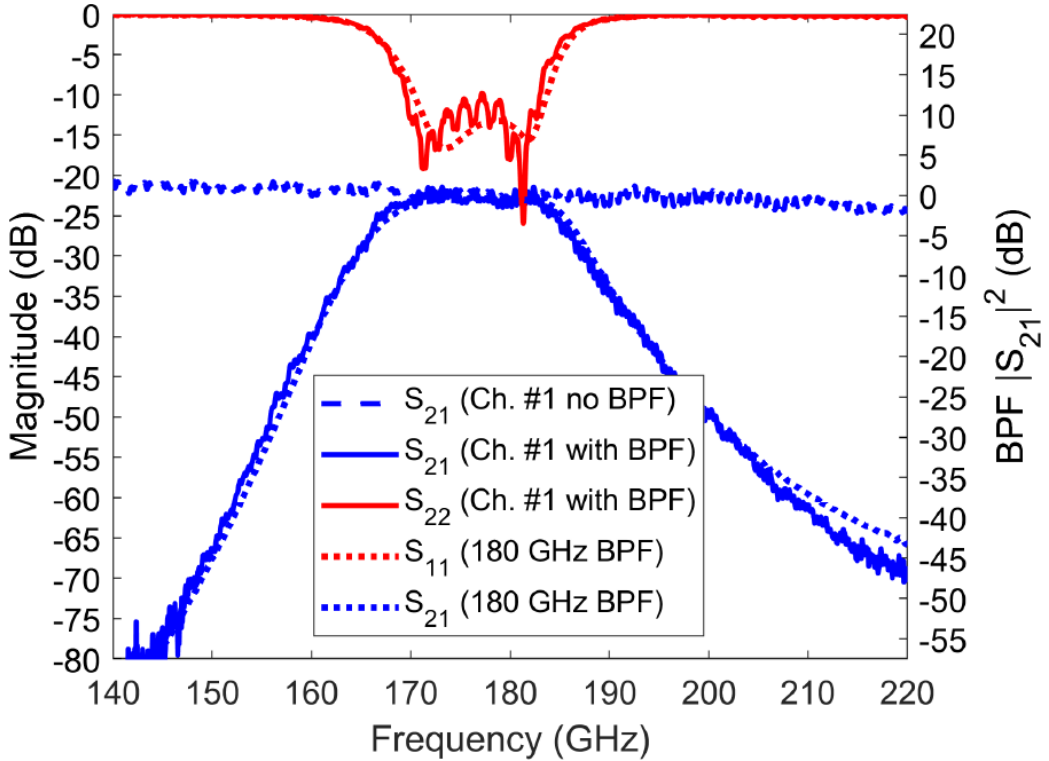


FIGURE 8.5: Assembled subsystem measurement integrated with the 3-D printed and copper electroplated 183.3 GHz TOII-coupled BPF, introduced in Chapter 6.3.1.

8.5 Conclusions

This chapter has covered the basics of radiometer design, and has introduced an example of a spaceborne radiometer subsystem that is currently operational. This design was used as the basis for ICL’s 3-D printed integrated subsystem, with the waveguide network employing bandpass filters connected to feed horn antennas. The measured results showed very little performance degradation due to the introduction of the BPF.

In future, this 3-D printed subsystem can be improved by ensuring that all 3-D printed MPRWGs can be easily assembled, enabling more complex waveguide networks. Furthermore, 3-D printing can create integrated waveguide components, thereby eliminating several flange-to-flange connections. As the need for lower cost and lower mass radiometer instrument increases, these improvements can be expected in the near future.

8.6 References

- [1] S.-H. Shin, R. Payapulli, L. Zhu, M. Stanley, X. Shang, N. M. Ridler, and S. Lucyszyn, “3-D printed plug and play prototyping for low-cost sub-THz subsystems,” *IEEE Access*, vol. 10, pp. 41708–41719, Apr. 2022.
- [2] World Meteorological Organization and International Telecommunications Union, “Use of radio spectrum for meteorology: weather, water and climate monitoring and prediction,” ITU, 2017.
- [3] D. G. Andrews, “An introduction to atmospheric physics,” 2nd ed., Cambridge, U.K.: Cambridge University Press, 2010.
- [4] F. S. Marzano and G. Visconti, Eds., *Remote sensing of atmosphere and ocean from space: models, instruments and techniques*, Dordrecht, The Netherlands: Kluwer, 2002.
- [5] J. J. Condon and S. M. Ransom, “Essential radio astronomy,” 1st ed., Princeton, NJ, U.S.A.: Princeton University Press, 2016.
- [6] N. Skou and D. M. Le Vine, “Microwave radiometer systems, design and analysis,” 2nd ed., Norwood, MA, U.S.A.: Artech House, Inc., 2006.
- [7] J. Sun, F. Hu and S. Lucyszyn, “Predicting atmospheric attenuation under pristine conditions between 0.1 and 100 THz,” *IEEE Access*, vol. 4, pp. 9377–9399, Nov. 2016.
- [8] M. A. Janssen, “MWR: microwave radiometer for the Juno mission to Jupiter”, *Space Science Reviews*, vol. 213, pp. 139–185, Mar. 2017.
- [9] J. W. Waters et al., “The Earth observing system microwave limb sounder (EOS MLS) on the Aura Satellite,” *IEEE Transactions on Geoscience and Remote Sensing*, vol. 44, no. 5, pp. 1075–1092, May 2006.
- [10] T. Kawanishi et al., “The advanced microwave scanning radiometer for the earth observing system (AMSR-E), NASDA's contribution to the EOS for global energy and water cycle studies,” *IEEE Transactions on Geoscience and Remote Sensing*, vol. 41, no. 2, pp. 184–194, Feb. 2003.

- [11] F. Weng, L. Zhao, R. R. Ferraro, G. Poe, X. Li and N. C. Grody, "Advanced microwave sounding unit cloud and precipitation algorithms," *Radio Science*, vol. 38, no. 4, Aug. 2003.
- [12] C. Muth, P. S. Lee, J. C. Shiue and W. Allan Webb, "Advanced technology microwave sounder on NPOESS and NPP," *2004 IEEE International Geoscience and Remote Sensing Symposium*, Anchorage, AK, USA, 2004, pp. 2454-2458, vol. 4.
- [13] M.-L. Frery et al., "Sentinel-3 microwave radiometers: instrument description, calibration and geophysical products performances," *Remote Sensing*, vol. 12, no. 16, p. 2590, Aug. 2020.
- [14] U. Frisk et al., "The Odin satellite- I. radiometer design and test." *Astronomy & Astrophysics*, vol. 402, no. 3, pp. 27-34, Mar. 2003.
- [15] S. Lucyszyn, X. Shang, W. J. Otter, C. Myant, R. Cheng, and N. M. Ridler, "Polymer-based 3D printed millimeter-wave components for spacecraft payloads," *IEEE MTT-S International Microwave Workshop Series on Advanced Materials and Processes (IMWS-AMP)*, Ann Arbor, USA, Jul. 2018 (Invited).

9. Discussion and Conclusions

This thesis, and the research articles given in the next Chapter, represent the current state-of-the-art in polymer-based 3-D printing of metal-pipe rectangular waveguide (MPRWG) components at G-band. First, a unique and exhaustive up-to-date literature review for 3-D printed MPRWG thru lines, twists and BPFs is given in Chapter 1. This timely review reveals three main challenges for G-band split-block designs: (i) EM radiation leakage loss; (ii) assembly part alignment; and (iii) manufacturing accuracy limitations. Chapters 2 and 3 provide an overview of the background to 3-D printing, rectangular waveguides, and millimeter-wave measurements.

1st Gen. MPRWG BPFs and 90° twists used a conventional symmetrical E-plane split design, with the former also employing an RF choke to mitigate against EM radiation leakage. However, fabricated components exhibited significant insertion loss, as EM radiation leakage was not mitigated against sufficiently. 2nd Gen. thru lines were fabricated as single-block waveguides, with metalization of the internal channel undertaken through a simple silver electroless plating process. Measured results exhibited a very high insertion loss, though this improved with added plating, suggesting that an insufficient plating thickness was the cause. Nevertheless, further plating applications and other potential solutions (e.g., using microfluidic pumps to push plating fluid directly into the channel) were not feasible at that time.

As a solution to the design challenges presented by the previous two Gens., I investigated the design and application of a ‘trough-and-lid’ assembly solution, using an H-plane *a*-edge split and lips that extend beyond the sidewalls to connect with the upper wall. This was used to realize 3rd and 4th Gen. thru lines, 4th Gen. 90° twists, 4th Gen. transverse offset inductive iris-coupled (TOII)-coupled BPFs, and symmetrical diaphragm inductive iris (SDII)-coupled BPFs; the latter three are the first such components to operate above 110 GHz. Fabrication was undertaken using an ultra-low-cost desktop MSLA 3-D printer. When compared to the 3-D printing, our outsourcing plating costs are high, but the overall cost is still low. In-house plating would dramatically reduce this cost.

In Chapter 4, it is shown that 4th Gen. 3-D printed thru line measurements demonstrate

an average α'_D across G-band of 12.7 dB/m (0.032 dB/ λ_g) for the 7.4 mm exemplar and 13.7 dB/m (0.035 dB/ λ_g) for the 10.4 mm exemplar, which compares well with all previously reported D- and G-band 3-D printed thru lines. Commensurate performance to the COTS counterparts is achieved above *ca.* 200 GHz. However, below *ca.* 200 GHz, rectangular-to-trapezoidal cross-sectional distortion (due to lip bending) causes additional attenuation. This was confirmed with EM re-simulations, by applying the measured effective mean aperture width $a_{mean} < a$; the resulting increase in the TE₁₀ mode cut-off frequency, from 116 GHz to 130 GHz, significantly increases the level of attenuation in the lower-half of the band. A more robust lip design should be investigated, having a reduced height and increased width, to mitigate lip bending.

In Chapter 5, it is shown that the 3-D printed and COTS #1 90° twists exhibit commensurate quantitative worst-case return losses of 13.2 dB and 12.9 dB, respectively. Furthermore, from two-port measurements, both exhibit commensurate qualitative average insertion losses, being approximately 0.62 dB. The retail cost of the measured COTS counterpart is a factor of $\times 8.5$ greater than the manufacturing cost of our ruggedized 3-D printed/plated 90° twist.

Detailed TDR analyses, for the thru lines and the twists, confirm that the flange-to-flange interfaces are the main source of reflections, with a qualitative comparison made between port wave impedance matching. Moreover, when tightly fixed to the measurement setup, the 3-D printed components are mechanically compressed in the longitudinal direction – approximately 0.5 mm (6.8%), 0.9 mm (9.1%) and 1.6 mm (5.0%) for the 7.4 mm thru line, 10.4 mm thru line and the twist, respectively. With the twists, TDR suggests that there is a significant return loss contribution from internal defects in COTS #1, which cannot be verified without destructive visual inspection.

In Chapter 6, for the TOII-coupled BPFs, the 150 GHz, 183.3 GHz, and 204.5 GHz exemplars exhibit respective minimum passband insertion losses of 1.0 dB, 0.5 dB, and 0.5 dB, with respective center frequency down-shifting of 2.3%, 3.7%, and 6.8%. To correct the passband down-shifting effects of iris corner rounding (ICR), a unique, systematic ICR compensation technique is introduced and subsequently applied to three 3-D printed SDII-coupled BPFs. As a result, the 155 GHz and 175 GHz exemplars exhibit

a low minimum passband insertion loss of 0.5 dB and 0.4 dB, with center frequency up-shifting of only 2.3% and 0.5%, respectively. Due to dimensional inaccuracy, the 200 GHz exemplar exhibited a minimum passband insertion loss of 0.7 dB, with center frequency up-shifting of 2.9%. Further improvement can be expected with: (i) close visual inspection and early part selection/rejection during manufacture; (ii) improved manufacturing process characterization and control; (iii) design iteration; and (iv) the additional application of pixel quantization pre-distortion for MSLA printers.

Chapter 7 introduces conductor surface roughness as an important contributor to additional insertion loss in all fabricated components. Two modifications of the Hemispherical model were investigated: the Extended and Huray-Hemispherical models, with $K(180 \text{ GHz}) = 1.32$ and 1.28, respectively. Both were applied to EM re-simulations in Chapters 4, 5, and 6, adding approximately 2-3 dB/m of additional attenuation across G-band. This is the first example of their use with 3-D printed MPRWGs.

Finally, Chapter 8 introduces the use of 3-D printed MPRWGs in radiometer front-end subsystems. This is expected to be an important future application of this technology, as it would enable satellite payloads with significantly lower mass and lower cost. First, the basic principle of radiometer design is introduced. Then, the Submillimeter Wave Radiometer (SMR) onboard the Odin satellite is introduced and explained, as this is an operational system that is reported in the open literature. This was used as the basis for a polymer-based 3-D printed G-band radiometer front-end subsystem, which employs six channels that operate within three frequency bands that are allocated for scientific purposes. This demonstrated the integration of a 183.3 GHz TOII-coupled waveguide BPF with a quasi-optical network, which was introduced in Chapter 6.3. Measured results demonstrate a minimal degradation in transmission loss due to the insertion of the BPF, corresponding to the low insertion loss of the individual component. In future, it is expected that more complex MPRWG networks will be integrated with quasi-optical networks, with the potential for hybrid active/pассиве circuit integration, which would represent further steps toward commercial application.

In summary, the continual advancements in desktop UV photocurable resin printing is leading to significant improvements in dimensional accuracy and surface finish quality. As a result, in the near future, this technology is expected to extend the trough-and-lid

assembly solution to MPRWG components operating at higher frequency bands and with a wider range of geometrical complexity (e.g., waveguide 90° bends and orthogonal mode transducers). Furthermore, integration of external components within the waveguide and integration into subsystems is also expected. The trough-and-lid assembly is now a viable solution for new upper-mm-wave MPRWG components. In specific areas of application for which performance and cost are the main drivers, this paradigm shift in the manufacture of millimeter-wave components and subsystems is likely to compete with traditional machined technologies in the not too distant future.

Publications

Published and Peer-Reviewed Journal Articles

1. **R. Payapulli**, L. Zhu, S.-H. Shin, M. Stanley, N. M. Ridler and S. Lucyszyn, “Polymer-based 3-D printed 140 to 220 GHz metal waveguide thru lines, twist and filters,” *IEEE Access*, vol. 11, pp. 32272-32295, Mar. 2023.
2. L. Zhu, **R. Payapulli**, S.-H. Shin, M. Stanley, N. M. Ridler and S. Lucyszyn, “3-D printing quantization predistortion applied to sub-THz chained-function filters,” *IEEE Access*, vol. 10, pp. 38944 - 38963, Mar. 2022.
3. S. H. Shin, **R. Payapulli**, L. Zhu, M. Stanley, X. Shang, N. M. Ridler, and S. Lucyszyn, “3-D printed plug and play prototyping for low-cost sub-THz subsystem”, *IEEE Access*, vol. 10, pp. 41708-41719, Apr. 2022.
4. L. Zhu, S.-H. Shin, **R. Payapulli**, T. Machii, M. Motoyoshi, N. Suematsu, N. M. Ridler, and S. Lucyszyn, “3-D printed rectangular waveguide 123-129 GHz packaging for commercial CMOS RFICs,” *IEEE Microwave and Wireless Component Letters*, vol. 33, no. 2, pp. 157-160, Jan. 2023.
5. L. Zhu, I. W. Rossuck, **R. Payapulli**, S.-H. Shin, and S. Lucyszyn, “3-D printed W-band waveguide twist with integrated filtering,” *IEEE Microwave and Wireless Component Letters*, (Early Access), DOI: 10.1109/LMWT.2023.3247942.

Appendix

Silver Electroless Plating Procedure

Equipment

- Beakers (250 ml). Labels: “Organic Solvents”, “Glucose”, “Silver Nitrate / Tollens’ Reagent”, “Sodium Hydroxide”, “Tollens’ Reagent”, ”Nitric Acid”, “DI Water”
- Conical flasks (250 ml). Labels: “Sodium Hydroxide”, “Glucose”, “Silver Nitrate / Tollens’ Reagent”
- Measuring cylinders: 10 ml and 100 ml
- Glass rods
- Petri dish
- Spatula spoon. Labels: “Sodium Hydroxide”, “Glucose”, “Silver Nitrate”
- Funnel
- Filter paper
- Pipettes (labelled). Labels: “Ammonium Hydroxide”, "Nitric Acid"
- Dropper bottle. Labels: “Ammonium Hydroxide”
- 2.5 L Winchester bottles
- Labelling tape
- Air jet cleaner
- Heated ultrasonic cleaner
- Thermometer
- Electronic balance
- Magnetic stirrer
- Magnetic stirring beads
- Tweezers
- Solvent wash bottles
- Lid for nitric acid beaker

Personal Protective Equipment

- Double gloves, large Marigold on top of small nitrile
- Splash goggles, face shield
- FFP2 mask
- PVC apron
- Clean room suit

Procedure

For a single plating run on one part:

1. Clean all equipment (beakers, conical flasks, glass rods, magnetic stirring beads): clean with acetone and isopropyl alcohol (IPA), rinsing with DI water after each solvent is used. Pour excess liquid into a **Winchester bottle** labelled “*Organic Solvent Waste ONLY*” and leave this aside in the fume hood.

For thorough cleaning, ensuring no contaminants exist on equipment surfaces that may reduce plating quality, rinse with a small amount of dilute nitric acid. Measure one part 68% nitric acid by using a **glass pipette** (labelled “*Nitric Acid*”) to decant the acid into a **measuring cylinder**, and add this to a **beaker** labelled “*Nitric Acid 1*”. Then measure 9 parts DI water in a larger **measuring cylinder**, pouring carefully to ensure there is no splashing, and add to the acid. Use this dilution to rinse the equipment. Pour the used nitric acid into a **different beaker** (labelled “*Nitric Acid 2*”, put a lid on it to stop fumes escaping, and leave aside. This can be used to neutralize the excess Tollens' reagent or dissolve plated silver at the end of the experiment.

Finally, rinse thoroughly with DI water and leave to dry (use an air jet if necessary).

2. Remove grease and residue from 3D-printed parts: fill an ultrasonic cleaner with water heated to 40°C. Place the 3D-printed parts in a **large beaker** of acetone

(labelled “*Organic Solvents*”), and then place the beaker(s) in the bath and clean for three minutes. Pour the used acetone into the organic solvent waste Winchester bottle, rinse the part in DI water, and then repeat this process with ethanol and then IPA in place of acetone. Pour excess ethanol and IPA into the organic solvent waste Winchester bottle and leave in the fume hood with the lid loosely screwed on.

For even more thorough cleaning, the parts can also be initially cleaned in soapy water (using washing up liquid) at 40°C for three minutes in the ultrasonic bath.

Dry the parts using an air jet (do NOT use a tissue as this would cause small fibers to stick to the parts, which could reduce plating quality) and keep them in a **clean container**.

Do NOT pour organic solvents directly into the ultrasonic cleaner.

3. Prepare the reducing agent solution: in a **beaker or conical flask** labelled “*Glucose*”, weigh 0.4g of glucose ($C_6H_{12}O_6$) using a **balance** and a **spatula / spoon** to decant the glucose powder. Dissolve in 10 ml of DI water, using a **glass rod**, vigorous agitation in a conical flask, or with a **magnetic stirrer**.

Note that, if changing the quantities used, the ratio of reducing agent to Tollens’ reagent must be kept at 5:1.

4. Prepare Tollens’ reagent: in **two separate beakers or flasks**, labelled “*Silver Nitrate / Tollens’ Reagent*” and “*Sodium Hydroxide*” respectively, weigh 0.5 g of silver nitrate ($AgNO_3$) and 0.35 g of sodium hydroxide ($NaOH$) using an electronic balance for measurement and a spatula / spoon to decant the chemical granules. Using a glass rod, swirling, or a magnetic stirrer, dissolve each in 25 ml of DI water to create solutions of 2% (w/v) silver nitrate and 1.4% (w/v) sodium hydroxide.

Next, ensure that there is a sufficient amount of 28% ammonium hydroxide (NH_4OH) contained in a designated **dropper bottle** labelled “*Ammonium*

Hydroxide" (add more from the original ammonium hydroxide bottle using a **glass pipette** labelled "*Ammonium Hydroxide*" if necessary). Add ammonium hydroxide dropwise to the silver nitrate solution, mixing well between drops by using a glass rod, swirling, or magnetic stirring. A brown precipitate of silver oxide will form. Continue to slowly add and mix drops of ammonium hydroxide until the solution becomes clear (all silver oxide reacts with the ammonium hydroxide and forms a diamminesilver(I) complex).

Then add all of the sodium hydroxide solution. A brown silver oxide precipitate will again form. Add and mix drops of ammonium hydroxide until the solution becomes clear again - this is the final Tollens' reagent, which is an alkaline diamminesilver(I) complex. This technique is used to ensure that the minimum necessary amount of ammonium hydroxide is used, so ammonia off-gassing should be negligible. Filter to remove any suspended particulates (which may reduce plating quality) using a **particulate filter and a funnel**, draining into **another beaker** labelled "*Tollens' Reagent*".

Keep used glassware aside. Use the Tollens' reagent IMMEDIATELY after producing it.

5. Plating: immerse the 3D-printed sample into the Tollens' reagent, agitating vigorously with a glass rod and shaking / swirling to remove trapped air bubbles within internal channels. Pour all of the glucose solution into the Tollens' reagent and agitate moderately with a **glass rod** and with shaking / swirling. Keep in mind that it is possible that ammonia may be released during agitation. A black to light brown precipitate will form, and silver will slowly begin to be deposited on all surfaces exposed to the solution. Keep agitating to ensure that liquid is continually flowing across exposed surfaces and internal channels. The silver deposition reaction takes place for 1 to 5 minutes, and is finished when the solution becomes clear and all the available silver has been deposited on the part and equipment surfaces.
6. Final clean: remove the plated part with tweezers and thoroughly rinse with DI water to remove loosely attached particles. Finally, dry using an air jet. Keep in a

clean container.

7. **Chemical disposal:** ALL reacted and unreacted Tollens' reagent must be neutralized in plenty of dilute nitric acid IMMEDIATELY after plating to prevent the formation of explosive silver nitride.

In a **measuring cylinder**, measure 10 ml of 68% (v/v) nitric acid (using a pipette labelled “*Nitric Acid*” to decant from the bottle) and add it to a beaker labelled “*Nitric Acid I*”. Then measure 90 ml DI water and add carefully to the same beaker. Pour the 100 ml acid solution through the used filter and funnel and into the beaker labelled “Tollens’ Reagent” (in which the plating was done). Any excess alkali will react with nitric acid vigorously, so make sure to be aware of this; if necessary, stop the neutralization by extracting the filter and funnel and placing them into the beaker labelled “*Silver Nitrate / Tollens’ Reagent*”. Stir the solution for 30 seconds with the used glass rod to make sure all silver and ammonium compounds are neutralized to silver nitrate and ammonium hydroxide, respectively. Plated silver should be dissolved to silver nitrate by the acid. Add this solution to a fresh, empty 2.5 L amber **Winchester bottle** labelled “*Inorganic Liquid Waste ONLY*”. The bottle should also be labelled with the chemicals that are expected to be main constituents of the liquid waste.

Rinse the beaker / flask labelled “*Silver Nitrate / Tollens’ Reagent*” with a small amount of nitric acid (use the contents of the beaker labelled “*Nitric Acid 2*”, if there are any, or prepare as above in the beaker labelled “*Nitric Acid I*”) and add to the inorganic waste Winchester bottle. Then rinse with a small amount of water and add to the inorganic waste bottle. Finally, rinse thoroughly with a large volume of water over the sink.

If there is still deposited silver on used glassware, this can be cleaned using dilute nitric acid (preparation steps as above). Add waste liquid to the Winchester and then rinse the equipment thoroughly in the sink.

The remaining glassware and measuring cylinders can be rinsed out with plenty of water over the sink.

Do not put the lid on the waste bottles for about fifteen minutes after filling to release any gas that may be coming from the waste mixtures. Then put the lids on and keep them loose. They can be kept in the fume hood until full, at which time it must be placed in the inorganic waste liquids section of the grey area.

8. Repeat the above process (omitting the cleaning step) if applying multiple coatings of silver.

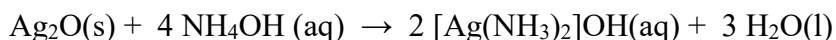
The entire process is repeated if plating on a new 3D-printed part.

Chemical Equations

1. Silver nitrate + ammonium hydroxide → silver oxide + ammonium nitrate+ water



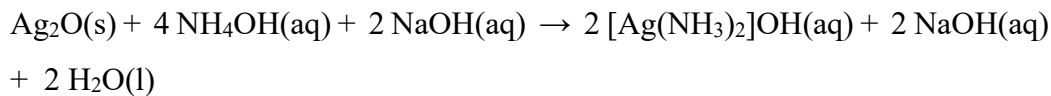
2. Silver oxide + ammonium hydroxide → diamminesilver(I) complex (Tollens' reagent) + water



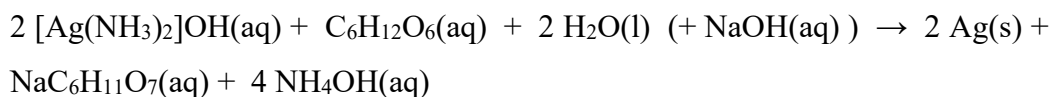
3. Silver nitrate + sodium hydroxide → Silver oxide + sodium nitrate + water



4. Silver oxide + ammonium hydroxide + sodium hydroxide + water → diamminesilver(I) complex (Tollens' reagent) + sodium hydroxide (reformed) + water



5. Tollens' reagent + glucose + water (+sodium hydroxide) → silver + sodium gluconate + ammonium hydroxide



6. Tollens' reagent + nitric acid → silver nitrate + ammonium nitrate + water

